

Investigating the Tensile Creep of Steel Fibre Reinforced Concrete

By

Christiaan Johannes Mouton

Thesis presented in fulfilment of the requirements for the degree of

Master of Science in Civil Engineering

at the Stellenbosch University



Promoter:

Prof. W.P. Boshoff

March 2012

Declaration

By submitting this thesis electronically, I declare that the entirety of the work contained therein is my own, original work, that I am the authorship owner thereof (unless to the extent explicitly otherwise stated) and that I have not previously in its entirety or in part submitted it for obtaining any qualification.

Date.....

SUMMARY

Research in concrete has advanced to such an extent that it is now possible to add steel fibres to concrete in order to improve its durability and ductility. This led to a research group in Europe, FIB, who has provided guidelines to designing Steel Fibre Reinforced Concrete (SFRC) structures. They have found that it is possible for SFRC beams in flexure to be in static equilibrium. However, the time-dependent behaviour of SFRC has not been researched fully and it requires further investigation.

When looking at a concrete beam in flexure there are two main stress zones, the compression zone and the tension zone, of which the tensile zone will be of great interest. This study will report on the investigation of the tensile time-dependent behaviour of SFRC in order to determine how it differs from conventional concrete. The concrete has been designed specifically to exhibit strain-softening behaviour so that the material properties of SFRC could be investigated fully. Factors such as shrinkage and tensile creep of SFRC were of the greatest importance and an experimental test setup was designed in order to test the tensile creep of concrete in a simple and effective manner.

Comparisons were made between the tensile creep behaviour of conventional concrete and SFRC where emphasis was placed on the difference between SFRC specimens before and after cracking occurred in order to determine the influence of steel fibre pull-out. The addition of steel fibres significantly reduced the shrinkage and tensile creep of concrete when un-cracked. It was however found that the displacement of fibre pull-out completely overshadowed the tensile creep displacements of SFRC. It was necessary to investigate what effect this would have on the deflection of SFRC beams in flexure once cracked.

Viscoelastic behaviour using Maxwell chains were used to model the behaviour of the tensile creep as found during the tests and the parameters of these models were used for further analyses. Finite Element Analyses were done on SFRC beams in flexure in order to simulate creep behaviour of up to 30 years in order to determine the difference in deflections at mid-span between un-cracked and pre-cracked beams.

The analyses done showed that the deflections of the pre-cracked SFRC beams surpassed the requirements of the Serviceability Limit States, which should be taken into account when designing SFRC beams.

OPSOMMING

Die navorsing in beton het gevorder tot so 'n mate dat dit nou al moontlik is om staal vesels by die beton te voeg sodat dit beton se duursaamheid en duktiliteit te verbeter. Dit het gelei tot 'n groep in Europa, FIB, wat dit moontlik gemaak het om Staal Vesel Beton (SVB) strukture te ontwerp. Hulle het gevind dat dit moontlik is vir SVB balke om in statiese ewewig te wees tydens buiging. Die tyd afhanklike gedrag van SVB is egter nog nie deeglik ondersoek nie en benodig dus verdere ondersoek.

Wanneer 'n balk in buiging aanskou word kan twee hoof spanningzones identifiseer word, 'n druk zone en 'n trek zone, waarvan die trek zone van die grootste belang is. Hierdie studie gaan verslag lewer oor die ondersoek van tyd-afhanklike trekgedrag van SVB om te bepaal hoe dit verskil van konvensionele beton. Die beton was spesifiek ontwerp om vervormingsversagtende gedrag te wat maak dat die materiaal eienskappe van SVB ten volle ondersoek kan word. Faktore soos krimp en die trekkruip van SVB was van die grootste belang en 'n eksperimentele toets opstelling was ontwerp om die trekkruip van beton op 'n eenvoudige en effektiewe manier te toets.

Daar was vergelykings getref tussen die trekkruip gedrag van konvensionele beton en SVP en groot klem was geplaas op die verskil tussen SVB monsters voor en na die monsters gekraak het om te bepaal wat die invloed was van staalvesels wat uittrek. Die byvoeging van staalvesels het beduidend die kruip en trekkruip van beton verminder. Daar was alhoewel gevind dat die verplasing van die uittrek van staalvesels heeltemal die trekkruip verplasing van SVB oorskadu het. Dit was nodig om te sien watse effek dit op die verplasing van SVB balke in buiging sal hê.

Viskoelastiese gedrag deur Maxwell kettings was gebruik om die gedrag van trekkruip, soos gevind deur die toetse, te modelleer en die parameters van hierdie modelle was verder gebruik vir analyses. Eindige Element Analises was gedoen op SVB balke in buiging om die trekkruip gedrag tot op 30 jaar te simuleer op die verskil tussen die defleksies by midspan tussen ongekraakte en vooraf gekraakte balke te vind.

Die analyses het gewys dat die defleksies van die vooraf gekraakte balke nie voldoen het aan die vereistes van die Diensbaarheid limiete nie, wat in ag geneem moet word wanneer SVB balke ontwerp word.

Acknowledgments

I would like to thank the following people for their support and their assistance:

- The staff of the Concrete Laboratory of the Structural Department of Civil Engineering of Stellenbosch University, with special recognition given to the Concrete Lab Manager, Mr Charlton Ramat.
- The staff of the Geotechnical Department of Civil Engineering for allowing me to use their equipment, with special recognition given to the Geotechnical Laboratory Manager, Mr Matteo dal Ben.
- The Structural Laboratory Manager, Mr Adriaan Fouché, for his assistance and guidance with the equipment used and his support and effort throughout my thesis.
- My promoter, Prof Billy Boshoff, for his guidance, support and critical questions, improving my knowledge about concrete and myself.
- Prof Gideon van Zijl, for his guidance, ideas and improving my knowledge about the time dependent behaviour of concrete.
- Dr Breda Strassheim for his effort and guidance with DIANA.
- Prof Peter Dunaiski, in his absence, for his guidance and knowledge for the steel design part of the thesis. Without him the design process would not have been the same.
- The staff of the Civil Engineering Workshop, Mr Dion Viljoen and Mr Johan van der Merwe, for their assistance, new ideas and guidance throughout the thesis period. They have improved my practical thinking to a large extent.
- My Lord and Saviour for His guidance and strength and for teaching me many virtues, of which patience is one.
- The administration department consisting of Ms Natalie Scheepers, Mrs Amanda De Wet and Arthur Layman for their assistance and diligence.
- Lastly my family, friends and colleagues who have supported me throughout my thesis period.

Without the people listed above the completion of my thesis would have been substantially more difficult and I sincerely thank all of them once again for all their support and guidance.

Table of Contents

1.	Introduction	11
2.	Background Information on SFRC, Creep and Shrinkage	14
2.1	The Advances in Concrete.....	14
2.2	Beam Section Theory	15
2.2.1	Conventional Reinforcing.....	16
2.2.2	Steel Fibre Reinforcing	19
2.3	SFRC.....	21
2.4	Creep.....	23
2.4.1	Compressive Creep	26
2.4.2	Tensile Creep.....	27
2.4.3	Fibre Pull-out.....	29
2.5	Shrinkage.....	31
2.6	Approaches to Creep and Shrinkage Modelling	33
2.6.1	Creep Modelling.....	33
2.6.2	Shrinkage Modelling	38
2.7	Concluding Summary	39
3.	Testing and Sample Production Procedures	40
3.1	Mix Design.....	40
3.1.1	SCC	40
3.1.2	SFRSCC.....	42
3.2	Sample Productions	44
3.2.1	Mould Design	44
3.2.2	Manufacturing of Steel Hooks	47
3.2.3	Casting Procedure	50
3.3	Tensile Tests.....	52
3.4	Steel Frames.....	56
3.5	Calibration.....	59
3.6	Tensile Creep Test Setup.....	62
3.7	Shrinkage Test Setup.....	66
3.8	First Creep Tests.....	67
4.	Experimental Results	68
4.1	Shrinkage.....	68
4.2	SCC Creep.....	71

4.3	SFRSCC Creep	72
4.4	SFRSCC Notched Un-Cracked Creep.....	74
4.5	SFRSCC Notched Pre-Cracked Creep.....	75
4.6	Comparison	78
5.	Analysis Procedures	82
5.1	FIB Model Code 2010.....	82
5.2	Maxwell Chain Model	85
5.2.1	SCC	86
5.2.2	SFRSCC.....	88
5.2.3	SFRSCC – N/P1.....	91
5.2.4	SFRSCC – N/P 2.....	92
5.2.5	SFRSCC – N/P 3.....	93
6.	Modelling Creep.....	95
6.1	Modelling Flexural Creep	95
6.1.1	Un-Cracked Flexural Creep.....	99
6.1.2	Pre-Cracked Flexural Creep.....	100
6.1.3	Serviceability Limit State.....	104
7.	Conclusions and Future Prospects	105
7.1	Conclusions	105
7.2	Future Prospects	106
8.	References	108
A.	Specimen Design	115
B.	Frame Design	118
B.1	Determine the Tensile Capacity.....	118
B.2	Frame Setup.....	121
B.3	Determining the Applied Force.....	121
B.4	Determine M_{max}	122
B.5	Detail A – Pivot Beam	129
B.6	Detail B – Compression Column	130
B.7	Detail C – Frictionless Pinned Connection	131
B.9	Detail D – Parallel Flat Bar Columns	133
B.10	Detail E – Stopper and Top Connecting Beam	136
B.10.1	Bending Capacity of Top Connecting Beam:.....	136
B.10.2	Axial Capacity of Stopper	139

B.11 Detail F – Bottom Connecting Beam.....	140
B.12 Detail G – Base Plate.....	142
B.13 Detail H – Frictionless Connection.....	154
B.14 Detail I – Weld Designs.....	156
C. Basic Kinematic Assumption.....	157
C.1 Zone 1:.....	162
C.2 Zone 2:.....	164
C.3 Zone 3:.....	169

Table of Figures

Figure 1 Section at mid-span of a conventionally reinforced concrete beam in flexure. _____	17
Figure 2 Beam section demonstrating stresses and forces being in equilibrium. _____	17
Figure 3 Tensile Stress vs Strain graphs of a) plain concrete and b) SFRC specimens. _____	19
Figure 4 Tensile Stress vs Strain graphs of a) plain concrete and b) SFRC specimens. (Lim et al., 1987) _____	23
Figure 5 Strain vs Time graph presenting the viscoelastic properties of concrete. _____	24
Figure 6 Figure presenting a single fibre embedded into concrete. (Gray, 1984) _____	30
Figure 7 Figure presenting the stresses acting on the fibre. _____	31
Figure 8 Graphical presentation of a spring-dashpot system. (Aklonis, 1981; Bower, 2002) _____	36
Figure 9 Maxwell model with multiple chains. (Aklonis, 1981) _____	37
Figure 10 Graphical presentation of the Slump Flow Test. _____	41
Figure 11 Graphical presentation of a hooked steel fibre. _____	43
Figure 12 Section of a SFRSCC cube demonstrating the lack of segregation _____	43
Figure 13 Schematic presentation of a typical beam mould. _____	45
Figure 14 Schematic presentation of the wooden blocks used in the beam moulds. _____	46
Figure 15 The wooden blocks fitted to the beam moulds. _____	46
Figure 16 The 18 mm hole drilled into the wooden blocks. _____	47
Figure 17 Steel hook specially modified for tensile strength tests. _____	49
Figure 18 Concrete specimen being tested in tension in the Zwick machine. _____	49
Figure 19 Figure demonstrating the interaction between the cables, connection and concrete specimen. _____	50
Figure 20 Steel Hooks incorporated into the beam moulds with wire loops used as spacers. _____	51
Figure 21 Beam mould ready for casting. _____	52
Figure 22 Presenting the concept of creep fracture. (Boshoff, 2007) _____	53
Figure 23 Concrete specimen being tested in tension. _____	54
Figure 24 Typical behaviour of SCC and SFRSCC prisms in tension. _____	55
Figure 25 Typical behaviour of SFRSCC prisms in tension with parameters defined _____	56
Figure 26 Graphical presentation of the steel frames used in the tensile creep tests. _____	57
Figure 27 Figure of steel frames to be used in tensile creep tests. _____	57
Figure 28 Figure of the stopper acting as a safety mechanism. _____	58
Figure 29 The loading was executed by weight plates. _____	63
Figure 30 The Spider8 data loggers used in the experiments. _____	64
Figure 31 An example of the LVDTs and aluminium frames used. _____	64
Figure 32 The secondary safety mechanisms a) Fitted to the frames with a spacing of b) more of less 5 mm. _____	65
Figure 33 The Shrinkage Beams were a) supported by PVC tubes and b) fitted with Perspex blocks. _____	67
Figure 34 Strain over time behaviour in SCC shrinkage specimens. _____	68
Figure 35 Strain over time graph with predicted shrinkage behaviour for SCC specimens. _____	69
Figure 36 Strain over time behaviour in SFRSCC shrinkage specimens. _____	70
Figure 37 Strain over time graph with predicted shrinkage behaviour for SFRSCC specimens. _____	70
Figure 38 Strain over time behaviour in SCC creep specimens, measured. _____	71
Figure 39 Calculated creep strains for SCC specimens. _____	72
Figure 40 Displacement over time behaviour in SFRSCC creep specimens, measured. _____	73
Figure 41 Calculated creep strains for SFRSCC specimens. _____	73
Figure 42 Displacement over time behaviour in notched SFRSCC creep specimens, measured. _____	74
Figure 43 Calculated creep strains for notched SFRSCC specimens. _____	74
Figure 44 Displacement over time behaviour in notched, pre-cracked SFRSCC creep specimens, measured. _____	75
Figure 45 Time-dependent behaviour of notched, pre-cracked SFRSCC Specimen 1. _____	76
Figure 46 Time-dependent behaviour of notched, pre-cracked SFRSCC Specimen 2. _____	77
Figure 47 Time-dependent behaviour of notched, pre-cracked SFRSCC Specimen 3. _____	77
Figure 48 Tensile creep displacements of notched, pre-cracked SFRSCC specimens. _____	78

Figure 49 Shrinkage strains of SCC and SFRSCC specimens. _____	79
Figure 50 Tensile creep strains of SCC and SFRSCC specimens. _____	79
Figure 51 The adjusted tensile creep strain of notched SFRSCC specimens. _____	80
Figure 52 Comparison of the creep displacements of the notched SFRSCC specimens. _____	81
Figure 53 Example of curve fitting done on the SCC experimental data. _____	83
Figure 54 Predicted tensile creep for SCC. _____	84
Figure 55 Maxwell curve fitted to SCC tensile creep curve. _____	88
Figure 56 Maxwell curve fitted to SCC tensile creep curve – logarithmic scale. _____	88
Figure 57 Maxwell curve fitted to SFRSCC tensile creep curve. _____	90
Figure 58 Maxwell curve fitted to SFRSCC tensile creep curve – logarithmic scale. _____	90
Figure 59 Maxwell curve fitted to notched, pre-cracked SFRSCC 1 tensile creep curve – logarithmic scale. _____	92
Figure 60 Maxwell curve fitted to notched, pre-cracked SFRSCC 2 tensile creep curve – logarithmic scale _____	93
Figure 61 Maxwell curve fitted to notched, pre-cracked SFRSCC 3 tensile creep curve – logarithmic scale _____	94
Figure 62 Beam model to be used in FEA. _____	96
Figure 63 Meshed beam, 10 x 10 mm elements. _____	96
Figure 64 Detail A – Left end of the modelled beam. _____	97
Figure 65 Detail B – Elements in mid-span. _____	97
Figure 66 Right end of the modelled beam. _____	98
Figure 67 Mid-span deflection of SFRSCC beam. _____	100
Figure 68 Stress distribution with compressive stress being at the top and tensile stress being at the bottom. _____	101
Figure 69 Mid-span deflection of the first pre-cracked SFRSCC beam _____	102
Figure 70 Graphical presentation of the first pre-cracked SFRSCC beam in deflection with mesh on display. _____	102
Figure 71 Elements of the first pre-cracked SFRSCC beam at mid-span. _____	103
Figure 72 Typical tensile concrete specimen. _____	116
Figure 73 Detailed design of steel hook _____	117
Figure 74 Cross-section of tensile concrete specimen. _____	119
Figure 75 Graphical presentation of tensile concrete specimens with forces applied. _____	120
Figure 76 Graphical presentation of a typical steel frame _____	121
Figure 77 FBD of pivot beam _____	121
Figure 78 Pivot beam with forces applied. _____	122
Figure 79 Modelled pivot beam with forces applied. _____	123
Figure 80 Pivot beam with forces applied and reaction forces included. _____	123
Figure 81 Pivot beam with all forces known. _____	124
Figure 82 Section $0 < x < 0.03$ of pivot beam. _____	124
Figure 83 Section $0 < x < 0.15$ of pivot beam. _____	125
Figure 84 Section $0 < x < 1.35$ of pivot beam. _____	125
Figure 85 Section $0 < x < 1.35$ of pivot beam. _____	126
Figure 86 Elements used in Prokon analysis of the pivot beam. _____	127
Figure 87 Supports and point-load _____	127
Figure 88 Supports and point load modelled on the pivot beam. (Prokon) _____	127
Figure 89 Supports and distributed load modelled on the pivot beam. (Prokon) _____	127
Figure 90 Maximum bending moments acting on pivot beam. (Prokon) _____	128
Figure 91 Maximum shear forces acting on pivot beam. (Prokon) _____	128
Figure 92 Graphical presentation of one of the pivot beams. _____	131
Figure 93 Section A-A clearly shows the steel bar passing through the needle roller bearing. _____	131
Figure 94 The relationship between F_{max} and F_{app} . _____	132
Figure 95 Graphical presentation of the parallel flat bar columns. _____	134
Figure 96 Section B-B presenting the pivot beam fitting through parallel flat bar columns. _____	135
Figure 97 Force acting on the top connecting beam. _____	136

Figure 98 Pivot beam modelled to find the forces acting on the top connecting beam. _____	136
Figure 99 Pivot beam with reaction forces included. _____	137
Figure 100 Model of top connecting beam. _____	138
Figure 101 Model of top connecting beam with forces included. _____	138
Figure 102 Model of top connecting beam with forces included analysed symmetrically. _____	138
Figure 103 Graphical presentation of the relationship between the top connecting beam and the stopper. ____	139
Figure 104 Graphical presentation of the bottom connecting beam. _____	140
Figure 105 Model of bottom connecting beam. _____	141
Figure 106 Model of bottom connecting beam with forces included. _____	141
Figure 107 Model of bottom connecting beam with forces included analysed symmetrically. _____	141
Figure 108 Plan view of the steel frames used in the experimental setup. _____	143
Figure 109 Geometrical design of the base plate. _____	144
Figure 110 Worst case loading scenario _____	144
Figure 111 Worst case loading scenario with reaction forces included. _____	145
Figure 112 Forces acting on the base plate. _____	146
Figure 113 Combined effect of the forces acting on the base plate. _____	146
Figure 114 Model of base prepared for design process. _____	147
Figure 115 Geometry of base plate viewed from the side _____	149
Figure 116 Section of base plate presenting the forces acting on the edge. _____	149
Figure 117 Simplified forces acting on the edge of the base plate. _____	150
Figure 118 Base plate viewed from the longitudinal side. _____	150
Figure 119 Effective cross-section of the base plate. _____	151
Figure 120 Longitudinal side view of the welds of the base plate. _____	152
Figure 121 Plan view of the base plate welds _____	152
Figure 122 Side view of the forces resisted by the base plate welds. _____	153
Figure 123 Graphical presentation of the frictionless connection. _____	154
Figure 124 Horizontal prismatic beam with cross-section included. _____	157
Figure 125 Prismatic beam in flexure. _____	158
Figure 126 Stress distribution of prismatic beam in flexure. _____	160
Figure 127 Stress distribution of prismatic beam in flexure with parameters defined. _____	160
Figure 128 Graphical presentation of strain softening depicted linearly. _____	161
Figure 129 Strain - stress distribution in a section of a beam in flexure exhibiting purely elastic behaviour. ____	162
Figure 130 Strain - stress distribution in a section of a beam in flexure before initial failure. _____	164
Figure 131 Strain - stress distribution in a section of a beam in flexure after initial failure. _____	167
Figure 132 Strain - stress distribution in a section of a beam in flexure after total failure occurred. _____	169

Chapter 1

1. Introduction

Research in concrete has advanced over the years to such an extent that it is widely used as a building material internationally (Shi and Mo, 2008). Research in concrete has allowed contractors and engineers to design structures knowing what to expect. The material properties of concrete such as the compressive strength, the elastic behaviour and even time-dependent behaviour are all factors required to design structures made from concrete. After years of research it is now possible to obtain these parameters and to use them in the design procedure. Coupled with the advantages of concrete, mainly its strong compressive strength and versatility during construction, it is easy to see why concrete is such a popular building material.

The biggest disadvantages of concrete are its low tensile strength and brittleness. The low tensile strength of the concrete is remedied by the high tensile strength of reinforcing steel bars cast into the concrete. Conventional reinforcing design has allowed the use of concrete and reinforcing steel bars in the same structure, however the detailing and fixing of the reinforcing steel bars can prove to be cumbersome. The brittleness of concrete also results in surface cracks appearing in the concrete during the service of the structure. The cracks have proven to be detrimental to the concrete because of moisture seeping into the cracks and causing the oxidation of the steel reinforcing bars which leads to corrosion of the steel.

These disadvantages have inspired researchers to combine fibre technology and concrete to make the concrete more ductile and to lessen the effect of cracking (You et al., 2011; ACI Committee 224, 2001). One advantage of incorporating fibres in reinforced concrete is that it is possible to mix the fibres with the concrete and casting it in situ. There are several different types of fibres that are available for commercial and experimental use. The basic categories are steel, glass, synthetic and natural fibre materials (ACI Committee 544, 2001). The main areas of concern of using fibres are fibre pull-out and fibre breakage. Fibre pull-out occurs after the composite has cracked with the load still applied, which will cause the fibres to debond from the concrete and pull out of the composite if the stress is high enough. The fibre pull-out is mainly influenced by the interfacial bond strength

between the concrete and the fibres. However, with steel fibres it is possible to change the geometry of the fibres in such a manner as to aid in the resistance of fibre pull-out. Hooked fibres would resist fibre pull-out more effectively because of the mechanical anchorage provided by the hooked ends (Lim et al., 1987; Li and Stang, 1997). Fibre breakage can most likely be avoided by using stronger fibres or lowering the applied forces.

Recently a design committee in Europe, FIB (Fédération Internationale du Béton), developed a new model code, FIB Model Code 2010, to be used for the design of fibre reinforced concrete with conventional reinforcement. Research in SFRC has advanced to such an extent that it was possible to incorporate the design of SFRC structures in the new model code. This design method made it possible to design SFRC beams in flexure that are in static equilibrium, but the time dependant effects have not been taken into account.

When a beam is loaded in flexure two stress zones will develop in the beam, namely a compressive stress zone and a tensile stress zone. The compressive stress can be managed by the compressive resistance of the concrete, but the tensile stress has to be managed by the reinforcing bar once the concrete has cracked. This situation led to the conventional concrete design method. However, with SFRC the tensile stress has to be withstood by the fibres bridging the crack, which makes it possible for the concrete to be structurally stable if it has been designed to exhibit strain-hardening behaviour. Little research has been done to determine what the time-dependent effects are of SFRC structures and/or designs.

During this study the time-dependent behaviour of Steel Fibre Reinforced Concrete (SFRC) was investigated in order to determine whether the use of SFRC is a viable option for designing structures. The type of fibres used was the hooked steel fibres and the type of concrete was Self Compacting Concrete (SCC). It has been found that there is little difference between the compressive creep of SCC and SFRC; however, the difference between the tensile creep of SCC and SFRC is unknown (Chern and Young, 1988). It was therefore necessary to determine whether the tensile creep of SFRC was more than the tensile creep of SCC and to see whether fibre pull-out had a significant effect on the tensile creep phenomenon. This would assist with the designs of SFRC structures.

A new testing procedure had to be designed in order to perform direct tensile creep tests on the concrete specimens. The most positive aspects of the few designs from the past were combined to create a simple and effective design (Kovler, 1994; Bisonette and Pigeon, 1995). The design used in this study consisted of steel frames that were loaded through a pivot arm with weights in order to

create a tensile stress in the concrete test samples. This design proved to be efficient in testing the tensile creep of the SCC and SFRC specimens and useful data was obtained from these tensile creep tests.

In Chapter 2 theoretical background information is given regarding the advances in concrete and Fibre Reinforced Concrete (FRC), typical time-dependent behaviour of cement-based materials and approaches to modelling these behaviours.

In Chapter 3 the test setup is explained, along with the manufacturing of the test samples. Important information, for example the casting procedure, the tensile tests of the specimens and the calibration methods are discussed as well.

In Chapter 4 the test results are presented and discussed. These results are processed so that they can be used for analysis procedures and it will be compared in order to understand the different mechanisms affecting the tensile behaviour of the test specimens.

The different analysis and modelling procedures used are explained in Chapter 5 and the tensile creep modelling of SFRC is done in Chapter 6, with the main focus on the effects of cracks on tensile creep.

The results and conclusions will be summarised in Chapter 7 along with future research prospects. In this chapter the possible shortcomings of the testing methods used are also discussed briefly to improve future research.

In the appendixes the design of the concrete specimens and steel frames are discussed in detail. The mechanisms acting in beams in flexure are also discussed to explain why certain assumptions were made.

Chapter 2

2. Background Information on SFRC, Creep and Shrinkage

2.1 The Advances in Concrete

Concrete is a common building material that has been used for the past 7000 years. In ancient times the Egyptians used concrete for the construction of the pyramids and the Romans used concrete as a building material for their structures for example the Colosseum, the Pantheon and the aqueducts. Research in concrete has advanced since Roman times to a point that concrete is now used for wider applications as a building material in modern society. These applications range from roads to exotic high rise buildings (Hunt, 2000).

SCC and SFRC have been some of the more recent additions to the advances in concrete technology and they can make a significant difference in concrete structures. SCC removes the need to compact concrete through external vibration (Colleparidi et al., 2007) and SFRC the ductility of concrete (Li and Stang, 2004). When combining the two different concretes to form Steel Fibre Reinforced Self Compacting Concrete (SFRSCC), it is possible to reduce the amount of labour and time of the casting process. This can be achieved by the elimination of the need to fix the reinforcing steel and vibrating the concrete. As seen in Appendix C it is theoretically possible to design SFRC structures with no conventional reinforcing, however the method found in FIB Model Code 2010 combines fibres with conventional concrete.

SCC is a type of concrete that can fill formwork and encapsulate reinforcing bars through the action of gravity while remaining homogenous. The general characteristics of SCC are that it has excellent flow properties and it has a high resistance to segregation. The mix constituents are similar to conventional concrete with the biggest difference being that SCC has a higher cement matrix-aggregate ratio with respect to conventional concrete (Colleparidi et al., 2007). In order to improve the mobility and to reduce the segregation of the concrete, superplasticiser and viscosity-modifying

admixtures are added. In addition, the aggregate used is reduced in volume and size and higher fines content is used, which aids in reducing segregation. It is usually necessary to make a few trial mixes in order to find a concrete mix that adheres to the requirements specified by the EFNARC 2002 Manual (EFNARC Specification and Guidelines for Self-Compacting Concrete, 2002).

Various tests were performed on concrete with different fibres added to investigate how these fibres changed the properties of conventional concrete (Soroushian and Bayasi, 1991). The most commonly used types of fibres are glass fibres, steel fibres, synthetic fibres and natural fibres, each with their own advantages. The biggest advantage of fibres is that they span the gaps formed by the cracks in the concrete, thereby improving the ductility of concrete (Brown et al., 2002). The two main types of fibres being used in concrete can be classified as follows: Low-modulus, High-elongations Fibres¹ and High-strength, High-modulus Fibres² (Swamy et al., 1974).

The main focus of this study was to use steel fibres to form SFRC and to investigate the time-dependent effects of SFRC in tension. In general steel fibres allow for the production of composites with ductile tensile mechanical behaviour. Steel fibres have a higher modulus of elasticity than concrete and by spanning the gap formed by cracking they can improve the ductility and tensile strength concrete. If the fibre content is high enough it is possible to improve the tensile strength of concrete after failure has taken place (Lim et al., 1987). If the tensile resistance of the composite increases after initial failure takes place it is called strain-hardening. However, this ductile tensile response comes to an end when the fibres break or fibre pull-out takes place.

Certain uncertainties, for example the shrinkage, tensile creep and fibre pull-out have to be investigated in order to make sure that SFRSCC is a viable building material. It was mentioned in the previous paragraph that SFRC can have a higher tensile strength than normal concrete mainly after cracking occurred, especially when it is designed in such a manner that strain-hardening takes place. The biggest area of concern is whether fibre pull-out occurs and if time will have an effect on fibre pull-out. The other uncertainty is if there is a difference between the tensile creep of SCC and SFRC. Experiments and investigations will give more clarity on these two areas of concern to further the development of concrete technology.

2.2 Beam Section Theory

This section will provide some insight to assumptions made in the designing methods and the stresses that occur in conventional concrete and SFRC beams that are subjected to flexural loading.

¹ Generally does not lead to strength improvement, but helps control cracking.

² Imparts strength and stiffness to the composite.

Short explanations will be given on how to determine the resisting moment in each case. These explanations will not go into detail because this would move away from the scope of the study. The mechanisms of beams in flexure can be found in Appendix C – Basic Kinematic Assumption.

2.2.1 Conventional Reinforcing

In order to understand the basic principles of conventional reinforcing design it is necessary to look at a section of a reinforced concrete beam in flexure, with the resisting stresses displayed. From this section certain basic assumptions are made:

- The tensile concrete resistance is ignored, which is logical seeing that the reinforcing steel will withstand the tensile stresses in the section.
- The strain distribution across the section is assumed to be linear. This means that the sections that were plane before bending occurred remain plane after bending.
- The ULS is reached if the compression strain at the extreme compressive fibre reaches a specified value. This is usually 0.0035 unless specified otherwise.
- The strains in the concrete and reinforcing steel are directly proportional to the distances from the Neutral Axis, at which the strains are zero.

From Figure 1 it can be seen that the section is divided into two main sections: the compression zone and the tension zone. The compression zone is above the Neutral Axis (NA) and represents the compressive stress (σ_{conc}) that is resisted by the concrete, also known as the compression block. The tension zone contains the tensile stresses (σ_{steel}) which are withstood by the reinforcing steel. The tensile resistance of the concrete is neglected because of the high tensile resistance provided by the reinforcing steel. By taking these stress resistances and converting them to forces it is possible to determine the internal moment of the section through equilibrium.

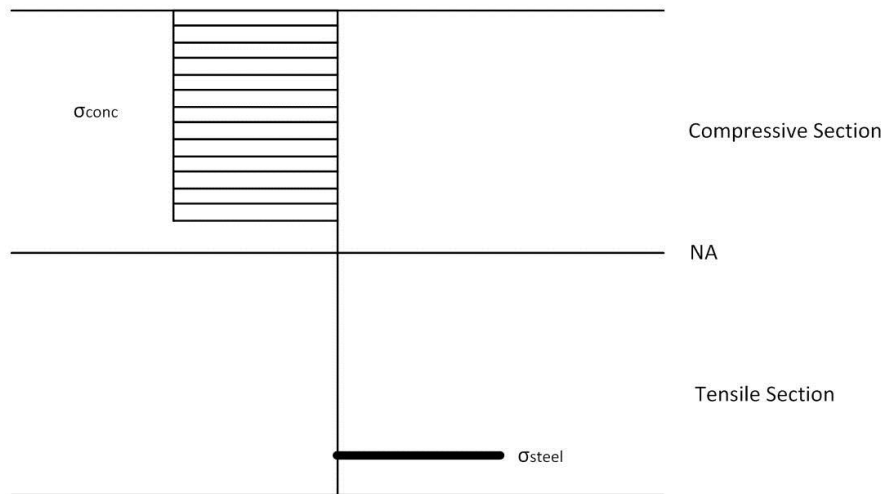


Figure 1 Section at mid-span of a conventionally reinforced concrete beam in flexure.

Considering the stresses and the forces in equilibrium:

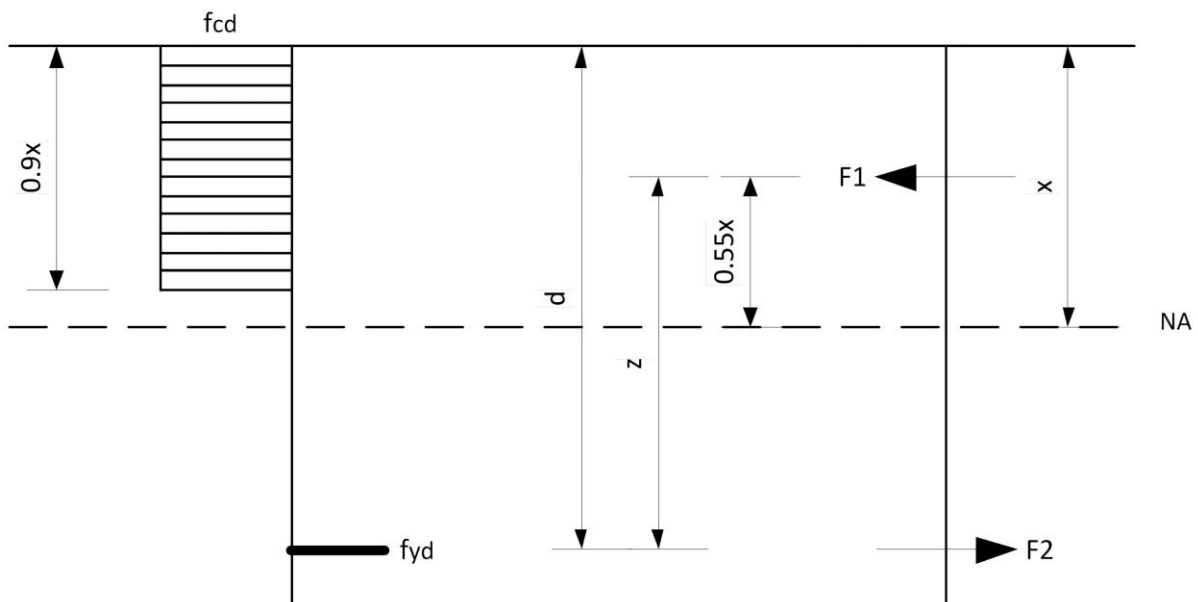


Figure 2 Beam section demonstrating stresses and forces being in equilibrium.

From Figure 2 the factor d is the distance from the extreme fibre of the compression zone to the centre of the reinforcing bars, z is the lever arm between forces $F1$ and $F2$ and x is the location of the NA, to be determined through equilibrium, demonstrated by the following calculations:

$$F1 = f_{cd} \times 0.9x \times b \quad (2.1)$$

$$F2 = f_{yd} \times A_s \quad (2.2)$$

Where f_{cd} is the compressive strength of concrete, f_{yd} is the tensile strength of the reinforcing steel, b is the width of the beam and A_s is the cross-sectional area of steel. When designing a conventional reinforced concrete beam to withstand a certain bending moment capacity it is

necessary to provide the abovementioned parameters. The compressive strength f_{cd} is usually specified at the beginning of the design process along with the width b of the beam. The tensile strength f_{yd} of the reinforcing steel is also specified by the engineer, which leaves the cross-sectional area A_s to be provided by the designer. The designer has to choose a certain diameter for the reinforcing steel in order to obtain A_s and then it is necessary to determine whether the diameter of the reinforcing steel is sufficient in withstanding the stresses and forces in the beam. This is done by taking the forces in equilibrium:

$$F1 = F2 \quad (2.3)$$

Which means

$$f_{cd} \times 0.9x \times b = f_{yd} \times A_s \quad (2.4)$$

From Equation 2.4 the following can be obtained:

$$x = \frac{f_{yd}A_s}{0.9f_{cd}b} \quad (2.5)$$

All the factors except x are known parameters, which makes it possible to determine a value for x . With x representing the location of the NA, where the stresses and strains in the section are zero, it is apparent that the process is a function of the reinforcing steel. All the other parameters are prerequisites for the design, but the designer can choose the amount of steel reinforcing as mentioned before. This means that the location of the NA relies on the amount of steel used in the design. From Figure 2 it is also apparent that

$$z = d - 0.45x \quad (2.6)$$

By substituting Equation 2.5 into Equation 2.6 it is now possible to calculate a value for z , which is necessary to determine the resisting moment. This is done by taking forces $F1$ or $F2$ resisted by the different materials and multiplying them with the distance z between these forces in order to find the resisting moment Mr as demonstrated by Equation 2.7.

$$Mr = F1z \text{ or } Mr = F2z \quad (2.7)$$

By substituting the different factors into Equation 2.7 the resisting moment Mr is as follows:

$$Mr = F1z = 0.9bf_{cd}xz \quad (2.8)$$

Or

$$Mr = F2z = f_{yd}A_s \left(d - 0.45 \left(\frac{f_{yd}A_s}{0.9f_{cd}b} \right) \right) \quad (2.9)$$

From Equations 2.8 and 2.9 the factor z is dependent on x , which in turn is dependent on A_s . This means that both expressions for determining the moment resistance of a conventionally reinforced

concrete beam are dependent on the diameter of steel chosen by the designer. Seeing that the amount of steel affects the position of the NA and the equilibrium of the section great care has to be taken to ensure that the compressive strength of the concrete is not exceeded. A certain point is reached when increasing the percentage of steel reinforcing leads to no advantage because the compressive strength of concrete will not be able to provide enough resistance, which leads to optimisation of the design.

The design can be optimised by prescribing a stronger concrete, by deepening the beam or by incorporating compression steel in the compression zone to aid in resisting the compressive forces. The design method explained above is a simplified method that is used throughout the majority of engineering communities with slight modifications made to incorporate safety factors according to the different design manuals of different countries.

2.2.2 Steel Fibre Reinforcing

The stress vs. strain ($\sigma - \epsilon$) Design Method has been designed by a Reunion Internationale des Laboratoires d'Essais et de Recherches sur les Matériaux et les Constructions (RILEM) committee in order to acquire design methods for SFRC ($\sigma - \epsilon$ Design Method, 2003). The design is based on the same fundamentals as the design of conventionally reinforced concrete. The Eurocode has been used as a framework for the development of this design method. The design method was originally developed without size-dependent safety factors, however after a comparison of the predictions of the design method and of experimental results of structural elements consisting of various sizes revealed an overestimation of the carrying capacity by the design method. Size dependent safety factors were therefore introduced. Figure 3 represents the stresses in a SFRC beam section:

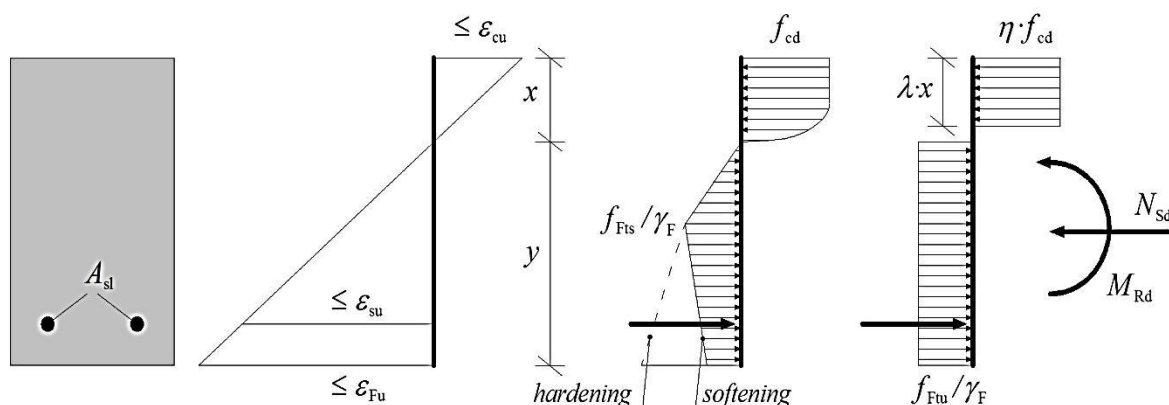


Figure 3 Tensile Stress vs Strain graphs of a) plain concrete and b) SFRC specimens.

Upon inspection it is noted that the figures in Figure 3 are similar to Figure 2 depicting the stresses in a conventional concrete section, with the biggest difference being that the concrete in the tensile

section has to withstand tensile stresses as well. The NA changes position in order to retain equilibrium as the stresses in the section change with the flexure. Figure 3 represents the combination of SFRC and reinforcing steel. It is possible to design a beam consisting purely of steel fibres and concrete, but it is more complex. The basic method of determining the bending capacity of a pure SFRC beam will be discussed in Appendix C – Basic Kinetic Assumption where Popov (1990) explains the mechanisms of bending.

After assessing the ultimate resistance of a cross-section of a SFRC beam certain assumptions had to be made:

- The plane sections remained plane and perpendicular.
- The stresses in the SFRC in compression and tension are obtained from the combined stress-strain diagram from Figure 3.
- The limiting compressive strain is taken as 0.0035 for cross sections not fully in compression, which is applicable for applications in flexure. This strain limit is the same as the strain limit for conventional reinforced concrete. The strain limit for cross-sections subjected to pure axial compression, as with columns, is taken as 0.002.
- For SFRC additionally reinforced with reinforcing steel bars, the strain is limited to 0.025.
- To ensure a sufficient anchorage capacity for the steel fibres, maximum deformation in the ULS is restricted to a crack width of 3.5 mm. If the crack width exceeds this limit special measures have to be taken.
- For certain exposure classes the contribution of the steel fibres near the surface should be reduced. In these cases the steel fibres in a layer close to the surface should not be taken into account.

For now it is necessary to see how steel fibres affect the design of conventional design parameters. A few parameters that are not included in the figures above have to be introduced in order to simplify the process. The parameter d_{SF} is introduced, d_{SF} is equal to the cover of the concrete with half the diameter of the reinforcing steel added. Another parameter h_{sp} is introduced, which is the depth of the beam with d subtracted. It is also noticeable that the stress in the reinforcing steel f_y/γ_m has been neglected. The parameters η , λ , γ_F and γ_m are all coefficients and safety factors to be chosen by the designer and do not affect the design process directly.

Now that the parameters have been introduced the next step is to determine the moment resistance M_{Rd} .

From equilibrium:

$\sum M = 0$:

$$M_{Rd} + (\eta \cdot f_{cd})(\lambda x)(0.5x - 0.5\lambda x) + \left(\frac{f_y}{\gamma_m}\right)(A_{sl})(y - d_{SF}) + \left(\frac{f_{Ftu}}{\gamma_F}\right)(y)(0.5y) = 0 \quad (2.10)$$

But $y = h_{sp} - x$

That leads to Equation 2.11:

$$-M_{Rd} = (\eta \cdot f_{cd})(\lambda x)(0.5x - 0.5\lambda x) + \left(\frac{f_y}{\gamma_m}\right)(A_{sl})(h_{sp} - x - d_{SF}) + \left(\frac{f_{Ftu}}{\gamma_F}\right)(h_{sp} - x)\left(\frac{h_{sp} - x}{2}\right)$$

After simplification:

$$M_{Rd} = -0.5(\eta \cdot f_{cd})(\lambda x^2 - \lambda^2 x^2) - \left(\frac{f_y}{\gamma_m}\right)(A_{sl})(h_{sp} - x - d_{SF}) - \left(\frac{f_{Ftu}}{\gamma_F}\right)(h_{sp} - x)^2 \quad (2.12)$$

From the expression above it is apparent that the design process for SFRC beams is complex and that several variables are needed in order to determine the moment resistance of the section. The whole method is explained fully in the FIB Model Code 2010 with all the methods to obtain these absent variables made available.

2.3 SFRC

The use of SFRC has been introduced commercially into the European market since the late 1970's. The early types of steel fibres were straight fibres produced by normal wire-drawing techniques. The use of these fibres was phased out because of the fibre pull-out being more significant with straight fibres than with hooked fibres (Li and Stang, 1997). It is relatively expensive to produce these straight fibres from the method mentioned above and the once the fibres debonded with the concrete, the straight smooth fibres produced little frictional resistance. This geometrical shortcoming led to the design of hooked and crimped fibres which provide some resistance once debondment took place. In this study hooked fibres were used.

Fibre reinforcement creates the possibility to improve the tensile strength and ductility of concrete after cracking has occurred. High strength, high modulus fibres like steel fibres produce strong composites, primarily imparting characteristics of strength and ductility to the composite. The reinforcing action by fibres occurs through the fibre-matrix interfacial bond stress when cracks form after the composite has exceeded the cracking strain of the matrix. Since the fibres are stiffer than the matrix, they experience less deformation and exert a pinching force at the crack tips, in this way acting as crack arrestors. In this manner the cracks are prevented from propagating until the composite ultimate stress is reached when failure occurs. This failure can happen either by the simultaneous yielding of the fibres and matrix or by the fibre-matrix interfacial bond failure.

Studies have shown SFRC with hooked steel fibres had higher ultimate strengths under flexural loading than straight or crimped fibres (Soroushian and Bayasi, 1991). Even though the descending branch of flexural load-deformation characteristics was steeper for the hooked fibres, it still had superior flexural strength. This led to a desirable post-peak energy absorption capacity when compared to the straight fibres.

The inclusion of steel fibres reduces the workability of concrete in its fresh state and it was found that the workability depends on the volume and type of steel fibres (Shah and Modhere, 2009). The workability improves when superplasticiser is used in such a manner that it is possible to pump SFRC successfully (ACI Committee 544, 1984). A study found that SFRC with hooked steel fibres have a lower slump value than SFRC with crimped fibres, which is desirable when SFRSCC is used (Soroushian and Bayasi, 1991). It is also possible to produce the hooked steel fibres into bundles using water-soluble glue, which makes them significantly easier to use. This method can effectively overcome the balling of fibres when mixing fresh concrete and improves the workability as a whole, even when higher volumes of fibres are used.

Steel fibres usually produced from slit sheet steel have the advantage of being cost effective when supplies of scrap metal are readily available. It is also possible to produce fibres from corrosion-resistant alloys when corrosion is considered. Another characteristic of SFRC is that the elastic modulus in compression and modulus of rigidity in torsion are the same than with plain concrete before cracking takes place. It has also been reported that steel fibres increase the fatigue resistance of concrete (Johnston and Zemp, 1991), which can be an advantage when the cyclic behaviour of structures is considered.

The biggest advantage of SFRC is that it is possible for structures to have a higher strength after failure because of an effect called strain-hardening. When looking at typical stress-strain graphs of tensile tests the effect can be explained more clearly in Figure 4.

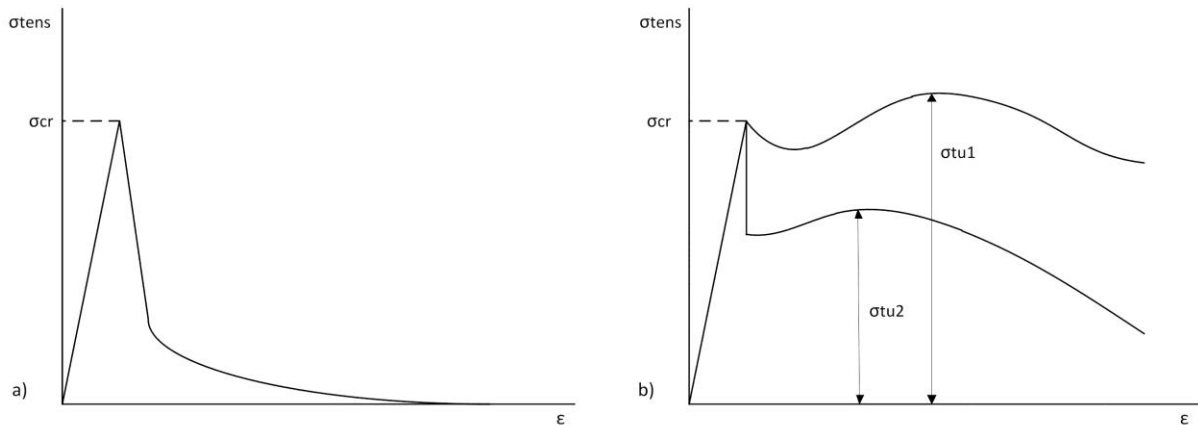


Figure 4 Tensile Stress vs Strain graphs of a) plain concrete and b) SFRC specimens. (Lim et al., 1987)

Figure 4 a) presents the tensile behaviour of plain concrete. It can be seen that a peak in the concrete strength is reached, which would be the ultimate strength of the concrete, but after the peak the concrete fails and offers little to no resistance. Figure 4 b) illustrates the behaviour SFRC under a tensile load. Like plain concrete a peak is reached and then failure occurs, but the steel fibres offer some resistance to increase the post-peak energy absorption capacity of the concrete.

In Figure 4 b) it can be seen that SFRC reacts differently according to the different volumes of concrete. The two main cases presented here are strain-softening (σ_{tu}^1) and strain-hardening (σ_{tu}^2). If the volume of fibres V_f is less than the critical volume V_{cr} , strain-softening occurs and for strain-hardening to occur, the opposite needs to happen. In this case the critical volume of fibres will cause the peak to be reached and the strength of the cracked composite will not be exceeding the ultimate tensile strength. From these results it can be seen that SFRC absorbs more energy than plain concrete, which is one of its advantages. Designers can use this information design structures that will be more ductile.

The SFRC used in this investigative report was designed to exhibit strain-softening behaviour. The reason for this is that the concrete structure has to crack in order to see whether the tensile creep and fibre pull-out effects are detrimental. Strain-hardening may hamper these events from occurring because of the high resistance a high volume of steel fibres will present. To make sure that strain-hardening does not occur, it is necessary to use low volumes of steel fibres. Having a fibre volume of 0.5% will allow strain-softening to occur and will cause the concrete to have a decent post-peak absorption capacity to allow for the case of cracked concrete.

2.4 Creep

Creep is defined as the time-dependent deformation in a body under constant stress or loading. When a constant stress is applied to a concrete specimen, the specimen will show an immediate

strain, where deformation will progress at a diminishing rate so that it may become several times more than the original strain. The immediate strain is referred to as the elastic strain and the time-dependent strain is referred to as the creep strain (Kong and Evans, 1987). This explains the viscoelastic behaviour concrete exhibits during time-dependent investigations. This becomes more apparent when the load is removed and the part of the strain which recovers immediately (instantaneous recovery) is less than the elastic strain. The delayed recovery of creep is called the creep recovery, which is much less than the creep (Kong & Evans, 1987). Figure 5 illustrates these phenomena.

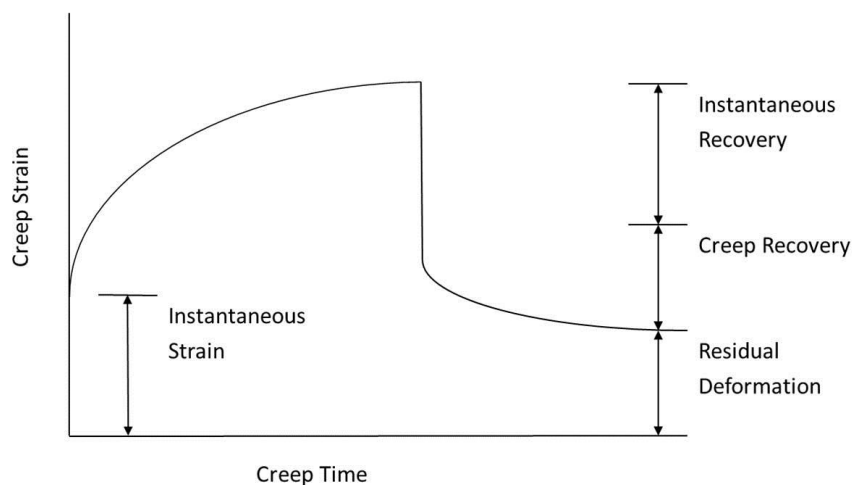


Figure 5 Strain vs. Time graph presenting the viscoelastic properties of concrete.

Figure 5 illustrates the concept of creep. It can be seen that instantaneous recovery took place immediately after the load had been released. The creep recovery happens with time after the load had been removed, but will never reach the zero point leaving residual deformation indicating permanent deformation.

Seeing that creep is affected by a constant load it can be assumed that creep will occur in concrete at all stress levels. Depending on the boundary conditions, stress relaxation also takes place, which is desirable unless the concrete structures surpass the serviceability state by deforming too much. These increased deflections can result in cracking when the strains exceed the strain capacity of concrete, which can lead to a loss in strength in the structure and corrosion of the reinforcing steel. Creep in slender structures could lead to large deflections, which can cause the structure to become unstable and fail.

The type of cement used only affects creep if it affects the different hardening rates of concrete. Other factors that do not affect creep significantly are factors whose effects are mainly due to their influence on the w/c ratio and cement-paste content. It has been found that concrete consisting out

of aggregates with high elasticity moduli and which are hard and dense have lower creep strains. The size, shape, surface texture and grading of the aggregates affects creep mainly due to their effects on the amount of water in the mix (Kong & Evans, 1987).

It is assumed in the FIB Model Code 2010 that there is a linear relationship between the creep of concrete and the applied stress for applied stresses up to 40% of the ultimate strength, which makes it possible to model creep. After that the behaviour of creep can be described as non-linear and it becomes more complex to model its behaviour. This study will have a phenomenological approach to creep modelling, seeing that many of the theories surrounding the mechanisms of creep are too complex. The one mechanism scholars agree upon that is essential to creep is the presence of evaporable water. The two time-dependent behaviours that are most significant in concrete are based on the diffusion of pore water, mainly creep and shrinkage.

Powers' (1965) opinion on creep is that it is caused by a diffusion of a load bearing water, because and external load changes the free energy of the adsorbed water. He describes creep and shrinkage as two different names for the same phenomenon with the only main differences being that shrinkage occurs whether loading occurs or not, but creep is dependent on an external load (Powers, 1965).

Wittmann (1982) argues that shrinkage and creep are based not only on a diffusion of water but on several other mechanisms in the ultramicroscopic scale namely: Expansion of single cell particles, expansion of pores and displacement of gel particles to name a few. When in the region of nanometres it becomes more difficult to research a material like concrete which is non-homogenous on a microscopic level seeing that the effects will differ greatly within the same material and the research will be too specific (Wittman, 1982).

To fully investigate the effects of creep one has to look at the macro-scale and investigate phenomenon itself. It can be conceived that macroscopic deformation of concrete caused by various stress, temperature and humidity regimes is a result of the cement/paste system at the micro level. That is why it is necessary to look at concrete as a homogenous material in the macro-scale and to find models through mathematical expressions which represent its time-dependent behaviour. These models can be used to predict what is most likely to happen with regard to deformation over time.

When looking at the creep of SFRC it has to be considered that the steel fibres mainly take effect when micro-cracking appears. The fibres will not affect the compressive creep significantly seeing that the fibres will mainly be in compression and the cracks that appear will be minimal and mostly

parallel to the load applied. However, with tensile creep the cracks will appear perpendicular to the load applied and it can therefore be deduced that the fibres will have a greater effect. These deductions will be discussed further in the next sub-sections of this chapter. Seeing that this study focuses mainly on the tensile creep of SFRC, the compressive creep will be discussed briefly and the tensile creep will be discussed in more detail.

2.4.1 Compressive Creep

The compressive strength of concrete is influenced by its degree of hydration, w/c ratio, cement type, aggregate strength and cement content to name a few factors. This means that important factors such as curing, age, temperature and humidity, all of which influence cement hydration, will have an effect on the strength development of concrete. The main influence of fibres on the material behaviour of concrete depends on the interfacial bond strength between the fibres and the matrix. Therefore the factors influencing the concrete strength will also affect the bond strength.

Previous experiments were done by Chern and Young (1988) to investigate the compressive creep of SFRC. The steel fibre content ranged between 0 and 2% by volume of mix. It was found that concrete with a higher percentage of fibre volume has a higher compressive strength and elastic modulus than plain concrete. The results also indicate that steel fibre reinforcement led to significant reductions in the creep of concrete with the creep decreasing progressively as the volume of fibres increase. They have also found that the creep reduction was higher when the fibre volume increased from 0% to 1% than from 1% to 2%. The results also showed that the fibres became more effective in restraining creep of the cement matrices as the time under load increased.

Their main finding was that the age of loading has a significant effect on the magnitude of creep, meaning that creep depends on the degree of hydration. They also found that concrete specimens with a higher volume of fibres yielded less shrinkage, less basic creep and less total deformation in a drying condition (Chern and Young, 1988).

Another study done by Mangat and Azari (1985) explained that compressive creep consists primarily of two components: delayed elastic strain and flowing creep. The delayed elastic component of creep forms a high portion of creep immediately after the load is applied and it rapidly reaches a limiting value. However, the flowing creep is small immediately after loading and is a function of time, meaning it increases with time. Steel fibres do not directly influence the delayed elastic component of creep since this deformation is of the same nature as the elastic deformation of concrete. Fibres provide restraint to the sliding action of the matrix relative to the fibre due to the flow component of creep, which is due to the fibre-matrix interfacial bond.

Their study showed that steel fibres restrain the creep of concrete at a 0.3 stress-strength ratio, owing to smaller lateral deformation caused by the axial stress (Mangat and Azari, 1985). It can therefore be concluded that steel fibres will reduce creep when loaded in the linear range. The main reason for this behaviour is because the fibre-matrix interfacial bond τ is primarily a function of the shrinkage of the matrix and the radial deformation caused by the axial stress (Mangat and Azari, 1985). As time passes the shrinkage becomes more prominent which leads to higher τ values, which gives a higher bond strength leading to less creep. The other factor that has to be taken into account is that at a 30% loading stress, the shrinkage might be more prominent than the creep itself.

2.4.2 Tensile Creep

Limited research has been found concerning the tensile creep of SFRC. Steel fibres might not be the strongest of all the fibres, but their geometrical properties make them useful in concrete especially when cracks form. The fibres can span the crack widths quite successfully, even when randomly orientated, and they can improve the tensile strength of concrete when strain-hardening behaviour is designed for. Even though many tests have been performed on fibre pull-out to such an extent that it was possible to develop a theoretical model to calculate interface properties (Li et al., 1991), it is uncertain what will happen when the time-dependent behaviour is taken into account.

According to another study done by Altoubat and Lange (2003) steel fibres were found to have enhanced the basic creep mechanisms and to reduce the drying shrinkage mechanisms. To be consistent with material behaviour the creep mechanisms were divided into beneficial aspects associated with real creep mechanisms and detrimental aspects associated with apparent creep mechanisms like micro-cracking. The real creep mechanisms are associated with deformation of hydration products like basic creep and stress-induced shrinkage, whereas micro-cracking is considered to be detrimental because of the associated microstructural damage. Steel fibres usually tend to enhance the beneficial mechanisms and reduce the detrimental ones. (Altoubat and Lange, 2003)

Total tensile creep composes of two components namely: basic creep and drying creep. The basic creep of concrete is a material property and is defined as the creep of concrete when moisture content remains constant. Drying creep, also known as the Pickett-effect (Pickett, 1942), is the increase of creep observed in specimens undergoing drying. Research has found that there are two major mechanisms that cause the Pickett-effect namely: micro-cracking and stress-induced shrinkage (Altoubat and Lange, 2001a; Altoubat and Lange, 2002). Micro-cracking results from non-uniform drying of a concrete specimen, which is to be expected due the non-homogenous nature of concrete. Stress-induced shrinkage results from local diffusion of pore water under stress between

capillary and gel pores, which promotes debonding and rebonding processes that are the main sources of creep.

It has been found that steel fibres tend to reduce the initial rate of basic creep, but increase the creep at later stages (Altoubat and Lange, 2001b). That means that relaxation by creep mechanisms in fibre reinforced concrete continues for a longer time than in conventional concrete. This is mainly due to the fibres that have the ability to arrest micro-cracks and to engage a larger volume of the matrix in stress transfer. This leads to a lower and more uniform internal stress intensity, which affects the creep rate. The increase in total basic creep is due to a larger volume of material being subjected to creep mechanisms.

Tensile creep tests under drying conditions provide data on the total tensile creep, which includes all components like basic creep, stress-induced shrinkage and micro-cracking. The results of the study done by Altoubat and Lange (2003) revealed that stress-induced shrinkage was a major component of the Pickett-effect for plain concrete and SFRC, with less stress-induced shrinkage exhibited from fibre reinforced concrete. The surface micro-cracking component was only significant in plain concrete and was significantly reduced when fibres were introduced. This led to the conclusion that fibre reinforcement suppresses surface micro-cracking associated with drying.

These results led to the following insights in the tensile creep of concrete. The stress relaxation by creep mechanisms of fibre reinforced concrete needs to be approached differently than the conventional method of looking at total tensile creep. It is suggested that stress relaxation by creep mechanisms are divided into two categories: beneficial and detrimental. Beneficial mechanisms relax stresses without damaging the material integrity, while the detrimental mechanisms relax stresses through deformation associated with microstructural damage.

The types of creep associated with stress-induced shrinkage mechanisms are assumed to be beneficial primarily because of the sliding/densification of cement hydration products, which are real mechanisms related to the concrete material. Creep associated with micro-cracking is considered to be detrimental because this type of deformation causes damage to the microstructure, which leads to cracking of the concrete causing the relaxation of stresses on the expense of material integrity.

They came to the conclusion that fibre reinforcement enhances stress relaxation by real creep mechanisms and it reduces the micro-cracking creep component. The suppression of micro-cracking reduces the drying creep of fibre reinforced concrete with the added advantage that it also aids the

material in sustaining stresses longer before failure. In practical applications drying creep is a more realistic phenomenon when considering structures exposed to the outside environment.

Usually creep calculations are based on the assumption that free shrinkage can be subtracted from the total strain experienced by the specimen to get the creep of the specimen (Bazant, 1988). This method is especially useful when considering tensile creep because the shrinkage strains will be in the opposite direction than the tensile creep strains, which will affect the curves obtained from the experimental curves. This method of superposition will be used when analysing the data after the creep experiments have been completed.

2.4.3 Fibre Pull-out

Generally cement-based materials such as mortars and concrete are known for being weak in resisting tensile stresses. Incorporating fibres usually makes up for this deficiency by resisting tensile forces through a composite action where the matrix resists part of the tensile force and the fibres takes up the balance (Shannag et al., 1997). The improvement in composite properties is largely attributed to the bond known as the shearing stress at the interface between the fibre and the surrounding matrix. When this bond is broken fibre pull-out occurs, usually when cracks occur in the matrix.

The biggest area of interest when investigating the tensile creep of SFRC is when the specimens crack. When this occurs the fibres will be bridging the crack and they will be the main mechanism in keeping the structural integrity of a concrete specimen. Studies have found that fibre pull-out can lead to global failure of concrete structures and that it has a significant effect in the equilibrium of stresses (Shannag et al., 1997). Taking this into account one has to determine what effect the fibre pull-out has on the deformation of the specimen when taken into account with the tensile creep. The pull-out characteristics of steel fibres have been studied as a function of several variables, namely the rate of load application, temperature of the environment, matrix quality, fibre geometry and fibre orientation (Morton and Groves, 1974) among others. However, the time-dependent behaviour of the pull-out of steel fibres has not been researched extensively.

In order to explain the basic mechanism of the bond strength between fibres and the concrete it is necessary to make certain assumptions. It has to be assumed that the fibres are uniform in length, strength and radius and that the fibres are randomly distributed throughout the matrix. It also has to be assumed that the stress is transferred uniformly between the fibre and the matrix depending on the maximum shear stress (τ) which can be sustained by the interface so that τ can be determined by the frictional forces at the fibre-matrix interface.

The two most prominent approaches used to interpret the material properties for the fibre debonding and pull-out problem are a shear lag model and alternatively a formulation based on fracture mechanics principles using the energy release rate criteria (Li et al., 1991; Stang et al., 1990). The shear lag model is based on the maximum shear strength criterion where debonding takes place when the maximum shear stress at interface reaches a critical value. The fracture mechanics approach is based on the assumption that the propagation of the debonding zone requires a certain energy and that debonding will only occur when the energy flowing into the interface exceeds the value of the specific resistance energy (Li et al., 1991). These two approaches differ substantially and provide different ways of calculating the interfacial properties; however the mathematical equations that are required for the calculations will not be discussed in this study. Experts in fibre pull-out problems have refined these approaches and have made it possible to determine the interfacial properties from models they have developed (Stang et al., 1990).

Li et al. (1991) have found that fibre pull-out has three stages:

First stage: The system deforms elastically as long as debonding does not occur.

Second stage: This stage is called the partial debonding stage. It is when debonding initiates and a region of debonding is generated farther into the interface until the fibre has debonded.

Third stage: The pull-out stage where complete debonding of the fibre has taken place and displacement occurs. This displacement can be expressed in various mathematical ways.

Even though the matter of debonding can be quantified and determined, it is often complicated and complex. Figure 6 will aid in understanding the basic mechanics of fibre pull-out.

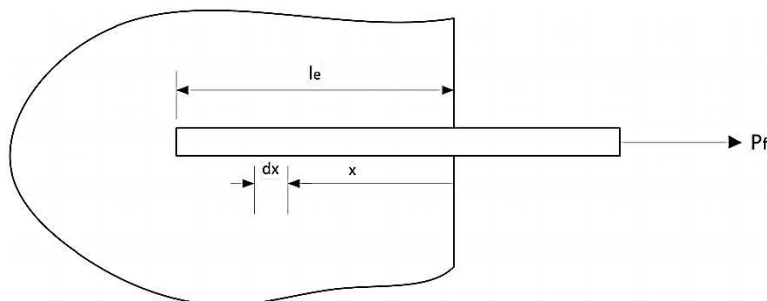


Figure 6 Figure presenting a single fibre embedded into concrete (Gray, 1984).

From Figure 6 it can be seen that l_e is the embedded length of the fibre, P_f is the load applied to the fibre and dx is a section in the fibre. Looking at section dx more closely in Figure 7 to examine the stresses affecting the fibre.

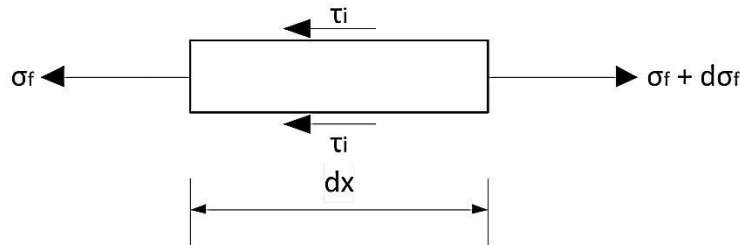


Figure 7 Figure presenting the stresses acting on the fibre.

The force P_f generates a stress σ_f in the fibre which is resisted by the shear stress τ_i . This simple model is generally used when considering the shear lag model in order to determine the material properties of the bond strength between the fibres and the matrix. From using the same principles as this model many researchers have developed different theories (Stang and Shah, 1986; Zhou et al., 1992; Naaman et al., 1991). These theories start off simple, but become more complicated as the calculations produce complex mathematical expressions.

However, the purpose of this study is not to look at the interfacial properties between steel fibres and concrete. The main focus of this study is to examine the phenomenological effects of fibre pull-out and tensile creep on the tensile deformation of concrete after cracking has occurred. It is important to investigate whether the fibre pull-out will overshadow the deformation caused by the tensile creep, causing the effect tensile creep to be considered negligible.

2.5 Shrinkage

As mentioned before, concrete experiences volume changes in both the fresh and hardened states whereas many of these changes are as a result of moisture movement into and out of concrete. The loss of moisture leads to the phenomenon of shrinkage and usually the biggest aspect of shrinkage is drying shrinkage because sealed concrete usually experiences less shrinkage than unsealed concrete (Bisonette and Pigeon, 1995). Drying shrinkage applies to this study seeing that all the concrete specimens were exposed to 60% ambient relative humidity and an ambient temperature of 23°C.

It should be noted that measured shrinkage of concrete in drying unsealed conditions will include two components, namely an autogenous component and a drying component (Holt, 2001). Autogenous shrinkage develops immediately after setting due to internal consumption of water in

hydration reactions and it reduces with time. Drying shrinkage is the shrinkage caused additionally by moisture loss from the concrete.

The type of volume change that is of the most concern is that which is associated with an interchange of moisture between hardened concrete and the environment. If the net flow of moisture is from the environment to concrete it results in an increase in volume called swelling, whereas the net flow of moisture from the concrete to the environment leads to a decrease in volume, which is termed drying shrinkage. Drying shrinkage can become detrimental, leading to the appearance of surface cracking.

Drying shrinkage can have two main effects, cracking (Benboudjema et al., 2004) and deflection (Gilbert and Wu, 2010), on structural performance. Short summaries about these two effects follow:

Cracking Effects: Unrestrained concrete will not crack due to shrinkage, but it is difficult to achieve a condition of zero restraint in a practical application. Usually the free shrinkage strain of concrete exceeds its tensile strain capacity and concrete that is restrained will crack. Cracking due to shrinkage may result in cracks of significant size, which may be aesthetically unacceptable and undesirable from a durability point of view. When it comes to liquid-retaining structures, cracks allowing leakage are unacceptable. Cracking commonly happens when the inner core dries more slowly than the outer zones, leading to surface cracking.

Deflection Effects: Shrinkage may affect deflections of flexural members in two distinct ways:

- In unsymmetrically-reinforced members the concrete experiences a greater degree of free shrinkage in the compression zone than the tension zone where the reinforcement provides a restraint.
- Time-dependent shrinkage may lead to additional tensile stress over and above the load-induced stresses in the tension zone. This leads to the existing cracks to increase in size, which can be detrimental to the structural integrity of the concrete as explained above.

Extensive studies have been done on the subject of shrinkage which led to various approaches in modelling shrinkage, all of them accurate to a certain degree. Some of the approaches to predict shrinkage in the design codes such as the SANS 10100-1:2000 and BS 8110 make use of tables and graphs to gain the relevant data concerning the shrinkage strain, making the process simple. Other

design manuals like the CEB-FIP model is more complicated and relies on a number of initial data that leads to higher degrees of estimation. The BS EN 1992:2004 distinguishes between drying and autogenous shrinkage and the total shrinkage strain is calculated by adding the two components together. The RILEM Model B3 is a sophisticated shrinkage model that was derived from the well-known researcher Bažant and his co-workers. This model incorporates the w/c ratio, cement type, cement content and aggregate:cement ratio along with the other factors, making this model too complicated to use at the preliminary mix design stage.

The modelling methods of shrinkage will be discussed briefly in the next chapter in order to obtain a modelling curve of the shrinkage experimental results, which is necessary to analyse the results of the creep experiments. As mentioned before the creep and shrinkage of concrete occurs simultaneously and superposition was used to find the creep strains.

2.6 Approaches to Creep and Shrinkage Modelling

Research in creep and shrinkage has advanced to such an extent that scientists were able to develop mathematical expressions that could model the behaviour of these two phenomena in an accurate manner. These expressions can incorporate many different factors that will influence the shape and magnitude of the curves these expressions produce.

2.6.1 Creep Modelling

The different design codes that are used in practice have different ways of modelling creep and even though they differ in method, there are a significant number of similarities. The most prominent similarities are that all the mathematical expressions produce an exponential curve, the expressions are dependent on the material properties and that the expressions incorporate the environmental effects on the concrete. This study focuses on the FIB Model Code 2010, therefore the creep model of this particular code will be discussed in more detail. Other models that are generally used to model a material's response under different loading conditions for creep are the Maxwell model (Aklonis, 1981), Kelvin-Voigt model (Bazant and Ashgari, 1974) and the Standard Linear Solid model (Bower, 2002). These models simulate viscoelastic behaviour by modelling the elastic and viscous components as linear combinations of springs and dashpots, respectively. Each model differs in the arrangement of these elements; however the Maxwell model proved to be quite simple and effective to use. The Maxwell chain will be discussed in more detail shortly.

2.6.1.1 FIB Model Code

The FIB Model Code 2010 models creep much in the same way as the Eurocode (BS EN 1992-1-1:2004) in the way that it uses the theory of Hooke's Law (Craig, 2000) in conjunction with a Creep

Factor. The Creep Factor can be calculated or estimated in different design codes, in order to find the strain as a function of time. Hooke's Law is a familiar theory that defines a linear elastic relationship between stress and strain and it is used extensively during theoretical and practical design processes. Hooke's Law is presented by Equation 2.13:

$$\sigma = E\varepsilon \quad (2.13)$$

In this case σ is the applied stress, E is the modulus of elasticity of the material and ε is the resulting strain caused by the stress applied to the material. The FIB Model Code 2010 adopts this same equation and rewrites it as a function of time to describe creep strain:

$$\varepsilon_{cc}(t, t_0) = \frac{\sigma_c(t_0)}{E_{ci}} \varphi(t, t_0) \quad (2.14)$$

Equation 2.14 is applicable for a constant stress $\sigma_c(t_0)$ applied at t_0 , where $\varphi(t, t_0)$ is the creep coefficient and E_{ci} is the modulus of elasticity at the age of 28 days. Upon inspection it can be seen that the creep coefficient is the only parameter that is a function of time, seeing that t_0 is a constant. In order for an exponential curve to exist, the creep coefficient has to contain a non-linear expression. The creep coefficient may be calculated from:

$$\varphi(t, t_0) = \varphi_0 \beta_c(t, t_0) \quad (2.15)$$

where:

φ_0 is the notional creep coefficient which can be estimated from an equation that will follow.

$\beta_c(t, t_0)$ is the coefficient to describe the development of creep with time after loading. This equation will have some form of a non-linear expression in order to plot an exponential curve that will describe creep.

t is the age of concrete in days at the moment considered.

t_0 is the age of concrete at loading in days, this is typically 28 days.

The notional creep coefficient may be estimated from:

$$\varphi_0 = \varphi_{RH} \cdot \beta(f_{cm}) \cdot \beta(t_0) \quad (2.16)$$

with

$$\varphi_{RH} = \left[1 + \frac{1-RH/100}{0.1 \cdot \sqrt[3]{h}} \cdot \alpha_1 \right] \cdot \alpha_2 \quad (2.17)$$

$$\beta(f_{cm}) = \frac{16.8}{\sqrt{f_{cm}}} \quad (2.18)$$

$$\beta(t_0) = \frac{1}{0.1+(t_0)^{0.2}} \quad (2.19)$$

where:

f_{cm} is the mean compressive cylinder strength at the age of 28 days in *MPa*

RH is the relative humidity of the environment in %

h is the notional size of the member in *mm* described as $2A_c/u$ where A_c is the cross-section in mm^2 and u is the perimeter of the member in contact with the atmosphere in *mm*.

$$\alpha_1 = \left[\frac{35}{f_{cm}} \right]^{0.7}, \alpha_2 = \left[\frac{35}{f_{cm}} \right]^{0.2} \quad (2.20)$$

The development of creep with time is described by a non-linear expression:

$$\beta_c(t, t_0) = \left[\frac{(t-t_0)}{\beta_H+(t-t_0)} \right]^{0.3} \quad (2.21)$$

with

$$\beta_H = 1.5 \cdot h \cdot [1 + (1.2 \cdot RH/100)^{18}] + 250\alpha_3 \leq 1500\alpha_3 \quad (2.22)$$

where:

RH is the relative humidity of the environment in %

h is the notional size of the member in *mm* as described above

$$\alpha_3 = \left[\frac{35}{f_{cm}} \right]^{0.5} \quad (2.23)$$

f_{cm} is the mean compressive cylinder strength as described above

In order to understand which factors affect the shape of the exponential curve the expression is written as follows:

$$\varepsilon_{cc}(t, t_0) = \frac{\sigma_c(t_0)}{E_{ci}} \varphi_0 \left[\frac{(t-t_0)}{\beta_H+(t-t_0)} \right]^{0.3} \quad (2.24)$$

Upon inspection it can be seen that the creep strain is dependent on the time t in *days* and that the part of the expression in brackets is the only part that cannot be condensed into one factor seeing

that it is also dependent on t , making it the function to the shape of the exponential curve. This information is extremely important, because it can be used to develop a prediction curve for creep behaviour.

2.6.1.2 Maxwell Chains

As mentioned before the Maxwell model simulates viscoelastic behaviour by modelling the elastic and viscous components as linear combinations of springs and dashpots (Aklonis, 1981; Bower, 2002). The elastic component is obtained from Hooke's Law and the viscous component can be modelled as dashpot so that the stress-strain rate relationship can be given as:

$$\sigma = \eta \frac{d\varepsilon}{dt} \quad (2.25)$$

where σ is the stress, η is the viscosity of the material and $\frac{d\varepsilon}{dt}$ is the time derivative of strain. The spring immediately responds if a fixed strain is suddenly applied by extension. As stress is produced in the spring, which is applied to the dashpot, the dashpot begins to be displaced at a rate proportional to the stress seeing that the dashpot cannot be displaced instantaneously. As time progresses the dashpot is displaced at a decreasing rate until the stress is zero, which makes this model applicable for stress relaxation. However, if a constant load is applied to this system, the initial strain will be the elastic strains of the springs. This strain will increase with time as the dashpots start to displace until they are fully extended and the springs are relaxed. The spring-dashpot system is depicted by Figure 8 the following way.



Figure 8 Graphical presentation of a spring-dashpot system. (Aklonis, 1981; Bower, 2002)

The spring and dashpot is connected in series whereas other models are arranged in other ways (Bower, 2002) . The model can be represented by Equation 2.26:

$$\frac{d\varepsilon_{Total}}{dt} = \frac{d\varepsilon_D}{dt} + \frac{d\varepsilon_S}{dt} = \frac{\sigma}{\eta} + \frac{1}{E} \frac{d\sigma}{dt} \quad (2.26)$$

With this model the stresses will gradually relax if the material is put under constant strain. When a material is put under constant stress, as is the case with creep, the strain has two components: an elastic component and a viscous component. As explained earlier the elastic component occurs instantaneously, corresponding to the spring, and relaxes immediately upon the release of the stress. The viscous component grows with time as long as the stress is applied. With these

components working together it will be possible to model the stress relaxation that happens when creep occurs. This model can combine many of these chains in parallel to model the material behaviour more accurately. Figure 9 represents a Maxwell model with the chains connected in parallel, with j representing an infinite number of chains.

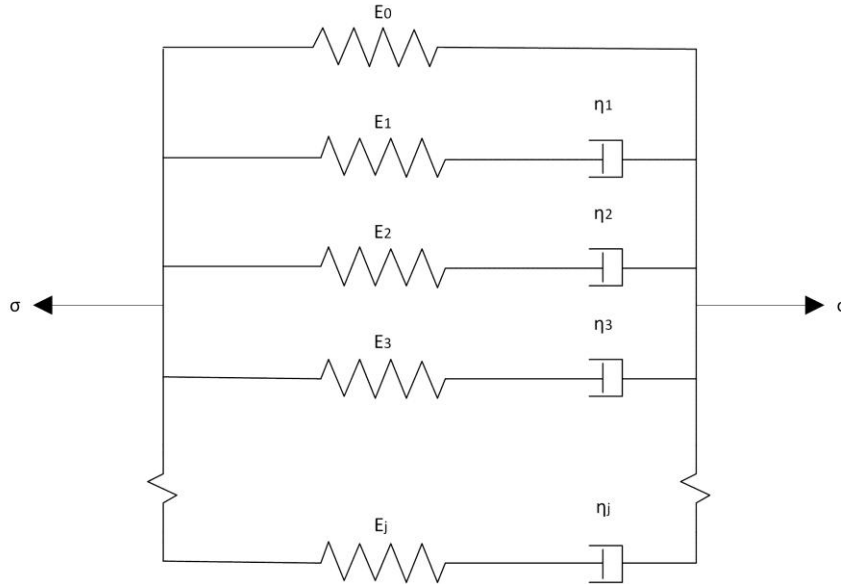


Figure 9 Maxwell model with multiple chains. (Aklonis, 1981)

The model depicted in Figure 9 can be used to do curve-fitting of existing data curves in order to give an idea to what time-dependent behaviour to expect in the future. When more than one Maxwell chains are incorporated into the model, Equation 2.27 is proposed: (Switek et al., 2010; Bažant and Wu, 1974)

$$\sigma(t, t_0) = \varepsilon_0 E_{tot}(t_0) \sum_{k=1}^n \frac{E_k(t_0)}{E_{tot}(t_0)} \cdot e^{-\frac{t}{\tau_k}}$$

where:

$$E_{tot}(t_0) = \sum_{k=1}^n E_k(t_0) \tag{2.28}$$

with τ_k being the retardation time of the dashpots, t the time in *days* and t_0 the time of loading in *days*. Equation 2.29 is proposed to describe the Maxwell model in a simpler manner:

$$\sigma = - \left[E_0 + E_1 e^{-\frac{t}{\lambda_1}} + \dots + E_n e^{-\frac{t}{\lambda_n}} \right] \varepsilon \tag{2.29}$$

In Equation 2.29 n represents the amount of chains in the Maxwell model and the negative sign is to describe the tensile creep behaviour. Equation 2.29 describes the behaviour of the Maxwell model accurately as can be seen in full simulations of this Maxwell model presented in Chapter 5.

2.6.2 Shrinkage Modelling

The FIB Model Code 2010 also adopted the same technique for modelling shrinkage as the Eurocode in the way that the total shrinkage is separated into autogenous shrinkage and drying shrinkage. According to the model code the drying shrinkage decreases with decreasing w/c ratio and decreasing cement content and the autogenous shrinkage increases with decreasing w/c ratio and decreases with decreasing cement content. The FIB Model Code 2010 expresses the total shrinkage or swelling strains as:

$$\varepsilon_{cs}(t, t_s) = \varepsilon_{cas}(t) + \varepsilon_{cds}(t, t_s) \quad (2.30)$$

In Equation FIB 5.1-75 it can be seen that the total shrinkage strains are divided into the autogenous shrinkage $\varepsilon_{cas}(t)$ and the drying shrinkage $\varepsilon_{cds}(t, t_s)$, which, in turn, is depicted by the following equations:

$$\varepsilon_{cas}(t) = \varepsilon_{cas0}(f_{cm}) \cdot \beta_{as}(t) \quad (2.31)$$

$$\varepsilon_{cds}(t, t_s) = \varepsilon_{cds0}(f_{cm}) \cdot \beta_{RH}(RH) \cdot \beta_{ds}(t - t_s) \quad (2.32)$$

where:

t is the concrete age in *days*

t_s is the concrete age at the beginning of drying in *days*

$(t - t_s)$ is the duration of drying in *days*

f_{cm} is the mean compressive cylinder strength at the age of 28 days in *MPa*

The notional autogenous shrinkage coefficient $\varepsilon_{cas0}(f_{cm})$ needed to calculate the autogenous shrinkage component $\varepsilon_{cas}(t)$ may be calculated by:

$$\varepsilon_{cas0}(f_{cm}) = -\alpha_{as} \left(\frac{f_{cm}/10}{6+f_{cm}/10} \right)^{2.5} \cdot 10^{-6} \quad (2.33)$$

Whereas the time function $\beta_{as}(t)$ also needed to calculate $\varepsilon_{cas}(t)$ may be calculated by:

$$\beta_{as}(t) = 1 - \exp(-0.2 \cdot \sqrt{t}) \quad (2.34)$$

The coefficient α_{as} depends on the type of cement and can be found in Table 5.1-13 of the FIB Model Code 2010. Coefficients like the notional drying shrinkage coefficient $\varepsilon_{cds0}(f_{cm})$, the coefficient taking the relative humidity into account $\beta_{RH}(RH)$ and the function describing the time-

development for calculating the drying shrinkage $\beta_{ds}(t - t_s)$ will be necessary to calculate the drying shrinkage. These coefficients are expressed the following way:

$$\varepsilon_{cds0}(f_{cm}) = [(220 + 110 \cdot \alpha_{ds1}) \cdot \exp(-\alpha_{ds2} \cdot f_{cm})] \cdot 10^{-6} \quad (2.35)$$

$$\beta_{RH} = -1.55 \cdot \left[1 - \left(\frac{RH}{100} \right)^3 \right] \text{ for } 40 \leq RH \leq 99\% \cdot \beta_{s1} \text{ and } 0.25 \text{ for } RH \geq 99\% \cdot \beta_{s1} \quad (2.36)$$

$$\beta_{s1} = \left(\frac{35}{f_{cm}} \right)^{0.1} \leq 1.0 \quad (2.37)$$

$$\beta_{ds}(t - t_s) = \left(\frac{(t - t_s)}{0.035 \cdot h^2 + (t - t_s)} \right)^{0.5} \quad (2.38)$$

The coefficients $\alpha_{ds1}, \alpha_{ds2}$ depend on the type of cement and can also be found in Table 5.1-13. The other coefficients have been defined in the previous section when the creep model of the FIB Model Code 2010 was discussed.

The expression that is most important in determining the shape of the exponential curve that is characteristic to shrinkage behaviour is the time-development function $\beta_{ds}(t - t_s)$. By substituting other factors in front of the function it is possible to do curve-fitting to data curves obtained from experimental results. Examples of curve fitting done by these expressions can be seen in Chapter 5.

2.7 Concluding Summary

The advances in concrete technology have led to the possibility of designing SFRC structures in order to produce concrete structures that are more ductile. The design methods for fibre reinforced concrete found in the FIB Model Code 2010 and $\sigma - \varepsilon$ Design Method do not take the time-dependent behaviour of fibre reinforced concrete into account. It is well-known that concrete experiences time-dependent behaviour such as creep and shrinkage. From the section of a SFRC beam it can be seen that the tensile stress capacities of the concrete are taken into account. It is therefore necessary to understand the time-dependent behaviour of concrete in tension as it could possibly be detrimental to the structural integrity of a concrete structure, especially after cracking occurred.

The fibre pull-out behaviour of fibres in cracked fibre reinforced concrete can have a significant effect on the stability of the structure as it is a mechanism that cause large deformations as the fibres pull out of the composite. Numerical models are therefore implemented to model and extrapolate the time-dependent behaviour of un-cracked and cracked SFRC in order to understand and investigate the implications it could have on the stability of SFRC structures.

Chapter 3

3. Testing and Sample Production

Procedures

In order to investigate the time-dependent behaviour of SCC and SFRSCC in tension it was necessary to develop different concrete mixtures in such a manner so that they would have approximately the same compressive strength. The concrete specimens were designed especially in order to be fitted to large steel frames that have been manufactured to perform tensile time-dependent tests.

3.1 Mix Design

3.1.1 SCC

When developing self-compacting concrete (SCC) it is important to have a concrete that exhibits sufficient flowing behaviour without segregation taking place. There are certain aspects and rules that have to be adhered to in order for a concrete to be classified as SCC, which are stipulated in the EFNARC 2002 Manual (EFNARC Specification and Guidelines for Self-Compacting Concrete, 2002). The mix design for SCC differs from conventional concrete mixes in the way that the aggregate used is reduced in volume and size, higher fines content is used and superplasticiser is usually added (Collepardi et al., 2007). In general other extenders like condensed silica-fume and other viscosity-modifying admixtures are added to achieve sufficient segregation resistance and stability. The mix design procedures rely heavily on experimental testing of trial mixes.

There are certain tests specified by the EFNARC 2002 Manual that can be performed in order to classify concrete as SCC. The simplest test to perform is the slump flow test (Department of Public Works, 1993), which is well known to concrete mix designers. There are some minor differences between the slump flow tests of conventional concrete and SCC. With SCC the slump cone is placed on a flat plate and filled with concrete, but it will not be compacted with a tamping rod as with conventional concrete. The cone is then lifted vertically in a smooth motion so that the concrete can

flow out at the bottom to create a circular pool of concrete on the flat plate. The concrete should reach a spread diameter of 500 mm within 3 – 7 seconds in order to be classified as SCC. The concrete is then examined visually to detect whether segregation takes place. Segregation is indicated by an accumulation of coarse aggregates in the centre of the pool. The coarse aggregates should be distributed evenly across the pool of concrete and should be present at the pool's periphery. This should also be checked for bleeding at the edges, which also indicates segregation of the mix. Figure 10 provides a good graphical presentation of the slump flow test.

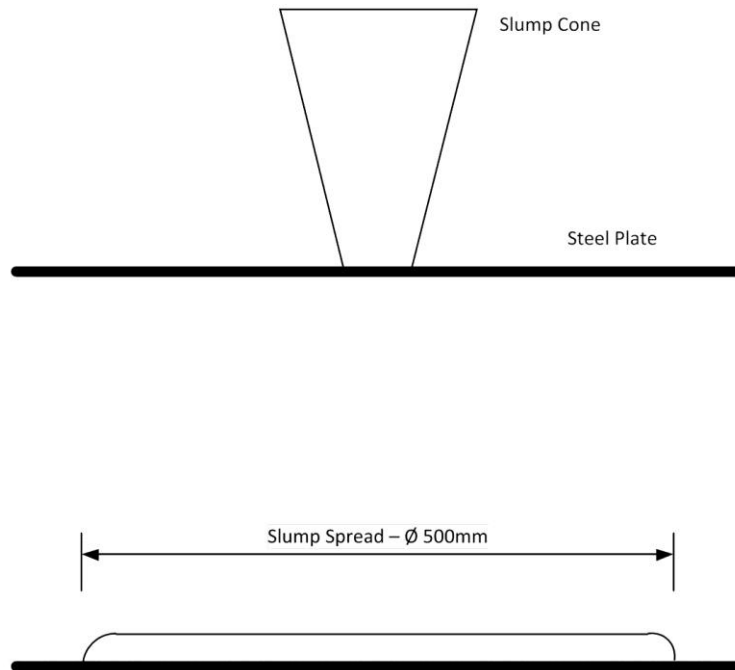


Figure 10 Graphical presentation of the Slump Flow Test.

Other testing methods include the slump flow and blocking resistance test, the V-funnel test, the U-box test, L-box test and segregation resistance (sieve) test. Further information about these testing procedures can be found in the EFNARC 2002. The mixes used in this study were only subjected to the slump flow test. It was deemed unnecessary to perform other tests seeing that the mixes exhibited a flow spread of more than 500 mm and showed no signs of segregation. Some of the cubes cast were cut in half after the concrete has set in order to verify the latter. The mix used consisted of the following:

Table 3.1 Proportions of SCC mix for 1 m³

SCC Mix			
Material	Amount (kg/m³)	Relative Density	Volume [litre]
Cement (CEM II 32.5)	376	3.1	121
Fly Ash (95% passing 45µm)	238	2.8	85
Stone 6 mm (Greywacke)	645	2.7	239
Sand (Malmesbury)	950	2.65	359
Water	193	1	193
Superplasticiser (0.5%)	3.07	1.2	2.56
		Total Volume	1000

The superplasticiser used was the Fluid Premia 310 supplied by Chryso. The mixing procedure will be explained in Chapter 3.2.3 in order to compare the difference in procedures of SCC and SFRSCC. The testing procedure was to test four batches of concrete specimens with each batch consisting of four identical concrete types:

Table 3.2 Batches of Tensile Creep specimens.

Batch	Quantity	Concrete Type	Description
1	4	SCC	Un-Notched
2	4	SFRSCC	Un-Notched
3	4	SFRSCC	Notched
4	4	SFRSCC	Notched and Pre-Cracked

3.1.2 SFRSCC

The SFRSCC mix was similar to the SCC mix with the only differences being that steel fibres were added and the superplasticiser amount was increased. The mix consisted out of the following:

Table 3.3 Proportions for SFRSCC mix for 1 m³

SFRSCC Mix			
Material	Amount (kg/m ³)	Relative Density	Volume [litre]
Cement (CEM II 32.5)	374	3.1	121
Fly Ash (95% passing 45µm)	237	2.8	85
Stone 6 mm (Greywacke)	642	2.7	238
Sand (Malmesbury)	946	2.65	357
Water	192	1	192
Superplasticiser (0.5%)	3.05	1.2	2.54
Steel Fibres (0.5%)	39.75	7.85	5.06
Total Volume			1000

The steel fibres used were Bekaert Dramix ZP 305 fibres and are shown in Figure 11 where $l_n = 30\text{ mm}$ represents the fibre length and the diameter of the fibre was $d = 0.55\text{ mm}$. The elastic modulus and minimum tensile strength of these fibres are 210 GPa and 1100 MPa , respectively.

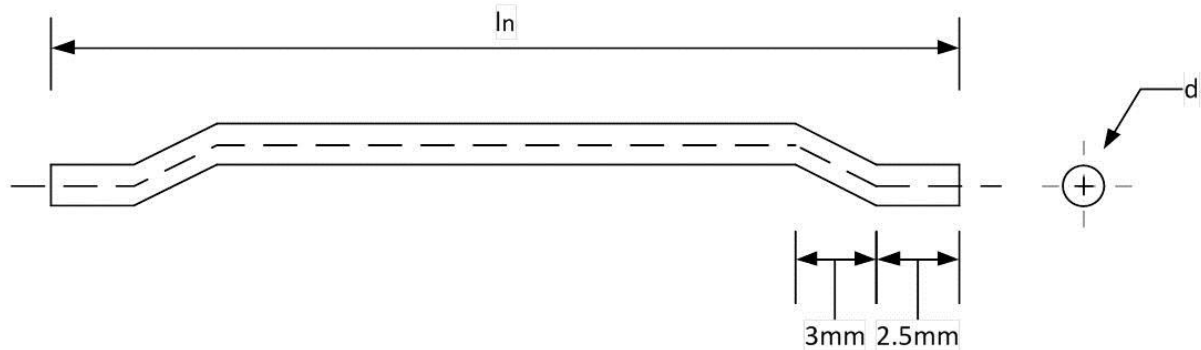


Figure 11 Graphical presentation of a hooked steel fibre.

The workability concern was overcome through using slightly higher (0.05%) doses of superplasticiser. The mix proved to be sensitive to adding superplasticiser, which led to volume changes of 0.05 % being added at a time. Even though the mix was sensitive to extra addition of superplasticiser, it was possible to acquire a SFRSCC mix that exhibited minimal segregation as shown in Figure 12.

Figure 12 Section of a SFRSCC cube demonstrating the lack of segregation

Figure 12 presents two halves of a $100 \times 100 \times 100 \text{ mm}$ SFRSCC cube which displays minimal segregation after the concrete has set. It is apparent that the aggregate and steel fibre distribution is constant throughout the concrete, which indicates that gravity did not affect the mix in its fresh state and that all the different components were in suspension, which is ideal for any concrete mix design.

The amount of superplasticiser used fluctuated slightly with every batch of SCC and SFRSCC mixed during the testing procedure. The tables depicting the mix proportions for SCC and SFRSCC given in this section and the previous section represented the mix proportions of the stable mixes found in the laboratory. While the mixes in the tables indicated that 0.5 % superplasticiser was used it was necessary to add between 0.1 % and 0.15 % superplasticiser during the mixing of the creep specimens in order to improve the flowing ability of the concrete. This was done with great care in order to avoid segregation of the concrete.

3.2 Sample Productions

3.2.1 Mould Design

The tensile test specimens were based on the specimen designs of Swaddiwudhipong et al. (2003) who cast steel hooks at the ends of concrete prisms to act as connections between the concrete and the testing equipment. In order to cast the manufactured hooks into the concrete specimens, the moulds had to be modified slightly. The moulds had the dimensions $500 \times 100 \times 100 \text{ mm}$ and were ideal to manufacture the concrete specimens with. A typical un-modified mould can be seen in Figure 13.

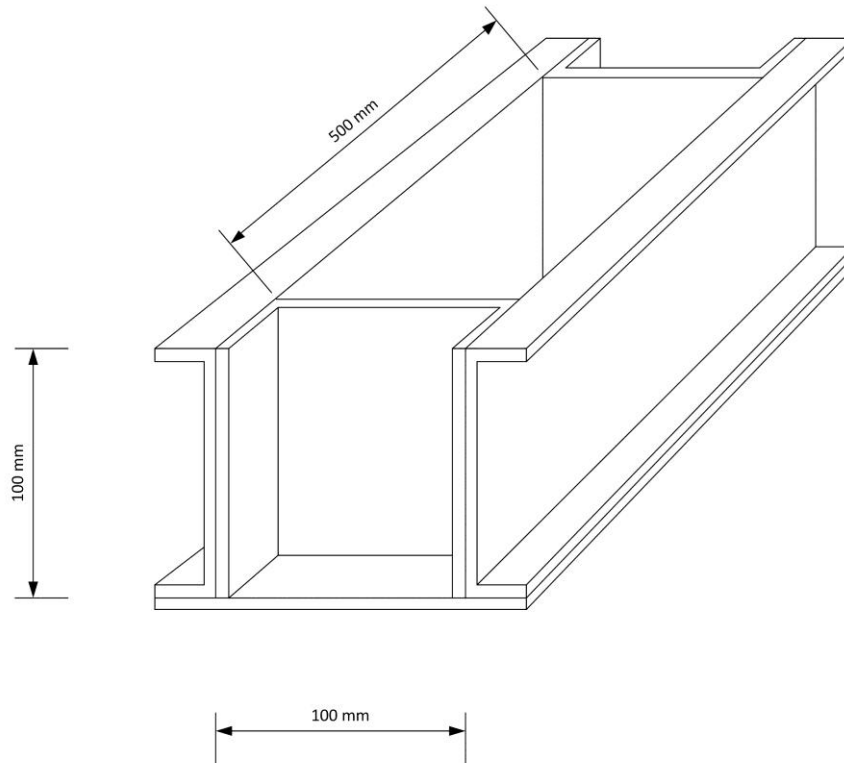


Figure 13 Schematic presentation of a typical beam mould.

The pieces of the mould were fixed together with bolts and winged nuts and could be disassembled completely. In order to incorporate the hooks in the mould the end plates had to be removed and replaced with two wooden blocks with semicircles cut into them.

These wooden blocks consisted out of two $100 \times 50 \text{ mm}$ plywood blocks, 20 mm thick with semicircles of 18 mm in diameter at one side of each block. These holes served in holding the steel hooks into position which allowed the hooks to be cast into the concrete. The practicality of these wooden blocks was that they could be removed easily after the concrete has set.

A schematic presentation of one of the wooden blocks can be seen in Figure 14.

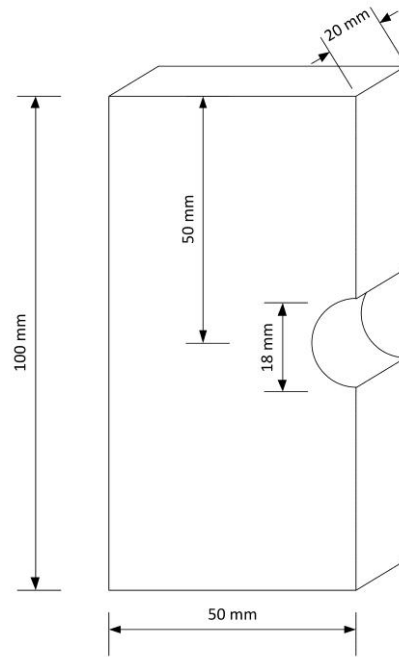


Figure 14 Schematic presentation of the wooden blocks used in the beam moulds.

These wooden blocks were symmetrically fitted to the end of the moulds with the semicircles facing each other. This allowed the 16 mm reinforcing steel bar to pass through the 18 mm holes, effectively prohibiting concrete from leaking out of the moulds. The mould design with the wooden blocks fitted is seen in Figure 15.

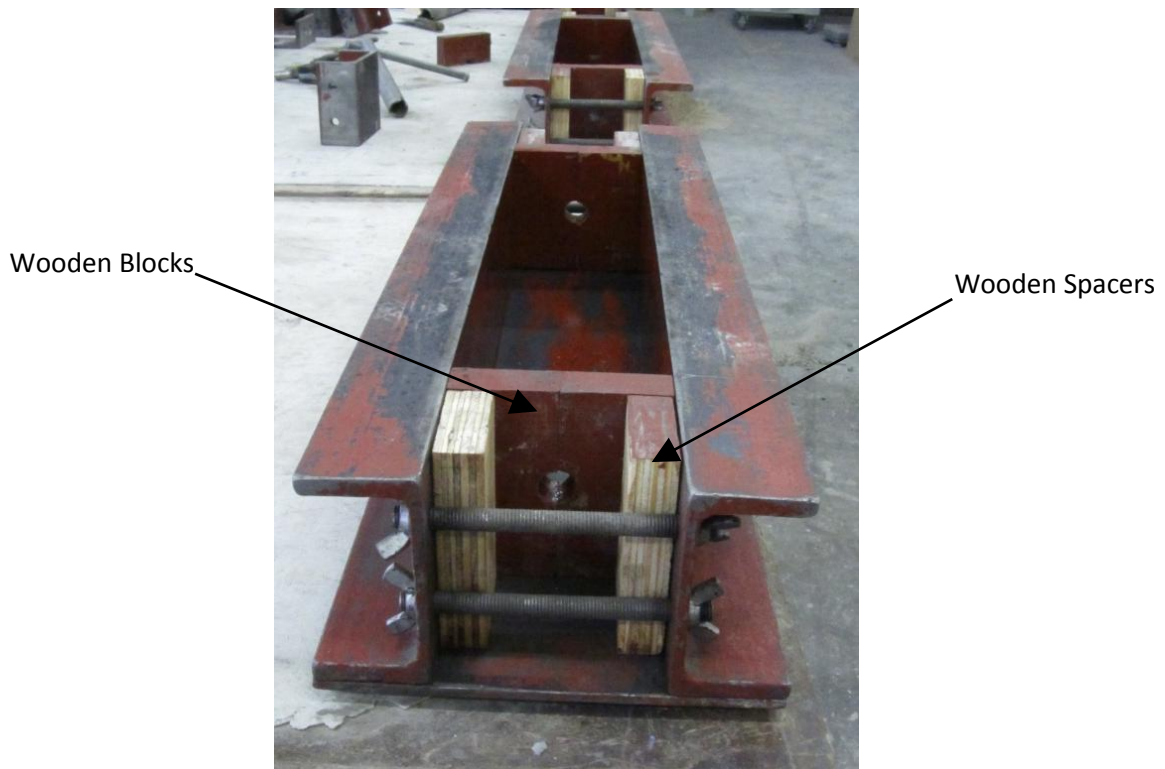


Figure 15 The wooden blocks fitted to the beam moulds.

In Figure 15 the wooden blocks were fitted to the ends of the mould. It has to be noted that this mould was modified in order to manufacture $400 \times 100 \times 100 \text{ mm}$ prisms. The prisms were later modified to be 500 mm in length, which meant that the wooden spacers were discarded. The change in specimen length was necessary to make the experimental procedure more practical. The full mould assembly with the hooks included can be seen in Figure 21 from Chapter 3.2.3.

The 18 mm hole in the wooden blocks would aid in orientating the steel hooks so that load eccentricities and internal moments could be minimized. The wooden blocks also sealed the bottom end of the mould effectively, thereby not allowing concrete to seep through the bottom as seen in Figure 16.

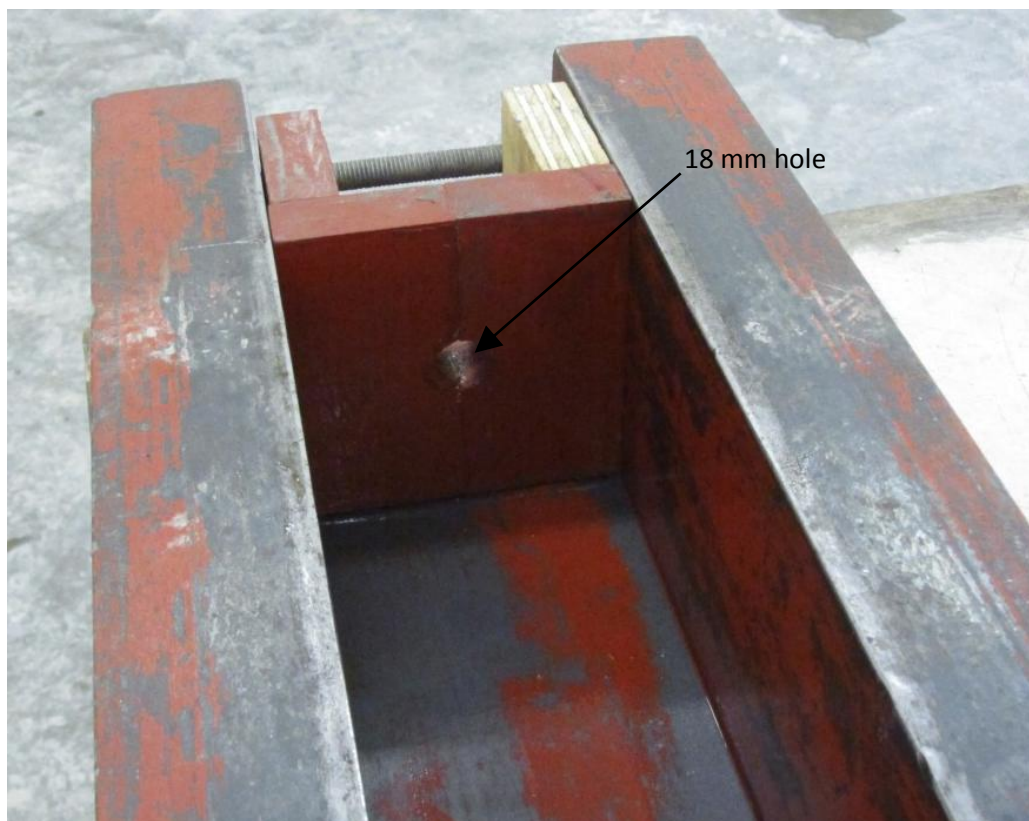


Figure 16 The 18 mm hole drilled into the wooden blocks.

Only six beam moulds were available so it was only possible to manufacture one batch of four specimens a day. The manufacturing of the steel hooks will be explained in detail in the following section.

3.2.2 Manufacturing of Steel Hooks

It was mentioned in the previous section that it was necessary to cast steel hooks into the ends of concrete specimens in order to perform direct tensile tests. These hooks would serve as a connection between the specimens and the testing apparatuses and were manufactured out of

reinforcing steel bars to improve the bond interface between the steel hooks and concrete. These steel bars ranged in different sizes, namely 8, 12 and 16 mm bars, in order to be practical.

The first area of concern was whether the reinforcing bars would be able to withstand the tensile stresses generated within the tensile test setup. In Appendix A it can be seen that the maximum allowable force is 76.2 kN before the welds start to fail in shear. The critical tensile force would be transferred through the 16 mm steel bars. The force would halve when transferring through the 12 mm bars connected to the 16 mm bars and would be four times less when being transferred through the 8 mm bars connected to the 16 mm bars. The yield strength of the reinforcing steel is typically 450 MPa.

The capacity of the 16 mm steel bars is as follows:

$$F_{R-Y16} = 450 \times \pi \times \frac{16^2}{4} = 90.478 \text{ kN}$$

$$F_{R-Y16} = 90.478 \text{ kN} > F_{app} = 76.2 \text{ kN} \therefore OK$$

The most critical aspect of the steel hooks had been addressed and it allowed the design to continue. The capacities of the 12 mm and 8 mm steel bars were calculated below:

$$F_{R-Y12} = 450 \times \pi \times \frac{12^2}{4} = 50.894 \text{ kN} > \frac{76.2}{2} = 38.1 \text{ kN} \therefore OK$$

$$F_{R-Y8} = 450 \times \pi \times \frac{8^2}{4} = 22.619 \text{ kN} > \frac{76.2}{4} = 19.05 \text{ kN} \therefore OK$$

With these capacities known it was possible to proceed with the design of these steel hooks. In total there were four bent 8 mm bars that would act as hooks welded to a straight 16 mm bar in the centre. These hooks were arranged in with 90° angles radially around the centre bar. The 12 mm bars were bent 180° in order to connect to the frictionless connections described in Appendix B and were welded to the ends of the centre 16 mm bars. In order to gain a better understanding about the geometry of the manufactured steel hooks, Figure 17 is provided.



Figure 17 Steel hook specially modified for tensile strength tests.

The steel hook shown in the Figure 17 has been designed especially in order to be tested in the Zwick Z250 Universal Materials Testing Machine. The reinforcing steel bar has been smoothed in order to fit through the notched grips of the machine. It was found that the smoothed steel bar slipped gradually when tensile strength test were performed on the concrete specimens. Figure 18 demonstrates how the hooks' ends fitted into the machine's grips when tensile strength tests were performed.

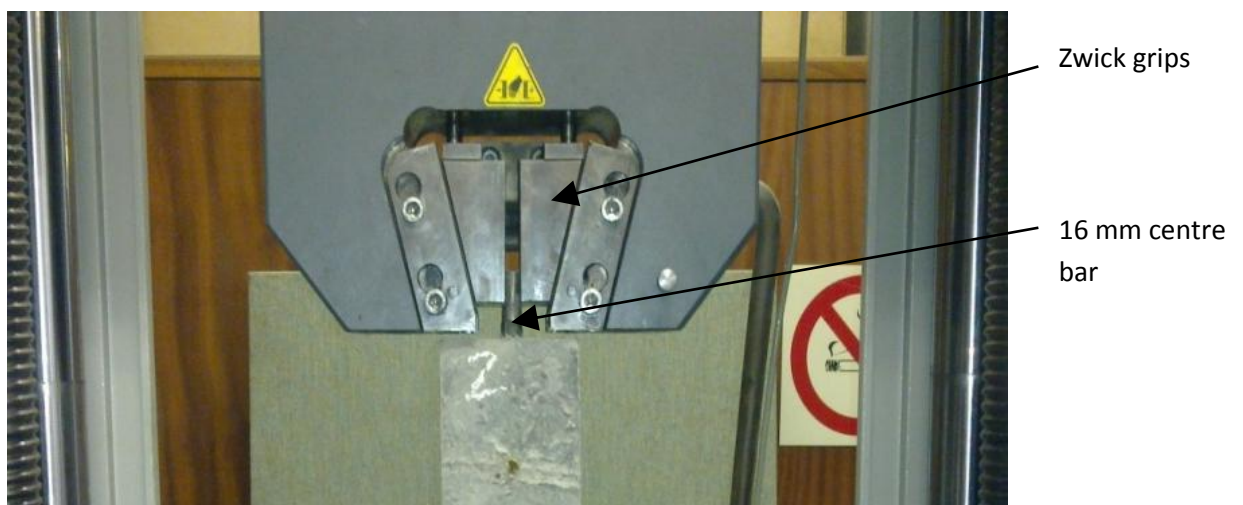


Figure 18 Concrete specimen being tested in tension in the Zwick machine.

As mentioned before the hooks were later modified with bent 12 mm steel bars welded to the ends, causing it to loop, enabling the concrete specimens to be tested in a more accurate manner by fitting chain links. Special chain links were designed to fit into the flat grips of the Zwick machine, which provided better grip during the tensile testing procedure. These links could fit through the 12 mm loops of the hooks which proved to be effective in removing any internal moments that could arise during the testing method.

Figure 19 demonstrates how the bent 12 mm bars were welded to the centre 16 mm bars in order to connect to the frictionless connection by manner of 20 mm bolts.



Figure 19 Figure demonstrating the interaction between the cables, connection and concrete specimen.

3.2.3 Casting Procedure

This section will explain the manufacturing procedures of the SCC and SFRSCC specimens. Great care was taken to ensure that the procedures were done in an accurate manner. All the specimens were cast in a concrete laboratory with precise measuring equipment.

The first step was to assemble and prepare the moulds for casting. The wooden blocks were fitted around the steel hooks and then fitted to the ends of the moulds. The bolts around the moulds were tightened and the inside of the mould was coated with mould oil. Special wire loops were looped around the centre 16 mm bar and a steel rod resting on the mould edges to act as spacers. This would ensure that the hooks were orientated as accurately as possible. An example of the wire loops used as spacers can be seen in Figure 20.

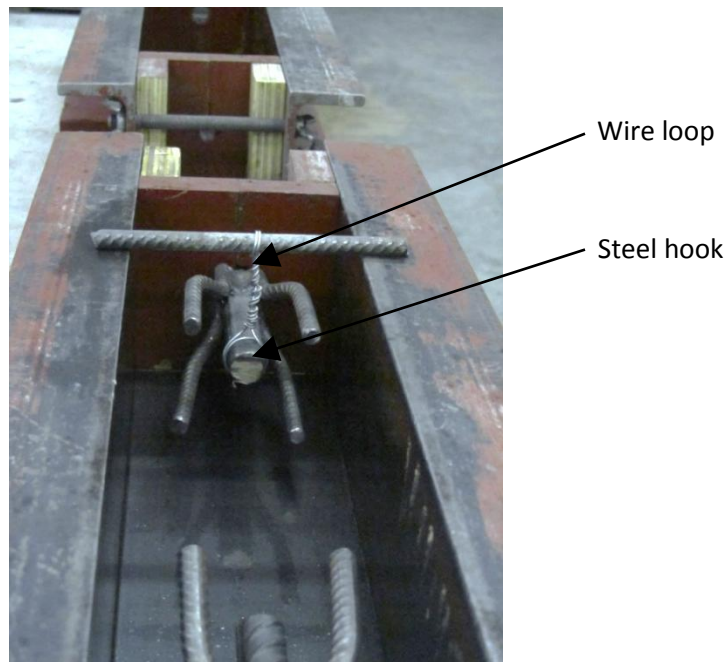


Figure 20 Steel Hooks incorporated into the beam moulds with wire loops used as spacers.

The moulds for the compression cubes were also prepared and coated with mould oil in order to cast the compression cubes needed to test the concrete strength.

The next step was to prepare the ingredients of the concrete mix and to ensure that the mixing drums were clean and dry. The coarse aggregate was added first, and the binder and sand were added subsequently. While the concrete mixer mixed the dry components, most of the water was added, with a little water left to rinse out the container with the measured amount of superplasticiser. The superplasticiser was added last.

The next step was to add the steel fibres when the mix required it. The mixer would then mix the concrete for 5 *min* in order to improve the homogeneity of the concrete and to allow the superplasticiser to fully activate. A slump flow test was performed in order to determine whether the concrete flowed enough. If required, superplasticiser was added in increments of 0.05% until the concrete complied with the requirements of the EFNARC 2002 Manual. In total the SCC mix used 0.6% superplasticiser and the SFRSCC mixes used 0.65% superplasticiser. Great care was taken during all the mixing processes to ensure that no segregation took place.

The concrete was cast into the centre of the moulds to ensure that it would fill all the voids in the mould and so that it would not misalign the steel hooks. A typical mould ready for casting can be seen in Figure 21.



Figure 21 Beam mould ready for casting.

After all four specimen moulds were filled the surplus of concrete was cast into the four cube moulds. The specimens and cubes were then left to set for 2 days before the moulds were removed and the concrete specimens were placed into the water baths for curing. The temperature of the water in the water baths ranged between 20° and 23° and the concrete was allowed to cure for 28 days. It was found that the average compressive strength of the SCC mix was 46.4 MPa and 44.3 MPa for the SFRSCC mix.

3.3 Tensile Tests

In order to perform tensile creep tests on the concrete specimens, it was necessary to know the average tensile capacity of the specimens. The reason for this is so that these specimens could be loaded to a certain percentage of the average maximum capacity in order to avoid creep fracture. If the specimens are subjected to forces that are too high i.e. too high loading percentage, creep fracture could occur, which is undesirable. The phenomenon of creep fracture is explained well by Boshoff (2007). Creep fracture is explained as the failure of the concrete if a sustained load higher than the peak of the creep limit is applied. The creep limit can be obtained by applying a sustained load at different load levels on a concrete beam. The deflection of the beam would increase until it reaches the creep limit as shown by Figure 22.

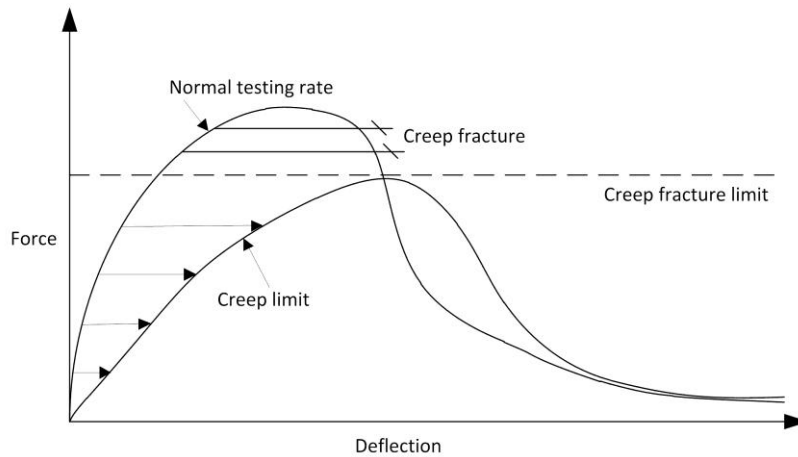


Figure 22 Presenting the concept of creep fracture (Boshoff, 2007).

The tensile tests were performed in the Zwick machine mentioned earlier, which had a capacity of 250 *kN*. The machine was calibrated regularly in order to insure its accuracy. It consists of an electro-mechanical loading mechanism that can move up and down at different rates and a top part which contains the load cell for measuring the resisting load of the materials tested. The machine was fitted with specialised grips that could increase their grip in a wedge-like fashion as the applied force increased.

As mentioned before, special chain links were manufactured in order to fit through the 12 *mm* bends welded to the steel hooks. These chain links were gripped by the Zwick machine and minimal slipping occurred during the tests. As the force applied increased, the slipping decreased to zero, which was confirmed by the Linear Variable Differential Transducers (LVDTs). A LVDT is an apparatus which measures displacement. The LVDTs were fitted by means of aluminium frames to the centres of the concrete specimens as seen in Figure 23 to obtain the true deformation.

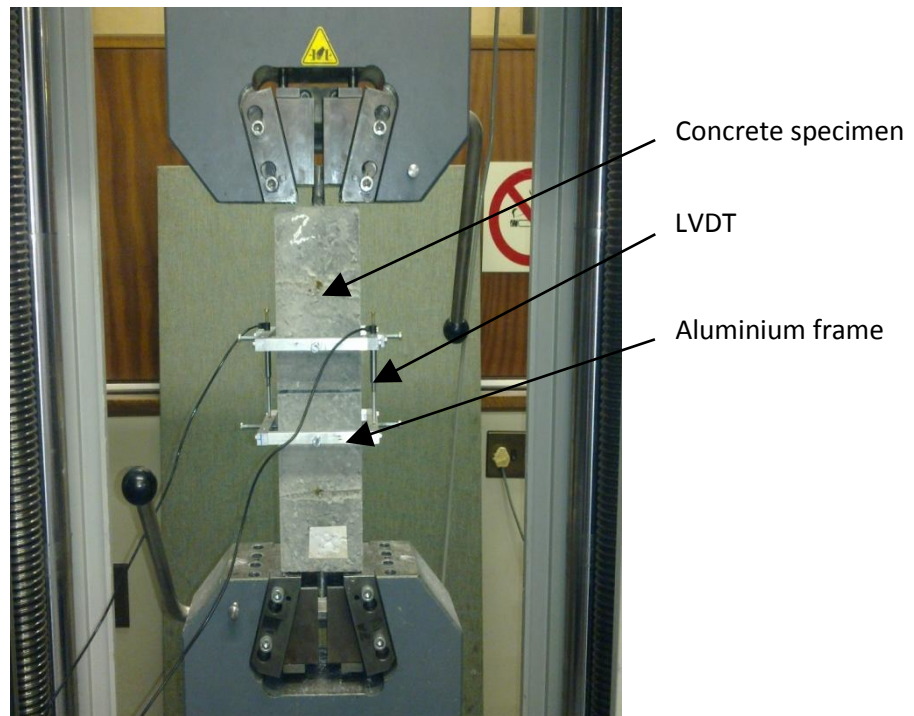


Figure 23 Concrete specimen being tested in tension.

The aluminium frames had a gauge length of 70 *mm* and were fitted to the concrete specimens by means of small screws. The LVDTs were fitted to the aluminium frames in such a manner to measure the longitudinal change in length of the concrete. From Figure 23 it can be seen that the concrete specimen had been notched horizontally around the centreline in order to ensure that the cracking would be localised. Even though this would cause stress concentrations, it was more important to ensure that the concrete specimens failed in an identical fashion. The 10 *mm* deep notches were cut around the specimen with a diamond cutter with a blade width of 3 *mm*.

The function of the LVDTs was to record the true deformation of the concrete specimens during the testing procedure. However, the main objective of these tests was to find the tensile strength of the specimens, so it was acceptable to use the crosshead displacement. The displacements from the LVDTs would be used in case anomalies appeared. A pre-load of 500 *N* was applied on the specimens in order to ensure the grips functioned effectively. After a visual inspection was made the testing procedure was allowed to continue by applying displacement at a measured rate until failure of the concrete specimens occurred.

The data for every specimen was saved and exported to a data processor for further analysis. The results were then used to plot the load resistance against the deformation of the concrete. Typical results for tensile strength tests performed on SCC and SFRSCC concrete specimens can be seen in Figures 24.

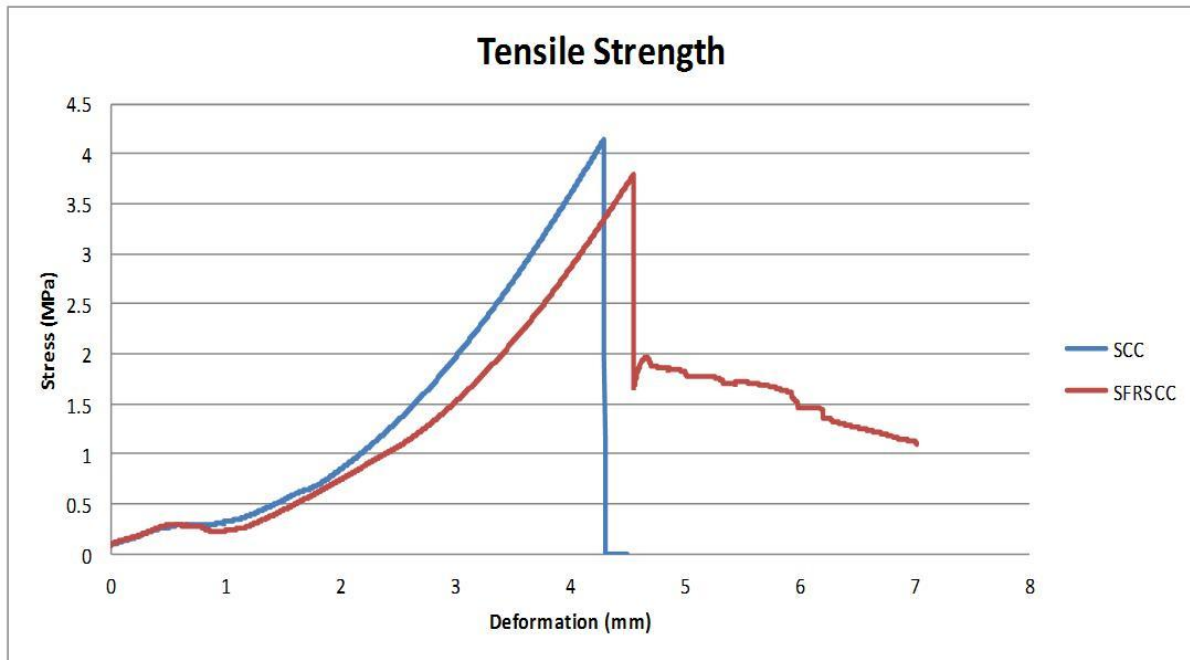


Figure 24 Typical behaviour of SCC and SFRSCC prisms in tension.

At first glance it can be seen that there was little difference between the maximum resistances of the two different concretes. This meant that they were similar in strength, which was expected. The biggest difference between these two materials concerning tensile behaviour was that the SFRSCC specimens offered significant resistance after failure. The fibres provided resistance to tensile stresses after failure, which is the biggest advantage of SFRSCC. The SFRSCC specimen presented a classic example of strain-softening behaviour, which occurs when the volume of fibres is below the critical volume (Lim et al., 1987).

Results of the tensile tests for SCC can be seen in Table 3.4.

Table 3.3 Tensile Strengths of SCC Specimens

Name	Specimen 1	Specimen 2	Specimen 3	Specimen 4	Std Dev	COV	Average	
$\sigma_{\max\text{notch}}$	3.812	4.153	4.557	3.634	0.407	0.101	4.039	MPa

Results of the tensile tests for SFRSCC can be seen in Table 3.5.

Table 3.5 Tensile Strengths of SFRSCC Specimens

Name	Specimen 1	Specimen 2	Specimen 3	Specimen 4	Std Dev	COV	Average	
$\sigma_{\max\text{notch}}$	3.773	3.793	4.251	4.086	0.233	0.059	3.976	MPa
σ_{break}	1.292	1.041	1.122	0.907	0.161	0.148	1.090	MPa
$\sigma_{\text{break}70\%}$	0.904	0.729	0.786	0.635	0.113	0.148	0.763	MPa

The maximum stress $\sigma_{maxnotch}$ was calculated the same way as with SCC. The stress σ_{break} was the average force resisted by the specimens after cracking, which was essential to the loading of the tensile creep tests performed on the pre-cracked specimens. The stress σ_{break} 70% was a fraction of σ_{break} and was the total stress that needed to be applied to the pre-cracked concrete specimens during the tensile creep tests. Figure 25 explains these terms more effectively.

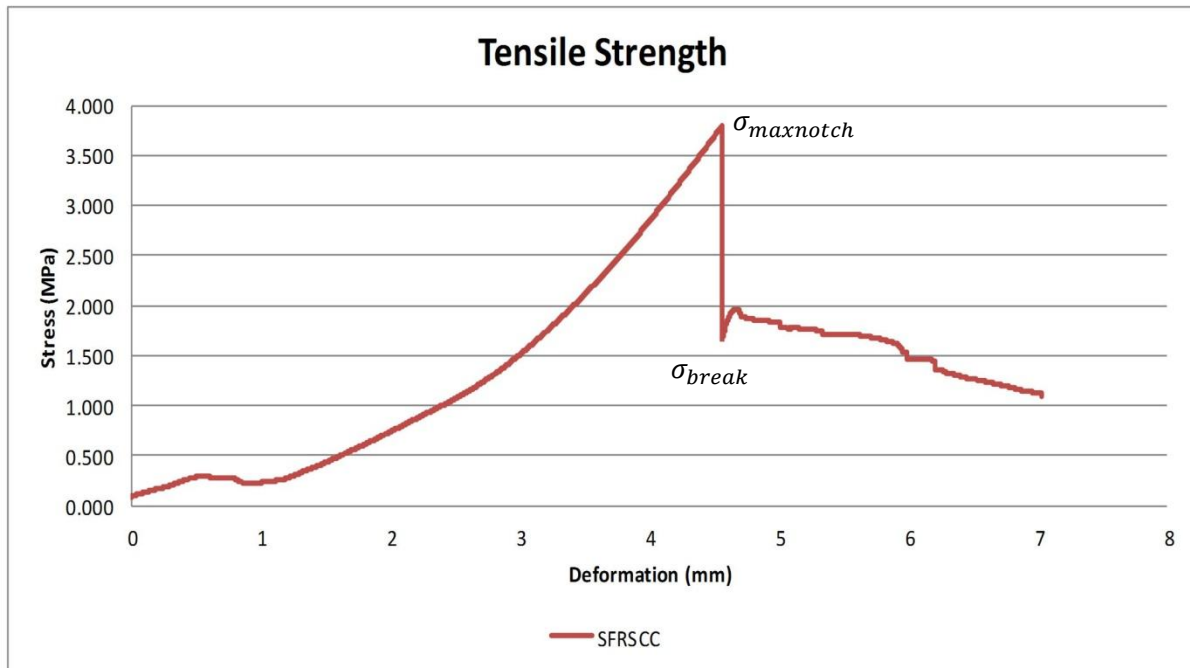


Figure 25 Typical behaviour of SFRSCC prisms in tension with parameters defined

3.4 Steel Frames

Steel frames were designed in order to perform the tensile creep tests. A detailed description of the frames can be found in Appendix B. The frames used weights attached to the pivot beams at different ratios as a loading mechanism as seen in Figure 26 and it was necessary to calibrate the frames in order to load the concrete specimens correctly. Certain factors could affect the difference between the load applied and the load acting on the specimens for example the own weight of the pivot beams and the cables, the slight inaccuracies of the ratios and the distribution of the forces through the frictionless pinned connection. In order to understand the calibration procedures, it was necessary to be familiar with the loading frames and their function.

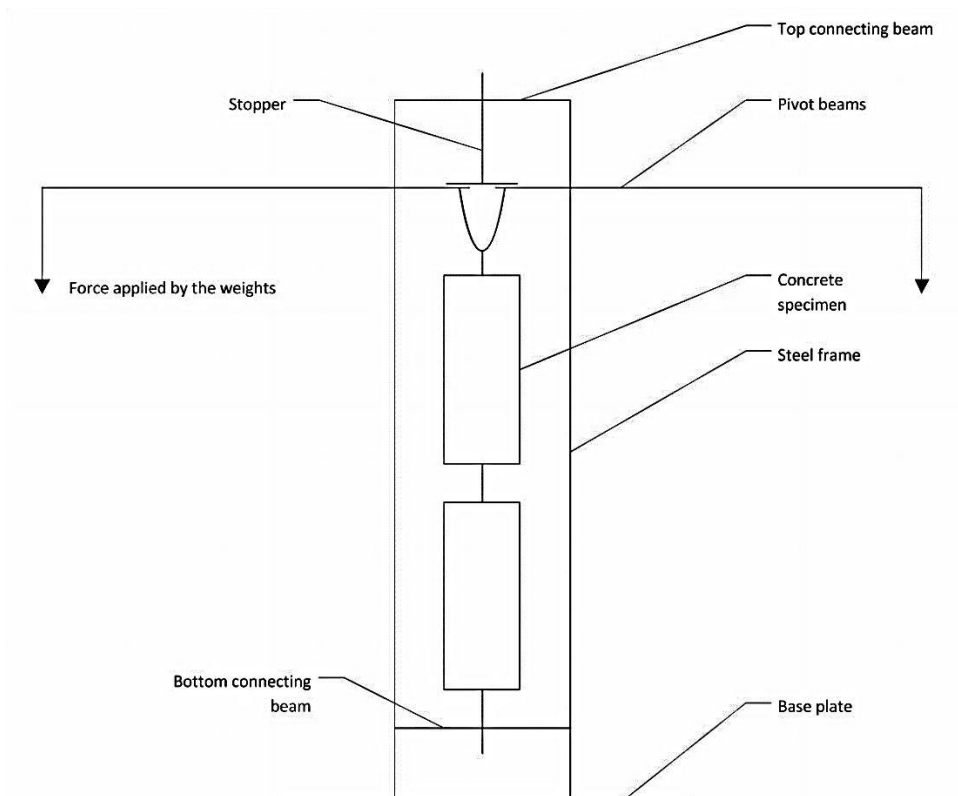


Figure 26 Graphical presentation of the steel frames used in the tensile creep tests.

It was mentioned before that four batches consisting of four concrete specimens had to be tested. Each steel frame could fit two specimens at a time, meaning eight steel frames were designed to perform the tensile creep tests. These frames were named Frames A – H in order to avoid confusion. Figure 27 presents the steel frames used in the tensile creep tests.

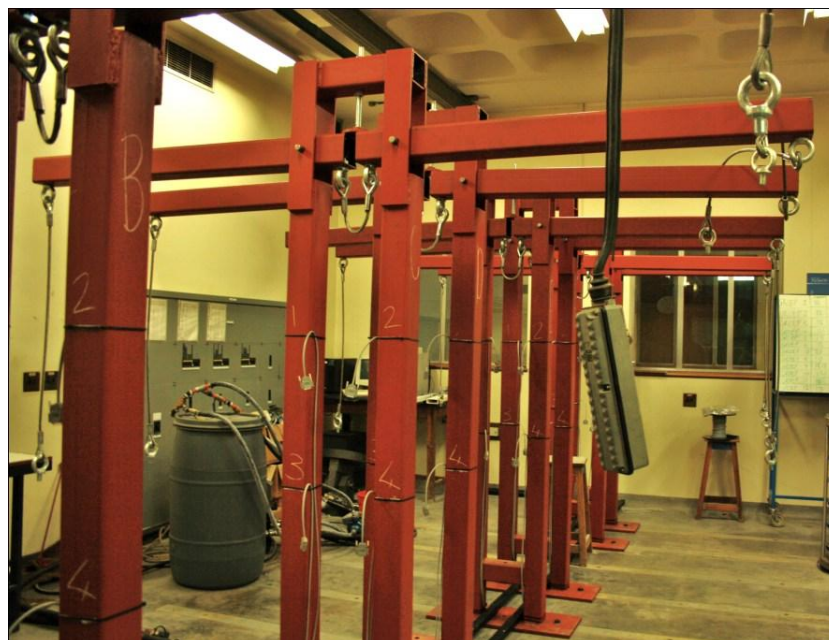


Figure 27 Figure of steel frames to be used in tensile creep tests.

From Figure 27 it can be seen that the pivot beams through which the applied load will be transferred to the specimens are resisted by the stopper, which acts as a loading mechanism and safety measure. The wire rope connections will ensure that minimal internal moments will occur during the testing procedure. The wire ropes used were 10 mm Maxipact high performance wire ropes with a minimum nominal capacity of 90.07 kN supplied by Fastlift Rigging Products (PTY) Ltd. The room used for the creep tests was fully climate controlled with the ability to generate different ambient temperatures and humidity.

Additionally, 20 mm threaded rods with chain links welded to it were used to connect the concrete specimens to the bottom of the frames. These rods had hex nuts fixed to them so that they could be adjustable as can be seen in Appendix B. The threaded rods acted in accordance with the stopper to ensure that the frames could be adjusted to accommodate the concrete specimens. Figure 28 represents the stoppers.

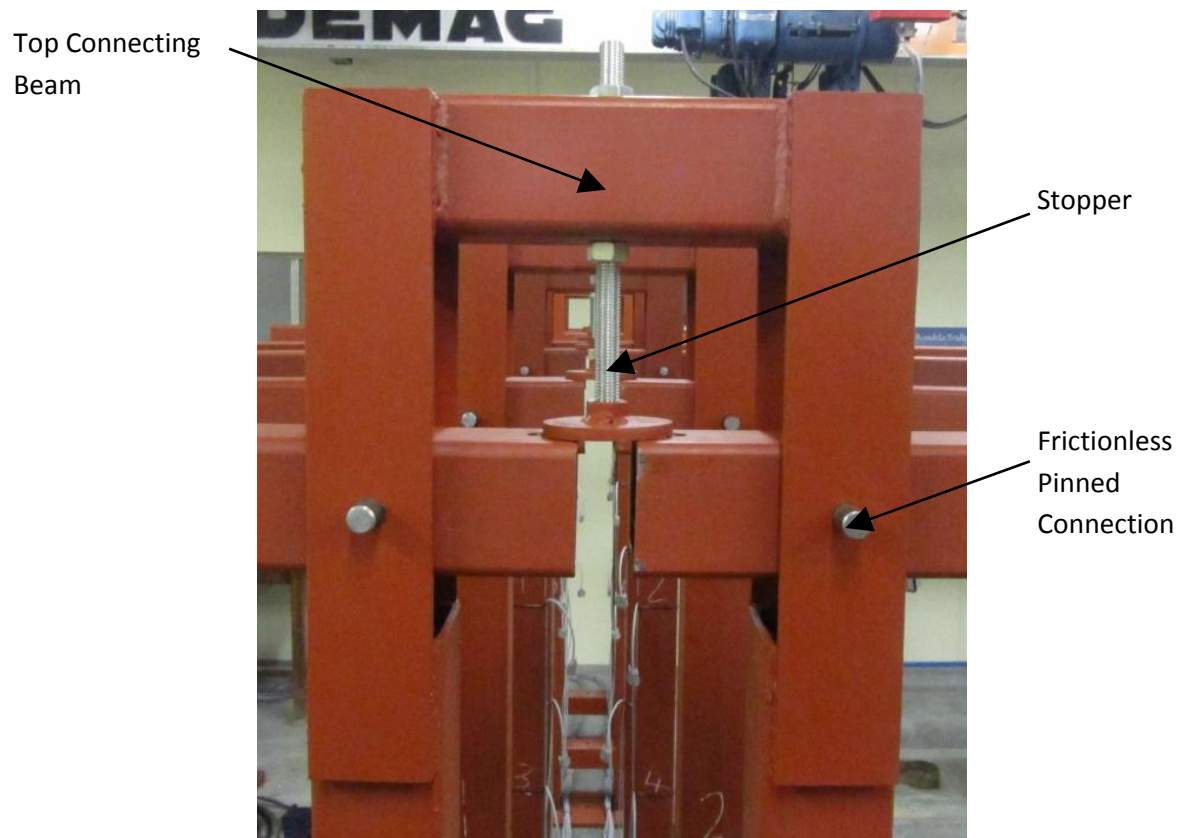


Figure 28 Figure of the stopper acting as a safety mechanism.

The stopper shown in Figure 28 was designed to act as a loading³ and a safety⁴ mechanism. The stoppers were designed in such a manner so that they were fully adjustable and were able to lock in

³ When the frames were loaded.

⁴ If the concrete specimens failed.

position. The steel disc was capable to withstand all forces generated by the frames and it was able to accommodate a wide range of rotations of the pivot beams. During the creep tests the stopper had been adjusted so that there was a gap of $\pm 5 \text{ mm}$ between the stopper and the pivot beams, enabling it to act as a safety mechanism if the concrete specimens fail. This ensured that the equipment would not damage if failure occurs.

The frictionless pinned connection described in Appendix B can also be seen in Figure 28. Steel bars were held in position by the round cir-clip fixed at both ends. This ensured that the bars stayed in position during testing. The bars went through the needle roller bearings fitted in the pivot beams and were capable of withstanding up to 55.9 kN of applied force. The pivot beams were designed in such a manner for the loading ratios to be fully adjustable. The ratios ranged between 1: 7 to 1: 10, making it possible to lessen the forces applied if so desired.

The aim of the frame design was to be as compact, simple and practical as possible. As mentioned before loading weights were used to generate the loads needed in order to test the specimens. In order to use a large amount of weight while keeping the design compact 100 kg lead weights were used. Smaller weights added the extra loads when they were needed.

It was necessary to calibrate the steel frames in order to make sure that the correct loads were applied to the specimens. In theory it is possible to determine the actual load applied by using the ratios after the weights were loaded. The theoretical equation for determining the actual load after the weights are applied is explained below:

$$F_{app} = ratio \times Weight \quad (3.1)$$

This ratio is expressed as 1: *ratio* and the weight is converted from *kg* to *N*. In Appendix B the ratio used in the calculations was 1: 10 in order to create the worst case scenario. This ratio could to be adjusted in order to accommodate the 100 kg lead weights.

3.5 Calibration

The calibration process was performed by connecting a tensile load cell with the capacity of 50 kN to the centre of the frames by using chains and the specially designed connections described in Appendix B. The load cell was connected to a Spider8 data logger which was connected to the computer and it could record the actual load applied by the loading weights. The data acquisition was performed by the Catman v.3.2 software program developed by HBM. This program allows the user to choose many different logging styles of which the real-time graph was chosen, which plotted the force against the time.

Before the loading started the load cell was zeroed to indicate a zero load. The stopper was released in order to load the self-weight of the pivot beams. The force generated by the self-weight of the pivot beams was added to the force applied by the loading weights. 10 kg weights were used in the calibration process and were added in increments of 20 kg at each side of the frame until the loads obtained from the tensile strength tests were reached. With every increment the load was given time to stabilise and the force was recorded from the computer. Ideally the increments of loading would behave in a linear manner. That would make it possible to foresee what amount of weight would generate the correct amount of force needed for the tensile creep tests. The expression for linear behaviour is well known and can be applied in the following manner:

$$y(x) = mx + c \quad (3.2)$$

Equation 3.2 was used for determining the applied load after the loading of the weights, with the self-weight taken into account. In this case, $y(x)$ was the load recorded by the load cell after the weights have been loaded, x was the load applied in N , c was the own weight in N of the pivot beams and the load cell and m was the loading ratio. With all these factors taken into account it can be seen that when no load is applied $y = c$. With every increment of load added it was found that the ratio m decreased. The calibration process of Frame B can be seen in Table 3.6 as a demonstration.

Table 3.6 Calibration figures for Frame B

x (kg)	x (N)	y(x) (N)	m	y_{calc}
0	0	0		
20	196.2	7520	17.84106	$y(20) = 7218.611$
40	392.4	10670	16.94805	$y(40) = 10417.64$
60	588.6	13620	16.31059	$y(60) = 13616.66$
80	784.8	16510	15.91541	$y(80) = 16815.69$
100	981	19230	15.50501	$y(100) = 20014.72$
110	1079.1	20540	15.30944	$y(110) = 21614.23$
		m_{avg}	16.30493	

The data obtained through the load cell during the calibration process can be seen in Table 3.6 where $x(kg)$ is the mass of the weights applied at each side of the frame and $x(N) = 9.81 \times x(kg)$. The factor $y(x)$ is the load recorded through the load cell and the own weight c was found to be 4019 N. The ratio m was calculated the following way:

$$m = \frac{y-c}{x} \quad (3.3)$$

It can be seen that m decreases as the weight applied increases. This can be explained as the elastic deformation of the steel frames as the load increased. It was therefore necessary to determine the average m needed to calculate y_{calc} , which was used to calculate the load needed for the creep tests.

The load percentage for Frames B – D were lowered from 70 % to 50 % after the specimens experienced creep fracture during the first tensile creep tests. From Table 3.4 in Section 3.3 the ultimate load was found to be $\pm 40.39 \text{ kN}$, so 50% of this load would be approximately 20.195 kN . Through back-substitution the weight needed to generate this load was calculated and found to be 101.13 kg , which was round down to 100 kg , which in turn was equal to 49.6 % of the ultimate load as can be observed in Table 3.7.

Table 3.7 Calculated loads from calibration results for Frame B

F_{req}	20194.88	
Weight_{req}	992.05	N
	101.13	kg
Weight_{app}	100	kg
F_{app}	20014.7	N
	49.6	%

All the frames were calibrated in the manner explained above in order to find the loads that should be applied to the concrete specimens. Table 3.8 presents the loading of all the frames with the loading percentages included.

Table 3.8 Summary of calibration and loading for the steel frames

Frame	Load/side	Newton	m	c	F _{ultimate}	F _{app}	%	Avg %	Avg Load (N)
A	105	1030.05	15.851	4119.6	40390	20447	50.6	50	20015
B	100	981	16.305	4019.6	40390	20015	49.6		
C	115	1128.15	14.689	3299.6	39756	19871	50.0	50	19732
D	110	1079.1	14.942	3469.6	39756	19593	49.3		
E	15	147.15	23.082	3908.4	10905	7305	67.0	65	7132
F	15	147.15	22.093	3708.4	10905	6959	63.8		
G	5	49.05	22.116	3828.4	10905	4913	45.1	48	5282
H	5	49.05	24.499	4448.4	10905	5650	51.8		

From Table 3.8 it is observed that the m factors differed substantially between Frames A – D and Frames E – F because the loading magnitudes differed significantly and the 100 *kg* lead weights had to be used in the first three frames, which influenced the loading ratios. The loading ratios for Frames A – D were 1:7 and 1:10 for Frames E – H.

What is also apparent is that all the specimens except the specimens from Frames E and F were loaded to 50 % of their respective average ultimate strengths obtained from the tensile tests. This was because the specimens from Frames A – D experienced creep fracture when they were loaded to 70 % in the first tensile creep tests performed as mentioned before. The specimens tested in Frames G and H were loaded to 50 % of the average maximum resistance of the concrete after failure, because one of the specimens failed during the 70 % loading. When this occurred, quick action had to be taken to ensure that valuable data could still be obtained from the remaining notched, pre-cracked SFRSCC specimens.

The specimens from Frames E and F were loaded to 65 % of the average maximum resistance of the specimens after failure so that it can be compared to the notched, pre-cracked SFRSCC specimens. However Frames E and F were loaded to approximately 18 % of the average ultimate load at which the SFRSCC tensile specimens failed. With this taken into account it can be foreseen that the tensile creep of the notched SFRSCC specimens would not be high and would need to be factored in order to compare it directly with the other results. The next section will explain the tensile creep test setup.

3.6 Tensile Creep Test Setup

After the frames were calibrated it was possible to load the frames with the weights. As seen in Table 3.8 the frames were loaded to different percentages of the average ultimate strengths. It would have been ideal if the frames could all be loaded to 70 % in order for non-linear behaviour to occur, but experiences with the first tensile creep tests showed that the loading percentage should be lowered as to avoid creep fracture.

The first step of setting up the tensile creep tests was load the weights on the frames, with the stopper making sure that the pivot beams stayed in one place. Figure 29 presents the weights used in loading.



Figure 29 The loading was executed by weight plates.

After loading it was necessary to prepare an Enerpac hydraulic cylinder in order to load the specimens gradually through means of a hand pump. The reason for using a hydraulic cylinder was because the loads generated by the weights were too high to loosen the nuts of the stopper by hand.

The concrete specimens were retrieved from the water baths where they had cured for 28 days. They were moved to the climate controlled laboratory room where the tensile creep tests would be performed. After the specimens were retrieved the aluminium frames to which the LVDTs would be fixed were fitted to the concrete prisms, which, in turn were connected to the steel frames through the connecting wire rope slings by means of the frictionless connections mentioned in Appendix B. The specimens were then fixed to the bottom connection beam by means of the threaded rod as explained in Appendix B and the hex nuts were tightened by hand. The LVDTs were fitted to the aluminium frames by means of small screws and connected to electrical cables leading to the Spider8 data loggers. An example of the data loggers can be seen in Figure 30.



Figure 30 The Spider8 data loggers used in the experiments.

The LVDTs were adjusted so that they could elongate and shorten in order to record creep and shrinkage effectively as can be seen in Figure 31.



Figure 31 An example of the LVDTs and aluminium frames used.

The final step was to load the specimens by using the Enerpac hydraulic cylinder that was connected to the hand-operated hydraulic pump mentioned earlier. Before the loading occurred the data logger was started so that it could start acquiring the data recorded by the LVDTs at one data point per second. The hydraulic cylinder was then inserted between the top connecting beam and the round disc of the stopper and it was extended until the cylinder pressed firmly against the top connecting beam and the stopper's disc. The hex nuts of the stopper were then loosened until the stopper was free to move thus enabling the hydraulic cylinder to carry the full load. The release

valve of the hydraulic pump was opened steadily so that the hydraulic cylinder could retract, causing the specimens to be loaded in a gradual manner. The hydraulic cylinder was relaxed until the stopper offered zero resistance and then the stopper was fixed 5 mm above the ends of the pivot beams.

To ensure that the equipment would not damage if the concrete specimens fail other safety mechanisms were added to the steel frames. These safety mechanisms consisted of two 50 × 50 mm angle iron lengths 400 mm long that were clamped to both sides of the frames through means of 8 mm threaded rods as seen in Figure 32 a). These mechanisms would halt the falling of the concrete specimens if they failed. This design was simple to manufacture and implement and proved to be effective in withstanding the weight of the specimens, should they fail and fall. These angle iron lengths were fitted below each specimen with a 4 – 5 mm gap between the angle iron and the specimen, demonstrated by Figure 32 b). Both safety measures used in the design could be adjusted to take the deformations of the concrete into account.



Figure 32 The secondary safety mechanisms a) Fitted to the frames with a spacing of b) more of less 5 mm.

The data was recorded at one data point per second for Day One of testing. It was then recorded at 5 min intervals at Day Two and 10 min intervals at Day Three. At Day 6 the data points were acquired every hour for seven days. At Day Thirteen the data points were recorded every two hours until the tensile creep and shrinkage tests were complete. This schedule was used for every batch of concrete specimens tested. The tests were performed in tandem and the data points were recorded to at least one hundred days of testing.

3.7 Shrinkage Test Setup

As mentioned before, only six moulds were available at a time, which allowed the manufacturing of two shrinkage specimens and four tensile creep specimens at a time from each batch for the first two batches. The shrinkage specimens were set up during the same time as the setup of the tensile creep specimens for the SCC and SFRSCC batches. The reason for manufacturing the shrinkage specimens during the first two batches is so that the shrinkage tests could carry on for as long as possible in order to obtain a stable strain/time curve.

In order to test shrinkage in a relevant manner it was important to test the specimens in the same environment as the creep tests were performed. Two specimens of each type of concrete were tested for shrinkage. The shrinkage specimens were identical to the creep specimens and were retrieved at the same time as the first two batches of creep specimens. They were taken to the climate controlled laboratory where the tensile creep tests were performed. The shrinkage strains were recorded by LVDTs attached to the specimens by means of Perspex blocks glued to the concrete specimens by means of an epoxy, with a gauge length of 70 mm (as seen in Figure 33 a).

Seeing that numerous aluminium frames were required for the creep tests it was more cost effective to use the Perspex blocks. The blocks were fixed to opposite sides of the concrete specimens so that the deformations in both axes in the plane of the cross-sectional area can be measured. These deformations can then be linearly interpolated in order to find the deformation along the centre line. The Perspex blocks were fitted with small clamps and screws in order to fit the LVDTs.

The concrete shrinkage specimens were placed on small PVC tubes acting as rollers as seen in Figure 33 b). These rollers were placed at the ends and at mid-span so that deflections will not take place. They provided minimal frictional resistance and did not deform significantly under the own weight of the concrete specimens. With the concrete specimens ready for testing it was necessary to fix the LVDTs to the Perspex blocks in order to measure the deformations. The LVDTs were fixed in the same way as the creep specimens as to allow extension and contraction in order to measure shrinkage and swelling effectively. The data acquisition schedule of the shrinkage tests were the same as the creep tests seeing that both tests were performed in tandem. Figure 33 presents the setup used in the shrinkage tests:

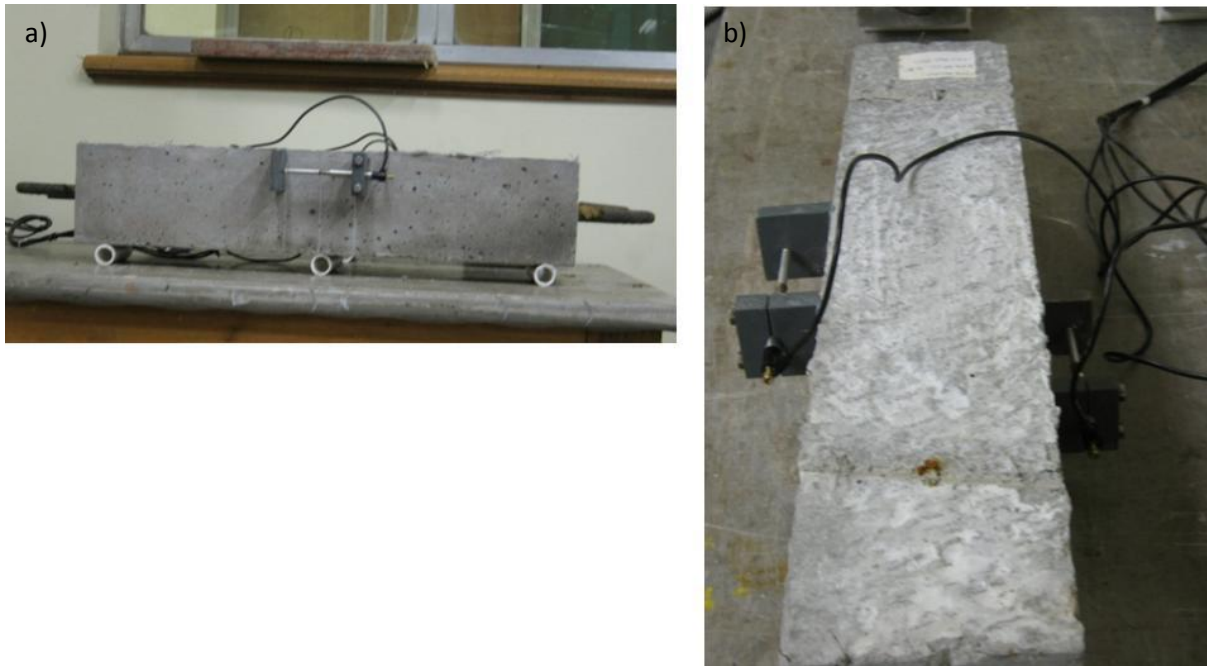


Figure 33 The Shrinkage Beams were a) supported by PVC tubes and b) fitted with Perspex blocks.

3.8 First Creep Tests

The failure of the first round of tensile creep tests will be discussed shortly. The first round of creep tests were done on the SCC and SFRSCC specimens with a 70 % loading percentage. This loading percentage proved to be too high as the specimens experienced creep fracture within the first few days after the testing started. The data turned out to be of no use as 90 *days'* worth of data was required in order to be comprehensive.

A second round of tensile creep tests had to be performed using a lower loading percentage, which led to the lowering of the loading ratios from 1:10 to 1:7 in order to reach a 50 % loading percentage with the same amount of weights used in the first round of tests. From the experience of the first tests it was also decided to implement an extra safety measure as mentioned earlier in order to protect the equipment if failure occurs, which led to implementation of the 50 × 50 *mm* angle iron lengths. The stopper safety mechanism proved to be effective and stable under the loading and failure conditions.

Chapter 4

4. Experimental Results

The experimental results of all tensile creep tests will be presented in this chapter. Compression tests were performed on the concrete cubes of the different batches and an average compressive strength of 38.8 MPa was found for SCC and 40.5 MPa was found for SFRSCC. These compressive strengths were similar to the compressive strengths of the trial mixes, which was 46.4 MPa and 44.3 MPa for the SCC mix and SFRSCC mix, respectively.

4.1 Shrinkage

The shrinkage results of the SCC and SFRSCC specimens are presented and discussed in this section. The graphs are presented as strain in mm/mm over time in *days* where the strain was obtained by dividing the deformations by the 70 mm gauge length. The unaltered results of the displacement of the two SCC specimens (SCC1 and SCC2) caused by the shrinkage effect can be seen in Figure 34.

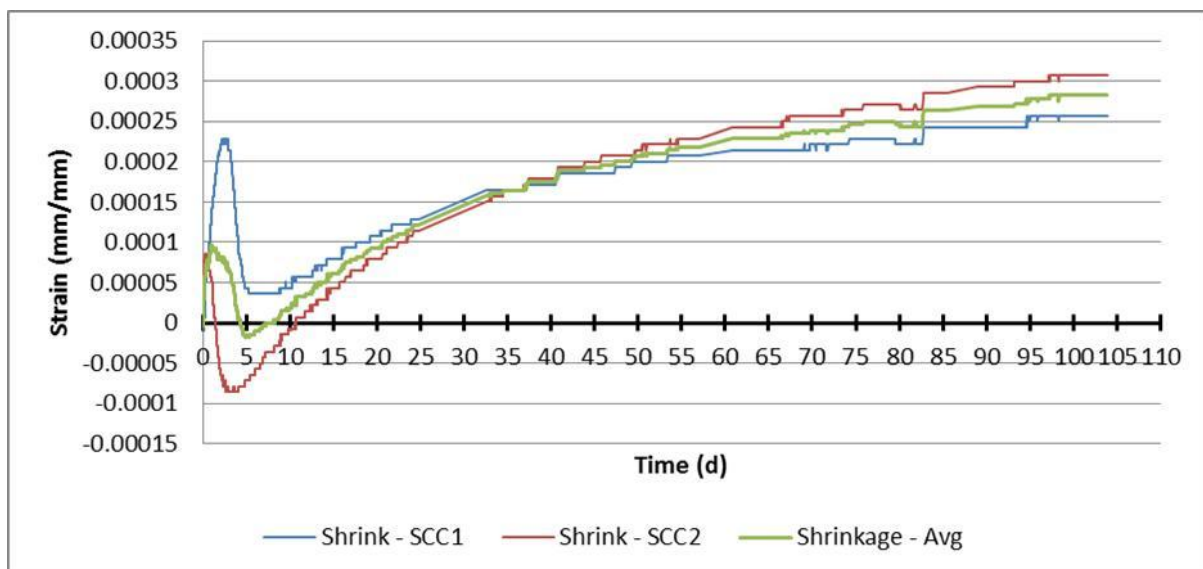


Figure 34 Strain over time behaviour in SCC shrinkage specimens.

From Figure 34 it is observed that the concrete behaved abnormally during the beginning stages of the shrinkage tests. It seemed that the concrete has swelled and shrunk during the first *5 days* of

the shrinkage test. Another explanation can be that the interfacial bond formed by the epoxy between the concrete and the Perspex blocks caused this phenomenon. In order to clarify whether this behaviour was caused by the concrete itself or the epoxy, further testing should be done with the LVDTs being fixed to aluminium frames; however, because of the limited time available to complete the study, this was not possible.

With the shrinkage data exhibiting abnormal behaviour it was necessary to estimate the shrinkage behaviour of the concrete through curve fitting. This was done by using the mathematical expression used for predicting shrinkage of concrete provided by the FIB Model Code 2010 and the data obtained from the shrinkage tests. The shrinkage data obtained was still considered valid because it exhibited behaviour typical to the shrinkage of concrete, but it had to be adjusted in order to be more accurate and useful. With the help of curve fitting it was possible to obtain the curve shape for the first 5 *days*. The curve fitting procedure will be explained in detail in Chapter 5.

The altered SCC shrinkage strain curve is presented in Figure 35.

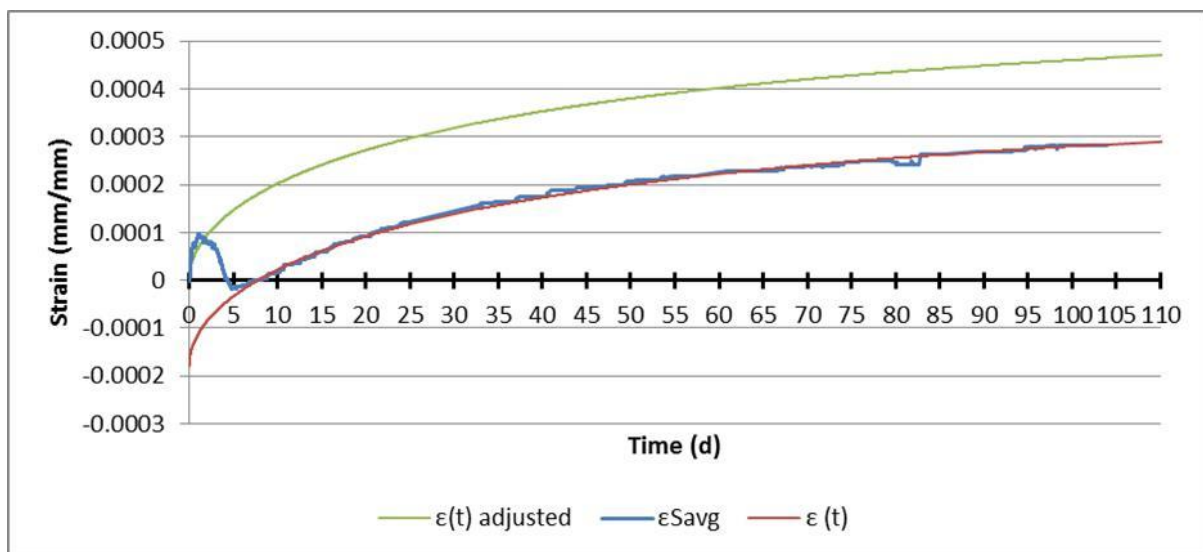


Figure 35 Strain over time graph with predicted shrinkage behaviour for SCC specimens.

In Figure 35 three curves have been plotted in order to find the shrinkage strain of the SCC specimens. The shrinkage strain obtained from the experimental results is represented by ϵ_{Savg} while $\epsilon(t)$ is the shrinkage predicted by the modified mathematical expression obtained from the FIB Model Code 2010 that was used for curve fitting. It can be seen that this curve does not start at zero, which is remedied by $\epsilon(t)_{adjusted}$. After these steps were taken it was assumed that $\epsilon(t)_{adjusted}$ describes the typical shrinkage behaviour of SCC.

The unaltered results of the shrinkage strains of the two SFRSCC specimens (SFRSCC 1 and SFRSCC 2) are presented in Figure 36.

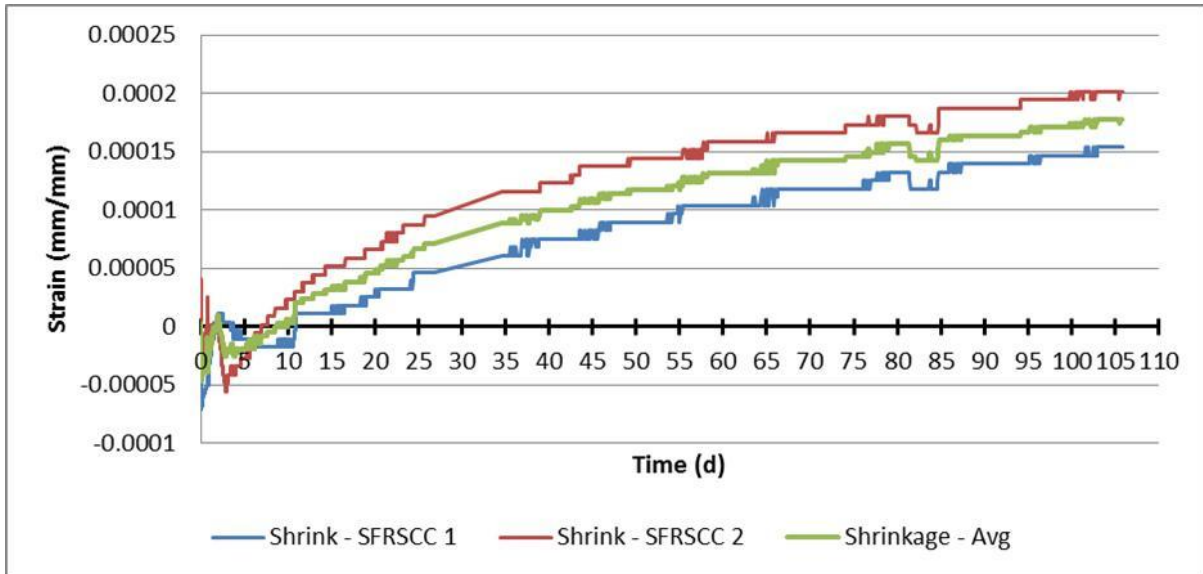


Figure 36 Strain over time behaviour in SFRSCC shrinkage specimens.

In Figure 36 it can be seen that the shrinkage strains of SFRSCC exhibited the same peculiar behaviour as with SCC. Even though the behaviour was not as prominent with SFRSCC it was uncertain whether the fibres caused the behaviour. The same assumptions as for SCC were made and the problem was remedied in the same way. The altered SFRSCC shrinkage strain curve is presented in Figure 37.

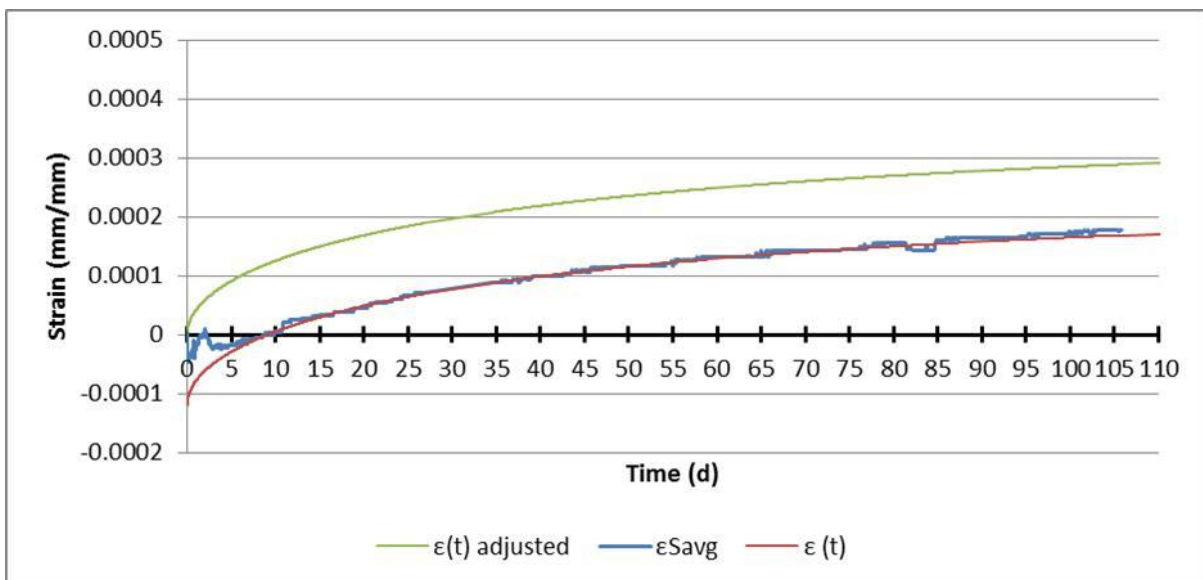


Figure 37 Strain over time graph with predicted shrinkage behaviour for SFRSCC specimens.

As with SCC, curve fitting was done in order to estimate the true shrinkage behaviour with the parameters being the same as with SCC. It was also assumed that $\varepsilon(t)_{adjusted}$ represents the true shrinkage behaviour of SFRSCC. The tensile creep curves of SCC and SFRSCC are presented separately in the sections that follow.

4.2 SCC Creep

The experimental data obtained from the tensile creep tests performed on the SCC specimens will aid in understanding the time-dependent behaviour of SCC. Two specimens failed during the onset of the tensile creep tests. The curves seen Figure 38 are from the two remaining SCC specimens (SCC1 and 2) and represent the creep and shrinkage effects that occurred during the duration of the experiments.

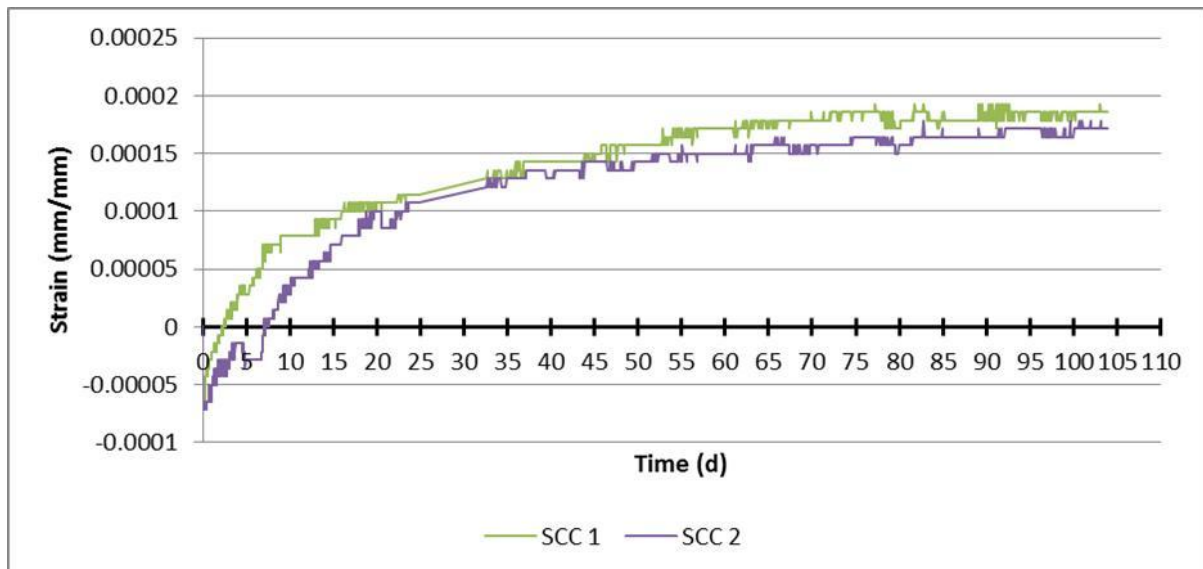


Figure 38 Strain over time behaviour in SCC creep specimens, measured.

The curves from Figure 38 were the measured displacements obtained from the creep experiments divided by the cross-sectional area with the elastic strain included and shrinkage not yet subtracted. The elastic strain was subtracted to start the curves at zero. An average was taken from these curves and shrinkage was then subtracted in order to find the tensile creep of SCC, as seen in Figure 39.

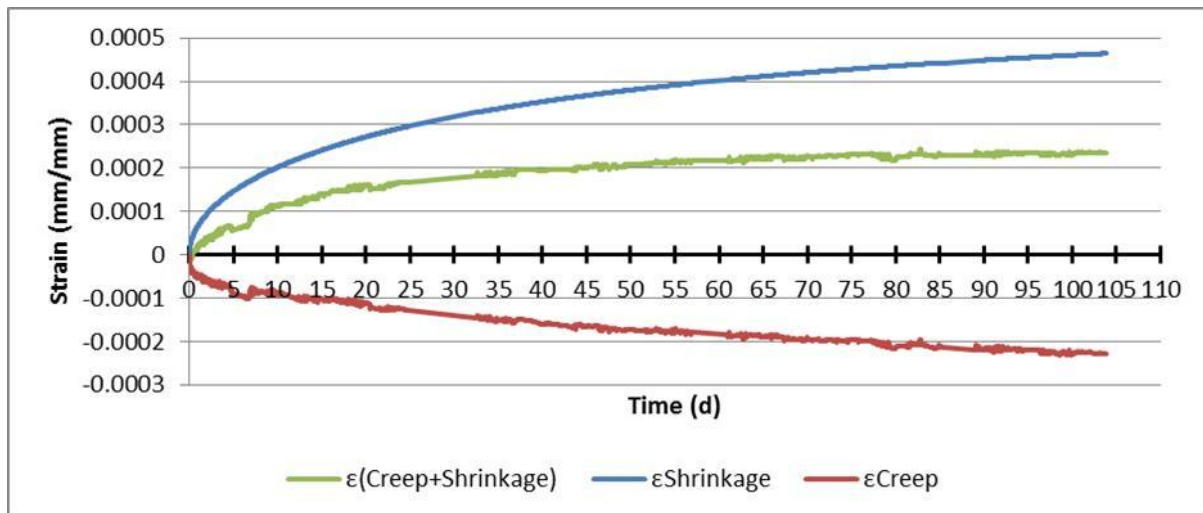


Figure 39 Calculated creep strains for SCC specimens.

With the shrinkage being the dominant factor it is still possible to obtain valid tensile creep curves as seen in Figure 39. The curve represented by ϵ_{Creep} is the resulting creep curve after the shrinkage were subtracted from the measured creep and it represents the tensile creep behaviour of SCC. This curve was used to do curve fitting with Maxwell chains in order to predict long term tensile creep behaviour of SCC being loaded under the same conditions. The curve fitting will be explained in Chapter 5.

4.3 SFRSCC Creep

The experimental data obtained from the tensile creep tests presented tensile creep curves for the SFRSCC specimens will aid in understanding the behaviour of SFRSCC subjected to tensile stress over time. In total four specimens were tested but one of the specimens proved to be an outlier, which could be explained as the LVDTs from that specimen most likely being faulty. The curves seen in Figure 40 are from the three remaining SFRSCC specimens (SFRSCC 1 to 3) and represent the creep and shrinkage effects that occurred during the duration of the experiments:

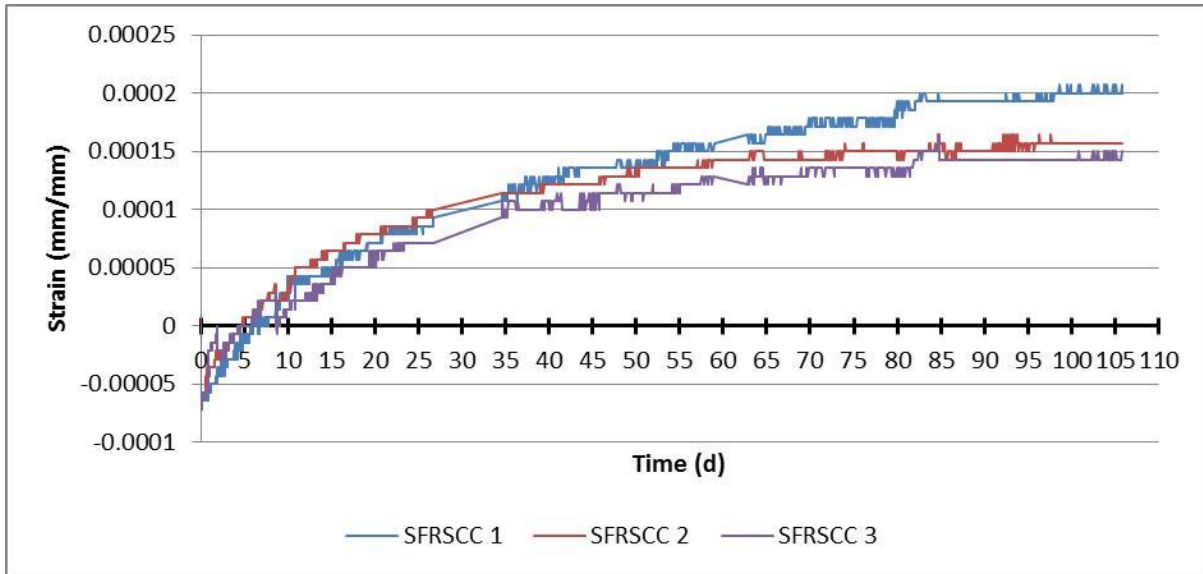


Figure 40 Displacement over time behaviour in SFRSCC creep specimens, measured.

The curves from Figure 40 are the measured displacements obtained from the creep experiments divided by the cross-sectional area with the elastic strain included and shrinkage not yet being subtracted. An average was taken from these curves and then shrinkage and the elastic strain were subtracted in order to find the tensile creep of SFRSCC, as seen in the Figure 41.

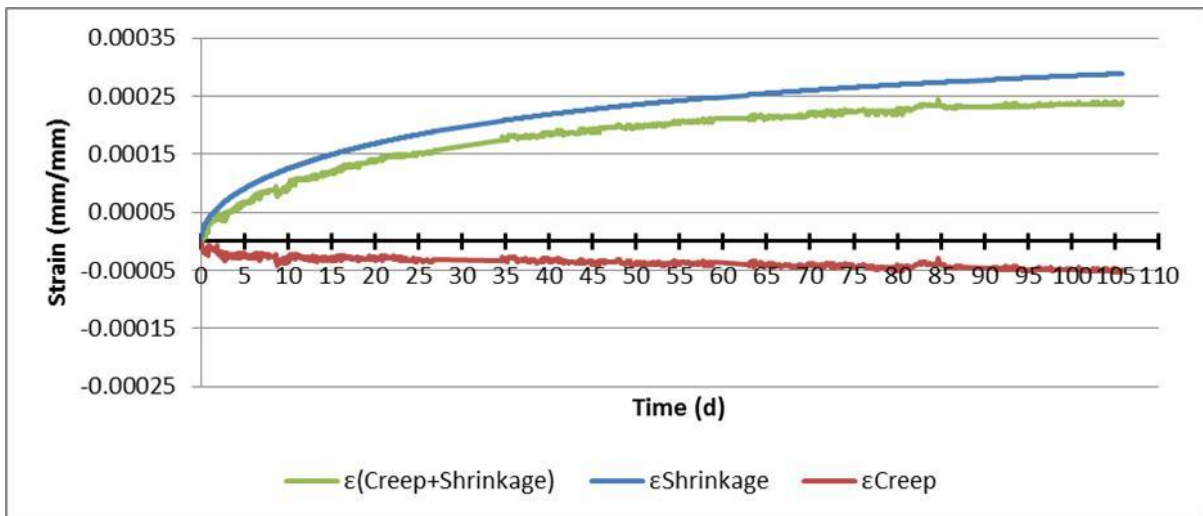


Figure 41 Calculated creep strains for SFRSCC specimens.

From Figure 41 it is noticeable that the shrinkage strain and the average measured creep strain are nearly similar, which leads to the conclusion that the shrinkage was the dominating factor during the tensile creep experiments of SFRSCC. As with SCC it was now possible to do curve fitting with Maxwell chains which would make it possible to predict future tensile behaviour of SFRSCC under the same conditions.

4.4 SFRSCC Notched Un-Cracked Creep

The experimental results of the third batch of tensile creep tests are presented and discussed in this section. Only two notched SFRSCC specimens (SFRSCC 1 and 2) were tested and their measured creep strains are presented in Figure 42.

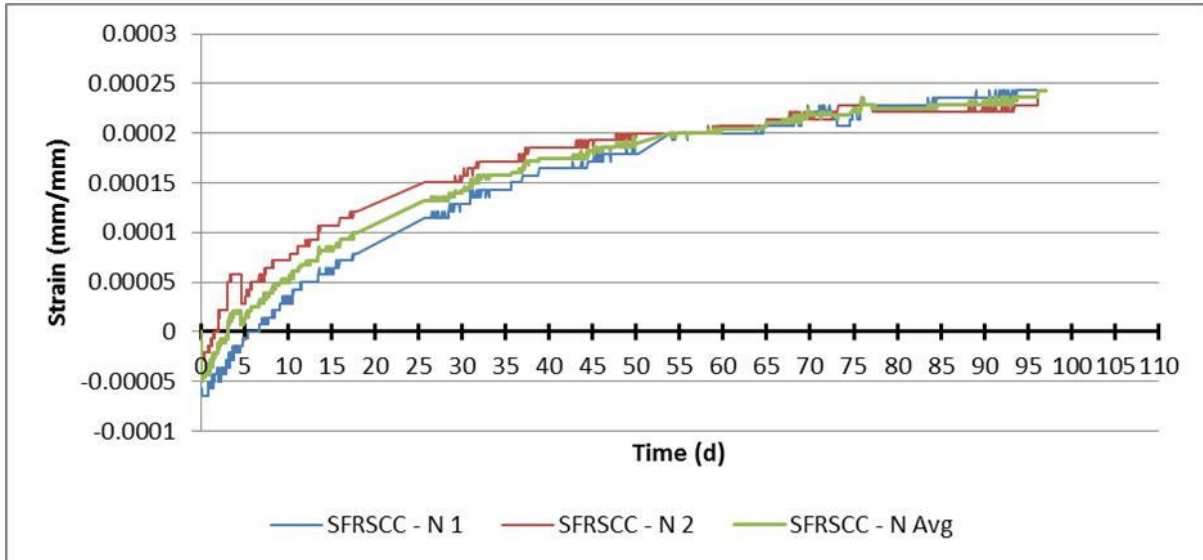


Figure 42 Displacement over time behaviour in notched SFRSCC creep specimens, measured.

What is noticeable from Figure 42 is that the two specimens behaved in similar manner under the same loading and conditions, which makes it possible to obtain an average creep strain. Figure 43 will represent the average tensile creep strain of these specimens.

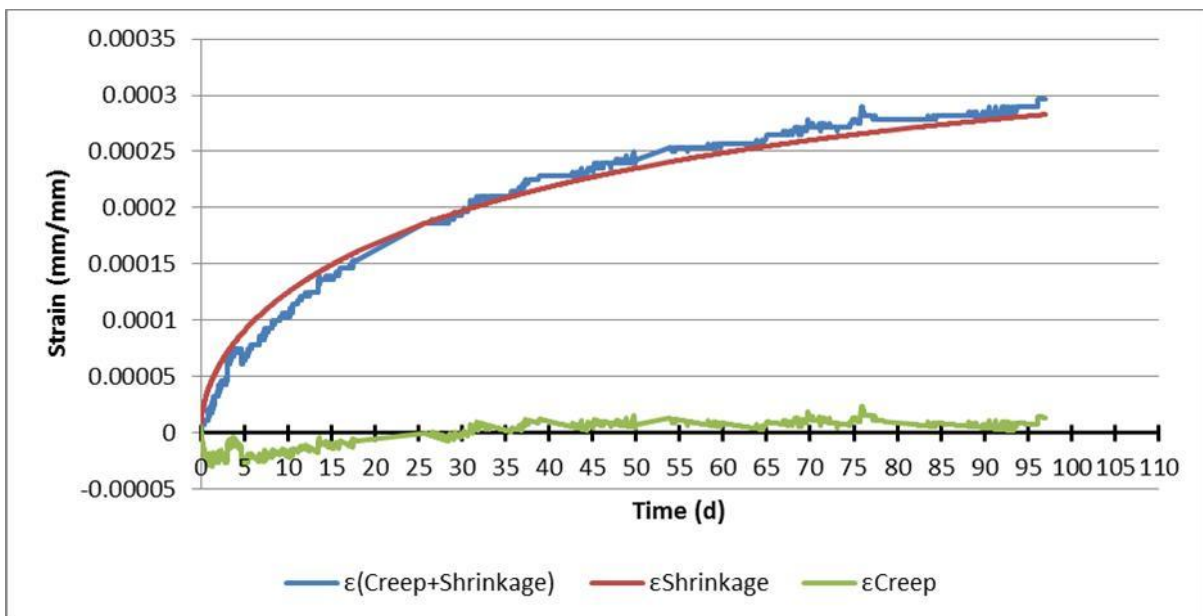


Figure 43 Calculated creep strains for notched SFRSCC specimens.

From Figure 43 it can be seen that the tensile creep ϵ_{Creep} is close to zero, which corresponds to the results of the tensile creep tests performed on the SFRSCC specimens. Even though only two specimens were tested, the specimens behaved in a similar manner. What is also apparent in Figure 43 is that the measured creep strain was approximately the same as the shrinkage strain, which indicated that little or no tensile creep took place, leading to the low tensile creep values. The curve obtained from the notched SFRSCC specimens will be compared directly to the curves of the notched, pre-cracked SFRSCC specimens in order to determine the effect of fibre pull-out.

The comparisons will be discussed in detail in Chapter 4.6. The tensile behaviour of the notched, pre-cracked specimens will be discussed next.

4.5 SFRSCC Notched Pre-Cracked Creep

In order to test pre-cracked specimens it was important to crack the specimens beforehand without causing large crack widths. Large crack widths could cause the bond between the fibres and concrete to break, which could weaken the specimens significantly and therefore affect the results of the tensile creep tests. The specimens were cracked beforehand by the Zwick machine and the Zwick software made it possible to stop the tests immediately after initial failure occurred, thereby avoiding large crack widths. The average tensile strength of the notched, pre-cracked SFRSCC specimens was 4.15 MPa . The measured tensile creep displacements of the three pre-cracked, notched SFRSCC specimens (SFRSCC N/P 1 to 3) are presented in Figure 44.

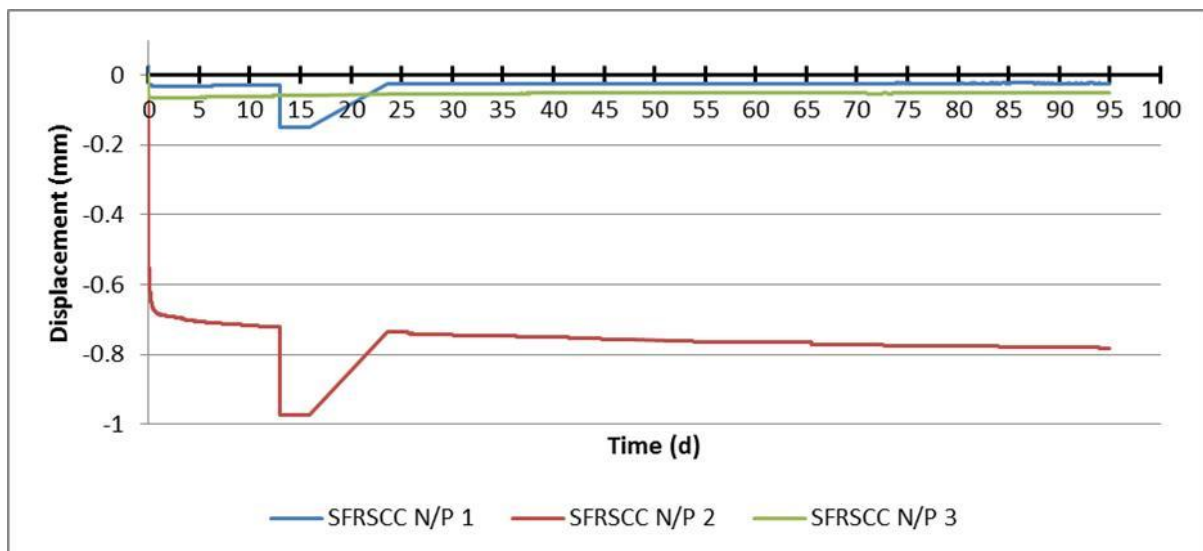


Figure 44 Displacement over time behaviour in notched, pre-cracked SFRSCC creep specimens, measured.

From Figure 44 it can be seen that large displacements occurred during the tensile creep tests. When looking at the results the initial crack widths are identified by the large displacements that occurred during the beginning of the tests. With the different crack widths making the concrete specimens

behave differently, it was difficult to find an average displacement of the three specimens. It is also noticeable that SFRSCC 2 exhibits large displacements. However, it behaved similarly to SFRSCC 1 and 3 after the initial displacement, making it viable for analysis procedures. It was therefore necessary to look at the displacements of the three specimens individually.

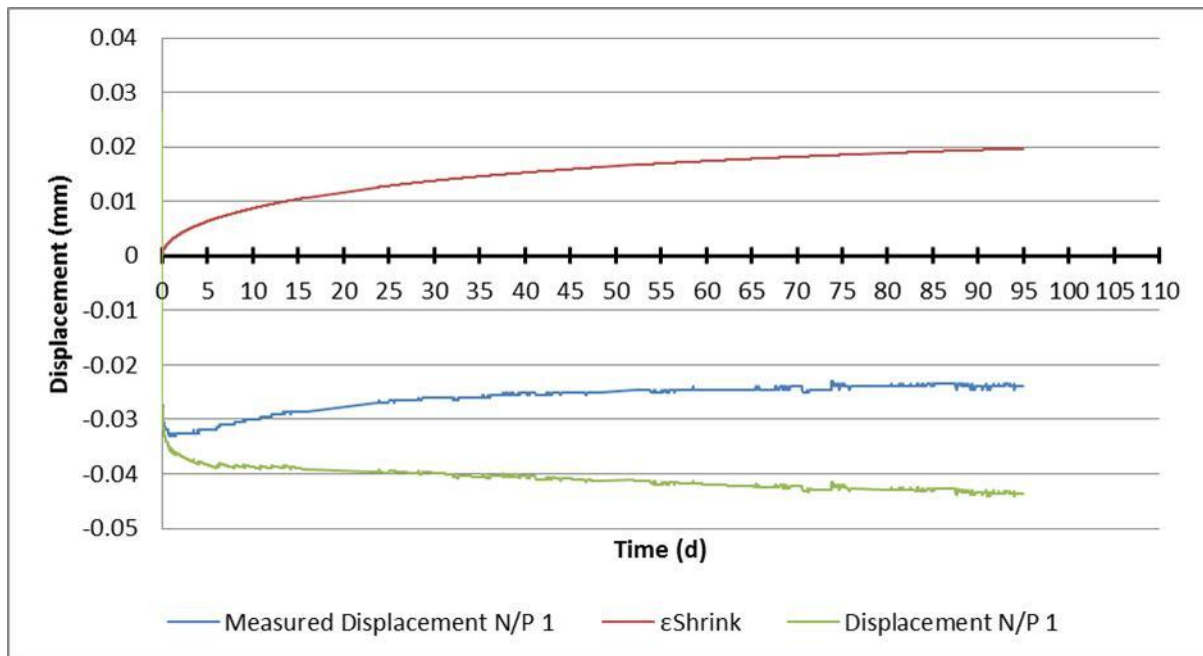


Figure 45 Time-dependent behaviour of notched, pre-cracked SFRSCC Specimen 1.

Figure 45 represents the measured displacement of the first notched, pre-cracked SFRSCC specimen with the shrinkage displacement included. Displacements were used because the creep phenomenon was localised at the cracks, therefore not representing the material behaviour. When taking the tensile creep behaviour of SFRSCC in account it was concluded that the creep displacements were mainly caused by the fibre pull-out. It was however still important to look at the other curves as well to gain better perspective about fibre pull-out behaviour. The tensile creep

displacements of the other two specimens follow in Figures 46 and 47.

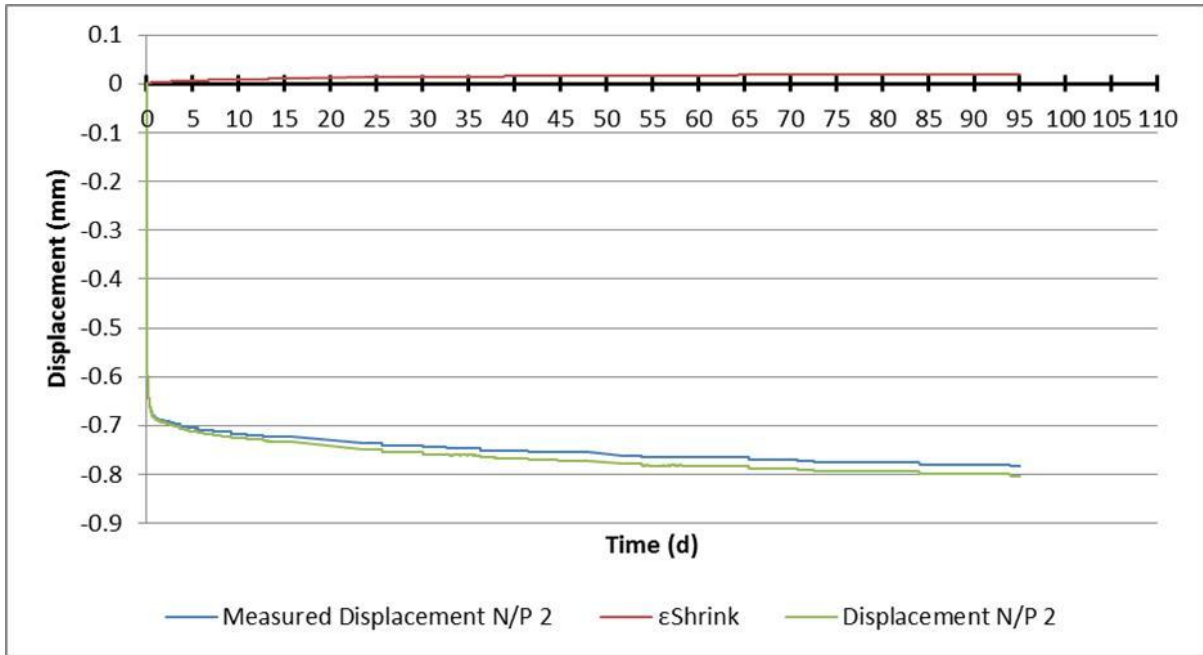


Figure 46 Time-dependent behaviour of notched, pre-cracked SFRSCC Specimen 2.

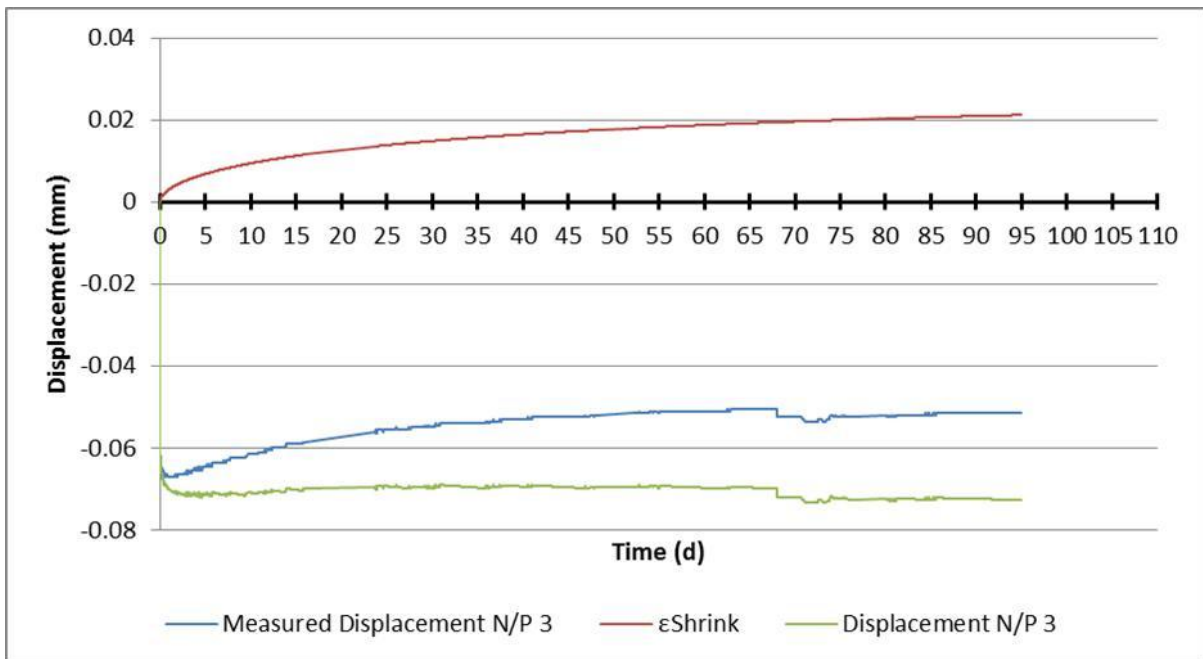


Figure 47 Time-dependent behaviour of notched, pre-cracked SFRSCC Specimen 3.

A summary of the tensile tests performed on the notched, pre-cracked SFRSCC specimens is presented in Figure 48.

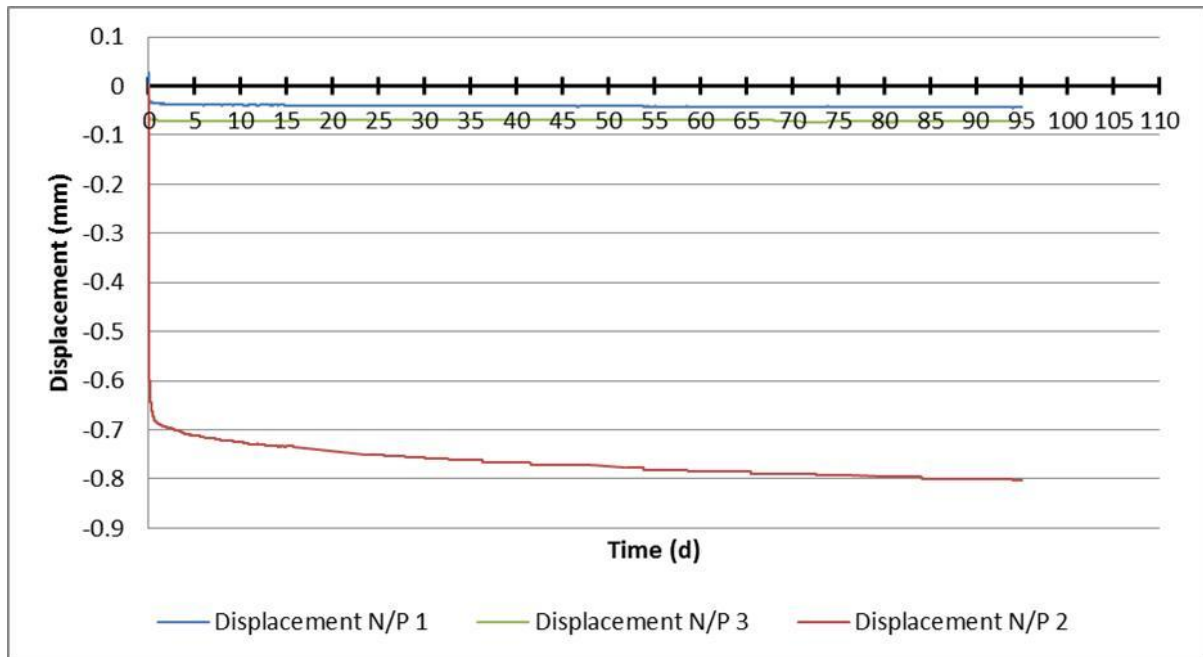


Figure 48 Tensile creep displacements of notched, pre-cracked SFRSCC specimens.

From Figures 45 to 47 it can be seen that the shrinkage had a significant effect on the measured displacements. This was expected seeing that the loading percentage was 50 % of σ_{break} , but it was only about 15 % of $\sigma_{maxnotch}$. Shrinkage was a dominating factor in the creep results of the un-notched SFRSCC specimens loaded at 50% of $\sigma_{maxnotch}$, therefore the effect of shrinkage on the pre-cracked specimens was expected. Another prominent factor that influenced the displacement of the specimens was the effect of fibre pull-out. From the two main factors listed above, it could be concluded that little to no tensile creep occurred in the concrete during the tensile creep tests performed on the notched, pre-cracked specimens. In Section 4.6 the results of the relevant tests are compared in order to be more conclusive.

4.6 Comparison

In this section, different comparisons are made in order to investigate the time-dependent behaviour of SCC and SFRSCC with and without tensile loading. In order to compare the results directly, the measurements at 90 *days* from the start of the tests will be compared. The first comparison compares the shrinkage strains between the SCC and SFRSCC specimens. The predicted shrinkage strains of the two different concretes are seen in Figure 49.

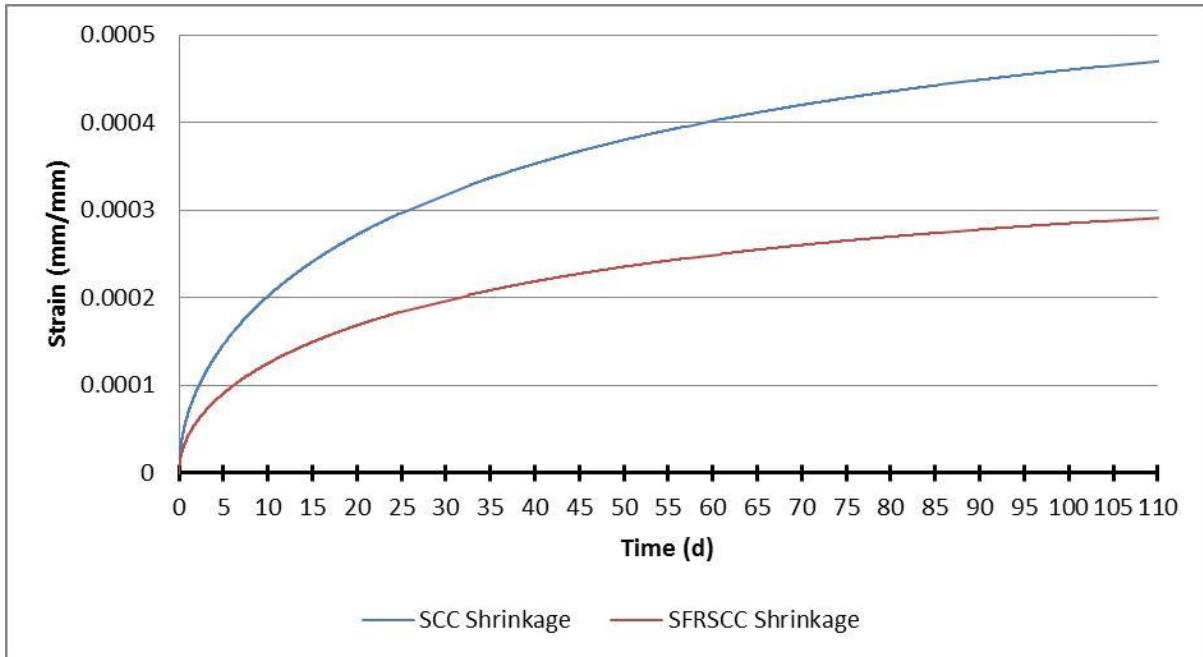


Figure 49 Shrinkage strains of SCC and SFRSCC specimens.

From Figure 49 it is clear that steel fibres reduced the shrinkage of concrete significantly by almost 50%. After 90 days the shrinkage strain for SCC was $449\mu mm/mm$ and $278\mu mm/mm$ for SFRSCC. The next step would be to compare the tensile creep between SFRSCC and SCC in Figures 50.

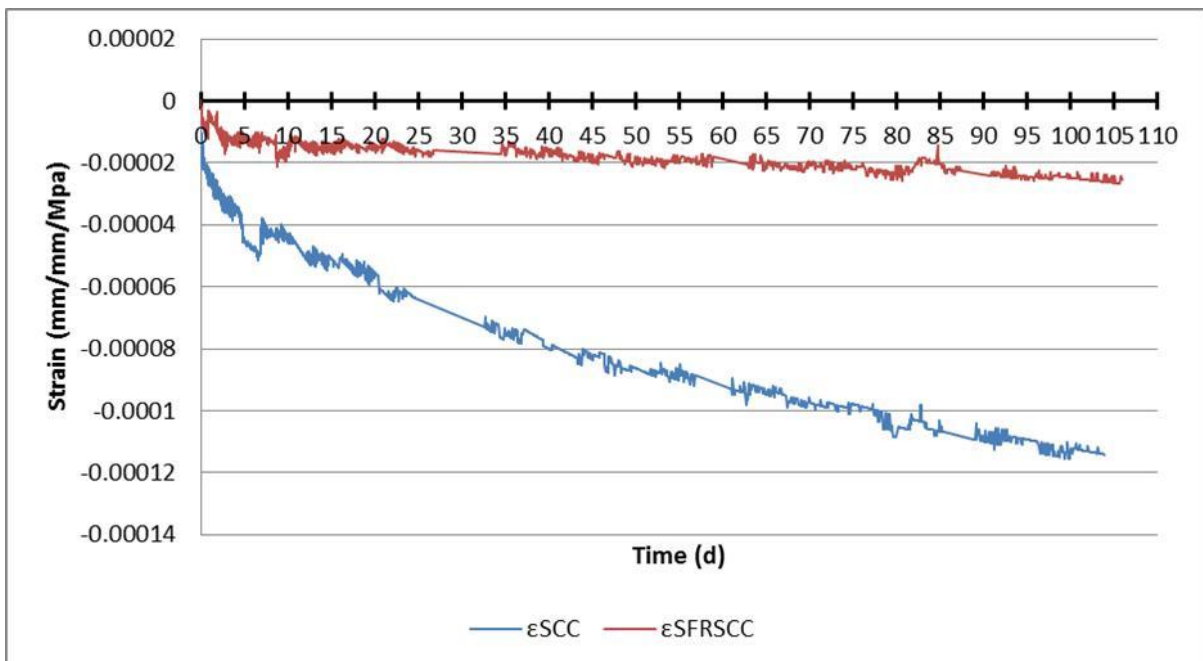


Figure 50 Tensile creep strains of SCC and SFRSCC specimens.

From Figure 50 the significant influence of steel fibres on the tensile creep of concrete is apparent. The maximum creep strain at 90 days for SCC was found to be $109.8\mu mm/mm/MPa$ and for

SFRSCC it was $24\mu\text{ mm/mm/MPa}$. It appears from this result that steel fibres reduce the tensile creep of concrete. So far it was seen that the advantages of steel fibres was that they reduced the shrinkage and creep strains of concrete. The only unknown factor was whether fibre pull-out played a significant role in the tensile behaviour of cracked SFRSCC.

The next step was to compare the notched SFRSCC results with the notched, pre-cracked SFRSCC results. The creep behaviour was localised at the cracks, which was why the displacements of these batches were compared. The average displacement of the notched SFRSCC specimens was scaled so that it could be compared directly to the notched, pre-cracked specimens.

As mentioned before, the notched SFRSCC specimens were loaded to 18 % of $\sigma_{maxnotched}$ and 65 % of σ_{break} . The loading percentage of Frames G and H was 50 % of σ_{break} , therefore the results of the notched SFRSCC specimens had to be factored to a loading percentage of 50%.

$$\varepsilon_{factored}(t) = \varepsilon_{notched}(t) \times \frac{50\%}{65\%}$$

This leads to Figure 51.

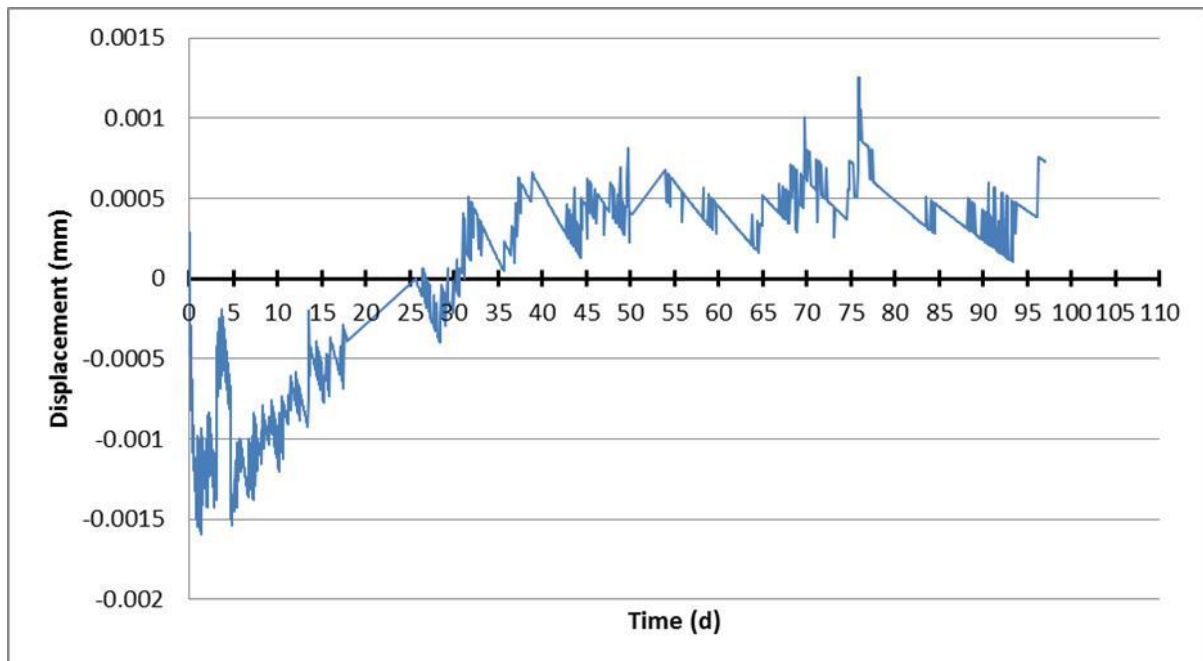


Figure 51 The adjusted tensile creep strain of notched SFRSCC specimens.

When comparing the displacements of the notched specimens to the displacements of the notched, pre-cracked specimens, it is apparent in Figure 52 that the latter was the most significant. Figure 52 represents the average displacement of the notched SFRSCC specimens plotted against the displacements of the notched, pre-cracked SFRSCC specimens against time.

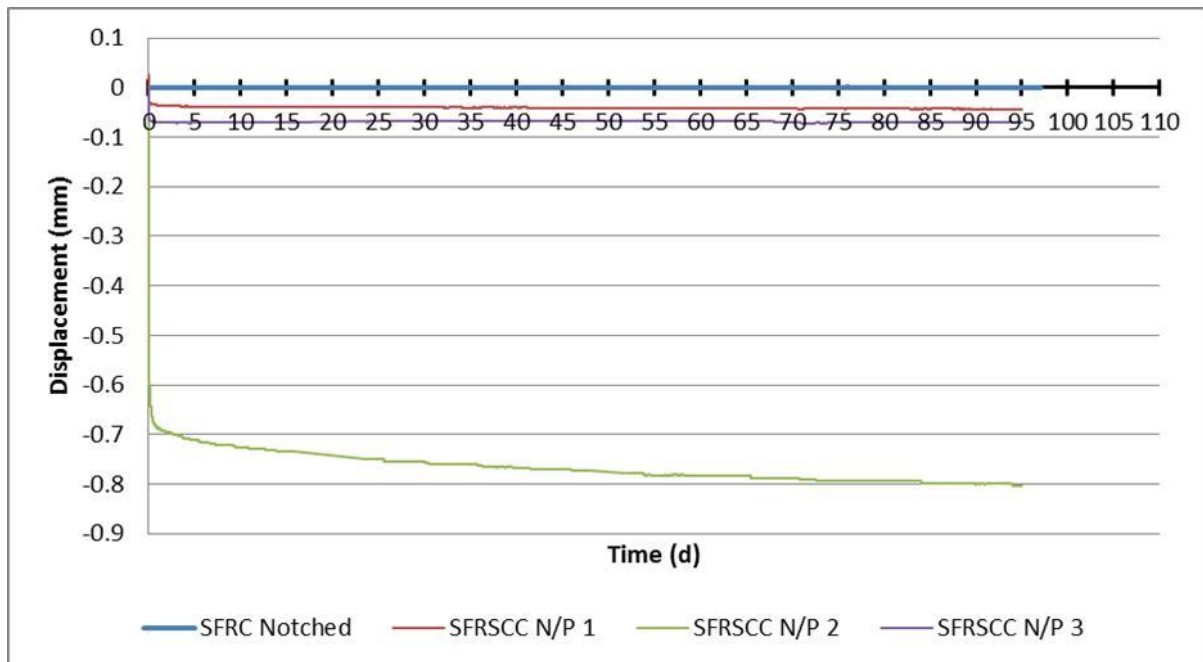


Figure 52 Comparison of the creep displacements of the notched SFRSCC specimens.

From Figure 52 it is apparent that the fibre pull-out overshadowed any effects the tensile creep might have had on the concrete after cracking occurred. The comparisons of the un-notched specimens identified definite advantages to SFRSCC, which might be rendered insignificant when looking at the comparison of the notched specimens' results. In order to determine whether the results of the notched, pre-cracked specimens are disadvantageous, further investigation is needed.

From the results of the notched specimens it was difficult to see whether fibre pull-out would be a significant detrimental factor as time progresses, which made it necessary to perform analyses using the results of the un-cracked and pre-cracked notched specimens. These analyses would give a good indication of what tensile behaviour to expect after the concrete has cracked. The different analysis procedures used in the curve fitting and finite elements analyses are described in detail in the next chapter.

Chapter 5

5. Analytical Procedures

Curve fitting and the software analyses performed have been mentioned earlier without detailed explanations. Throughout the experimental procedures data were acquired and processed, but certain procedures were needed in order to make the data useful and applicable. The different data procedures are explained in the next few sections.

5.1 FIB Model Code 2010

The model provided in the FIB Model Code 2010 to predict the shrinkage strain of concrete was modified and adjusted so that it could be used to extrapolate the shrinkage results. The expressions for predicting the shrinkage of concrete were explained in Chapter 2.6.2. In order to simplify the curve fitting process the expressions that were obtained from the FIB Model Code 2010 were modified slightly in order to make them simpler. Another reason for modifying the expressions provided in the FIB Model Code 2010 was because they were more applicable to conventional concrete than for SCC or SFRSCC. These expressions have been condensed into one single expression:

$$y(t - t_s) = A \times \sqrt{\frac{t - t_s}{87.5 + (t - t_s)}} + B \quad (5.1)$$

Where A and B are functions relying on the humidity, concrete type, time of loading, concrete cylinder strength and the notional size h . The value of 87.5 mm^2 was calculated by using the notional size of the member. The most important aspect of Equation 5.1 is that it is a function of time t_s seeing that this will play a part in the curve behaviour. The autogenous shrinkage was considered to be insignificant and was left out of Equation 5.1.

The process of curve fitting was to plot the curve obtained by Equation 5.1 against the shrinkage results in order to model the shrinkage behaviour as accurately as possible. Certain points were chosen from the shrinkage results to which the curve obtained from the expression had to correspond with. Values were estimated for A and B and were adjusted until the curve from the

expression corresponded with the shrinkage curves of the SCC and SFRSCC. The factor A determined the shape of the curve and, which would normally be zero, had to have a certain value because of the faulty shrinkage data previously mentioned. The fitted curve produced a simple expression that was able to describe the shrinkage behaviour of concrete.

Figure 53 gives an example of curve fitting for SCC.

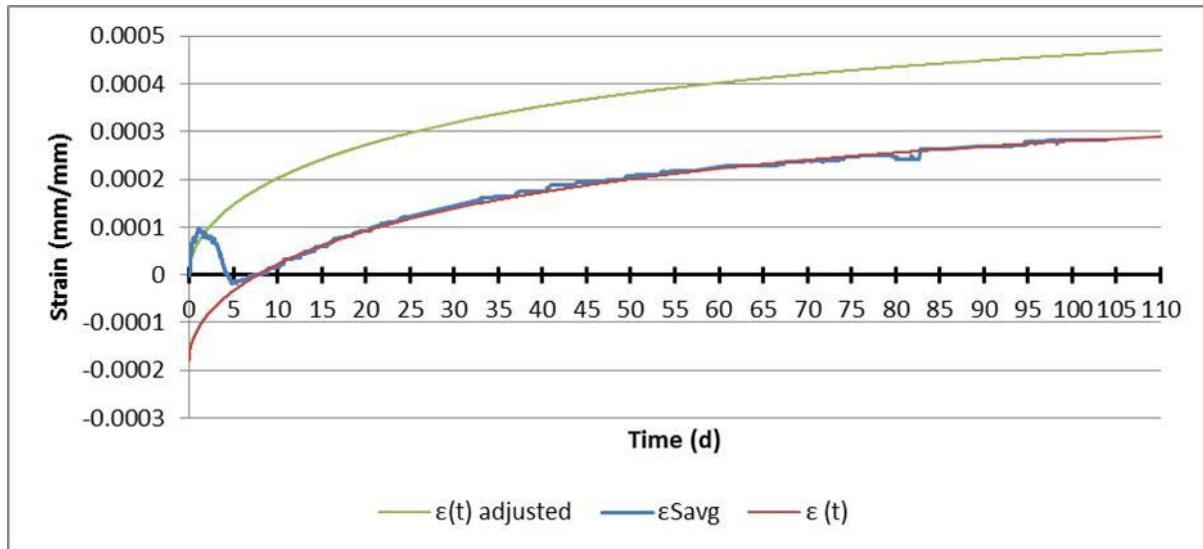


Figure 53 Example of curve fitting done on the SCC experimental data.

From Figure 53 the factor $eSavg$ was the shrinkage strains of SCC, $\varepsilon(t)$ is the curve obtained from Equation 5.1 and $\varepsilon(t)adjusted$ is the same as $\varepsilon(t)$ with B removed in order to represent the predicted shrinkage. The factor B had the value of $-181\mu mm/mm$ in order for the curve shape to fit the shrinkage shape of SCC, whereas A had the value of $630\mu mm/mm$. Equation 5.1 managed to represent the shrinkage behaviour of SCC, which made it possible to use the expression to calculate the shrinkage strains of SCC. The expression was used to calculate the shrinkage behaviour for SCC for the design period of 30 years. It was mentioned in Chapter 4.6 that the shrinkage strain at 90 days, ε_{Sh-90d} was $449\mu mm/mm$ and it had been calculated that the shrinkage strain at 30 years, ε_{Sh-30y} was $627\mu mm/mm$. The shrinkage expressions from the FIB Model Code estimated $\varepsilon_{Sh-90d} = 337.9\mu mm/mm$ and $\varepsilon_{Sh-30y} = 452.5\mu mm/mm$.

The same procedures as with SCC were followed when the curve fitting was done on the shrinkage behaviour of SFRSCC. The factors A and B had the values of $390\mu mm/mm$ and $-120\mu mm/mm$, respectively. After the prediction curve was obtained the values for shrinkage were calculated as $\varepsilon_{Sh-90d} = 278\mu mm/mm$ and $\varepsilon_{Sh-30y} = 388\mu mm/mm$.

The FIB Model Code 2010 also provided mathematical expressions to predict the creep of conventional concrete. The expressions provided by the FIB model code have been modified and adjusted in a similar fashion to the shrinkage expressions in order to make the curve fitting process simpler. The expressions have been described in detail in Chapter 2 and it is apparent that the expressions relied on a number of functions. Taking in mind that many of these functions were parameters that were constant they could therefore be condensed into a single function, which led to Equation 5.2:

$$y(t - t_0) = C \times \left(\frac{t - t_0}{300.9102 + (t - t_0)} \right)^{0.3} + D \quad (5.2)$$

The factor C represented all the different constants from the original expressions being condensed into one single function, which allowed it to change the shape of the curve. D was included in the expression in case the curve needed to be adjusted along the vertical axis. The curve fitting was done in a similar manner as with shrinkage. An example of the curve fitting performed on the creep of SCC is given in Figure 54.

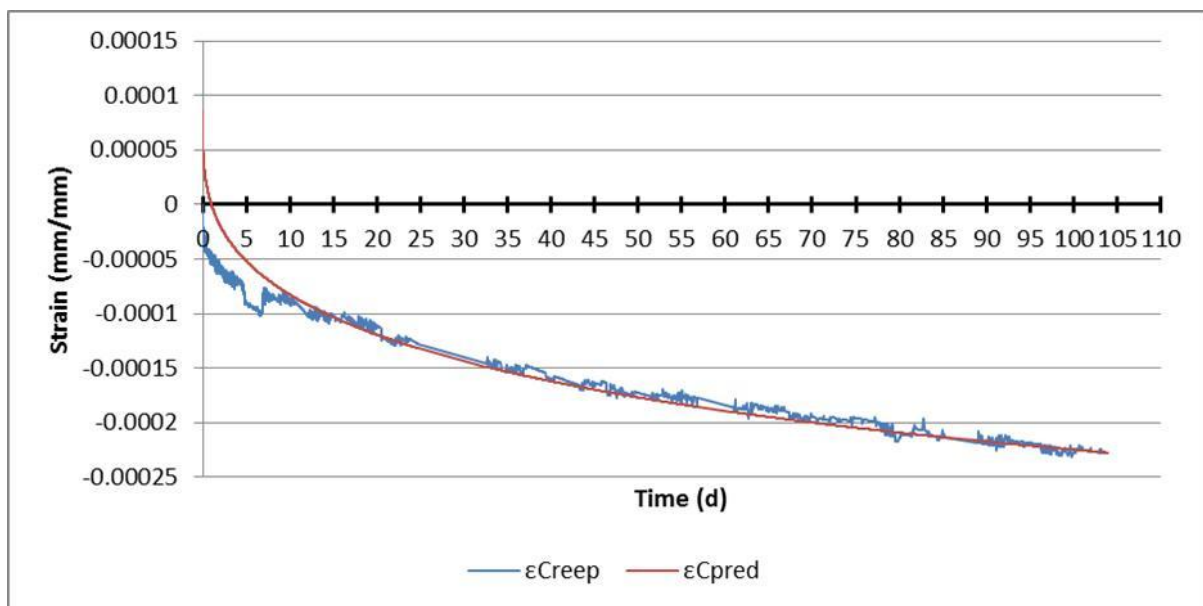


Figure 54 Predicted tensile creep for SCC.

From Figure 54 ϵ_{Creep} represented the creep strains of SCC and ϵ_{Cpred} was the creep calculated by Equation 5.2. The factors C and D from Equation 5.2 had the values of 470μ and -85μ , respectively. Upon inspection it can be seen that the predicted creep does not start at zero, because the function provided by the FIB Model Code 2010 restricted the shape of the curve. If D had a zero value, the chosen points between the expression and the data would not have corresponded. With the value of D being prominent with regards to the creep strain of SCC it was necessary to use

another method of curve fitting. Another flexible method of curve fitting was to use Maxwell chains instead of the expression provided by the FIB Model Code 2010, which will be discussed in the next section.

The creep predictions done above would be used to calculate a creep strain value at 30 years, which was necessary in order to do curve fitting with Maxwell chains. For SCC $\varepsilon_{Cr-90d} = 220\mu\text{ mm/mm}$ and $\varepsilon_{Cr-30y} = 381\mu\text{ mm/mm}$ and for SFRSCC $\varepsilon_{Cr-90d} = 47\mu\text{ mm/mm}$ and $\varepsilon_{Cr-30y} = 73\mu\text{ mm/mm}$.

5.2 Maxwell Chain Model

The Maxwell chain model was more flexible than the expression derived from the FIB Model Code 2010 when used for curve fitting, because it was possible to use as many chains as desired. This makes it possible to modify the curves as needed. The Maxwell chains model were explained in Chapter 2.6.1 and this section will demonstrate its application to the data obtained from the creep experiments.

From Chapter 2 comes the simplified general equation for Maxwell chains presented by Equation 5.3:

$$\sigma = - \left[E_0 + E_1 e^{-\frac{t}{\lambda_1}} + \dots + E_n e^{-\frac{t}{\lambda_n}} \right] \varepsilon \quad (5.3)$$

Equation 5.3 can be rewritten in order to find the strain as a function of time with a constant stress σ applied:

$$\varepsilon(t) = - \frac{\sigma}{\left[E_0 + E_1 e^{-\frac{t}{\lambda_1}} + \dots + E_n e^{-\frac{t}{\lambda_n}} \right]} \quad (5.4)$$

Equation 5.5 will be used to do curve fitting with the SCC, SFRSCC and pre-cracked SFRSCC experimental data. Upon inspection it can be seen that for $t = 0$ days the dashpots will not be active yet and the system is in its full elastic state. This is confirmed by Equation 5.5:

$$\varepsilon(0) = - \frac{\sigma}{[E_0 + E_1 + E_2 + E_3 + E_4 + E_5 + E_6 + E_7]} \quad (5.5)$$

From Equation 5.5 the elastic strain $\varepsilon(0)$ is required in order to know what the total elasticity of the system should be. The total elasticity of the system should represent the modulus of elasticity of the material, meaning:

$$\sum_{n=7} E_n = E_{28}$$

Where E_{28} is the modulus of elasticity for the concrete at 28 days.

So far all the predictions have been done for a time period of 30 *years*. This was applied to the Maxwell chain method. It was therefore assumed that stress relaxation would be complete at $t = 30 \text{ years}$, which meant that the dashpots would be fully extended and that all the springs would be relaxed except for the spring E_0 that was not connected to a dashpot:

$$\varepsilon(30 \text{ years}) = -\frac{\sigma}{E_0} \quad (5.6)$$

It is seen from Equation 5.6 that the end strain value $\varepsilon(30 \text{ years})$ is needed in order to calculate the elastic component E_0 . The creep value calculated at 30 *years* by the simplified expression (Equation 5.2) describing the tensile creep behaviour in the previous section provided a good indication of what $\varepsilon(30 \text{ years})$ should be. As soon as $\varepsilon(0)$ and $\varepsilon(30 \text{ years})$ were known it was possible to continue with the curve fitting.

The next step was to estimate values for the springs and dashpots, which was done by hand, which required the values of the unknowns to be changed individually until the calculated curve points and the experimental data points corresponded. The factors $\varepsilon(0)$ and $\varepsilon(30 \text{ years})$ were represented by ε_{el} and ε_B respectively, where ε_{el} was the elastic strains and ε_B was the strain calculated at 30 *years* by Equation 5.2 with the elastic strain added. The curve fitting solutions will follow next.

5.2.1 SCC

The applied tensile stress $\sigma_{T-SCC} = 2.001 \text{ MPa}$ was calculated by using the cross-sectional area. The elastic modulus E_{28} was estimated from SANS 10100-1 to be $33\,700 \text{ MPa}$ (SANS 10100-1, 2000). The elastic modulus E_0 of the spring element can be calculated by Equation 5.7:

$$E_0 = -\frac{\sigma_{T-SCC}}{\varepsilon_B} \quad (5.7)$$

The factor ε_B is calculated by adding the elastic strain to Equation 5.2:

$$\varepsilon_B = -(y(t - t_0) + \varepsilon_{el}) \quad (5.8)$$

Equation 5.8 can be rewritten as:

$$\varepsilon_B = -\left(C \times \left(\frac{t-t_0}{300.9102+(t-t_0)}\right)^{0.3} + D\right) + \varepsilon_{el} \quad (5.9)$$

From Equation 5.9 the term $(t - t_0)$ will have the value of 10 800 *days*, C and D will have the values 0.00047 and -0.000085 respectively and the factor ε_{el} was calculated by $\varepsilon_{el} = \sigma_{T-SCC}/E_{28} = -5.93908 \times 10^{-5} \text{ mm/mm}$. These factors led to the calculation of $\varepsilon_B =$

$-6.16796 \times 10^{-4} \text{ mm/mm}$, which led to the calculation of $E_0 = 4543 \text{ MPa}$. Equation 5.9 was used to calculate all values for ε_B for the SFRSCC specimens. With all the factors known it was possible to continue with the curve fitting. Table 5.1 presents all the different values for the springs and dashpots in the five-chain system after the curve fitting procedure was completed.

Table 5.1 Maxwell chain parameters for SCC

Tens. Strength	$\sigma_{T\text{-SCC}}$	2.001	MPa	Elastic Strain	ε_{el}	-5.939E-05	mm/mm
Comp. Strength	f_{c28}	38.8	MPa	End Strain	ε_B	-6.168E-04	mm/mm
Elastic Mod.	E_{28}	33700	MPa				
E. Mod. Spring	E0	4543	MPa				
E. Mod. Spring	E1	12450.7	MPa	Damp. Viscosity	λ_1	0.06	t^{-1}
E. Mod. Spring	E2	7000	MPa	Damp. Viscosity	λ_2	2	t^{-1}
E. Mod. Spring	E3	8156	MPa	Damp. Viscosity	λ_3	50	t^{-1}
E. Mod. Spring	E4	1300	MPa	Damp. Viscosity	λ_4	700	t^{-1}
E. Mod. Spring	E5	250	MPa	Damp. Viscosity	λ_5	5000	t^{-1}

From Table 5.1 it can be seen that

$$\sum_{n=5} E_n = E_{28} = 33700 \text{ MPa}$$

The estimated factors from Table 5.1 were estimated by hand until the Maxwell curve and the SCC experimental curve corresponded. Figure 55 presents the two corresponding curves:

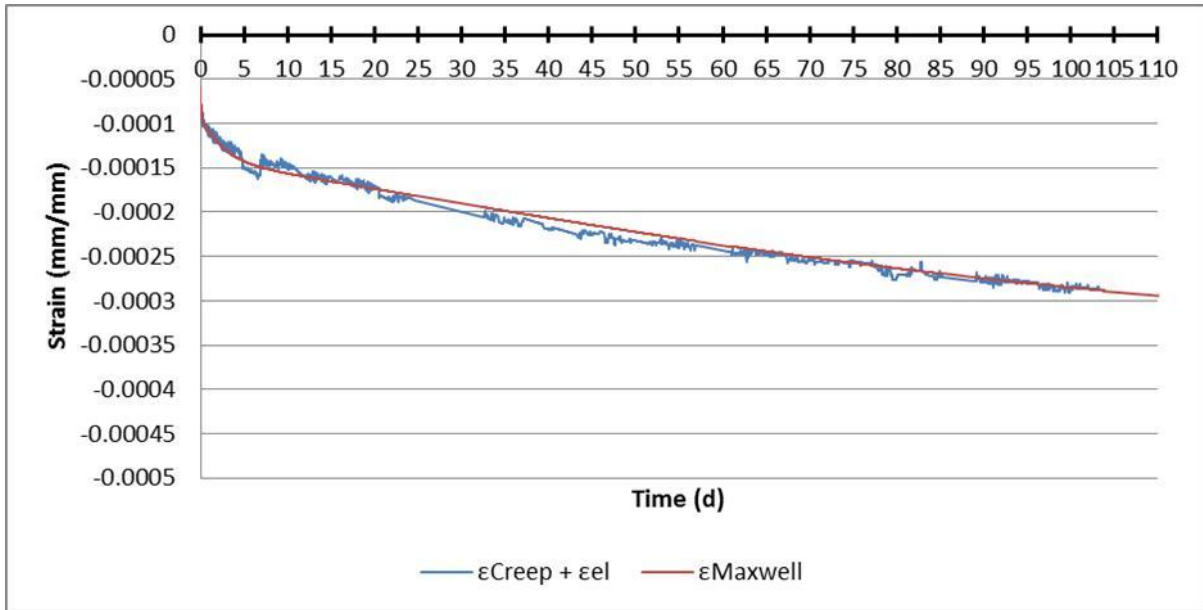


Figure 55 Maxwell curve fitted to SCC tensile creep curve.

Observing Figure 55 it is noticeable that the SCC creep curve does not start at zero, which is because the elastic strain was added seeing that the Maxwell model already incorporates the elastic strain. Figure 56 presents the same Maxwell curve, but on a logarithmic horizontal axis, which further demonstrates the accuracy of the curve fitting done.

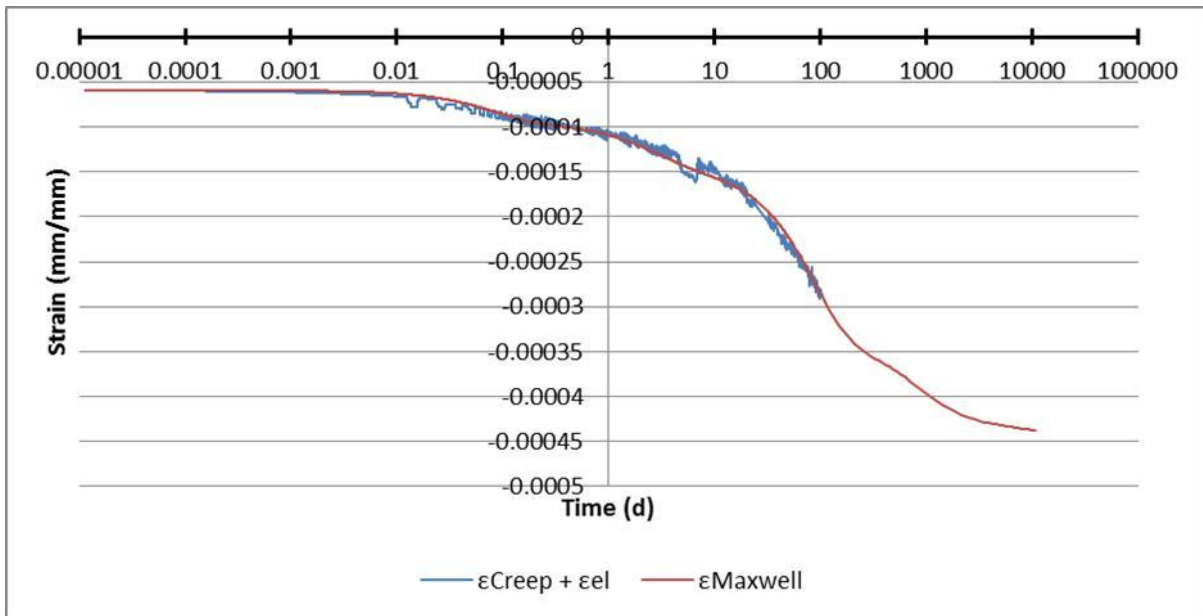


Figure 56 Maxwell curve fitted to SCC tensile creep curve – logarithmic scale.

5.2.2 SFRSCC

The procedure for curve fitting was done exactly the same as was done with the SCC creep results; the only difference being that the SFRSCC test results were analysed with seven chains instead of

five. The applied tensile stress was obtained the same way with $\sigma_{T-SFRC} = 1.987 \text{ MPa}$. The elastic modulus E_{28} was estimated to be $34\,125 \text{ MPa}$.

The other factors had the values of 0.00008 and 0.0 for C and D , respectively. The elastic strain $\epsilon_{el} = -5.82288 \times 10^{-5} \text{ mm/mm}$ was used to calculate ϵ_B , with $\epsilon_B = -1.37572 \times 10^{-4} \text{ mm/mm}$. The elastic modulus E_0 of the spring was calculated and was found to be $14\,443.8 \text{ MPa}$. With all these factors calculated it was possible to continue with the curve fitting. After the curve fitting was completed the unknown factors were estimated as seen in Table 5.2.

Table 5.2 Maxwell chain parameters for SFRSCC

Tens. Strength	σ_{T-SCC}	1.987	MPa	Elastic Strain	ϵ_{el}	-5.823E-05	mm/mm
Comp. Strength	f_{c28}	40.5	MPa	End Strain	ϵ_B	-1.376E-04	mm/mm
Elastic Mod.	E_{28}	34125	MPa				
E. Mod. Spring	E_0	14443.8	MPa				
E. Mod. Spring	E_1	5000	MPa	Damp. Viscosity	λ_1	0.06	t^{-1}
E. Mod. Spring	E_2	3486	MPa	Damp. Viscosity	λ_2	1	t^{-1}
E. Mod. Spring	E_3	3140	MPa	Damp. Viscosity	λ_3	15	t^{-1}
E. Mod. Spring	E_4	2910	MPa	Damp. Viscosity	λ_4	300	t^{-1}
E. Mod. Spring	E_5	2350	MPa	Damp. Viscosity	λ_5	70	t^{-1}
E. Mod. Spring	E_6	1295	MPa	Damp. Viscosity	λ_6	100	t^{-1}
E. Mod. Spring	E_7	1500.24	MPa	Damp. Viscosity	λ_7	3100	t^{-1}

From Table 5.2 it is apparent that

$$\sum_{n=7} E_n = E_{28} = 34125 \text{ MPa}$$

which was the estimated modulus of elasticity of the SFRSCC. The corresponding curves are presented by Figure 57:

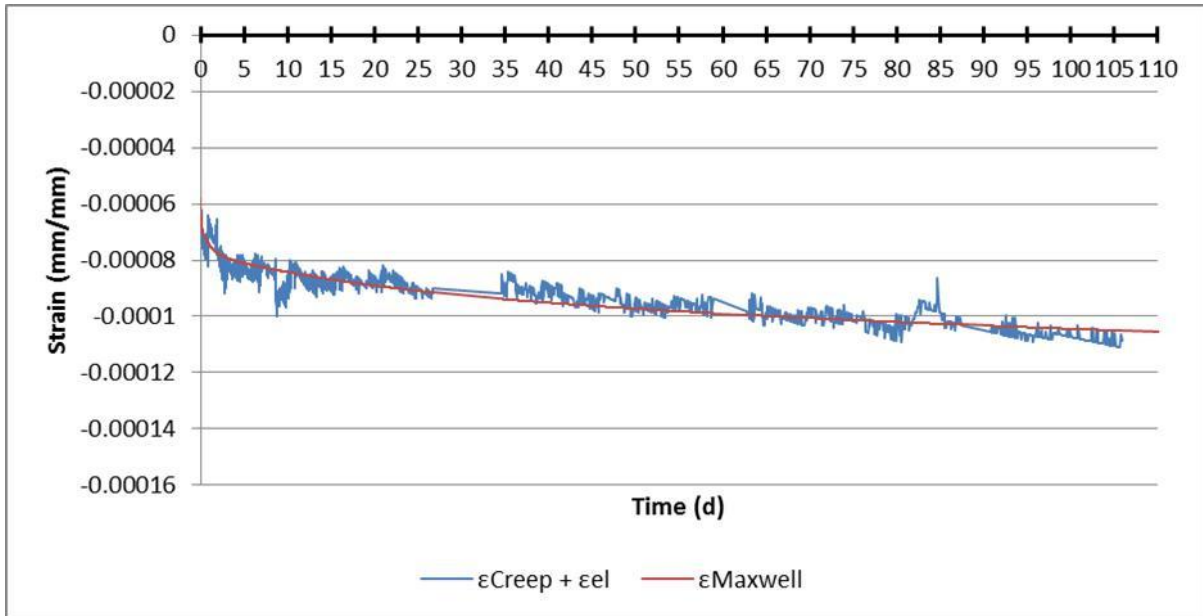


Figure 57 Maxwell curve fitted to SFRSCC tensile creep curve.

Looking at Figure 57 it may be difficult to see whether the Maxwell curve and the SFRSCC experimental data curve correspond because of the “noise” produced by the LVDTs. With Figure 58 displayed over a logarithmic horizontal axis it can be seen more clearly that it was possible to let the curves correspond closely. Figure 58 also displays an improved geometrical curve shape, which suggests that more Maxwell chains provide a smoother curve.

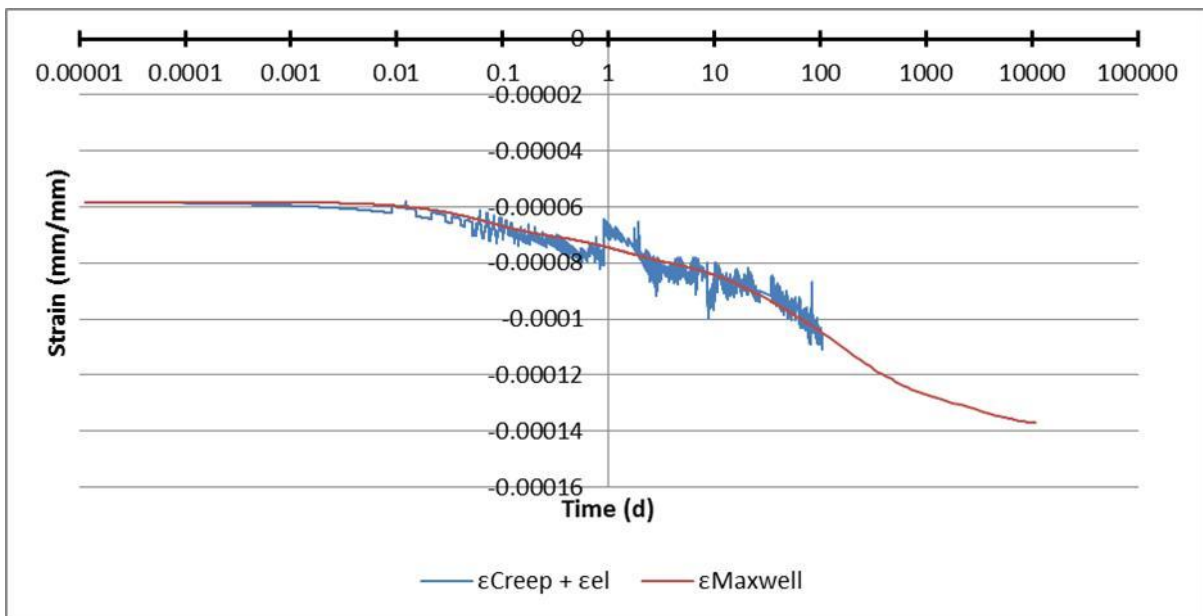


Figure 58 Maxwell curve fitted to SFRSCC tensile creep curve – logarithmic scale.

The curve fitting for the pre-cracked specimens was done in the same way as with the SFRSCC specimens. These curves are of the biggest importance seeing that they contain information about

the pull-out behaviour of SFRSCC in tension once cracking has occurred. The curve fitting of all three cracked specimens will be discussed next.

Upon consideration of the material behaviour of cracked SFRSCC it was necessary to follow a slightly different procedure. The cracked concrete would have a different modulus of elasticity because of the behaviour of the crack. Previously it was possible to estimate/calculate the modulus of elasticity of the concrete through expressions, but no such expressions exist for cracked SFRSCC. The new modulus of elasticity E_{new} will be calculated by dividing the applied stress by the strain calculated from the experimental data. The strain was calculated by dividing the displacements by an element size of 10 mm and it was decided to use the strain at 14.4 min because that is when the displacement curve has stabilized. The unknowns and curves of the three pre-cracked SFRSCC specimens will be presented next.

5.2.3 SFRSCC – N/P 1

Table 5.3 Maxwell chain parameters for pre-cracked SFRSCC specimen 1

Tens. Strength	σ_{T-SCC}	0.883	MPa	Elastic Strain	ϵ_{el}	-2.729E-03	mm/mm
E. Mod. New	E_{new}	323.5	MPa	End Strain	ϵ_B	-7.684E-03	mm/mm
E. Mod. Spring	E0	115.4	MPa	Strain (14 min)	$\epsilon_{14.4min}$	-2.729E-04	mm/mm
E. Mod. Spring	E1	58.1	MPa	Damp. Viscosity	λ_1	0.15	t^{-1}
E. Mod. Spring	E2	30	MPa	Damp. Viscosity	λ_2	2	t^{-1}
E. Mod. Spring	E3	40	MPa	Damp. Viscosity	λ_3	180	t^{-1}
E. Mod. Spring	E4	20	MPa	Damp. Viscosity	λ_4	100	t^{-1}
E. Mod. Spring	E5	10	MPa	Damp. Viscosity	λ_5	500	t^{-1}
E. Mod. Spring	E6	20	MPa	Damp. Viscosity	λ_6	4000	t^{-1}
E. Mod. Spring	E7	30	MPa	Damp. Viscosity	λ_7	1100	t^{-1}

The end strain value ϵ_B was calculated to be $-7.68367 \times 10^{-3} \text{ mm/mm}$ with the factors C and D having the values of 0.00027 and 0.00044, respectively. The fitted Maxwell curve can be seen in Figure 59.

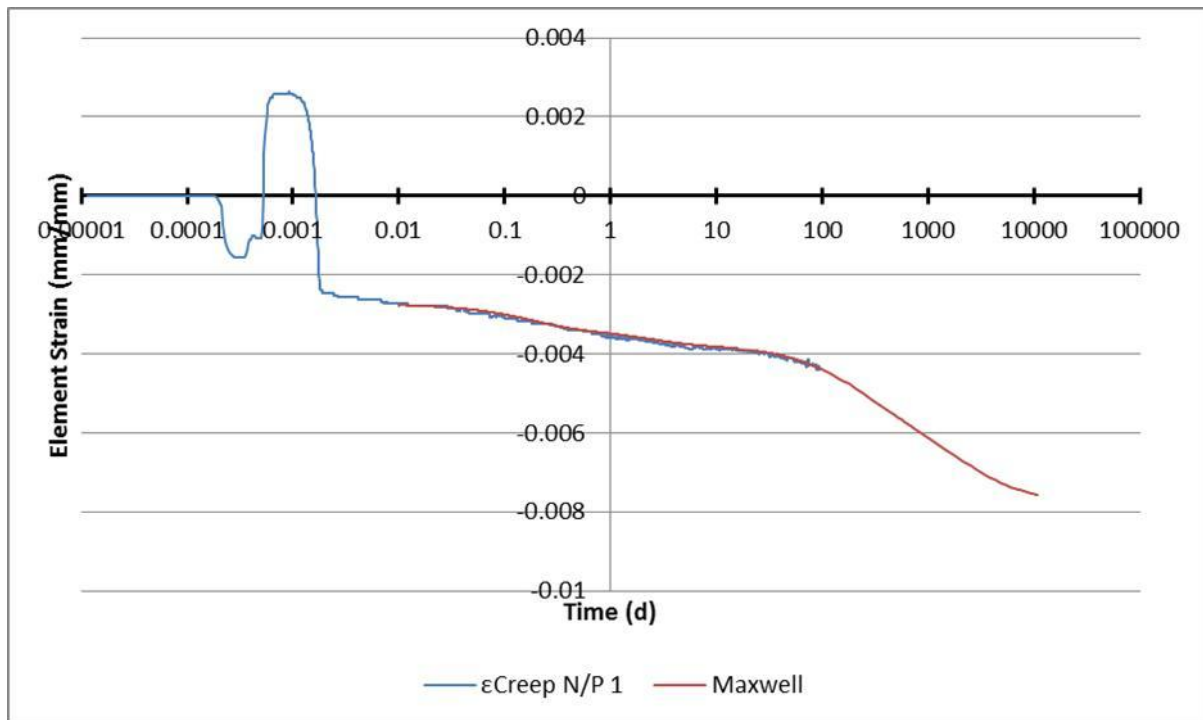


Figure 59 Maxwell curve fitted to notched, pre-cracked SFRSCC 1 tensile creep curve – logarithmic scale.

From Figure 59 it can be seen that the predicted Maxwell curve corresponded closely with the tensile creep curve of the first notched, pre-cracked SFRSCC specimen.

5.2.4 SFRSCC – N/P 2

Table 5.4 Maxwell chain parameters for pre-cracked SFRSCC specimen 2

Tens. Strength	σ_{T-SCC}	0.883	MPa	Elastic Strain	ϵ_{el}	-5.308E-02	mm/mm
E. Mod. New	E_{new}	16.636	MPa	End Strain	ϵ_B	-1.428E-01	mm/mm
E. Mod. Spring	E_0	6.2	MPa	Strain (14 min)	$\epsilon_{14.4min}$	-5.308E-02	mm/mm
E. Mod. Spring	E_1	3.436	MPa	Damp. Viscosity	λ_1	0.12	t^{-1}
E. Mod. Spring	E_2	1	MPa	Damp. Viscosity	λ_2	3	t^{-1}
E. Mod. Spring	E_3	2	MPa	Damp. Viscosity	λ_3	150	t^{-1}
E. Mod. Spring	E_4	0.9	MPa	Damp. Viscosity	λ_4	1000	t^{-1}
E. Mod. Spring	E_5	2	MPa	Damp. Viscosity	λ_5	1000	t^{-1}
E. Mod. Spring	E_6	1	MPa	Damp. Viscosity	λ_6	3500	t^{-1}
E. Mod. Spring	E_7	0.1	MPa	Damp. Viscosity	λ_7	100	t^{-1}

The end strain value ϵ_B was calculated to be $-1.42808 \times 10^{-1} \text{ mm/mm}$ with the factors C and D having the values of 0.00385 and 0.009, respectively. The fitted Maxwell curve can be seen in Figure 60.

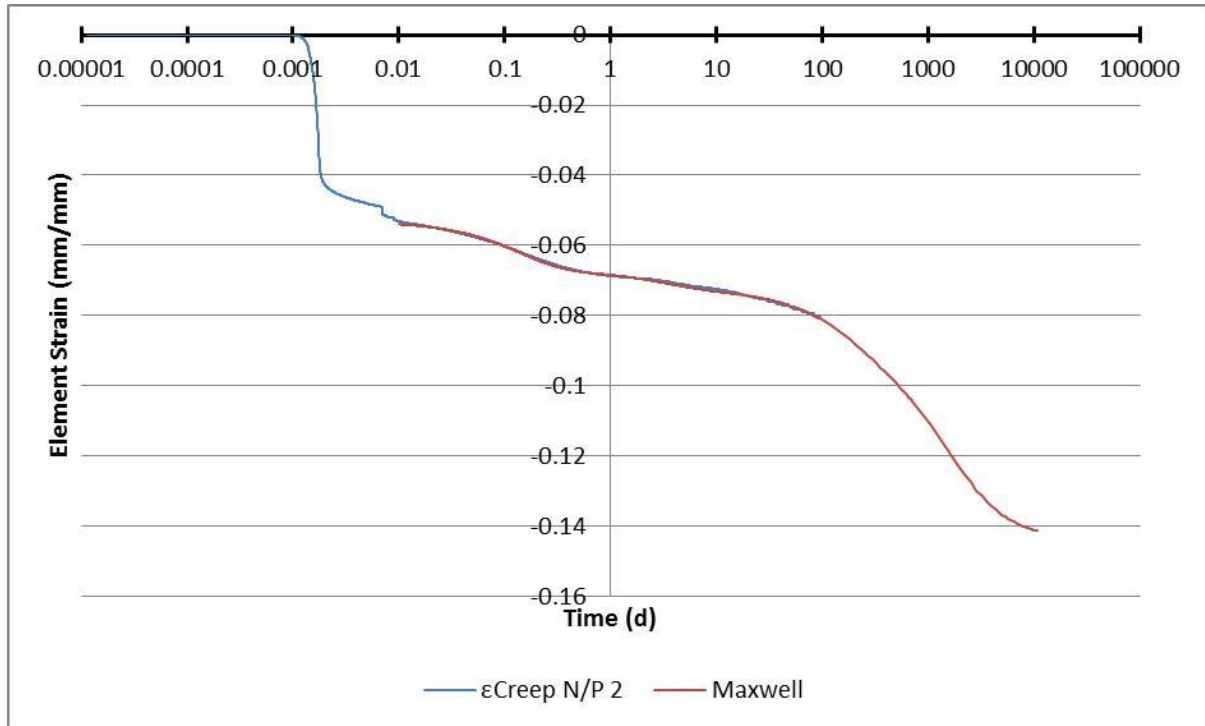


Figure 60 Maxwell curve fitted to notched, pre-cracked SFRSCC 2 tensile creep curve – logarithmic scale

From Figure 60 it can be seen that the predicted Maxwell curve corresponded closely with the tensile creep curve of the second notched, pre-cracked SFRSCC specimen.

5.2.5 SFRSCC – N/P 3

Table 5.5 Maxwell chain parameters for pre-cracked SFRSCC specimen 3

Tens. Strength	σ_{T-SCC}	0.883	MPa	Elastic Strain	ϵ_{el}	-6.179E-03	mm/mm
E. Mod. New	E_{new}	142.9	MPa	End Strain	ϵ_B	-1.400E-02	mm/mm
E. Mod. Spring	E_0	63.1	MPa	Strain (14 min)	$\epsilon_{14.4min}$	-6.18E-03	mm/mm
E. Mod. Spring	E_1	7	MPa	Damp. Viscosity	λ_1	1	t^{-1}
E. Mod. Spring	E_2	10	MPa	Damp. Viscosity	λ_2	0.1	t^{-1}
E. Mod. Spring	E_3	4	MPa	Damp. Viscosity	λ_3	1000	t^{-1}
E. Mod. Spring	E_4	5	MPa	Damp. Viscosity	λ_4	1000	t^{-1}
E. Mod. Spring	E_5	15	MPa	Damp. Viscosity	λ_5	1500	t^{-1}
E. Mod. Spring	E_6	35	MPa	Damp. Viscosity	λ_6	3500	t^{-1}
E. Mod. Spring	E_7	3.8	MPa	Damp. Viscosity	λ_7	100	t^{-1}

The end strain value ϵ_B was calculated to be $-1.40048 \times 10^{-2} \text{ mm/mm}$ with the factors C and D having the values of 0.00025 and 0.00087, respectively. The fitted Maxwell curve can be seen in Figure 61:

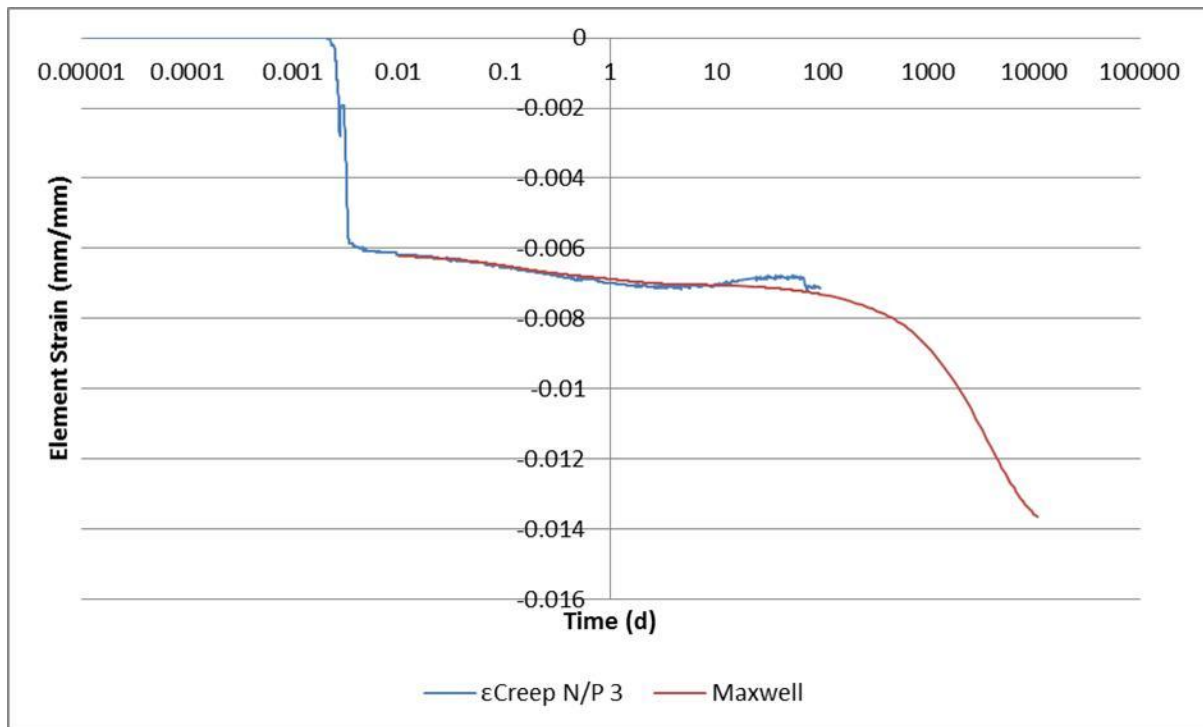


Figure 61 Maxwell curve fitted to notched, pre-cracked SFRSCC 3 tensile creep curve – logarithmic scale

From Figure 61 it can be seen that the predicted Maxwell curve corresponded closely with the tensile creep curve of the third notched, pre-cracked SFRSCC specimen. The specimens N/P 1 to 3 cannot be compared directly because of the difference in magnitude of the element strains.

The strains indicated on Figures 59 – 60 were not the displacements divided by the gauge length as with the previous specimens. The strains from the pre-cracked specimens were calculated as the displacements divided by the element size used in the finite element models explained in the next section. The strains from the pre-cracked models cannot be seen as the creep strains seeing that creep is a material property. If the gauge length would change to larger or smaller, it will not affect the creep strains of un-cracked concrete seeing that it depends on the material deformation. However, a changing gauge length will affect the strains obtained from the pre-cracked SFRSCC in the sense that if the gauge length becomes larger the strains will become smaller and vice versa because of the crack width.

These Maxwell chains obtained from curve fitting now had the ability to describe the material behaviour of the different concrete specimens used in the experiments in an accurate manner through means of a mathematical expression. This would enable one to do a number of simulations with the appropriate Finite Element Method (FEM) programs and the different Maxwell chains incorporated.

Chapter 6

6. Modelling Creep

The most effective way to investigate the effects of steel fibres on the tensile creep of concrete was to incorporate the behaviour of the SFRSCC specimens into a practical application such as a beam in flexure and to examine how the tensile creep of SFRSCC affected the displacement of the beam.

6.1 Modelling Flexural Creep

The most effective way to model the flexural creep of a beam was to do a Finite Element Analyses (FEA). DIANA is a FEA program that enables the user to model different materials and geometries under different conditions to investigate what effect these conditions would have on the structures analysed. For the purpose of this study DIANA was used to analyse SFRSCC beams in flexure and to study their behaviour under different conditions. With the Maxwell curves available from the previous section it was possible to do time-dependent analyses on the concrete beams in flexure to determine how they would behave with the emphasis being on the deflections at the mid-spans. It should be noted that the analyses performed is based on the results of the experiments. Due to time constraints it was not possible to perform additional creep flexure tests to confirm the results of the different analyses performed. It was decided to do the analyses in 2D.

The first step was to choose a beam of appropriate size and dimensions to be modelled and the loading conditions to be used in the model. The beam chosen was a rectangular prism with a cross-sectional area of $100 \times 100 \text{ mm}^2$ and length of 700 mm as seen in Figure 62. A point load of 20 kN was applied at mid-span and the beam was supported in the vertical and horizontal directions through means of translational supports. It has to be noted that flexural strength tests were not performed beforehand on any SFRSCC beams, therefore it was assumed that the 20 kN point load would not surpass the flexural capacity of the SFRSCC beams being modelled.

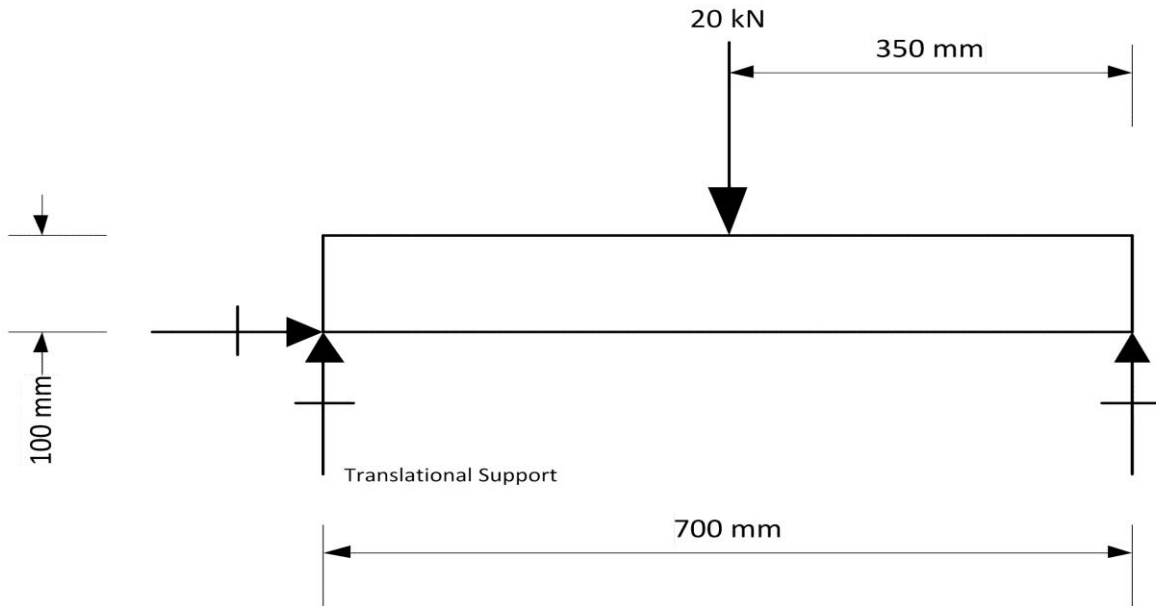


Figure 62 Beam model to be used in FEA.

The next step was to mesh the beam into smaller elements in order to do a FEA. The element dimensions chosen were $10 \times 10 \times 100 \text{ mm}$ with the 100 mm dimension being the depth or thickness of the element. The type of element chosen was a four-node quadrilateral isoparametric element. It was important to keep the model as simple as possible in order to reduce the computational time.

With the mesh chosen as $10 \times 10 \text{ mm}$ elements it can be seen that there would be 700 elements in total. Figure 63 represents the complete mesh of the elements in the beam:

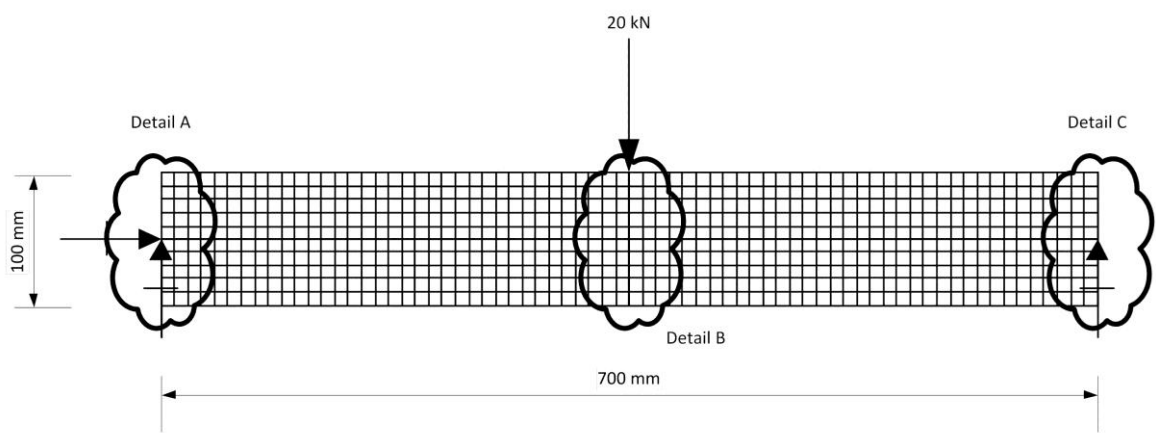


Figure 63 Meshed beam, 10 x 10 mm elements.

Detail A is presented by Figure 64.

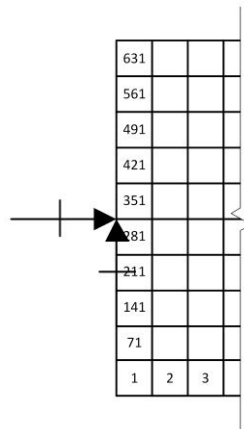


Figure 64 Detail A – Left end of the modelled beam.

Figure 64 presents the left support of the beam to be used in the FEA model. The supports were modelled to be at Node 356, which was situated at the centre of the beam, in order to eliminate any eccentricities that may have arisen during the FEA procedure. The beam could be viewed as being simply supported with no rotational resistance provided by the translational supports.

Detail B is presented by Figure 65.

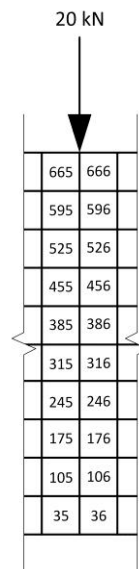


Figure 65 Detail B – Elements in mid-span.

Figure 65 represents the middle of the beam where the point load of 20 *kN* was applied and the maximum deflection would be take place.

Detail C is presented by Figure 66.

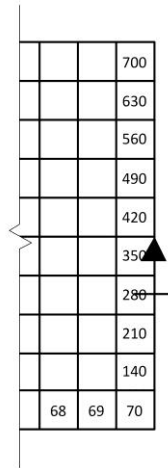


Figure 66 Right end of the modelled beam.

Figure 66 presents the right support of the beam which was situated at Node 426. The support was modelled as a single translational support in the vertical direction (y-axis).

In order to include the own weight of the beam into the analyses it was necessary to define the density of the concrete. The density of concrete was assumed to be:

$$\gamma_{concrete} = 2\,400 \text{ kg/m}^3$$

The units for force and length were specified in DIANA as N and mm respectively, so the concrete density had to be converted to N/mm^3 in order to incorporate the own weight of the beam:

$$\gamma_{conc-DIANA} = 2\,400 \times \frac{9.81}{(1\,000)^3} = 2.3544 \times 10^{-5} \text{ N/mm}^3$$

In DIANA it was possible to apply different time steps to the analyses and to specify the characteristics of these time steps. The time steps in this case were useful when it came to the creep analyses of specimens. The time step method was to take the total modelling time for the analyses of creep and to divide this time into different time steps. It was specified that a full time step will be equal to 1 *day*. In order to understand this more clearly it is necessary to look at the method below:

The total modelling time was 30 *years*, which means:

$$t_{total} = 30 \text{ years}$$

The unit for time was specified in DIANA as *days*, which means that an analyses modelling creep for 30 *years* would use 10800 *steps* with a step size of 1 *day*, assuming that there are 30 *days* in a month and 12 *months* in a year. Instead of applying this number of time steps to the model, which

would make the compilation process more difficult, this modelling time was divided into a smaller number of time steps with the step size varying.

It was decided that the time steps and step sizes chosen were initially small and that they would become larger until the time period of 30 *years* was reached. The time steps chosen are presented in Table 6.1.

Table 6.1 The time steps and sizes chosen for the FEA.

Step size descriptions	step size (d)	time steps	cumulative time (d)
1 second	1.157E-05	10	1.157E-04
10 seconds	1.157E-04	5	6.944E-04
1 min	6.944E-04	59	4.167E-02
1 hour	4.167E-02	23	1
1 day	1	29	30
2 days	2	35	100
10 days	10	30	400
100 days	100	16	2000
200 days	200	44	10800
Total time steps		251	

The model described above was the basic beam model used in the flexural creep analyses with minor modifications made to suit the specific behaviour of the different specimens. The analyses were only performed on beams with element sizes of $10 \times 10 \times 100 \text{ mm}$. Further analyses on different element sizes are necessary in order to determine its effect on the deflections of the concrete beams.

6.1.1 Un-Cracked Flexural Creep

One important assumption that had to be made is that the compressive creep and the tensile creep of SFRSCC would behave similarly. This had to be done in order to perform an FEA on the SFRSCC beams. In order to proceed with the modelling of the flexural creep of the SFRSCC beam it was necessary to incorporate the values from Table 5.2 obtained from the Maxwell chains used in the curve fitting.

After the flexural analysis was performed on the SFRSCC beam the deflection for every time step up to 30 *years* is displayed in Figure 67.

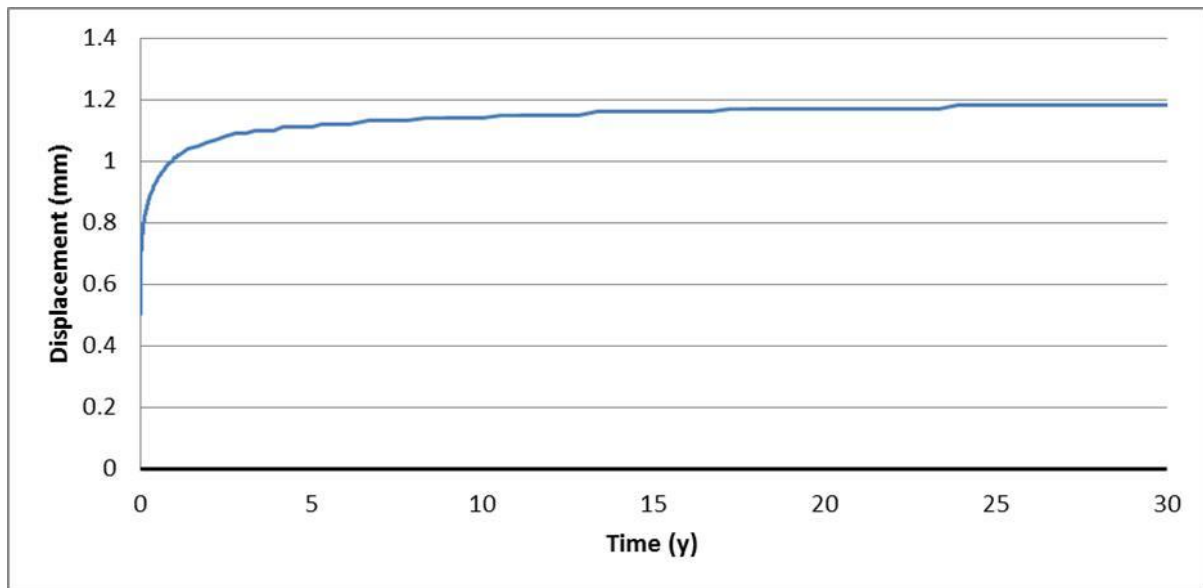


Figure 67 Mid-span deflection of SFRSCC beam.

Figure 67 presents the displacement behaviour that occurred in un-cracked SFRSCC under a constant tensile stress over time. A displacement of 0.501 mm occurred at the onset while the displacement increased to 1.18 mm at 30 years , which was the maximum vertical displacement. The displacement had increased with almost 136 %.

6.1.2 Pre-Cracked Flexural Creep

The analyses performed on the pre-cracked SFRSCC beams have been done similar to the un-cracked SFRSCC beams with some minor modifications made to simulate the crack that has formed. It was assumed that the concrete beam had cracked in the middle and to simulate this crack it was decided to choose one row of elements located at mid-span and to change their material properties in order to simulate a crack that had occurred in the SFRSCC beam.

When considering a beam in flexure there are two main stress zones: a compression zone and a tension zone. The crack would have occurred in the tension zone, which meant that it was necessary to find the NA to determine which elements experienced tensile stress. From Figure 68 it was found that the bottom six rows of elements along the mid-span of the beam experienced tensile stress.

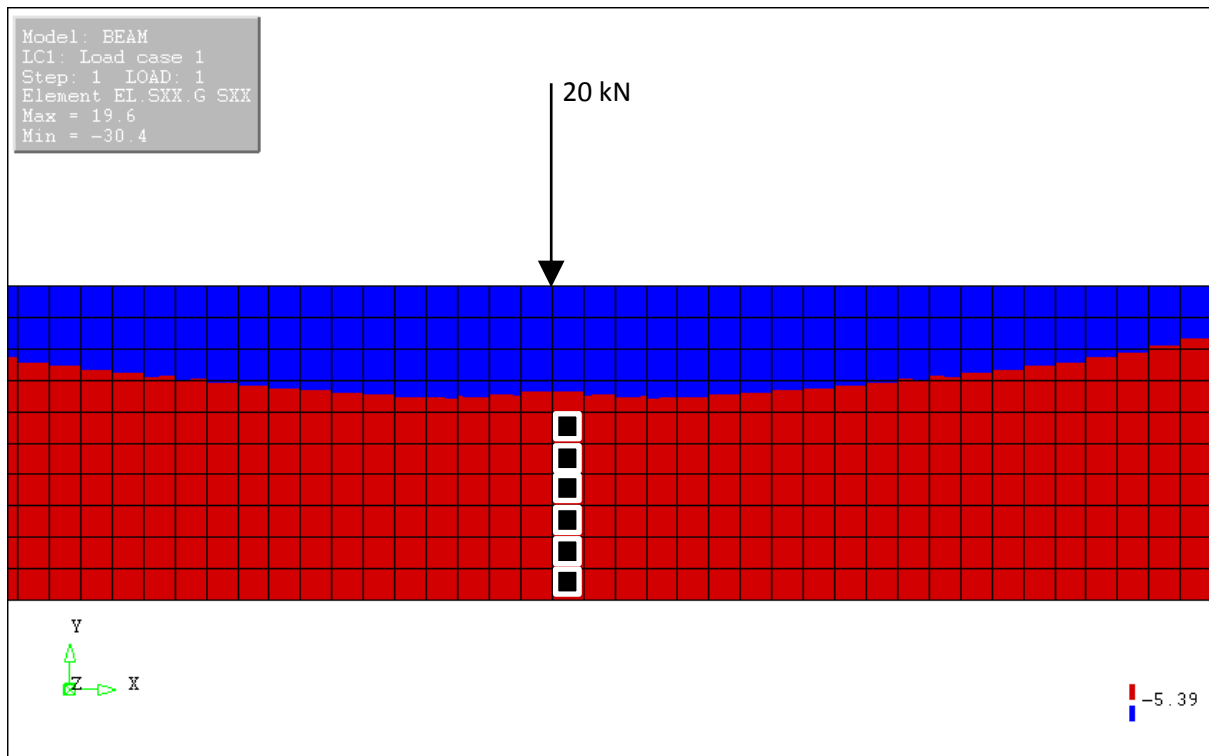


Figure 68 Stress distribution with compressive stress being at the top and tensile stress being at the bottom.

The six elements chosen were Elements 36, 106, 176, 246, 316 and 386 situated just to the right of the centre of the beam as seen in Figure 68. These elements were modelled as a different material, seeing that they represented the crack in the concrete. The materials properties were obtained from the Maxwell models after curve-fitting was completed for each pre-cracked SFRSCC specimen.

SFRSCC – N/P 1:

In order to perform an analysis on the first pre-cracked SFRSCC beam it was necessary to incorporate the data from Table 5.2 to represent the un-cracked concrete and from Table 5.3 to represent the cracked concrete. After the analysis was performed on the first pre-cracked SFRSCC beam the deflection for every time step up to 30 *years* is displayed in Figure 69.

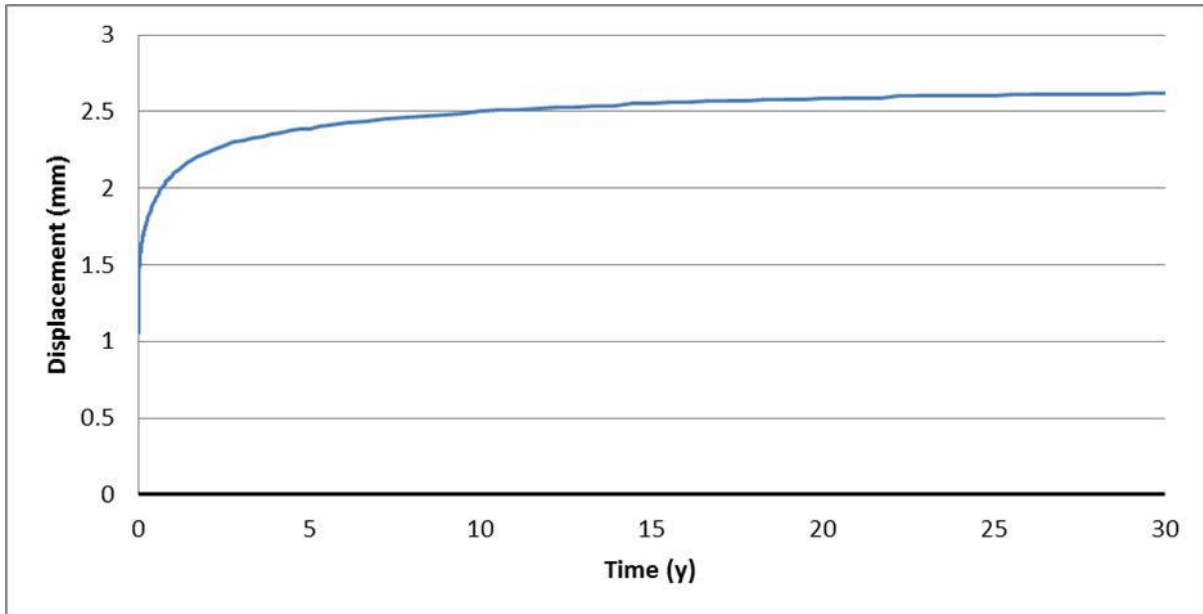


Figure 69 Mid-span deflection of the first pre-cracked SFRSCC beam

Figure 69 presents the displacement behaviour that occurred in the first pre-cracked SFRSCC beam under a constant tensile stress over time. A displacement of 1.06 mm occurred at the onset while the displacement increased to 2.62 mm at 30 years , which was the maximum vertical displacement. The displacement increased with almost 150 %. Figure 70 presents the deflection of the first pre-cracked SFRSCC beam. It is clear where the crack has widened by looking at the deformed lower elements at mid-span.

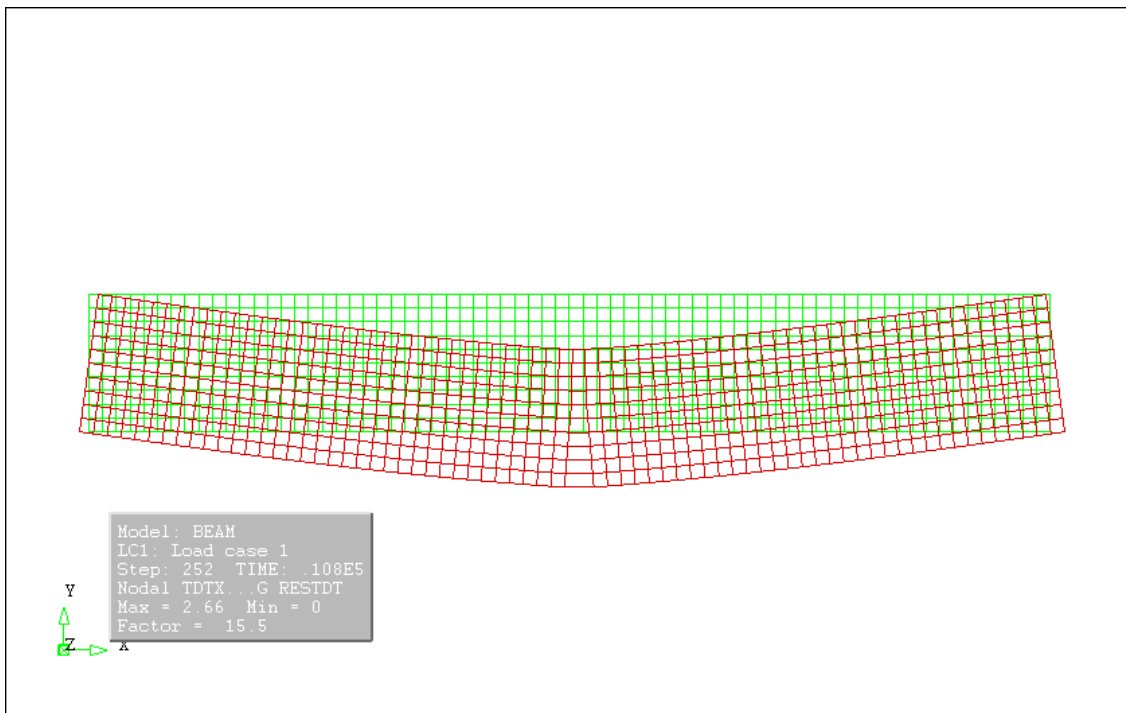


Figure 70 Graphical presentation of the first pre-cracked SFRSCC beam in deflection with mesh on display.

A closer inspection of the mid-span in Figure 71 reveals the widening of the crack more clearly.

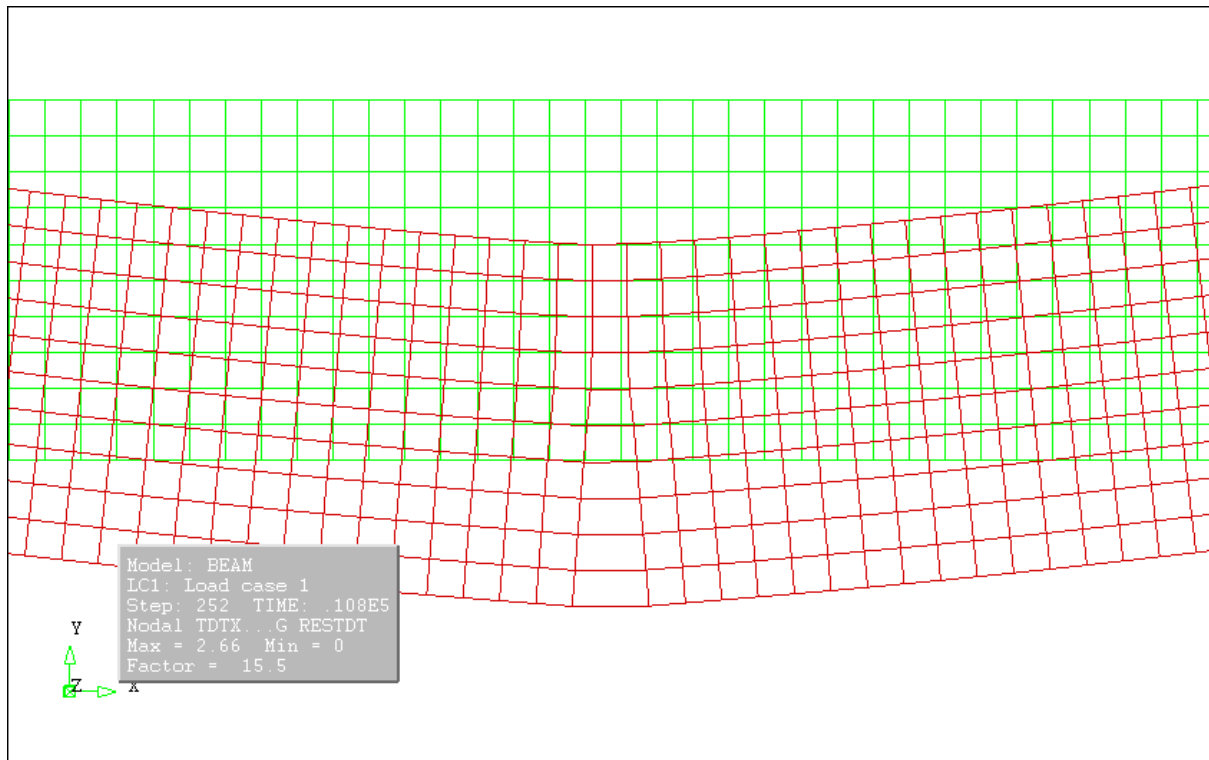


Figure 71 Elements of the first pre-cracked SFRSCC beam at mid-span.

The analyses on the second and third pre-cracked SFRSCC beams were performed in the same way and the deflections exhibited the same characteristics as the first specimen.

With the analyses complete it is necessary to compare these results with each other in order to examine the difference between un-cracked and cracked SFRSCC beams. Table 6.1 presents the deflections of interest of the four analyses done:

Table 6.1 Deflections at mid-span for the four different analyses.

	Initial Deflection (mm)	Final Deflection (mm)	Allowable Deflection (mm)
SFRSCC	0.501	1.18	2.8
SFRSCC Cracked 1	1.06	2.62	2.8
SFRSCC Cracked 2	1.81	4.29	2.8
SFRSCC Cracked 3	1.34	3.09	2.8

The deflections above are only applicable to beams with element sizes $10 \times 10 \times 100 \text{ mm}$ and further analyses on varying element sizes is necessary in order to be more conclusive. Further creep flexure experiments are also necessary in order to confirm the deflections from Table 6.1.

6.1.3 Serviceability Limit State

The FIB Model Code 2010 has definite requirements for deflections in Section 7.6.5 where it is considered that the appearance and the general utility of the structure could be impaired. These requirements are called the Serviceability Limit State (SLS) which are passed if:

$$\delta < \frac{span}{250} \quad (6.1)$$

In Equation 6.1, δ is the deflection of the beam and *span* is the length of the beam. This means that the maximum deflection δ_{Max} allowable is:

$$\delta_{Max} = \frac{700}{250} = 2.8 \text{ mm}$$

None of the initial deflections of the SFRSCC beams exceeded these limitations, but after 30 *years* some of the SFRSCC beams' deflections exceeded the maximum allowable deflection. The uncracked concrete beam is still well within the limits of deflection, whereas the cracked concrete beams are on the border or surpasses the limit. One might argue that the first cracked beam was still within limits, but if the span of the beam is taken into account this argument might become invalid. This is however a theory and further testing is needed to confirm the speculation. It has to be stressed that the deflections obtained from the analyses are only a presentation of the deflections expected and in no way presents the real creep deflections of concrete beams, which can only be obtained through further experiments and further analyses. The deflections of the analyses performed gives insight into the behaviour of cracked SFRSCC beams, which could be useful when further experiments are performed and the creep deflection behaviour is further investigated.

From the results in this section it was found that the fibre pull-out is a significant problem after the concrete has cracked, not necessarily in the Ultimate Limit State (ULS) but definitely when considering the SLS. These results have to be taken into account when designing steel fibre reinforced beams.

Chapter 7

7. Conclusions and Future Prospects

7.1 Conclusions

From the experiments and the analyses that were performed a number of conclusions could be made. The conclusions will be presented into two parts. The first part of the conclusions will focus on the experiments and the second part of the conclusions will focus on the analyses performed.

Experimental Conclusions:

The experiments performed on the different types of experiments yielded insight into the shrinkage and tensile creep behaviour of SFRSCC. From these insights the following conclusions could be made:

1. It was found that the addition of steel fibres greatly influenced the shrinkage of concrete. From the results it were seen that the shrinkage strains of SFRSCC at *90 days* was significantly smaller than the shrinkage strains of SCC at *90 days*, by as much as 38 %. From this result it can therefore be concluded that steel fibres decreases the shrinkage effect in concrete.
2. Another effect found through the addition of steel fibres is that steel fibres affected the phenomenological effects of tensile creep in concrete. It was found that the tensile creep strains at *90 days* of SFRSCC is almost five times less than the tensile creep strains at *90 days* of SCC, which means that steel fibres decreased the tensile creep effect in concrete.
3. The pre-cracked specimens produced large tensile deformations when they were tested. Their deformations completely overshadowed the deformations of the un-cracked SFRSCC specimens, the latter of which was insignificant. This leads to the conclusion that the fibre pull-out mechanism is the major contributing factor to the tensile deformations and that the tensile creep contributes insignificantly.

Analyses Conclusions:

The analyses performed on the beam models provided a better understanding of the time-dependent behaviour of SFRSCC beams in flexure. The negative effects of fibre pull-out could not be clearly comprehended from the experiments performed. After curve fitting was done by Maxwell chains on the curves acquired from the experimental results of the SFRSCC members the effects of fibre pull-out were more prominent. The following conclusions could be made from the different analyses performed:

1. The flexural creep of SFRSCC beams will have increased the deflections by more than double over the course of 30 years, but the deflections still conformed to the requirements of the SLS.
2. After the SFRSCC beams have cracked the fibre pull-out had a significant effect on the deflections of the flexural members over the course of 30 years. The deflections caused by the effects of fibre pull-out surpassed the SLS requirements.
3. From the results it is not advisable to use SFRSCC members in practice because once cracking occurred and a loading percentage of approximately 13 % is applied, the members will have large deflections and will not meet the SLS requirements.

It has to be taken into account that all these conclusions were based on SFRSCC that was designed to exhibit strain-softening behaviour. Further experiments have to be performed on SFRSCC that has been designed for strain hardening in order to see whether the fibre pull-out would be as detrimental as with strain softening.

7.2 Future Prospects

As mentioned in the previous section, it is necessary to perform the same types of experiments as this study on SFRSCC specimens that have been designed to exhibit strain-hardening behaviour in order to see whether the same outcome will be reached as with SFRSCC that have been designed to exhibit strain-softening behaviour. It would also be advantageous to perform flexural creep experiments in order to investigate the tensile creep behaviour of SFRSCC more thoroughly.

Seeing that the tensile creep experiments in this research paper were the first performed of their kind, some notes will be given to improve upon the manufacturing and experimental procedures:

- As mentioned before, the shrinkage data exhibited strange behaviour and it was speculated that this might be because of the interfacial bond between the Perspex blocks and the

concrete. It is advised to find a more effective way of attaching the LVDTs to the concrete specimens in order to eliminate problems with interfacial bond strength.

- Ensure that there are additional specimens available for when failure occurs. These specimens can be kept in the water baths for the first month after testing started to ensure that they can replace any of the specimens that fail.
- If possible it would be advantageous to be able to test more specimens of each respective batch in order to be more statistically correct.
- In order to ensure that the steel hooks are more identical, a more effective, streamlined manufacturing process needs to be developed.

Chapter 8

8. References

- $\sigma - \varepsilon$ Design Method, 2003. *Test and Design Methods for Steel Fibre Reinforced Concrete*, Final Recommendation, *Materials and Structures*, V. 36, October 2003, p. 560 – 567.
- ACI Committee 224, 2001. *Control of Cracking in Concrete Structures*, Reported by ACI Committee 224 in May 2011, American Concrete Institute, 2001.
- ACI Committee 544, 1984. *Guide for Specifying, Mixing, Placing, and Finishing Steel Fiber Reinforced Concrete*, Reported by ACI Committee 544, *ACI Journal* published March – April 1984, p. 140 – 147.
- ACI Committee 544, 2001. *State-of-the-Art Report on Fiber Reinforced Concrete*, Reported by ACI Committee 544, American Concrete Institute, 2001.
- Aklonis, J.J., 1981. *Mechanical Properties of Polymers*, *Journal of Chemical Education*, V. 58, No. 11, November 2011.
- Altoubat, S.A., and Lange, D.A., 2001a. *The Pickett Effect in Early Age Concrete under Restrained Conditions*, *Concrete Science and Engineering*, V. 3, p. 163 – 167.
- Altoubat, S.A., and Lange, D.A., 2001b. *Tensile Basic Creep: Measurements and Behaviour at Early Age*, *ACI Materials Journal*, V. 98, No. 5, p. 386 – 393.
- Altoubat, S.A., and Lange, D.A., 2002. *The Pickett Effect at Early Age and Experiment Separating its Mechanisms in Tension*, in press, *Materials and Structures*, 2002.
- Altoubat, S.A., and Lange, D.A., 2003. *A New Look at Tensile Creep of Fiber Reinforced Concrete*,

ACI Special Publication of Fiber Reinforced Concrete, edited by N. Banthia, 2003,
p. 1 – 22.

Bažant, Z.P. and Ashgari, A., 1974. *Computation of Kelvin Chain Retardation Spectra of Aging Concrete*, Cement and Concrete Research, V. 4, p. 797 – 806.

Bažant, Z.P. and Wu, S.T., 1974. *Rate – Type of Aging Concrete based on Maxwell Chain*, Matériaux et Constructions, V. 7, No. 37, 1974, p. 45 – 60.

Bažant, Z.P., 1988. *Mathematical Modelling of Creep and Shrinkage of Concrete*, John Wiley & Sons Ltd, p. 102 – 109.

Benboudjema, F., Meftah, F. and Torrenti, J.M., 2004. *Interaction between Drying, Shrinkage, Creep Creep and Cracking Phenomena in Concrete*, Elsevier, Engineering Structures, 27 (2005), p.239 – 250.

Bisonette, B. and Pigeon, M., 1995. *Tensile Creep at Early Ages of Ordinary, Silica Fume and Fiber Reinforced Concretes*, Cement and Concrete Research, V.25, No. 5, p. 1075 – 1085.

Boshoff, W.P., 2007. *Time – Dependant Behaviour of Engineered Cement – Based Composites*, PhD Thesis, Department of Civil Engineering, Stellenbosch University, South Africa, March 2007.

Bower, D. I., 2002. *An Introduction to Polymer Physics*, Cambridge University Press, 2002.

Brown, R. Shukla, A. and Natarajan, K.R., 2002. *Fiber Reinforcement of Concrete Structures*, prepared for the University of Rhode Island Transportation Centre, September 2002.

BS 8100-2:1985, *Structural Use of Concrete. Part 2: Code of Practice for Special Circumstances*, London: British Standards Institution, 1985.

BS EN 1992-1-1:2004, 2004, prepared by Technical Committee CEN/TC250, approved by the European Committee for Standardization (CEN), Management Centre Brussels,

Belgium, April 2004.

Chern, J. and Young, C., 1988. *Compressive Creep and Shrinkage of Steel Fibre Reinforced Concrete*,

The International Journal of Cement Composites and Lightweight Concrete, V. 11,

No. 4, November, p. 205 – 214.

Colleparidi, M., Colleparidi, S. and Troli, S., 2007. *Properties of SCC and Flowing Concrete*, Proceedings

of an International Conference: Sustainable Construction Materials and

Technologies, 11 – 13 June 2007 Coventry, Special Papers Proceedings, Pub. UW

Milwaukee CBU, p.25 – 31.

Craig, R.R., Jr., 2000. *Mechanics of Materials 2nd Edition*, John Wiley & Sons Inc., p. 47.

Department of Public Works, 1993. *Specification of Materials and Methods to be Used 4th Revision*,

October 1993, Pretoria.

EFNARC Specification and Guidelines for Self – Compacting Concrete, 2002, passed on February

2002, Association House, Hampshire, UK.

FIB Model Code 2010, 2010, prepared by FIB Special Activity Group 5, FIB, Federal Institute of

Technology Lausanne, Switzerland, 2010.

Gilbert, R.I. and Wu, H.Q., 2010. *The Effects of Shrinkage on Long-Term Slab Deflection*, Centre for

Infrastructure Engineering and Safety, The University of New South Wales, Sydney.

Gray, R.J., 1984. *Analysis of the Effect of Embedded Fibre Length on Fibre Debonding and Pull – Out*

from an Elastic Matrix, Part 1 Review of Theories, Journal of Materials Science,

V. 19, p. 861 – 870.

Holt, E.E., 2001. *Early Age Autogenous Shrinkage of Concrete*, VTT Publications 446, Technical

Research Centre of Finland, 2001.

Hunt, K., 2000. *Reinforced Concrete – Use, Deterioration and Repair*, Seminar Conserving Historic

Building Fabric, April 2000, NSW Heritage Office.

- Johnston, C.D and Zemp, W.R., 1991. *Flexural Fatigue Performance of Steel Fiber Reinforced Concrete – Influence of Fiber Content, Aspect Ratio, and Type*. ACI Materials Journal, 88 (4), p. 374 – 383.
- Kong, F.K. and Evans, R.H., 1987. *Reinforced and Prestressed Concrete 3rd Edition*, Chapter 2, p. 28 – 32.
- Kovler, K., 2004. *Testing System for Determining the Mechanical Behaviour of Early Age Concrete Under Restrained and Free Uniaxial Shrinkage*, Materials and Structures, V. 27, p. 324 – 330.
- Li, Z., Mobasher, B. and Shah, S.P., 1991. *Characterization of Interfacial Properties in Fibre – Reinforced Cementitious Composites*, Journal of the American Ceramic Society, V. 74, No. 9, p. 2156 – 2164.
- Li, V.C. and Stang, H., 1997. *Interface Property Characterization and Strengthening Mechanisms in Fiber Reinforced Cement Base Composites*, Advanced Cement Based Materials 1997, 6, p. 1 – 20.
- Li, V.C. and Stang, H., 2004. *Elevating FRC Material Ductility to Infrastructure Durability*, proceedings of BEFIB 2004, Varenna, Italy, September 2004.
- Lim, T.Y., Paramasivam, P. and Lee, S.L., 1987. *Analytical Model for Tensile Behaviour of Steel-Fiber Concrete*, ACI Materials Journal, July – August 1987, No. 84 – M30, p. 286 – 298.
- Mangat, P.S. and Motamedi Azari, M., 1985. *A Theory for the Creep of Steel Fibre Reinforced Cement Matrices under Compression*, Journal of Materials Science, No. 20, p. 1119 – 1133.
- Morton, J. and Groves, G.W., 1974. *The Cracking of Composites Consisting of Discontinuous Ductile Fibres in a Brittle Matrix – Effect of Fibre Orientation*, Journal of Materials Science, V. 9, p. 1436 – 1445.
- Naaman, A.E., Namur, G.G, Alwan, J.M. and Najm, H.S., 1991. *Fiber Pullout and Bond Slip. I: Analytical Study*, Journal of Structural Engineering, V. 117, No. 9, September 1991, p. 2769 – 2800.
- Naaman, A.E. and Najm, H., 1991. *Bond – Slip Mechanisms of Steel Fibers in Concrete*, ACI Materials

Journal, V. 88, No. 2, March – April 1991, p. 135 – 145.

Pickett, G., 1942. The Effect of Change in Moisture Content on the Creep of Concrete under a Sustained Load, ACI Journal, V. 38, 1942, p. 333 – 356.

Popov, E.P., 1990. *Engineering Mechanics of Solids*, edited by William J. Hall, Prentice-Hall Inc., 1990, p. 280 – 286.

Powers, T.C., 1965. *Mechanisms of Shrinkage and Reversible Creep of Hardened Cement Paste, The Structure of Concrete*, proceedings of an international conference, London, p. 319 – 344.

RILEM Draft Recommendation: 107-GCS: *Guidelines for the Formulation of Creep and Shrinkage Prediction Models: Creep and Shrinkage Prediction Model for Analysis and Design of Concrete Structures – Model B3*, Materials and Structures, vol. 28 no. 180, 1995.

SANS 10100-1, 2000. *The Structural Use of Concrete Part 1: Design*, Edition 2.2, published by Standards South Africa, Pretoria.

SANS 10162 – 1:2005 Edition 2, 2005. *The Structural Use of Steel Part 1: Limit-State Design of Hot-Rolled Steelwork* published by Standards South Africa, Pretoria, South Africa.

SASCH, 2008, compiled and published by the Southern African Institute of Steel Construction, Johannesburg, South Africa.

Shah, D.L. and Modhere, C.D., 2009. *Parameter-Study on the Influence of Steel and Polyester Fibers in the Self – Compacting Concrete*, The Pacific Journal of Science and Technology, V. 10, No. 2, p. 178 – 186.

Shannag, M.J., Brincker, R. and Hansen, W., 1997. *Pullout Behaviour of Steel Fibers from Cement – Based Composites*, Cement and Concrete Research, Elsevier, V. 27, No. 6, p. 925 – 936.

- Shi, C. and Mo, Y.L., 2008. *High-Performance Construction Materials – Science and Applications*, Edited by C. Shi and Y.L. Mo, World Scientific Publishing Co. Pty. Ltd., June 2008, p. 1 - 18
- Soroushian and Bayasi, 1991. *Fiber – Type Effects on the Performance of Steel Fiber Reinforced Concrete*, ACI Materials Journal, V. 88, No. 2, March – April 1991, p. 129 – 134.
- Stang, H., Li, Z. and Shah, S.P., 1990. *Pullout Problem: Stress versus Fracture Mechanical Approach*, Journal of Engineering Mechanics, V. 116, No. 10, October 1990, p. 2136 – 2150.
- Stang, H. and Shah, S.P., 1986. *Failure of Fibre – Reinforced Composites by Pull – Out Fracture*, Journal of Materials Science, V. 21, p. 953 – 957.
- Swaddiwudhipong, S., Lu, H. and Wee, T., 2003. *Direct Tension Test and Tensile Strain Capacity of Concrete at Early Age*, Cement and Concrete Research, Science Direct, V. 33, p. 2077 – 2084.
- Swamy, R.N., Mangat, P.S. and Rao, C.V., 1974. *Mechanics of Fiber Reinforcement of Cement Matrices*, Fiber Reinforced Concrete, SP-44, American Concrete Institute, Detroit, p. 1 – 28.
- Switek, A., Denarié, E. and Brühwiler, E., 2010. *Modeling of viscoelastic properties of Ultra High Performance Fiber Reinforced Concrete (UHPFRC) under low to high tensile stresses*, Symposium on Concrete Modelling, June 2010, Lausanne, Switzerland.
- Wittmann, F.H., 1982. *Fundamental Research on the Creep and Shrinkage of Concrete*, edited by F.H. Wittmann, Martinus Nijhoff Publishers, Boston, MA, 1982, p. 4 – 50.
- You, Z., Chen, X. and Dong, S., 2011. *Ductility and Strength Hybrid Fiber Reinforced Self-Consolidating Concrete Beam with Low Reinforcement Ratios*, 2011 International Conference on Risk and Engineering Management (REM), Systems Engineering Procedia 1, 2011, p. 28 – 34.

Zhou, L., Kim, J. and Mai, Y., 1992. *Interfacial Debonding and Fibre Pull – Out Stresses*, Part II A New Model Based on the Fracture Mechanics Approach, *Journal of Materials Science*, V. 27, p. 3155 – 3166.

Appendix A

A. Specimen Design

In order to test the tensile creep of concrete the specimens had to be adapted in order to be tested in tension. In this case it was efficient to choose concrete prisms with steel hooks cast in at both ends. The design was inspired by the tests performed by Swaddiwudhipong et al., (2003).

There are several advantages to this type of design:

- There will be no risk of debonding between the loading connection and the concrete specimen.
- The hooks can be designed in a simple way.
- The hooks can be customized in any manner to take geometry and applied forces into account.

The most prominent disadvantages were:

- The manufacturing of the hooks is labour intensive and accuracy to manufacture the hooks to be doubly symmetrical is difficult to achieve.
- It is difficult to cast the hooks into the concrete in such a precise manner so that the hooks are purely centralised and do not sway either horizontally or vertically.
- If the two points above are not taken into account, internal moments will exist within the concrete specimens, making a state of pure tension impossible.

Even though the disadvantages listed are prominent, the method of casting the hooks would still be efficient enough to provide valuable data when these concrete specimens are tested in tension. The concrete specimens with the steel hooks cast incorporated is presented in Figure 72.

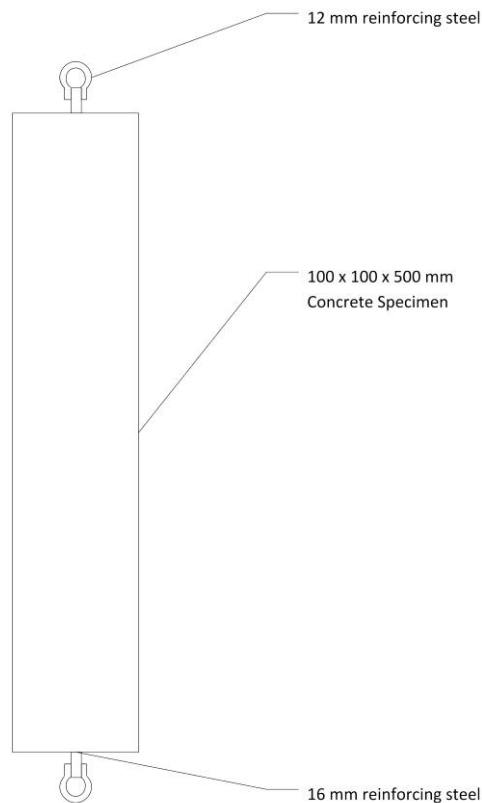


Figure 72 Typical tensile concrete specimen.

It can be seen that the concrete prism itself would be 500 mm long with the steel hooks cast in at the ends. These hooks would have 12 mm reinforcing steel bars at the ends that were bent into loops that would be able to connect to frictionless connections linking these specimens to the rest of the rig. A hook would mainly consist of a single Y16 steel reinforcing bar, 170 mm long, with four 8 mm steel reinforcing bars, 140 mm long, bent and arranged radially, welded to it. These welds should be able to withstand all the internal forces generated during the experimental procedures. It can be seen in Table 7.6 from the South African Steel Construction Handbook (SASCH, 2008) that the shear resistance of 5 mm fillet welds was 0.762 kN/mm with the direction of the force being in the same direction as the axis of the weld. With that taken into account it can be seen that for a 25 mm weld the weld resistance would be:

$$V_r = 0.762 \text{ kN/mm} \times 25 \text{ mm} = 19.05 \text{ kN}$$

The shear resistance of the welds between the 12 mm and 16 mm steel reinforcing bars is as follows:

$$V_r = 4 \times 19.05 = 76.2 \text{ kN}$$

The shear resistance of the welds between the 8 mm steel reinforcing hooks and the 16 mm steel reinforcing bars is as follows:

$$V_r = 4 \times 2 \times 19.05 = 152.4 \text{ kN}$$

The detailed design of the welded steel hooks is presented in Figure 73:

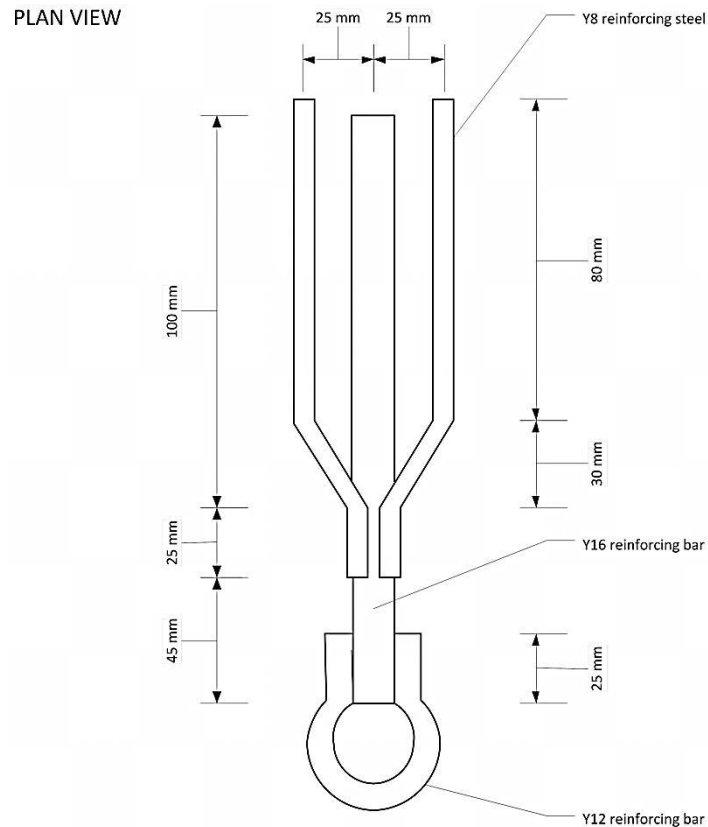


Figure 73 Detailed design of steel hook

Upon inspection it can be seen that the bent 12 mm steel reinforcing bars were manufactured in such a manner as to incorporate 20 mm galvanized bolts that would act as connections between the specimens and the rig. The lengths of the reinforcing bars were sufficient enough to ensure that debonding did not take place. With the weld resistances known it was possible to design the testing frames through which the tensile creep tests would be performed. From the calculations above the maximum forces the hooks would be able to withstand is 76.2 kN.

Appendix B

B. Frame Design

In order to perform tensile creep tests on concrete specimens it was necessary to determine which factors would be the most critical, so as to produce the purest experimental results. The main function of the testing apparatus should be to test concrete prisms in pure tension without causing any internal bending moments. The design of the testing apparatus had to be simple, effective and able to withstand all the forces and stresses it will be subjected to during the experimental procedure. In the next sub-sections the design procedure will be explained and discussed in full detail in order to ensure the safety and functionality of this design.

B.1 Determining the Tensile Capacity

Seeing that the frames are used to test the tensile creep of concrete prisms it can be assumed that the maximum force exerted on the frames is the force that is needed to test the specimens. Various different expressions from the South African National Standard (SANS 10162-1:2005 Edition 2) will be used during the design process.

The average maximum tensile capacity $\sigma_{tensmax}$ of the concrete specimens were assumed to be 8 MPa . In order to test the tensile creep of the specimens a certain stress had to be applied. This stress should be less than the maximum tensile capacity; otherwise the specimens would fail shortly after being subjected to the tensile stresses. By assuming that the applied stress was 70% of $\sigma_{tensmax}$ one can be assured that failure of the specimens would not likely occur.

Therefore the applied stress

$$\sigma_{tens70\%} = 0.7 \times 8\text{ MPa} = 5.6\text{ MPa}$$

The prisms had the dimensions $100 \times 100 \times 500$ in mm^3 with a cross sectional area of 100×100 in mm^2 .

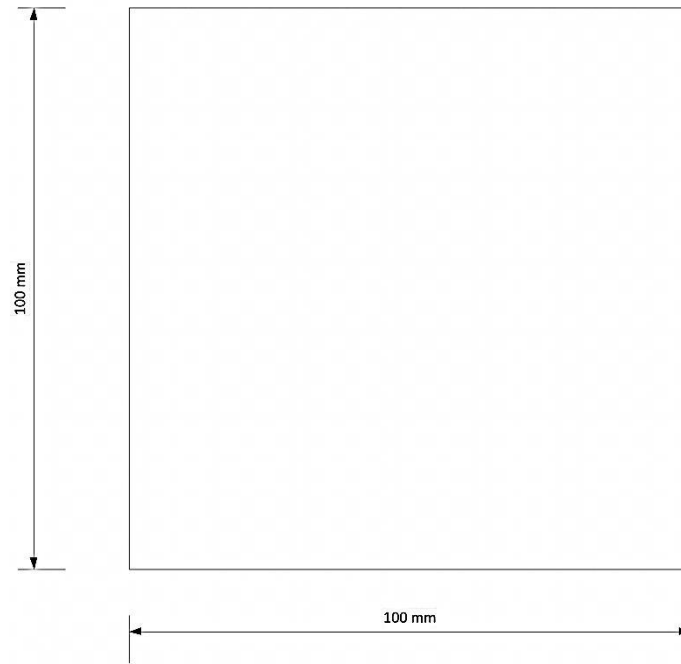


Figure 74 Cross-section of tensile concrete specimen.

To find the applied force one can use the formula for determining normal stress.

$$\sigma(\text{MPa}) = F(\text{N})/A(\text{mm}^2) \quad (9.1)$$

By rearranging Equation 9.1:

$$F(\text{N}) = \sigma(\text{MPa})A(\text{mm}^2) \quad (9.2)$$

Therefore from Equation 9.2:

$$F_{70\%} = 5.6 \text{ MPa} \times 10000 \text{ mm}^2 = 56000 \text{ N} = 56 \text{ kN}$$

In terms of mass

$$F_{70\%} = 56000/9.81 = 5708.461 \text{ kg}$$

It was also necessary to determine the own weight of the concrete specimens. As mentioned above, the volume of the concrete specimens are

$$Vol_{spec} = 100 \times 100 \times 500 = 5 \times 10^6 \text{ mm}^3 = 0.005 \text{ m}^3$$

By assuming a concrete density of 2400 kg/m^3 the weights calculated were:

$$w_{conc} = 2400 \text{ kg/m}^3 \times 0.005 \text{ m}^3 = 12 \text{ kg}$$

$$w_{steel\text{fibres}} = 0.5\% \times 7800 \text{ kg/m}^3 \times 0.005 \text{ m}^3 = 0.195 \text{ kg}$$

$$w_{total} = 12 + 0.195 = 12.195 \text{ kg}$$

Looking at Figure 75:

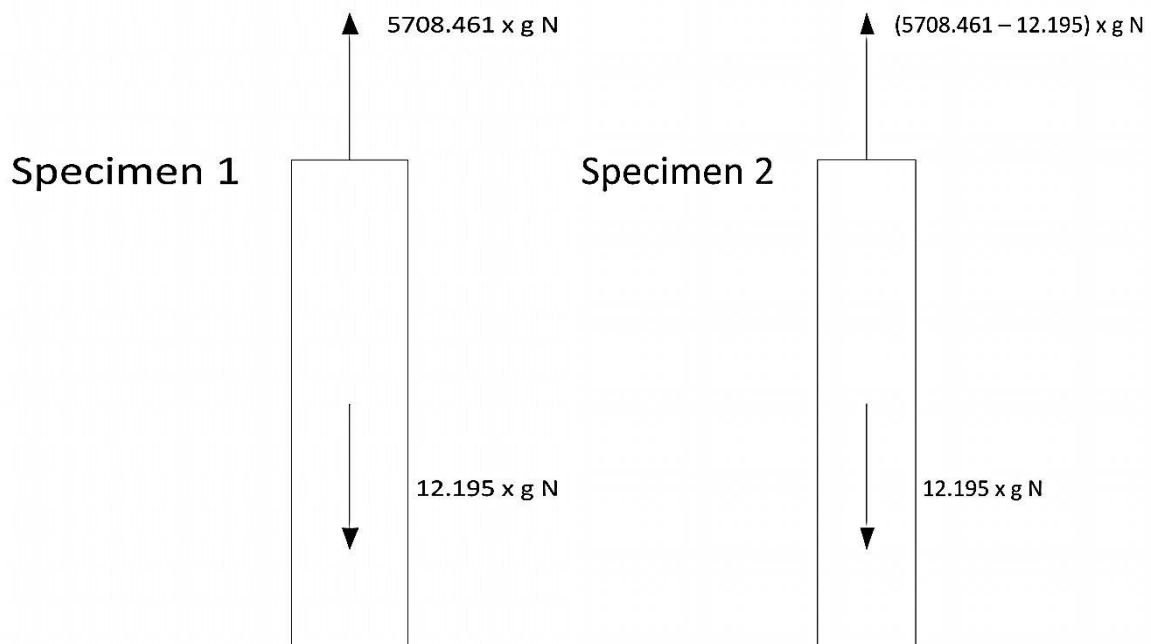


Figure 75 Graphical presentation of tensile concrete specimens with forces applied.

$$F_{required} = (5708.461 + 2 \times 12.195) \times g \text{ N} = 5732.851 \times g \text{ N} \quad \text{with } g = 9.81 \frac{\text{N}}{\text{kg}}$$

In terms of mass

$$F_{required} = 5732.851 \text{ kg} \approx 5800 \text{ kg}$$

When looking at the magnitude of forces needed to be generated in Figure 75 the next step would be to determine how these forces would be generated. The most effective way of generating large forces is to make use of levers and ratios. It was decided that the test setup would consist of a large vertical frame with two beams acting as levers with ratios of 1: 10. With weights applied to the ends of these beams it would be possible to generate forces of great magnitude. The reasons why weights were used instead of hydraulic cylinders were that weights were simpler and it would be more cost effective. It also eliminated the possibility of failure, should one of the hydraulic cylinders fail.

The frame chosen was made out of structural steel and was designed in such a manner so that it could test two specimens at a time. The next section will give a graphical representation of the steel frames.

B.2 Frame Setup

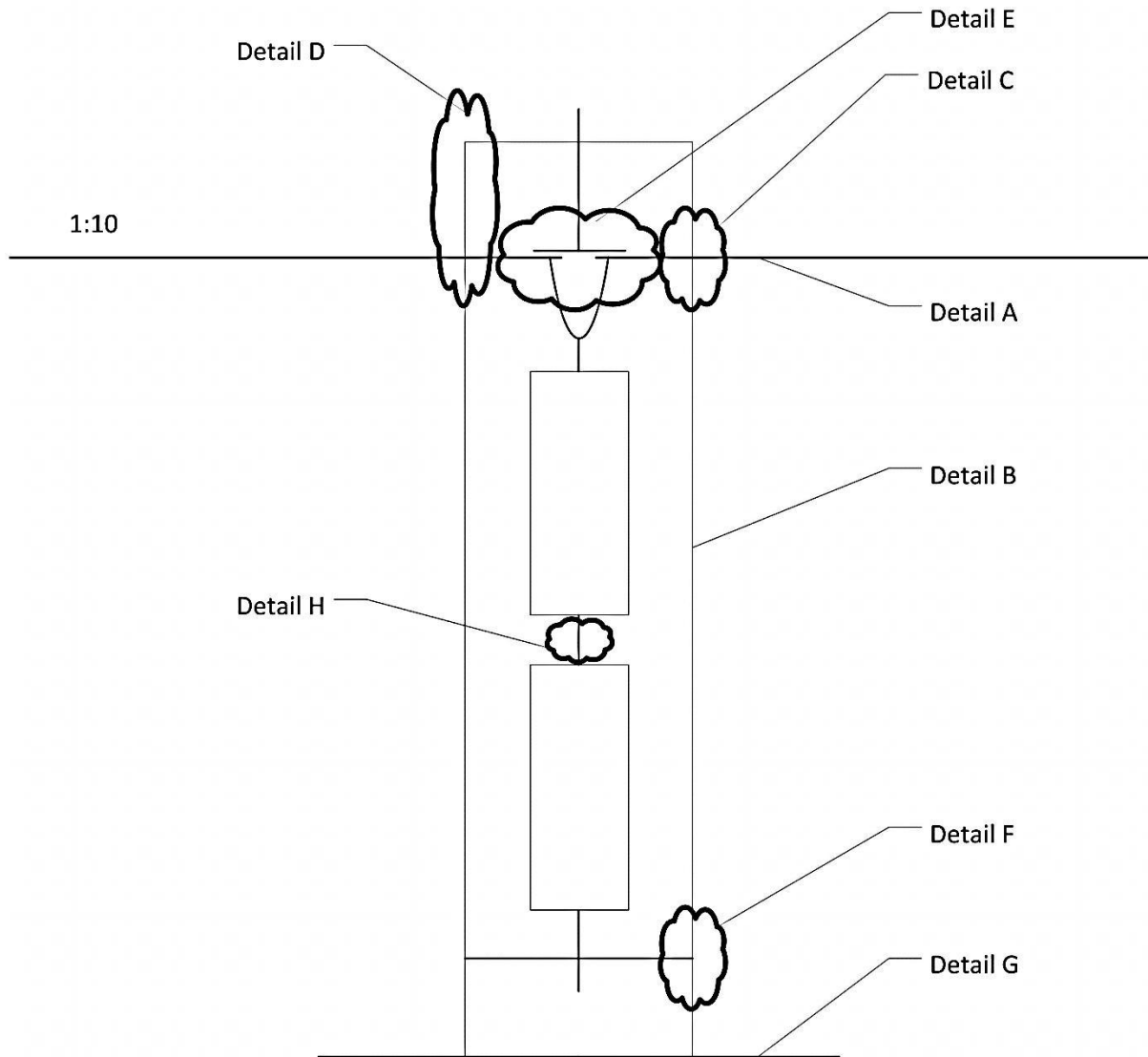


Figure 76 Graphical presentation of a typical steel frame

B.3 Determining the Applied Force

Figure 77 represents the Free Body Diagram (FBD) of the pivot beams to illustrate the ratios.

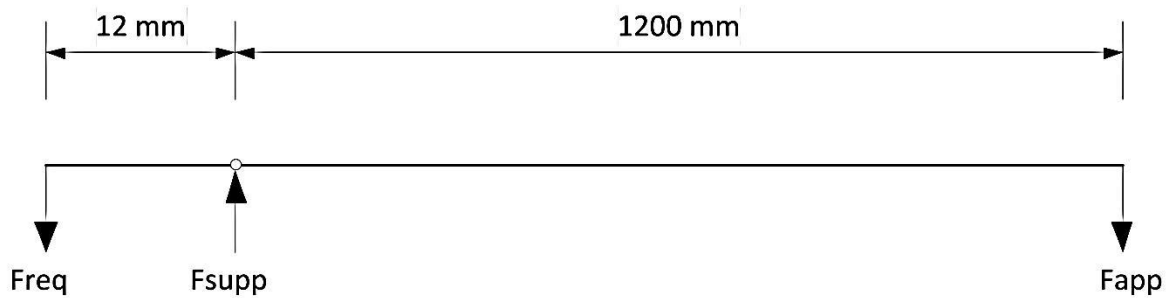


Figure 77 FBD of pivot beam

$$F_{req} = 5800/2 = 2900 \text{ kg} = 28449 \text{ N} = 28.449 \text{ kN}$$

Determine the unknown parameters through equilibrium:

$$\uparrow \Sigma F_y = 0:$$

$$F_{supp} = F_{req} + F_{app} = 2900 + F_{app} \text{ kg} \quad (9.3)$$

$$\curvearrowright \Sigma M_R = 0:$$

$$F_{app}(1.2) - F_{req}(0.12) = 0$$

$$\therefore F_{app} = \frac{F_{req}(0.12)}{1.2} = \frac{1}{10} F_{req} = \frac{2900}{10} = 290 \text{ kg} = 2844.9 \text{ N} = 2.845 \text{ kN} \quad (9.4)$$

Substituting Equation 9.4 into Equation 9.3:

$$F_{supp} = 2900 + 290 = 3190 \text{ kg} = 31293.9 \text{ N} \approx 31.294 \text{ kN}$$

B.4 Determining M_{max}

It was necessary to choose a section for the material of the beams to determine whether the section had the capacity to withstand the generated bending moments in the beams. The chosen section was a 100 x 100 x 6 Square Hollow Section which had the following properties:

$$m = 17.9 \text{ kg/m} \quad A = 2.13 \times 10^3 \text{ mm}^2 \quad J = 5.15 \times 10^6 \text{ mm}^4$$

$$r = 37.7 \text{ mm} \quad I = 3.04 \times 10^6 \text{ mm}^4 \quad Z_e = 60.7 \times 10^3 \text{ mm}^3$$

$$Z_{pl} = 73.5 \times 10^3 \text{ mm}^3 \quad f_y = 300 \text{ MPa} \quad f_u = 450 \text{ MPa}$$

$$\text{Own weight } w = 17.9 \times 9.81 = 176 \text{ N/m} = 0.176 \text{ kN/m}$$

With all the weights and forces taken into account the beam will look as in Figure 78.

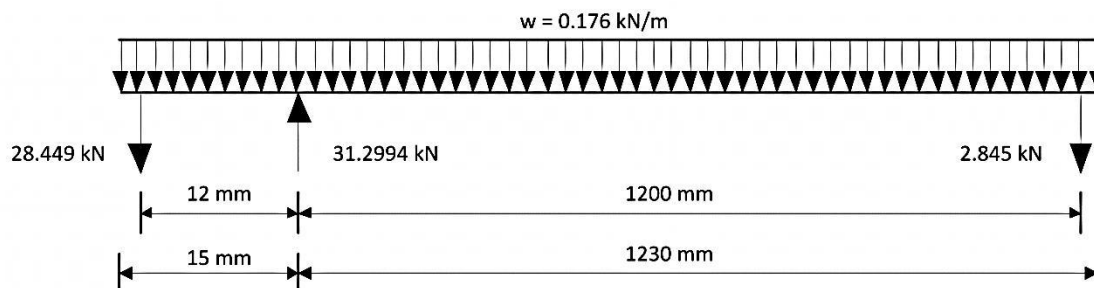


Figure 78 Pivot beam with forces applied.

Figure 78 could be modelled as Figure 79.

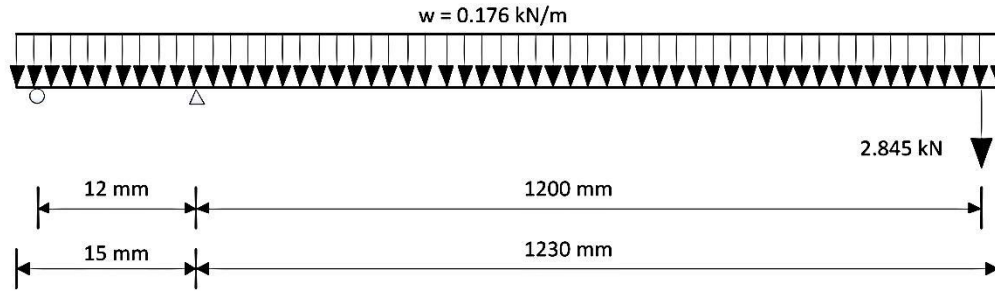


Figure 79 Modelled pivot beam with forces applied.

This would lead to Figure 80.

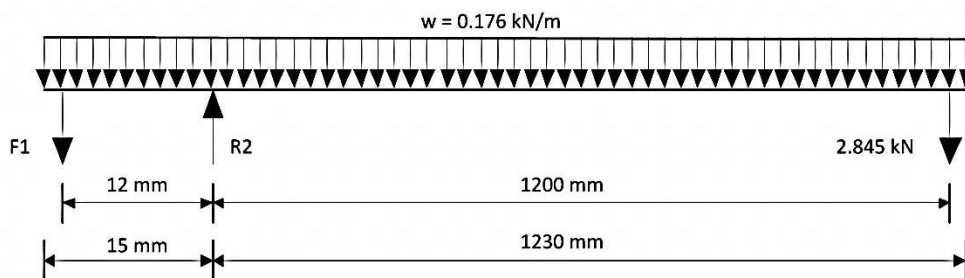


Figure 80 Pivot beam with forces applied and reaction forces included.

Solving the unknown parameters through equilibrium:

$$\curvearrowright \Sigma M_2 = 0:$$

$$0.12 \times F_1 - 2.845 \times 1.2 - 0.176 \times 1.23 \times 1.23/2 + 0.176 \times 0.15 \times 0.15/2 = 0$$

$$0.12 \times F_1 = 2.845 \times 1.2 + 0.176 \times 1.23 \times 1.23/2 - 0.176 \times 0.15 \times 0.15/2$$

$$0.12 \times F_1 = 3.414 + 0.13314 - 0.00198$$

$$F_1 = 29.543 \text{ kN}$$

$$\uparrow \Sigma F_y = 0:$$

$$R_2 - 29.543 - 2.845 - 0.176 \times 1.38 = 0$$

$$R_2 = 29.543 + 2.845 + 0.176 \times 1.38 = 32.631 \text{ kN (also } N_{max})$$

Determine the maximum bending moment M_{Max} in the beam:

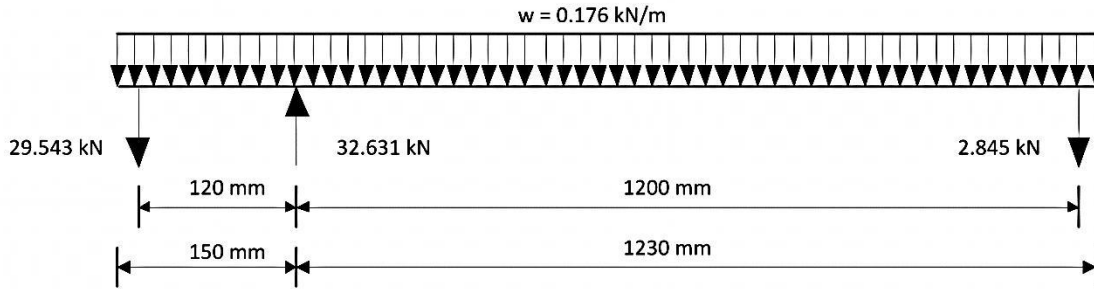


Figure 81 Pivot beam with all forces known.

Through equilibrium and basic algebraic methods it was possible to obtain expressions that would describe the situations of shear forces $V(x)$ and bending moments $M(x)$ in the beam. The following equations would be in shorthand to ease the reading of the calculations. For example: $5 \times x \times x/2 = 5(x)(x/2) = 2.5x^2$

1. $0 < x < 0.03$:

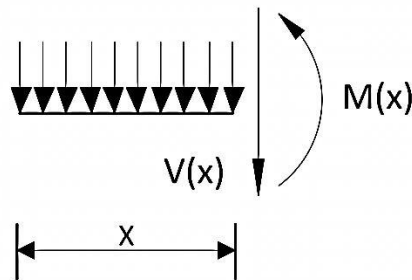


Figure 82 Section $0 < x < 0.03$ of pivot beam.

$$\uparrow \Sigma F_y = 0:$$

$$-V(x) - 0.176(x) = 0$$

$$\therefore V(x) = -0.176x \quad , \text{ which would give the following:}$$

$$V(0) = 0 \text{ kN}$$

$$V(0.03) = -0.00528 \text{ kN}$$

$$\curvearrowright \Sigma M = 0:$$

$$M(x) + 0.176(x)(x/2) = 0$$

$$\therefore M(x) = -0.088x^2 \quad , \text{ which would give the following:}$$

$$M(0) = 0 \text{ kNm}$$

$$M(0.03) = 7.92 \times 10^{-5} \text{ kNm}$$

2. $0 < x < 0.15$:

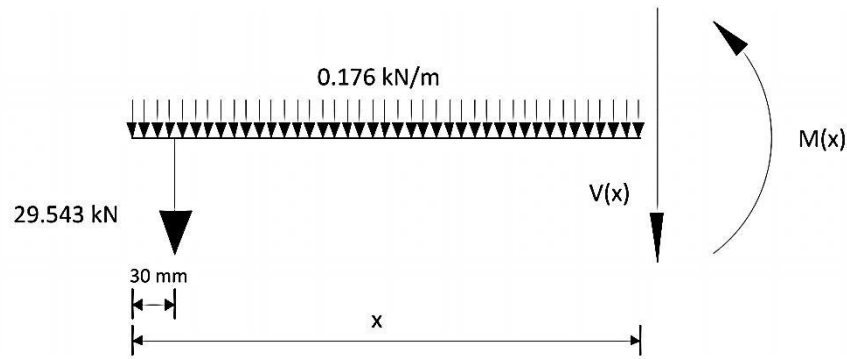


Figure 83 Section $0 < x < 0.15$ of pivot beam.

$$\uparrow \Sigma F_y = 0:$$

$$-V(x) - 29.543 - 0.176(x) = 0$$

$$\therefore V(x) = -0.176x - 29.543$$

$$V(0.03) = -29.548 \text{ kN}$$

$$V(0.15) = -29.569 \text{ kN}$$

$$\curvearrowright \Sigma M = 0:$$

$$M(x) + 29.543(x - 0.03) + 0.176(x)\left(\frac{x}{2}\right) = 0$$

$$\therefore M(x) = -29.543x + 0.886 - 0.088x^2 = -0.088x^2 - 29.543x + 0.886$$

$$M(0.03) = -3.692 \times 10^{-4} \text{ kNm}$$

$$M(0.15) = -3.547 \text{ kNm}$$

3. $0 < x < 1.35$:

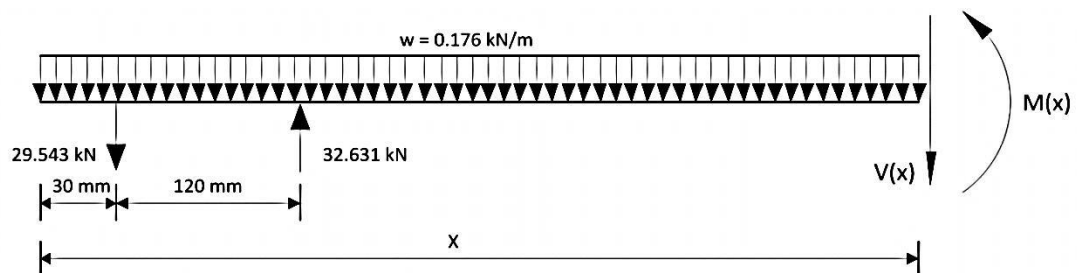


Figure 84 Section $0 < x < 1.35$ of pivot beam.

$$\uparrow \Sigma F_y = 0:$$

$$-V(x) - 0.176(x) - 29.543 + 32.631 = 0$$

$$\therefore V(x) = -0.176x + 3.088$$

$$V(0.15) = 3.062 \text{ kN}$$

$$V(1.35) = 2.8504 \text{ kN}$$

$$\curvearrowright \Sigma M = 0:$$

$$M(x) + 0.176(x)\left(\frac{x}{2}\right) + 29.543(x - 0.03) - 32.631(x - 0.15) = 0$$

$$\therefore M(x) = -0.088x^2 - 29.543(x - 0.03) + 32.631(x - 0.15)$$

$$\therefore M(x) = -0.088x^2 - 29.543x + 0.88629 + 32.631x - 4.89465$$

$$\therefore M(x) = -0.088x^2 + 3.088x - 4.00836$$

$$M(0.15) = -3.547 \text{ kNm}$$

$$M(1.35) = 0.00006 \text{ kNm}$$

4. $0 < x < 1.38$:

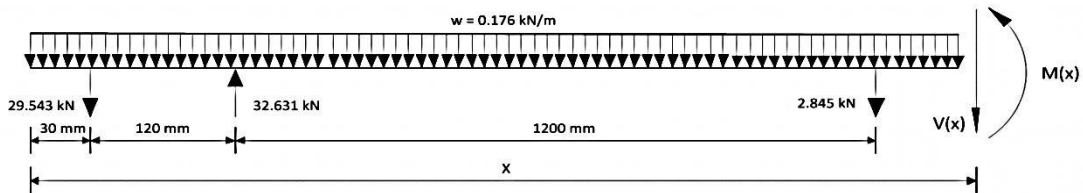


Figure 85 Section $0 < x < 1.35$ of pivot beam.

$$\uparrow \Sigma F_y = 0:$$

$$-V(x) - 29.543 + 32.631 - 2.845 - 0.176(x) = 0$$

$$\therefore V(x) = -0.176x + 0.243$$

$$V(1.35) = 0.0054 \text{ kN}$$

$$V(1.38) = 0.00012 \text{ kN}$$

$$\curvearrowright \Sigma M = 0:$$

$$M(x) + 29.543(x - 0.03) - 32.631(x - 0.15) + 2.845(x - 1.35) + 0.176(x)\left(\frac{x}{2}\right) = 0$$

$$\therefore M(x) = -29.543(x - 0.03) + 32.631(x - 0.15) - 2.845(x - 1.35) + 0.176(x)\left(\frac{x}{2}\right)$$

$$\therefore M(x) = -29.543x + 0.88629 + 32.631x - 4.89465 - 2.845x + 3.84075 - 0.088x^2$$

$$\therefore M(x) = -0.088x^2 + 0.243x - 0.16761$$

$$M(1.35) = 0.00006 \text{ kNm}$$

$$M(1.38) = 0.0001428 \text{ kNm}$$

From the above calculations the following was procured:

$$M_{max} = -3.547 \text{ kNm @ } 0.15\text{m}$$

$$V_{max} = -29.569 \text{ kN @ } 0.15\text{m}$$

The maximum normal force that would be exerted on the columns was:

$$N_{max} = 32.631 \text{ kN}$$

To ensure that the calculations done above were correct, a FEA was made with a FEM program called Prokon. The beam was modelled the following way:

1. Elements

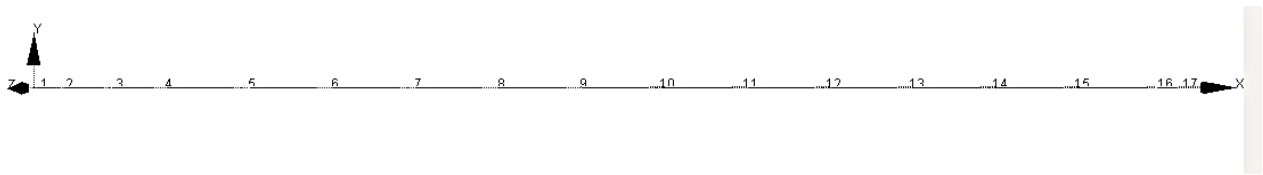


Figure 86 Elements used in Prokon analysis of the pivot beam.

2. Supports

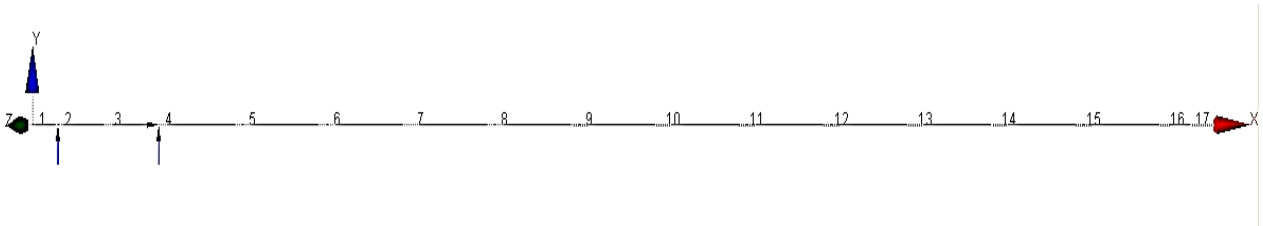


Figure 87 Supports and point-load

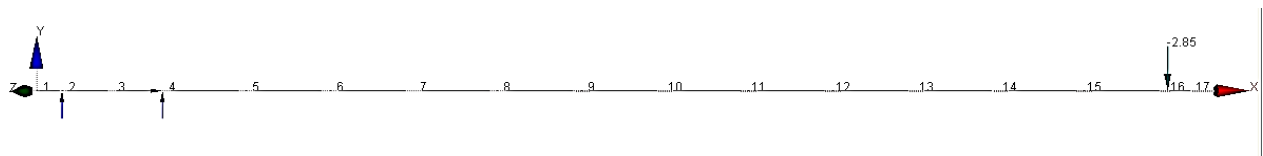


Figure 88 Supports and point load modelled on the pivot beam. (Prokon)



Figure 89 Supports and distributed load modelled on the pivot beam. (Prokon)

The model was analysed and the maximum shear forces and bending moments calculated were confirmed by the FEA as can be seen in Figure 90.

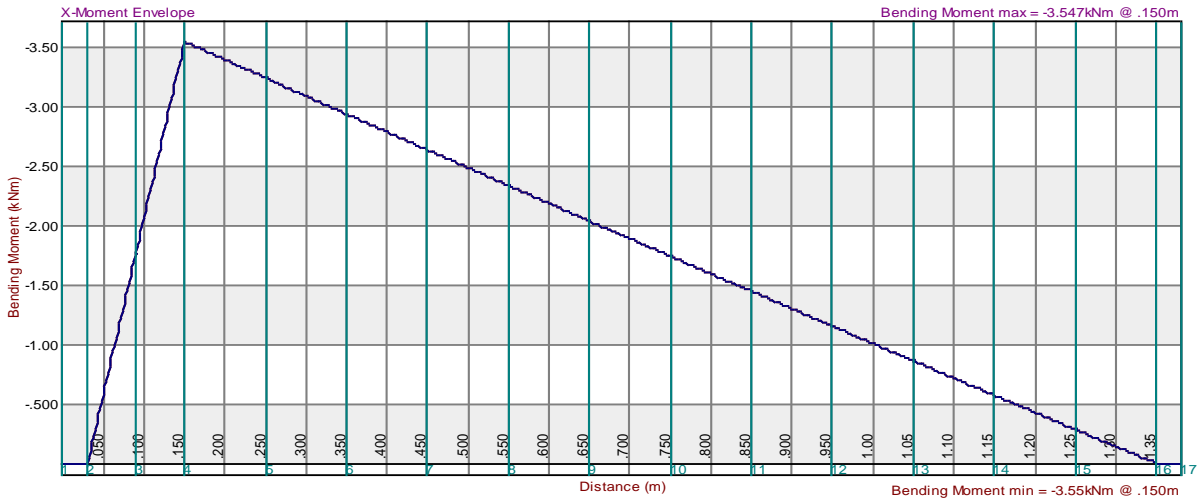


Figure 90 Maximum bending moments acting on pivot beam. (Prokon)

Figure 90 confirms that

$$M_{max} = -3.547 \text{ kNm @ } 0.15\text{m}$$

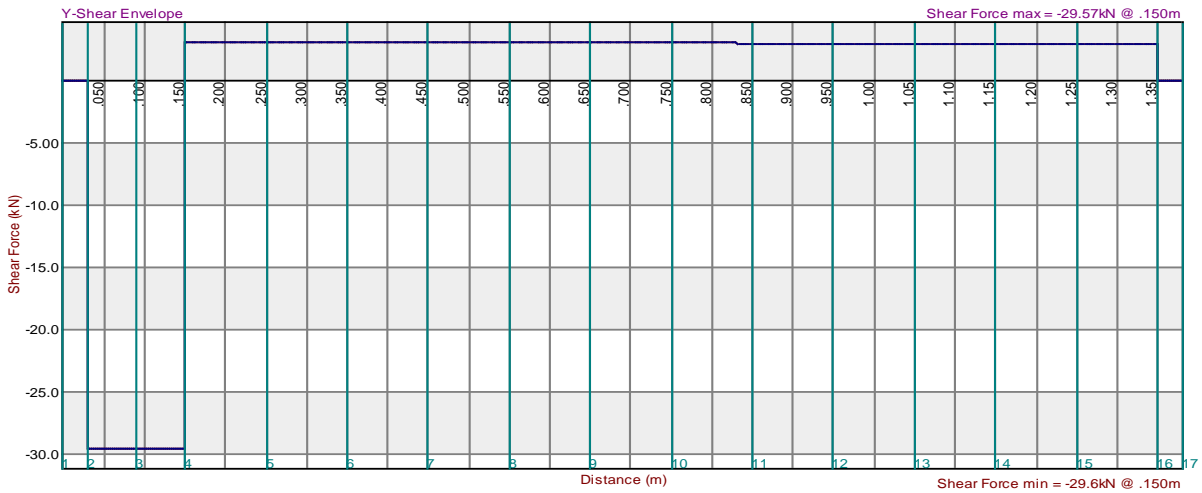


Figure 91 Maximum shear forces acting on pivot beam. (Prokon)

Figure 91 confirms that

$$V_{max} = -29.569 \text{ kN @ } 0.15\text{m}$$

The Prokon analysis showed that the calculations were done correctly and that all assumptions made during the design were valid.

B.5 Detail A – Pivot Beam

It was firstly necessary to find the classification of the hollow steel section in order to calculate whether the chosen steel section would be sufficient for the design. In order to find the classification of this section it is necessary to determine the width-to-thickness ratio or b/t ratio, with b being the effective width and t being the effective thickness. (SANS 10162-1:2005 11.3.2 b))

The effective width (b) will be the nominal outside dimension less four times the wall thickness:

$$b = 100 - 4(t) \quad (9.5)$$

Thus

$$b/t = \frac{100 - 4(t)}{t} = \frac{100 - 4(6)}{6} = 12.667$$

To calculate the capacity of the section with regard to the bending moments it was necessary to classify the web and the flange of the section. Because of symmetry:

Web:

$$h_w/t_w = b/t = 12.667 \leq \frac{1100}{\sqrt{f_y}} = \frac{1100}{\sqrt{300}} = 63.509 \therefore \text{Class 1} \quad (\text{SANS 10162-1:2005 Table 4})$$

Flange:

$$b/t = 12.667 \leq \frac{420}{\sqrt{f_y}} = \frac{420}{\sqrt{300}} = 24.249 \therefore \text{Class 1} \quad (\text{SANS 10162-1:2005 Table 4})$$

The factored moment resistance (M_r) was calculated by:

$$M_r = \phi Z_p f_y \quad (\text{SANS 10162-1:2005 13.5 a))}$$

$$\text{With } \phi = 0.9 \quad (\text{SANS 10162-1:2005 13.1 a))}$$

This would give

$$M_r = 0.9 \cdot 73.5 \times 10^3 \text{ mm}^3 \cdot 300 \text{ N/mm}^2 = 19845000 \text{ Nmm} = 19.845 \text{ kNm}$$

$$M_r = 19.845 > M_{max} = 5.6752 \text{ kNm} \therefore \text{OK}$$

The next step would be to calculate the shear capacity of the section. The factored shear resistance (V_r) developed by the web of a flexural member is taken as

$$V_r = \phi A_v f_s \quad (\text{SANS 10162-1:2005 14.1})$$

Where

A_v is taken as the shear area, in this case $t_w \cdot h \times 2$

$$f_s = 0.66f_y \text{ when } h_w/t_w \leq 440 \sqrt{\frac{k_v}{f_y}} \text{ where } k_v = 5.34$$

$$\text{Now } \frac{h_w}{t_w} = b/t = 12.667 \leq 440 \sqrt{\frac{5.34}{300}} = 58.703 \text{ which gives } f_s = 0.66f_y$$

Therefore

$$V_r = \phi \cdot t_w \cdot h \cdot 0.66f_y = 0.9 \cdot (2 \times 100 \cdot 6) \cdot 0.66 \cdot 300 = 213.84 \text{ kN}$$

$$V_r = 213.84 > 47.3104 \text{ kN} \therefore OK$$

B.6 Detail B – Compression Column

By using the same type of square hollow section (100 x 100 x 6 mm) that was used for the pivot beams the design would remain simple. It was necessary to see whether the structural section would be capable of resisting the compressive forces generated by the weights.

In order to determine the compressive capacity it was necessary to find the width-to-thickness (b/t) ratio of the section. From earlier calculations

$$b/t = 12.667 \leq \frac{670}{\sqrt{f_y}} = \frac{670}{\sqrt{300}} = 38.682 \therefore \text{Class 3} \quad (\text{SANS 10162-1:2005 Table 3})$$

The factored axial compressive resistance (C_r) of doubly symmetric sections is calculated by

$$C_r = \phi A f_y (1 + \lambda^{2n})^{-1/n} \quad (\text{SANS 10162-1:2005 13.3.1})$$

Where $n = 1.34$

$$\lambda = \frac{KL}{r} \sqrt{\frac{f_y}{\pi^2 E}}$$

The effective length of the column is given by KL . In this case the conservative approach would be to assume that the bottom-end of the column was fixed and the top-end of the column was free. This would make the K-value 2.0, which would make

$$\lambda = \frac{2.0 \cdot 2300}{37.7} \sqrt{\frac{300}{\pi^2 \cdot 200 \times 10^3}} = 1.504$$

Therefore

$$C_r = \phi A f_y (1 + \lambda^{2n})^{-1/n} = 0.9 \cdot 2.13 \times 10^3 \cdot 300 (1 + 1.504^{2(1.34)})^{-1/1.34} = 204.936 \text{ kN}$$

$$C_r = 204.936 \text{ kN} > N_{max} = 52.2096 \text{ kN} \therefore OK$$

B.7 Detail C – Frictionless Pinned Connection

Modelling one of the pivot beams and the forces working on it will look as follow:

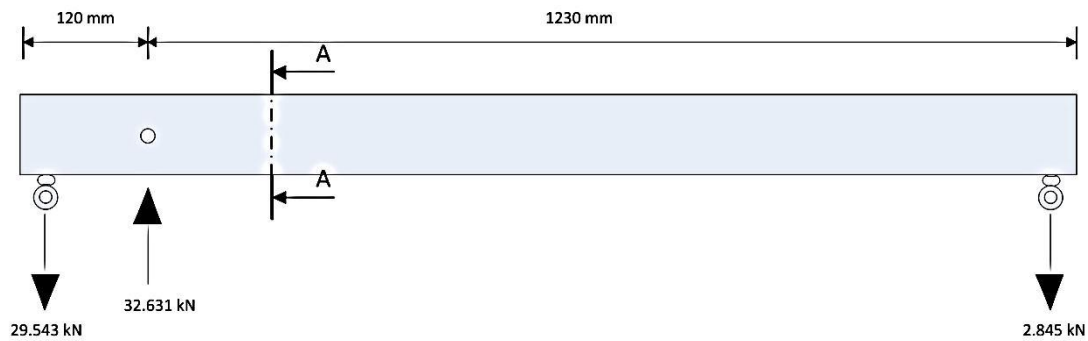


Figure 92 Graphical presentation of one of the pivot beams.

Section A-A is presented by Figure 93.

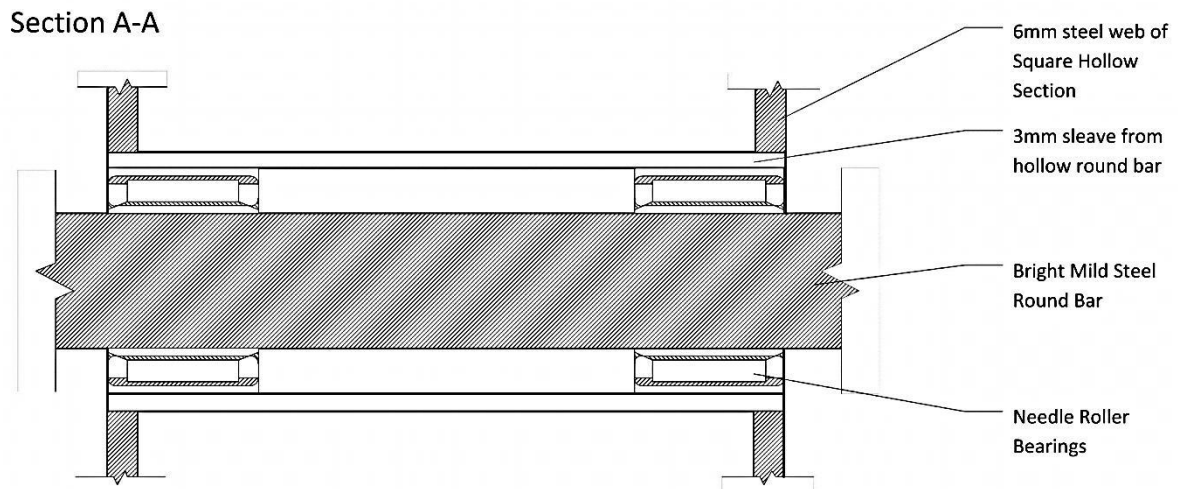


Figure 93 Section A-A clearly shows the steel bar passing through the needle roller bearing.

$$F_{max} = 1.6 \times 32.631 = 52.2096 \text{ kN}$$

This force was transferred through the webs of the steel square hollow section, which divided the force into two as can be seen in Figure 94.

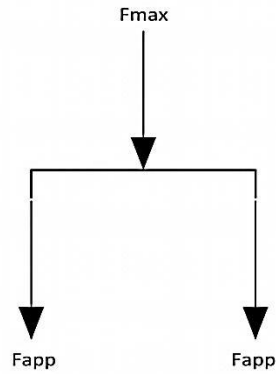


Figure 94 The relationship between F_{max} and F_{app} .

From Figure 94 it can be seen that $F_{app} = F_{max}/2$. That gives $F_{app} = 52.2096/2 = 26.1048 \text{ kN}$

The bright mild steel round bar was supplied by MACSTEEL, which is a well-known steel supplier in South Africa. For the purpose of this design a certain diameter had to be chosen, in this case 20 mm. Then it was necessary to calculate whether the round bar had the capacity to resist the forces it would be subjected to. The following properties are available from MACSTEEL:

MACSTEEL Classification: EN3A/B – COLD DRAWN (070.M.20/C.1018)

$$f_y = 350 \text{ MPa}$$

$$f_u = 420 \text{ MPa}$$

$$E = 205 \times 103 \text{ MPa}$$

The pinned connection could be considered as a bearing type connection seeing that the bending of the bar was negligible and the shear capacity was of the most interest. It could therefore be considered as a bar in shear. The factored shear resistance of bolts may calculated by:

$$V_r = 0.6 \cdot \phi_b \cdot n \cdot m \cdot A_b \cdot f_u \text{ with } \phi_b = 0.8 \quad (\text{SANS 10162-1:2005 13.12.1.2.b})$$

Seeing that the 20 mm bar served as a pinned connection, the total factored shear resistance of the nominal area of pins could also be calculated by

$$V_r = 0.66 \phi A f_y \quad (\text{SANS 10162-1:2005 13.4.3})$$

Upon inspection it can be seen that the two methods of calculating the shear resistance differed substantially:

$$V_r = 0.6 \cdot \phi_b \cdot n \cdot m \cdot A_b \cdot f_u$$

$$V_r = 0.66\phi A f_y$$

To be conservative, the lesser of the two shear resistance values calculated by abovementioned expressions would be taken as the design value

$$V_{r1} = 0.6 \cdot \phi_b \cdot n \cdot m \cdot A_b \cdot f_u = 0.6 \cdot 0.8 \cdot 1 \cdot 1 \cdot (\pi \cdot 10^2) \cdot 420 = 63.335 \text{ kN}$$

$$V_{r2} = 0.66 \cdot \phi \cdot A \cdot f_y = 0.66 \cdot 0.9 \cdot (\pi \cdot 10^2) \cdot 350 = 65.314 \text{ kN}$$

From the calculations above it can be seen that the design value for shear resistance is

$$V_r = 63.335 \text{ kN} > F_{app} = 26.1048 \text{ kN} \therefore OK$$

The needle roller bearing considered for the frictionless pinned connection is an IKO Needle Roller Bearing with specifications TAF 202820. The inside diameter is 20 mm, the width is 20 mm and the outside diameter is 28 mm. The bearing had a capacity (C_0) of 25.4 kN. The unfactored load ($R_2/2$) exerted on the bearing is 16.3155 kN and the factored load (F_{app}) exerted on the bearing is 26.1048 kN. To put everything into perspective

$$C_0 = 25.4 \text{ kN} > R_2/2 = 16.3155 \text{ kN} \therefore OK$$

However

$$C_0 = 25.4 \text{ kN} < F_{app} = 26.1048 \text{ kN} \therefore NOT OK$$

It can be seen that the capacity of the bearing was capable of handling the un-factored load. The factored load was marginally bigger than the bearing capacity, which would be a problem if the design approach were not conservative. However, with the design being overly conservative up to this point, the bearing's inability to deal with the factored load only presented a minor problem. This problem would not affect the efficiency of the design.

B.9 Detail D – Parallel Flat Bar Columns

The parallel flat bar columns is be modelled as Figure 95.

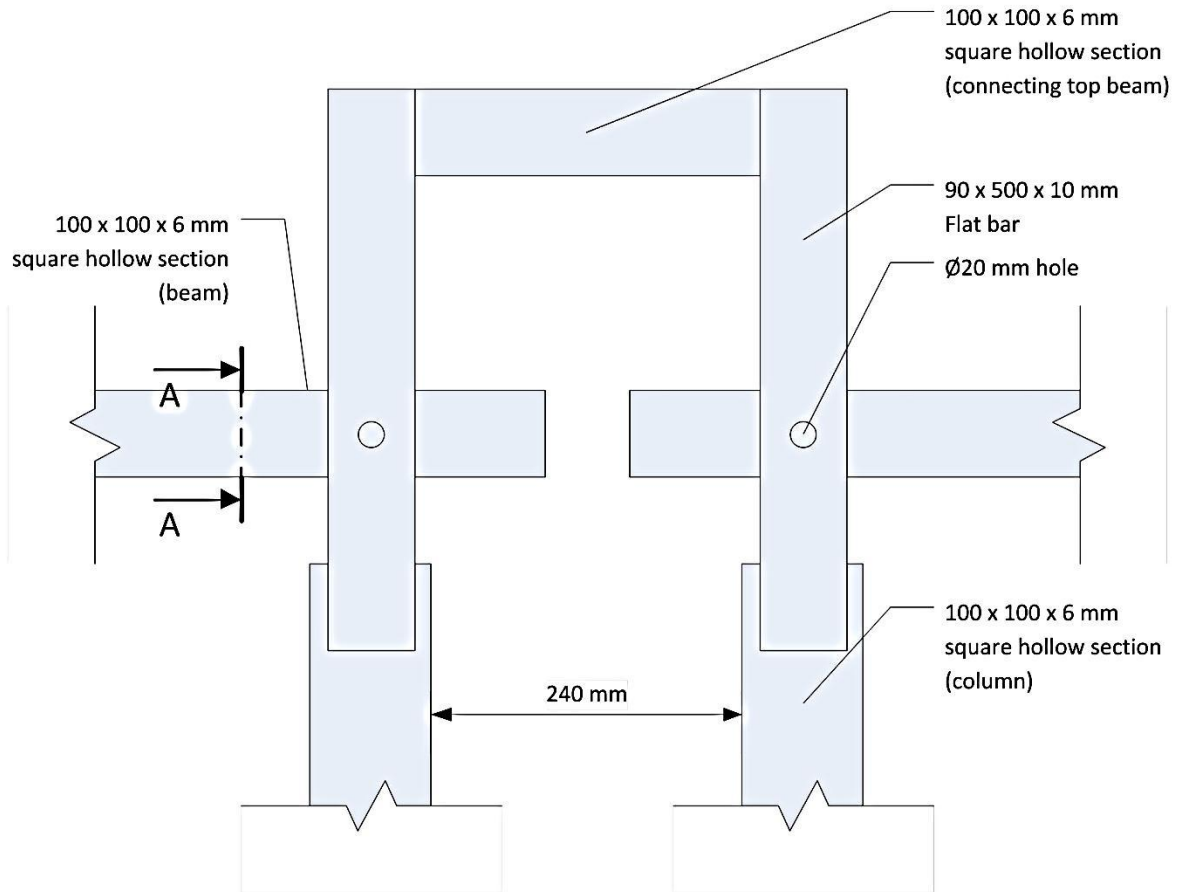


Figure 95 Graphical presentation of the parallel flat bar columns.

Section B – B is presented by Figure 96.

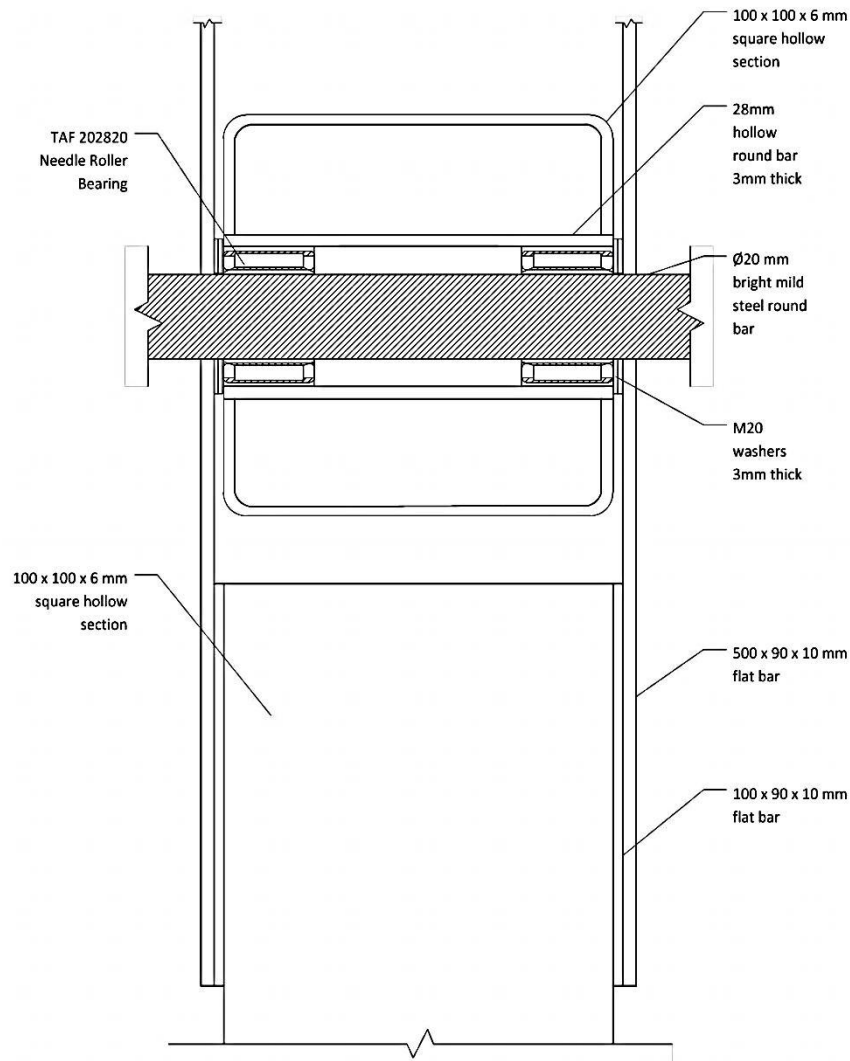


Figure 96 Section B-B presenting the pivot beam fitting through parallel flat bar columns.

It was necessary to see what effect the shear force exerted combined with the 34 mm hole had on the web of the square hollow section. The bearing capacity of the web can be calculated by:

$$B_{r1} = 3 \cdot \phi_{br} \cdot t \cdot d \cdot n \cdot f_u = 3 \cdot 0.67 \cdot 6 \cdot 38 \cdot 1 \cdot 450 = 206.226 \text{ kN}$$

$$B_{r1} = 206.226 \text{ kN} > F_{app} = 26.1048 \text{ kN} \therefore OK \quad (\text{SANS 10162-1:2005 13.10.c})$$

It was also necessary to calculate the bearing resistance of the 10 mm flat bar:

$$B_{r2} = 3 \cdot \phi_{br} \cdot t \cdot d \cdot n \cdot f_u = 3 \cdot 0.67 \cdot 10 \cdot 20 \cdot 1 \cdot 450 = 180.9 \text{ kN}$$

$$B_{r2} = 180.9 \text{ kN} > F_{app} = 26.1048 \text{ kN} \therefore OK$$

From the calculations above it can be seen that the frictionless pinned connection has the capacity to withstand the forces applied.

B.10 Detail E – Stopper and Top Connecting Beam

B.10.1 Bending Capacity of Top Connecting Beam:

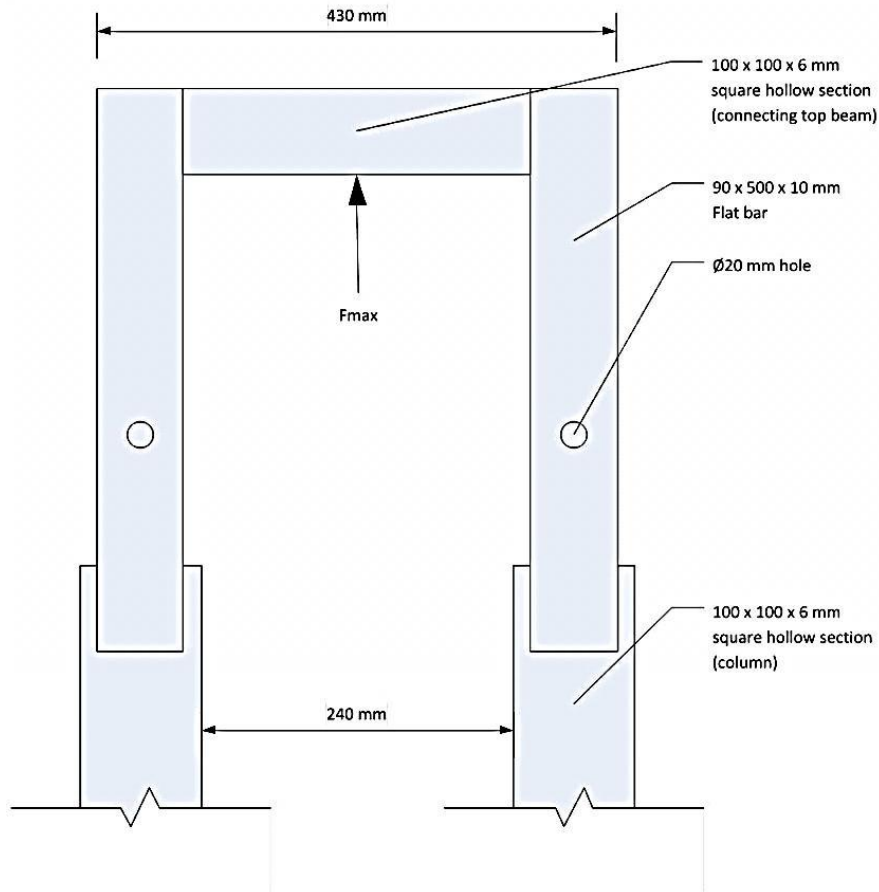


Figure 97 Force acting on the top connecting beam.

F_{max} is the force that would be exerted on the top beam by the stopper as can be seen in Figure 97. The stopper would act as a safety mechanism and a loading mechanism. F_{max} can be found the following way:

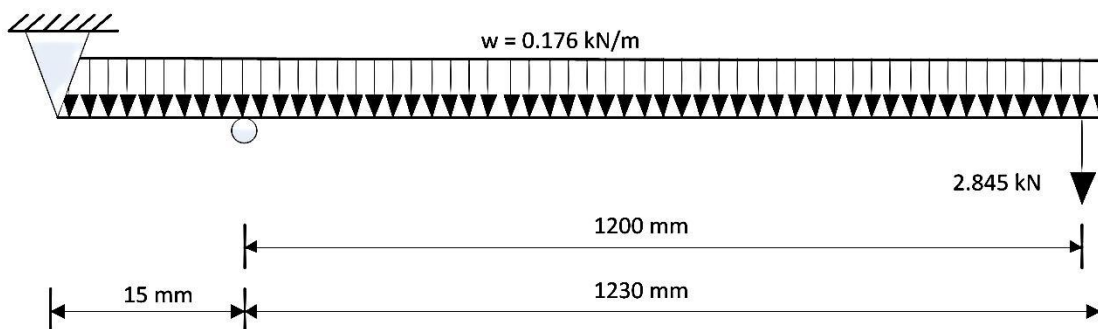


Figure 98 Pivot beam modelled to find the forces acting on the top connecting beam.

Figure 98 can be modelled as Figure 99

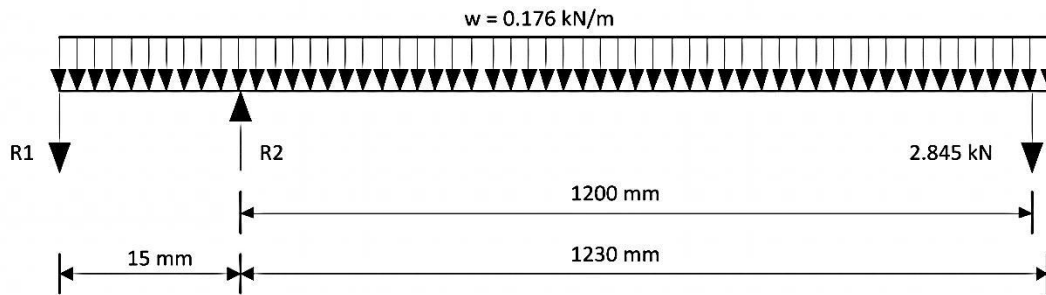


Figure 99 Pivot beam with reaction forces included.

$$\uparrow \Sigma F_y = 0:$$

$$R_2 - R_1 - 0.176(1.38) - 2.845 = 0$$

$$R_2 = R_1 + 2.845 + 0.243$$

$$\curvearrowright \Sigma M_1 = 0:$$

$$0.15R_2 - 0.176(1.38) \left(\frac{1.38}{2} \right) - 2.845(1.38) = 0$$

$$0.15R_2 = 0.168 + 3.962$$

$$R_2 = 27.533 \text{ kN}$$

That gives

$$R_1 = R_2 - 2.845 - 0.243$$

$$\therefore R_1 = 27.533 - 2.845 - 0.243$$

$$\therefore R_1 = 24.445 \text{ kN}$$

$$F_{max} = 2 \times R_1 = 48.89 \text{ kN}$$

$$\text{Factored } F_{max} = 1.6 \times F_{max} = 78.224 \text{ kN}$$

In order to find the maximum bending moment that will be generated in the top connecting beam by the stopper, the following model depicted by Figure 100 is applicable.

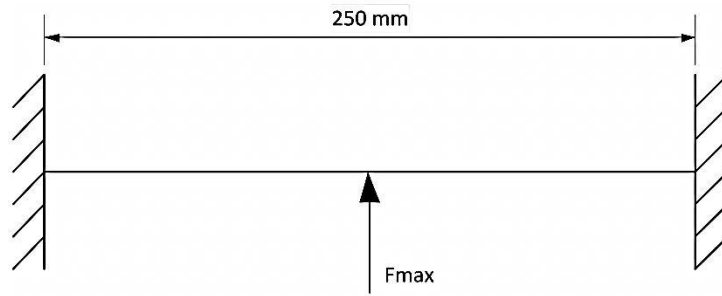


Figure 100 Model of top connecting beam.

Figure 100 can be modelled as Figure 101.

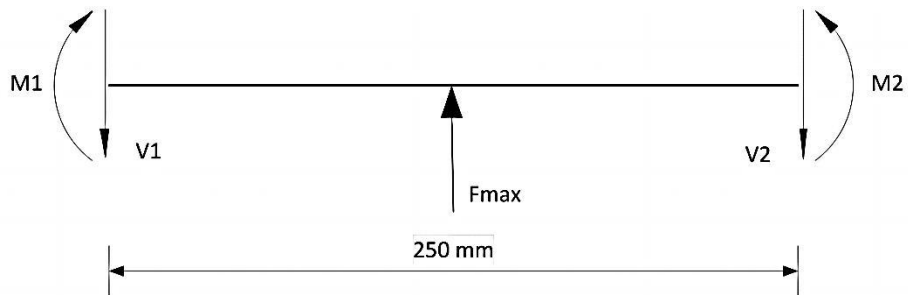


Figure 101 Model of top connecting beam with forces included.

Analysed symmetrically

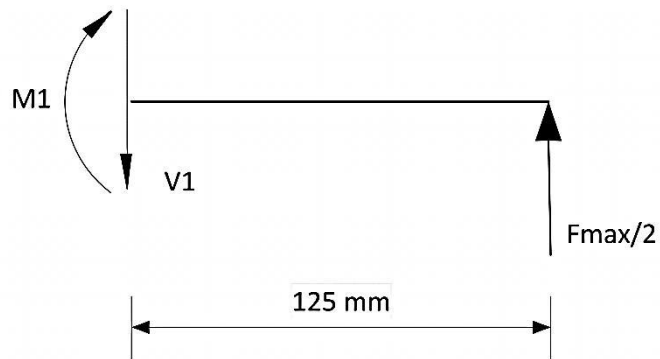


Figure 102 Model of top connecting beam with forces included analysed symmetrically.

$\uparrow \Sigma F_y = 0:$

$$-V_1 + F_{max}/2 = 0$$

$$\therefore V_1 = F_{max}/2 = 24.445 \text{ kN}$$

$$\sum M_1 = 0:$$

$$-M_1 + 24.445(0.125) = 0$$

$$M_1 = 3.056 \text{ kNm}$$

$$M_{max} = 3.056 \text{ kNm}$$

$$\text{Factored } M_{max} = 1.6 \times 3.056 = 4.89 \text{ kNm}$$

$$M_r = 19.845 \text{ kNm} > 4.89 \text{ kNm} \therefore \text{OK}$$

B.10.2 Axial Capacity of Stopper

The stopper consisted of a round disc fixed to a threaded rod. The round disc would have a radius of 50 mm and is 10 mm thick. The most crucial aspect of the stopper was the axial capacity of the threaded rod, which was chosen as a galvanized 20 mm threaded rod.

Figure 103 depicts the relationship between the threaded rod and the top connecting beam.

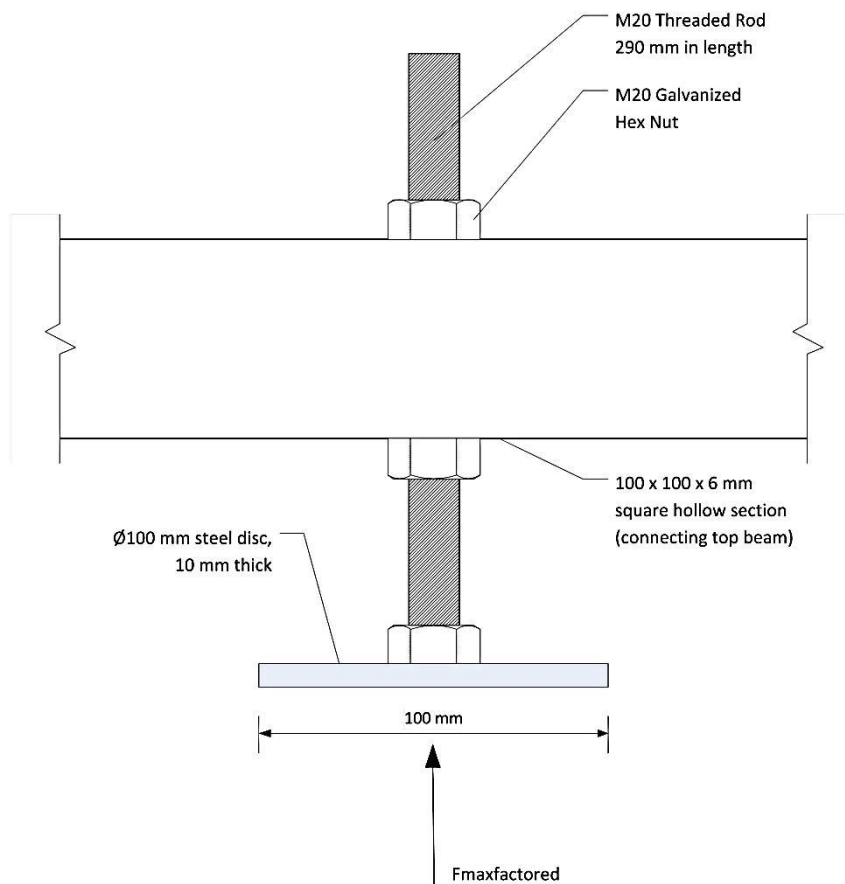


Figure 103 Graphical presentation of the relationship between the top connecting beam and the stopper.

The axial capacity (T_r) of the 20 mm threaded rod can be found in Table 7 of the SASCH.

$$T_{rM20} = 156 \text{ kN} > F_{\text{maxfactored}} = 78.224 \text{ kN} \therefore \text{OK}$$

The circular disc was fitted to the threaded rod through a welded 20 mm hex nut, which was welded to the circular disc and fitted to the 20 mm threaded rod. The top and bottom hex nuts were there to adjust the setup and to load the specimens.

B.11 Detail F – Bottom Connecting Beam

The bottom connecting beam is depicted by Figure 104.

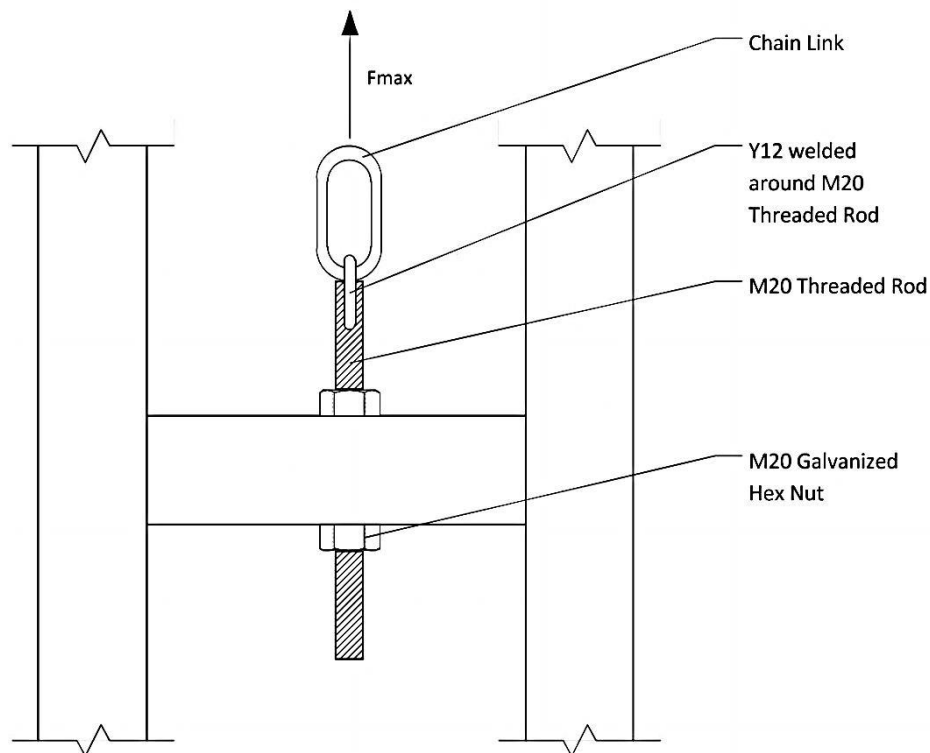


Figure 104 Graphical presentation of the bottom connecting beam.

The Figure 104 can be modelled as Figure 105

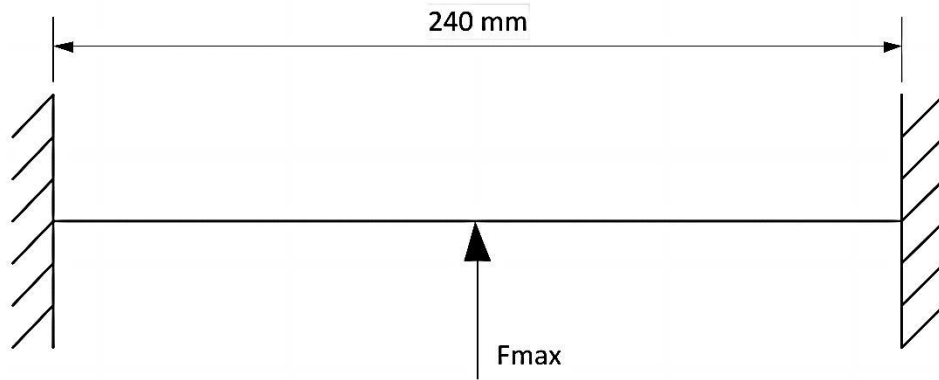


Figure 105 Model of bottom connecting beam.

Which can be simplified to:

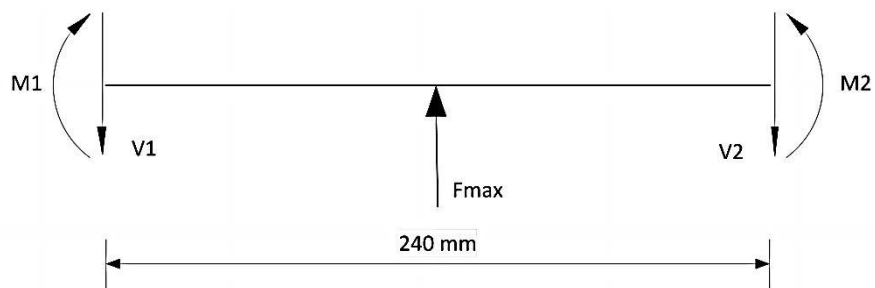


Figure 106 Model of bottom connecting beam with forces included.

Analyzed symmetrically

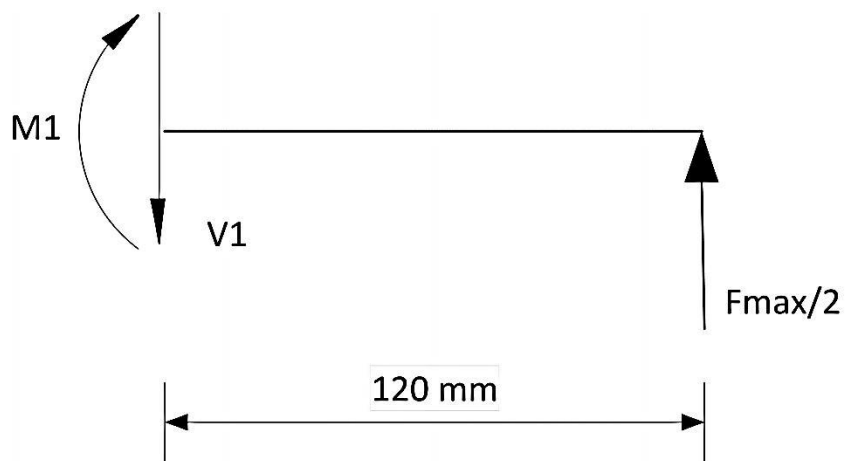


Figure 107 Model of bottom connecting beam with forces included analysed symmetrically.

$\uparrow \Sigma F_y = 0:$

$$-V_1 + F_{max}/2 = 0$$

$$\therefore V_1 = F_{max}/2 = 24.445 \text{ kN}$$

Here, $F_{max} = 48.41 \text{ kN}$.

$\sum M_1 = 0$:

$$-M_1 + 24.445(0.12) = 0$$

$$M_1 = 2.933 \text{ kNm}$$

$$M_{max} = 2.933 \text{ kNm} \therefore \text{Factored } M_{max} = 1.6 \times 2.933 = 4.693 \text{ kNm}$$

$$M_r = 19.845 \text{ kNm} > 4.693 \text{ kNm} \therefore \text{OK}$$

$$T_{rM20} = 156 \text{ kN} > F_{maxfactored} = 78.224 \text{ kN} \therefore \text{OK}$$

B.12 Detail G – Base Plate

The floor of the climate-controlled room had a grid of $600 \times 600 \text{ mm}$ holes of 20 mm diameter to which the base plate could be bolted. This led to the geometry of the base plate and the experimental setup. The experimental setup is presented by Figure 108.

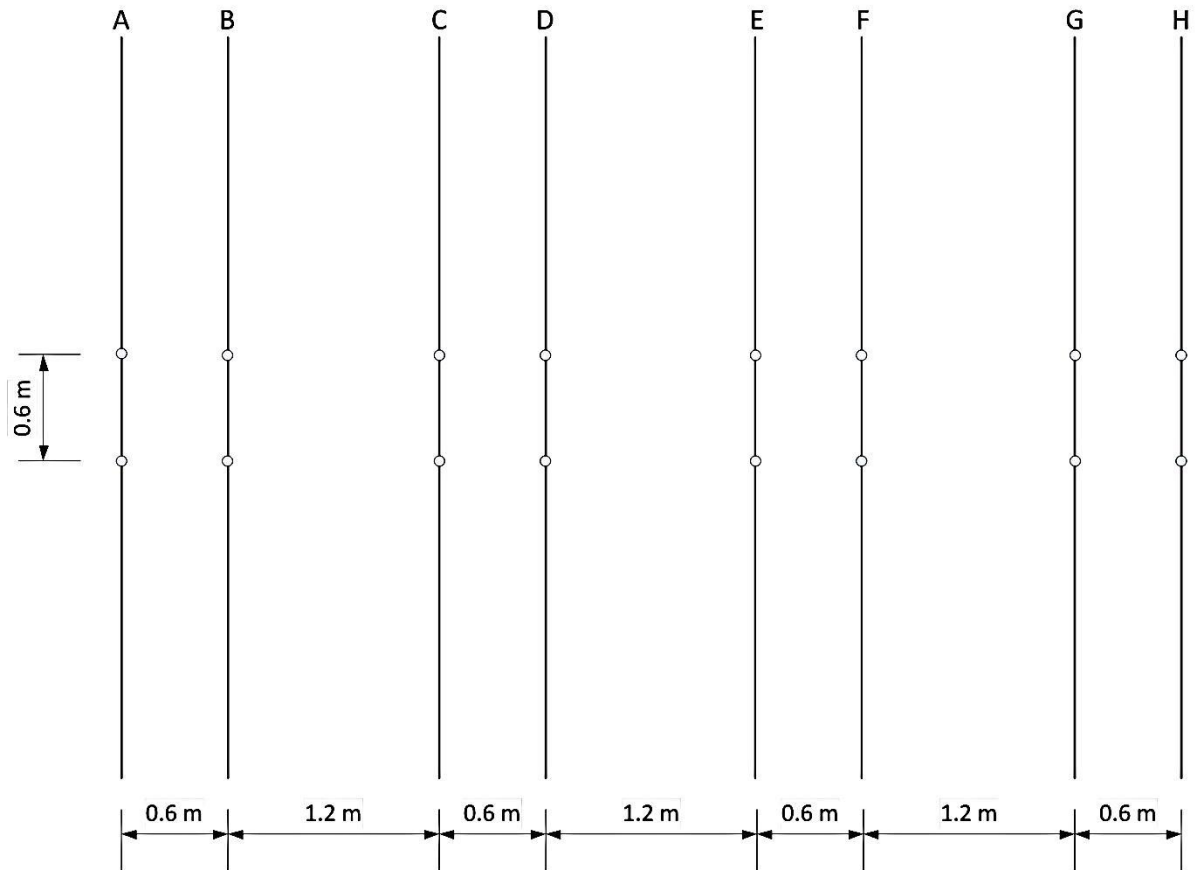


Figure 108 Plan view of the steel frames used in the experimental setup.

From Figure 108 it can be seen that there would be eight frames. These frames would be grouped into four pairs. The circles in Figure 108 represent the 20 mm holes in the floor to which the frames were bolted. The vertical lines represent the frames as seen in plan. The groups are explained below:

- Frames A and B: Creep of SCC un-notched
- Frames C and D: Creep of SFRSCC un-notched
- Frames E and F: Creep of SFRSCC notched un-cracked
- Frames G and H: Creep of SFRSCC notched pre-cracked

With the frames spaced 600 mm apart the width of the base plates will be affected. This leads to the following geometrical design of the base plate as seen with Figure 109.

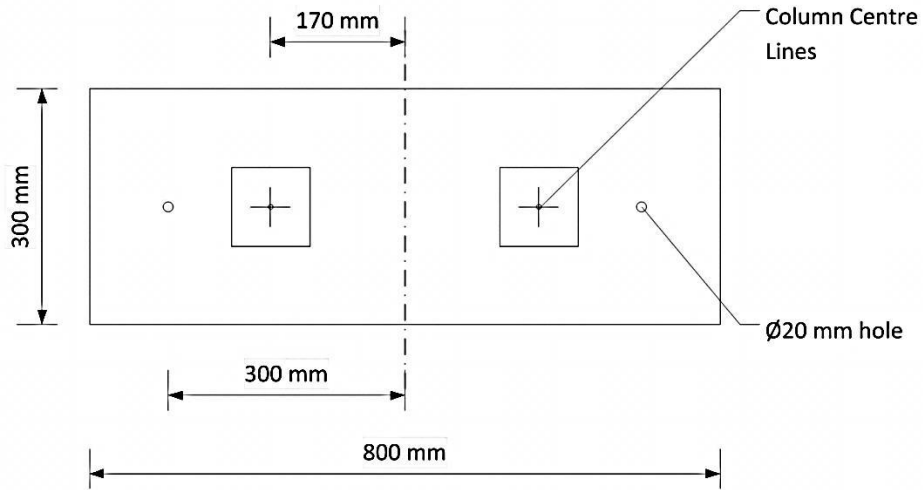


Figure 109 Geometrical design of the base plate.

It is necessary to determine the base plate thickness so that the base plate has the capacity to handle the bending moments. To create the worst case scenario it was assumed that the frames will be loaded on side at a time. This would lead to a lever arm and generate the highest internal bending moments. The scenario can be modelled by Figure 110.

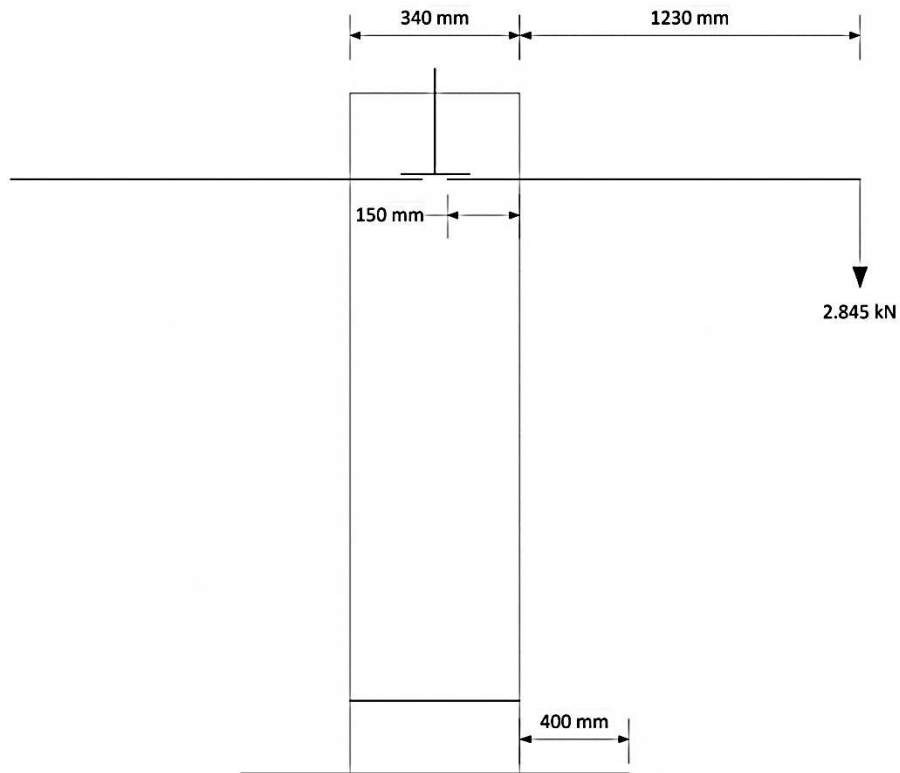


Figure 110 Worst case loading scenario

Taking the reaction forces into account:

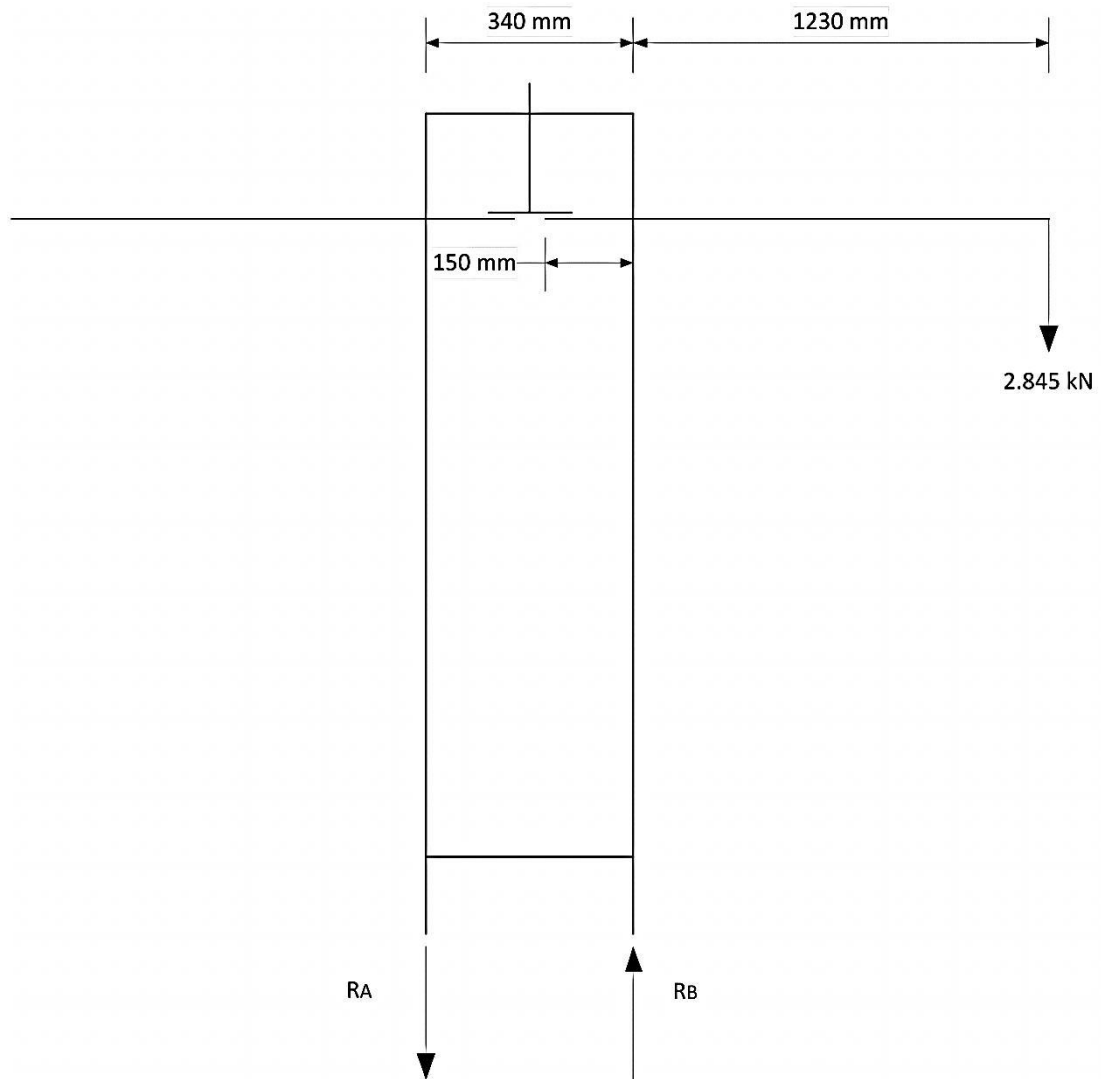


Figure 111 Worst case loading scenario with reaction forces included.

Determining the reaction forces:

$$\uparrow \Sigma F_y = 0:$$

$$-R_A + R_B - 2.845 = 0$$

$$\therefore R_B = R_A + 2.845$$

$$\curvearrowright \Sigma M_B = 0:$$

$$0.34R_A - 2.845(1.23) = 0$$

$$\therefore R_A = 10.292 \text{ kN}$$

Which gives

$$R_B = 10.292 + 2.845 = 13.137 \text{ kN}$$

Looking at the factored forces exerted on the base plate.

$$F_a = 1.6 \times 10.292 = 16.467 \text{ kN}$$

$$F_b = 1.6 \times 13.137 = 21.019 \text{ kN}$$

These forces are relevant in the following way:

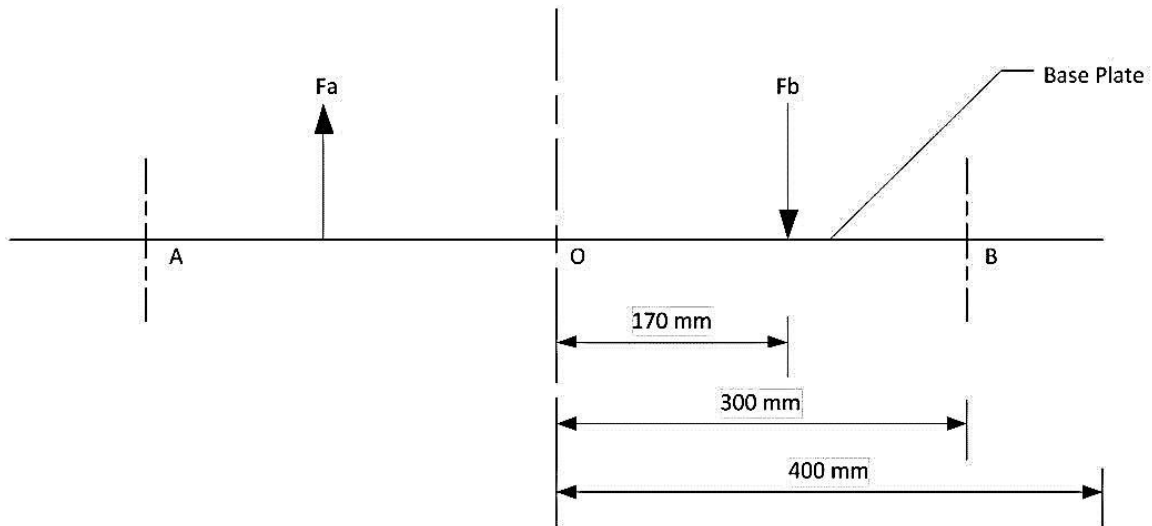


Figure 112 Forces acting on the base plate.

Their combined effect can be simulated by Figure 113.

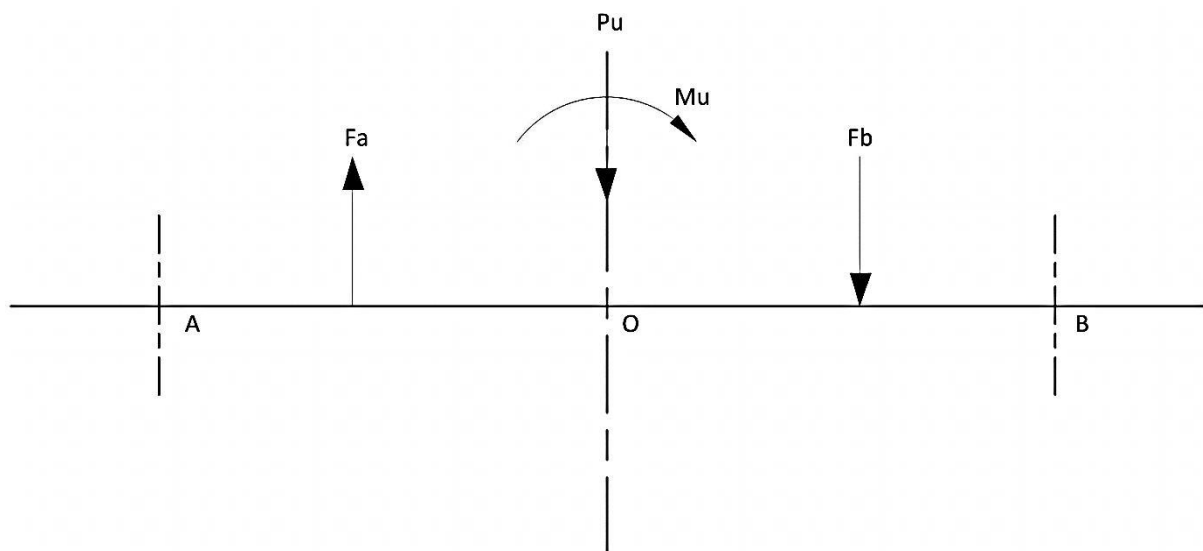


Figure 113 Combined effect of the forces acting on the base plate.

P_u and M_u will be substituting F_a and F_b , which will be needed to design the base plate. Calculating P_u through equilibrium:

$$\uparrow \Sigma F_y = 0:$$

$$-P_u - F_b + F_a = 0$$

$$\therefore P_u = -F_b + F_a = -21.019 + 16.467 = -4.552 \text{ kN}$$

In this case F_a and F_b causes a coupled moment, M_u :

$$M_u = 0.17(21.019) + 0.17(16.467) = 6.372 \text{ kNm}$$

For the design of the base plate, the abovementioned parameters will be used in the following way:

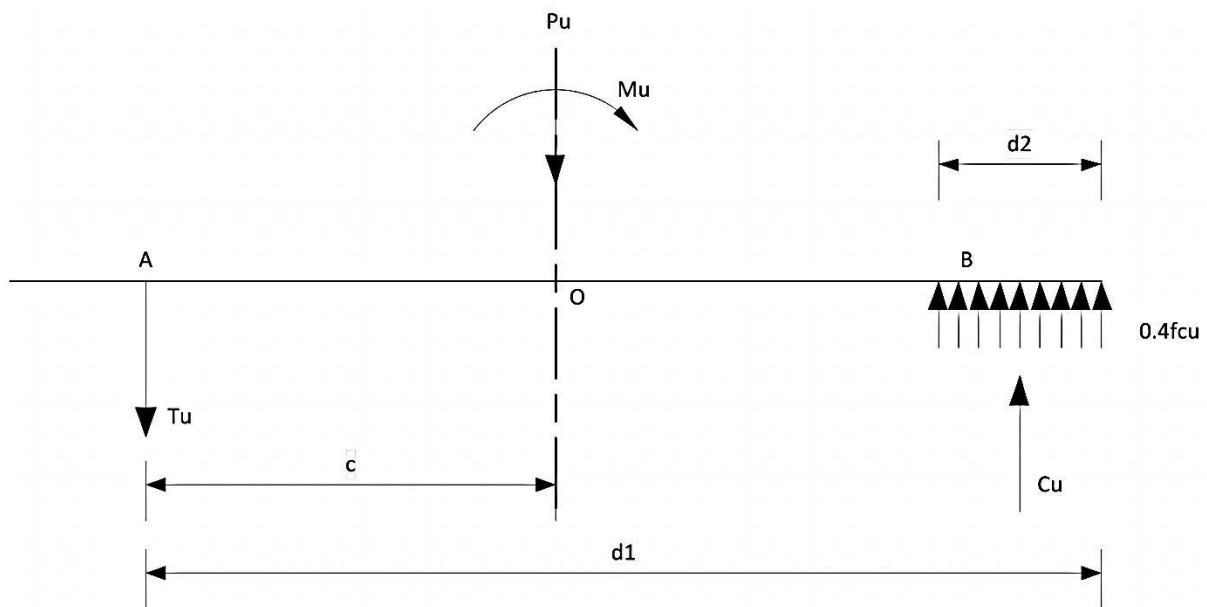


Figure 114 Model of base prepared for design process.

Here $c = 300 \text{ mm}$ and $d_1 = 700 \text{ mm}$ with T_u , C_u and d_2 to be calculated. Assuming that the compressive strength of the concrete floor $f_{cu} = 30 \text{ MPa}$. That would make

$$C_u = 0.4f_{cu} \times d_2 \times b = 0.4 \times 30 \times 300 \times d_2$$

Using equilibrium to solve the parameters:

$$\curvearrowright \Sigma M_B = 0:$$

$$M_u + P_u c - C_u \left(d_1 - \frac{d_2}{2} \right) = 0$$

$$M_u + P_u c - 0.4f_{cu}bd_2 \left(d_1 - \frac{d_2}{2} \right) = 0$$

$$M_u + P_u c = 0.4f_{cu}bd_1d_2 - 0.2f_{cu}bd_2^2$$

$$6.372 \times 10^6 + 4.552 \times 10^3(300) = 0.4 \cdot 30 \cdot 300 \cdot 700d_2 - 0.2 \cdot 30 \cdot 300d_2^2$$

$$6372 \times 10^3 + 1365.6 \times 10^3 = 2520 \times 10^3 d_2 - 1.8 \times 10^3 d_2^2$$

$$0 = -1.8d_2^2 + 2520d_2 - 7737.6$$

The only unknown now is d_2 . Calculating d_2 :

$$d_2 = \frac{-(2520) \pm \sqrt{(2520)^2 - 4(-1.8)(-7737.6)}}{2(-1.8)}$$

$$d_2 = \frac{-2520 \pm \sqrt{6294689.3}}{-3.6}$$

$$d_2 = \frac{-2520 - 2508.9}{-3.6} = 1396.9 \text{ mm}$$

Or

$$d_2 = \frac{-2520 + 2508.9}{-3.6} = 3.1 \text{ mm}$$

That leaves $d_2 = 1396.9 \text{ mm}$, which is bigger than 800 mm (the base plate's length) or $d_2 = 3.1 \text{ mm}$, which is more realistic. With d_2 known it is possible to calculate C_u :

$$C_u = 0.4f_{cu} \times d_2 \times b = 0.4 \cdot 30 \cdot 300 \cdot 3.1 = 11\,160 \text{ kN} = 11.16 \text{ kN}$$

The only unknown left is T_u , which can be calculated through equilibrium.

$\uparrow \Sigma F_y = 0$:

$$-P_u - T_u + C_u = 0$$

$$T_u = C_u - P_u = 11.16 - 4.552 = 6.608 \text{ kN}$$

The tensile force T_u will be the force handled by the M20 bolts bolted to the floor.

$$T_{rM20} = 156 \text{ kN} > T_u = 6.608 \text{ kN} \therefore \text{OK}$$

Now we have to determine the thickness required for the base plate. The geometry of the base plate can be seen in Figure 115.

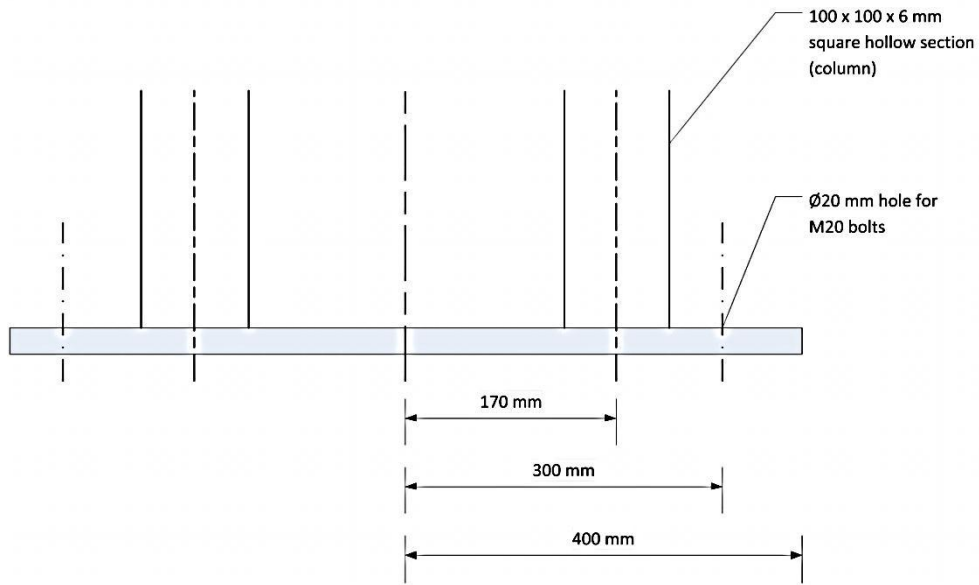


Figure 115 Geometry of base plate viewed from the side

From earlier calculations the forces exerted on the base plate has been found. To find out how thick the base plate should be, the maximum internal bending moment must be calculated. By examining the edge of the base plate it can be seen how the internal bending moment is generated. Looking at one of the columns attached to the base plate presented by Figure 116.

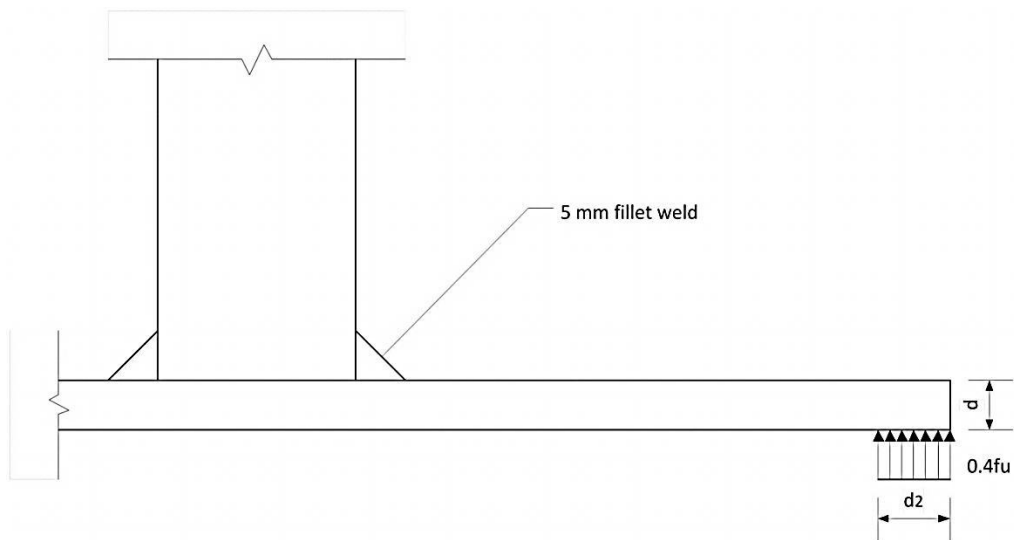


Figure 116 Section of base plate presenting the forces acting on the edge.

Which leads to Figure 117.

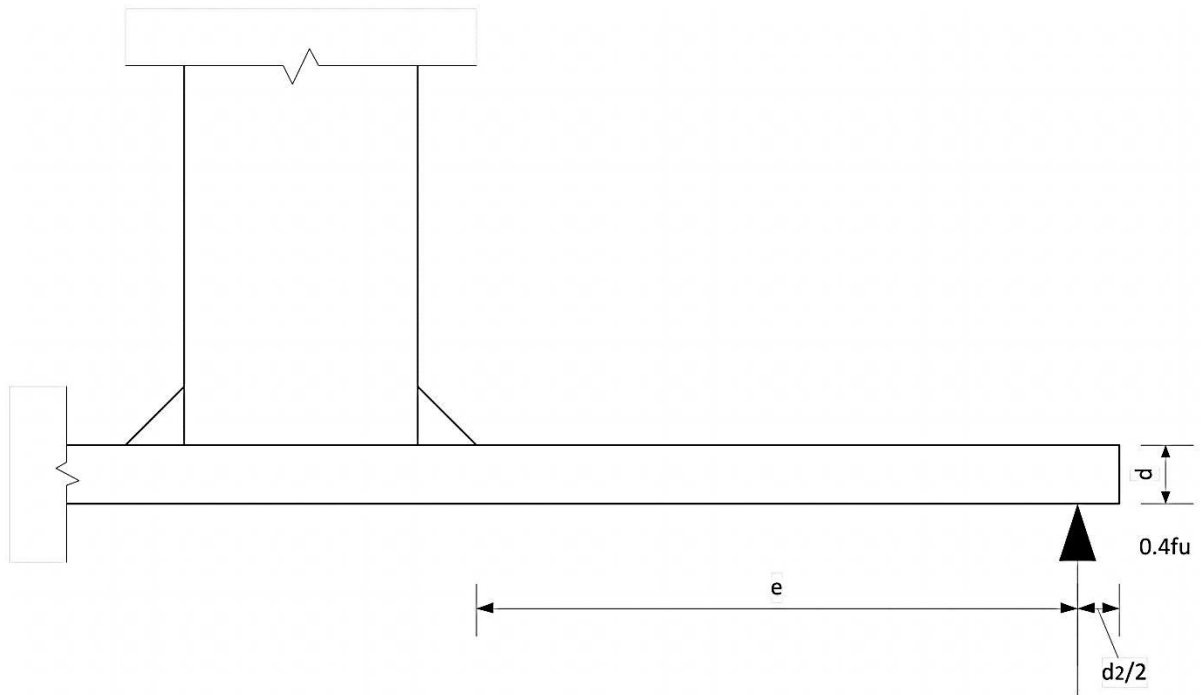


Figure 117 Simplified forces acting on the edge of the base plate.

$$M_{uz} = C_u e = 0.4f_{cu} b d_2 e = 2.756 \text{ kNm} = 2\,755\,575.2 \text{ Nmm}$$

Now it is possible to find the thickness of the base plate by using the following method:

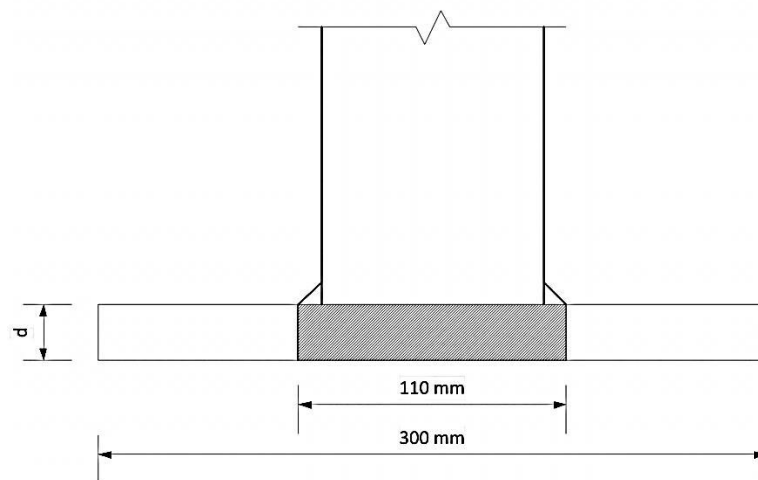


Figure 118 Base plate viewed from the longitudinal side.

The following properties (Z_{pl} and Z_e) can be found from the effective cross section. The effective cross section was found from Figure 119.

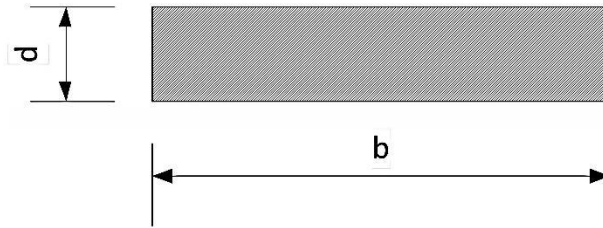


Figure 119 Effective cross-section of the base plate.

Where $b = 110 \text{ mm}$ and d is to be found.

$$Z_{pl} = bd^2/4 = 110d^2/4 = 27.5d^2$$

$$Z_e = bd^2/6 = 110d^2/6 = 18.333d^2$$

These properties can be used with the bending moment resistance equations to find the thickness d :

$$\text{Class 1: } M_r = \phi Z_{pl} f_y \quad (\text{SANS 10162-1:2005 13.5 a)})$$

And

$$\text{Class 3: } M_r = \phi Z_e f_y \quad (\text{SANS 10162-1:2005 13.5 b)})$$

$$\text{Where } M_r = M_{uz} = 2\,755\,575.2 \text{ Nmm}$$

Calculating d :

$$\text{Class 1: } 2\,755\,575.2 = 0.9 \cdot 27.5d^2 \cdot 300$$

$$\therefore d = 19.26 \text{ mm}$$

$$\text{Class 3: } 2\,755\,575.2 = 0.9 \cdot 18.333d^2 \cdot 300$$

$$\therefore d = 23.59 \text{ mm}$$

Choose the base plate thickness as 20 mm and take care not to load frames one side at a time.

The next step is to find out whether the weld connecting the column to the base plate is sufficient enough to handle the forces and stresses generated by the applied weights. To be conservative 5 mm welds will be used in the design. The resistance of welds depends on the weld length. The weld length around $100 \times 100 \times 6 \text{ mm}$ square hollow section columns is:

$$4 \times 100 \text{ mm} = 400 \text{ mm}$$

The force that the weld has to resist can be seen in Figure 120.

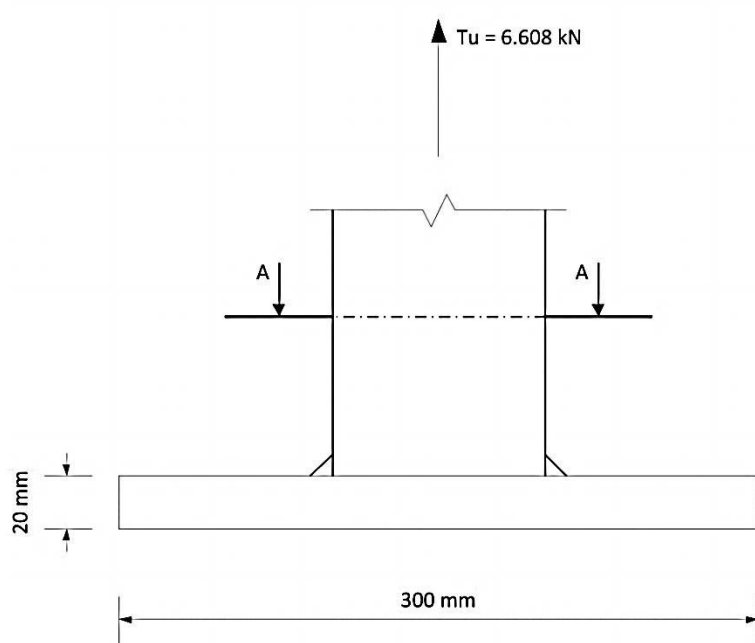


Figure 120 Longitudinal side view of the welds of the base plate.

Looking Figure 121, which represents Section A-A from Figure 120.

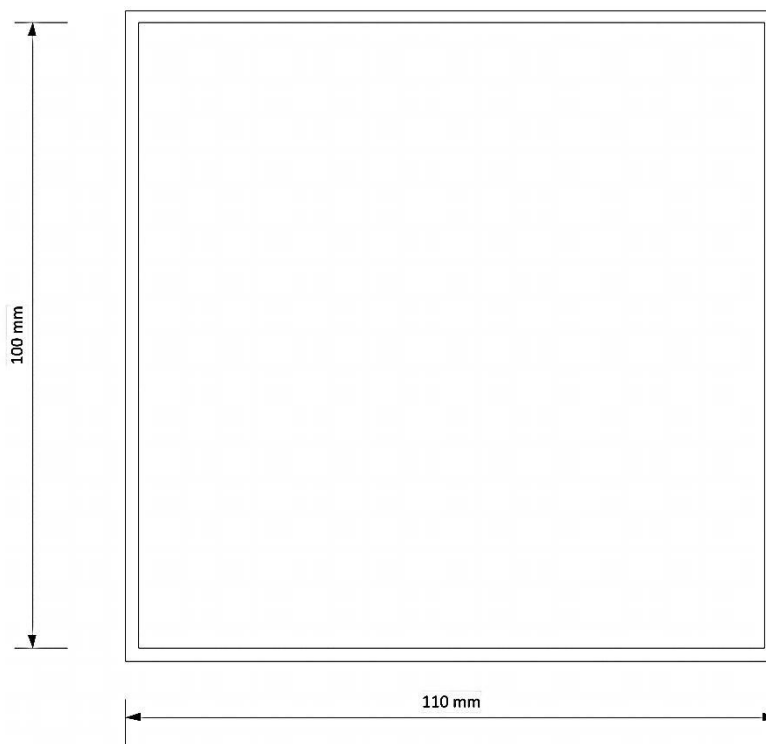


Figure 121 Plan view of the base plate welds

$$f_y = 300 \text{ MPa}$$

$$f_u = 450 \text{ MPa}$$

$$A_n = 110 \times 110 \text{ mm} - 100 \times 100 \text{ mm} = 2100 \text{ mm}^2$$

$$A_g = 100 \times 100 \text{ mm} = 10\,000 \text{ mm}^2$$

The tensile resistance of the weld can be calculated by using the following method:

$$T_r = \phi_w A_n f_u = 0.67 \cdot 2100 \cdot 450 = 633.15 \text{ kN} \quad (\text{SANS 10162-1:2005 13.13.3.2})$$

Or

$$T_r = \phi A_g f_y = 0.9 \cdot 10\,000 \cdot 300 = 2\,700 \text{ kN} \quad (\text{SANS 10162-1:2005 13.13.3.3})$$

In both cases $T_r \gg T_u$, meaning welds were sufficient enough to handle the tensile forces generated in the frame.

The next step was to determine whether the welds were sufficient in resisting the bending moment between the column and the base plate. After a Prokon analysis was done on the frame, it could be seen that the maximum bending moment generated between one of the columns and the base plate was $M_{max} = 0.954 \text{ kNm}$. This moment was generated when the frames were loaded one side at a time, which would be the worst case scenario. The loading can be modelled by Figure 122.

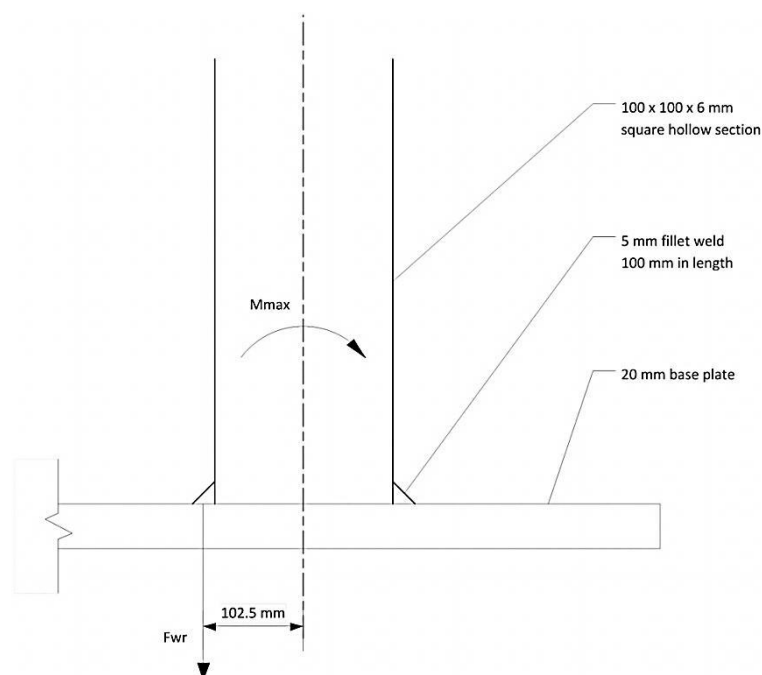


Figure 122 Side view of the forces resisted by the base plate welds.

According to Table 6.7 from the South African Steel Construction Handbook a 5 mm fillet weld can resist 1.08 kN/mm if the direction of the force applied $\geq 62^\circ$ and with the weld length being 100 mm the force resistance of the weld (F_{wr}) can be calculated as follows:

$$F_{wr} = 1.08 \times 100 = 108 \text{ kN}$$

This would lead to the following moment resistance (M_{wr}) of the weld:

$$M_{wr} = 108 \text{ kN} \times 0.1025 \text{ mm} = 11.07 \text{ kNm}$$

$$M_{wr} = 11.07 \text{ kNm} > M_{max} = 0.954 \text{ kNm} \therefore \text{OK}$$

In this case the welds are sufficient enough to withstand the bending moment created by the eccentric loading of the steel frames.

B.13 Detail H – Frictionless Connection

In order to connect the specimens to the top cable, to each other in series and to the bottom threaded rod a frictionless connection has to be designed. This connection should allow free rotational movement, meaning no internal moments should be generated. The most important reason for having no internal moments is so that the concrete specimens can be in the purest tensile state possible. These factors led to the following design:

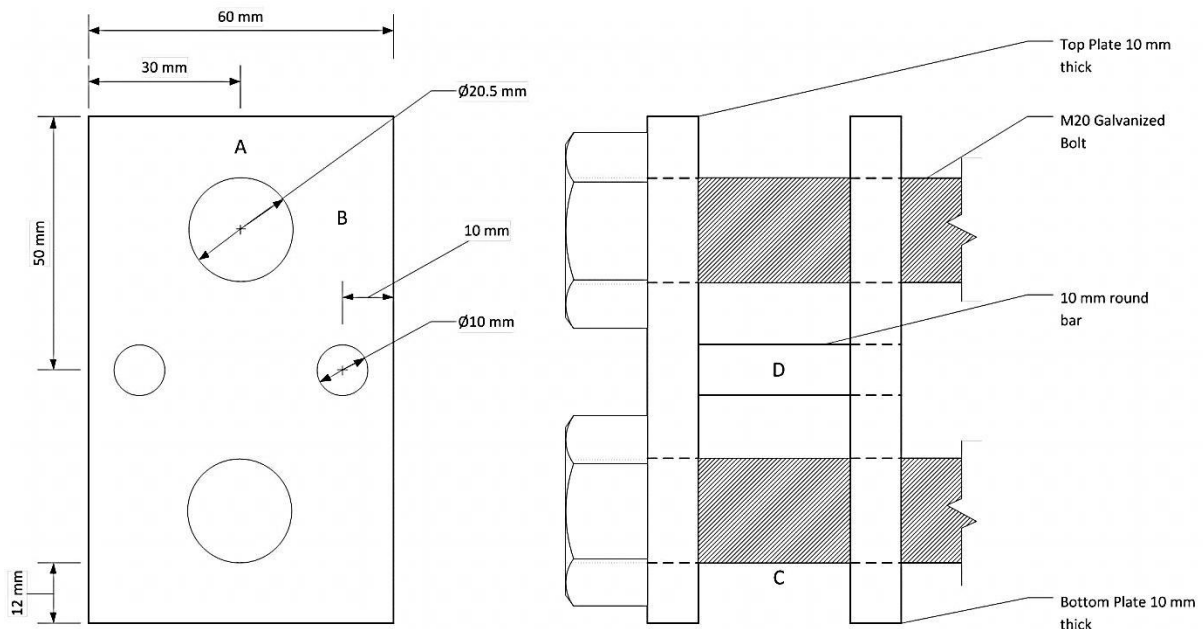


Figure 123 Graphical presentation of the frictionless connection.

From inspection of Figure 123 it can be seen that the only restriction the connection provides is in the longitudinal direction and that no internal moments will be generated during its use. The simple and practical design made the connection simple to manufacture and assemble. The 20 mm bolts would pass through the chain links and would provide the necessary resistance to act as a connection. The 10 mm round bar was pressed into a hole in the bottom plate to act as a spacer between the two plates. The only aspect that remained was to determine whether the connection would have the capacity to handle the forces exerted on it. This could be determined by looking at the most critical aspects:

Section A: Bearing Capacity

$$B_r = 3\phi_{br} t d f_u = 3 \cdot 0.67 \cdot 10 \cdot 20.5 \cdot 450 = 185.4 \text{ kN} \quad (\text{SANS 10162-1:2005 13.10 c})$$

Or

$$B_r = \phi_{br} a t f_u = 0.67 \cdot 12 \cdot 10 \cdot 450 = 36.18 \text{ kN} > 24.445 \text{ kN} \therefore \text{OK}$$

The bearing capacity is taken as the lesser of the two capacities as the design value.

Section B: Tensile Capacity

$$F_r = \sigma A = 300 \cdot 2 \cdot (19.75 \cdot 10) = 118.5 \text{ kN} > 24.445 \text{ kN} \therefore \text{OK}$$

The critical section is the webs on either side of the 20.5 mm hole.

Section C: Bending Capacity of Bolts

$$M_u = (24.445)(0.015) = 0.367 \text{ kNm}$$

The bending moment resistance can be determined the following way:

$$M_r = \phi Z_{pl} f_y = \phi \cdot d^3 / 6 \cdot f_y = 0.9 \cdot 20^3 / 6 \cdot (0.8 \cdot 830) = 0.797 \text{ kNm} \quad (\text{SANS 10162-1:2005 13.5 a})$$

$$M_r = 0.797 \text{ kNm} > 0.367 \text{ kNm} \therefore \text{OK}$$

Section D: Axial Capacity of Round Bar

$$\lambda = \frac{KL}{r} \sqrt{\frac{f_y}{\pi^2 E}} = \frac{0.5 \cdot 30}{2.5} \sqrt{\frac{300}{\pi^2 \cdot 200 \times 10^3}} = 0.07397 \quad \text{with } r = \sqrt{\frac{I}{A}} = \sqrt{\frac{\pi \cdot 5^4}{4 \cdot \pi \cdot 5^2}} = 2.5 \text{ mm}$$

$$C_r = \phi A f_y (1 + \lambda^{2n})^{-1/n} \quad \text{with } n = 1.34$$

$$= 0.9 \cdot \pi \cdot 5^2 \cdot 300(1 + 0.07397^{2.68})^{-1/1.34}$$

$$= 21.191 \text{ kN}$$

The 20 mm hex nuts used to tighten the bolts were tightened by hand. From the calculations above it can be seen that the frictionless connection had the capacity to withstand the tensile forces generated by the steel frames and loading weights.

B.14 Detail I – Weld Designs

The welds for the base plate were already designed at the end of Chapter B.12. These welds mostly experienced normal forces and bending moments. The rest of the welds used in the frame mostly experienced shear forces. The shear capacity of 5 mm fillet welds with the direction of the forces being in the same direction of the welds is:

$$V_{\text{welds}} = 0.762 \text{ kN/mm}$$

Because of the robust and simplistic design of the frames, all the welds subjected to shear forces were 100 mm of length. This means:

$$V_{\text{welds}} = 100 \times 0.762 \text{ kN/mm} = 76.2 \text{ kN}$$

The maximum shear force generated in the frames can be found in the bottom connecting beam.

$$V_{\text{max}} = 24.445 \text{ kN} < V_{\text{welds}} = 76.2 \text{ kN} \therefore \text{all 5 mm fillet welds are sufficient.}$$

Appendix C

C. Basic Kinematic Assumption

This section will discuss the basic kinematic assumption of beams in flexure. In the simplified engineering theory of bending it is needed to establish a relation among the applied bending moment, the cross – sectional properties of a member and the internal stresses and deformations. Consider a horizontal prismatic beam, consisting of any elastic material, having a cross section with a vertical axis of symmetry as presented by Figure 124.

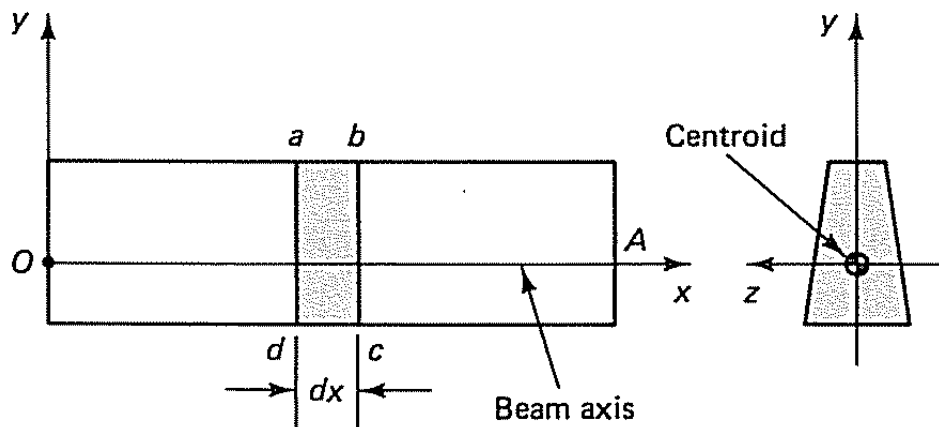


Figure 124 Horizontal prismatic beam with cross-section included.

The horizontal line through the centroid of the cross section will be referred to as the axis of the beam. A typical element of the beam is considered, being identified as $abcd$. The beam is subjected to equal end moments M_z acting around the z -axis as shown in Figure 125.

axial fibre deformation, and to replace ds by dx . Therefore by dividing $d\hat{u}$ with ds it can be approximated as

$$\frac{du}{dx} = \varepsilon_x = -\kappa y$$

Using Hooke's Law

$$\sigma_x = E\varepsilon_x = -E\kappa y$$

with y being able to assume both positive and negative values. There are two non-trivial equations of equilibrium available to solve the beam flexure problem. One of these equations determines the origin for y and the other one completes the solution for the flexure formula. Using the first one of these equations, requiring that in pure bending, the sum of all forces at a section in the x – direction must vanish, one has

$$\rightarrow \Sigma F_x = 0:$$

$$\int \sigma_x dA = 0$$

Which can be rewritten as

$$\int -E\kappa y dA = -E\kappa \int y dA = 0$$

By definition $\int y dA = \bar{y}A$, where \bar{y} is the distance from the origin to the centroid of an area A . Since the integral equals zero and $A \neq 0$, that means that $\bar{y} = 0$. That means that the z – axis must pass through the centroid of a section. This means that the normal stresses and strains are zero along the z -axis. Based on this result, linear variation in strain is shown below in Figure 126 along with the corresponding stress distribution in accordance with Hooke's Law.

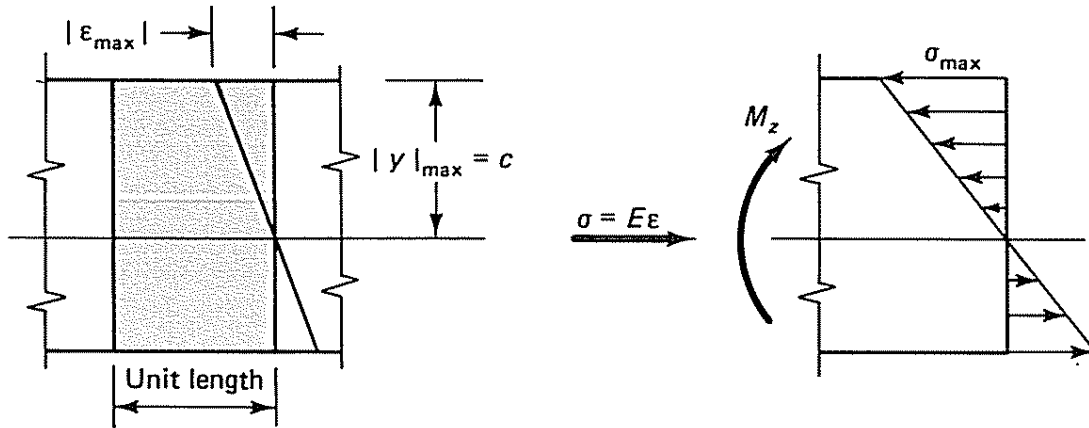


Figure 126 Stress distribution of prismatic beam in flexure.

Note that both the absolute maximum strain ϵ_{max} and the absolute maximum stress σ_{max} occur at the largest value of y . To complete the derivation of the flexure formula, the second relevant equation of equilibrium must be brought in: the sum of the externally applied and internal resisting moment should be equal to zero, in other words be in equilibrium. Looking at the beam segment in Figure 127:

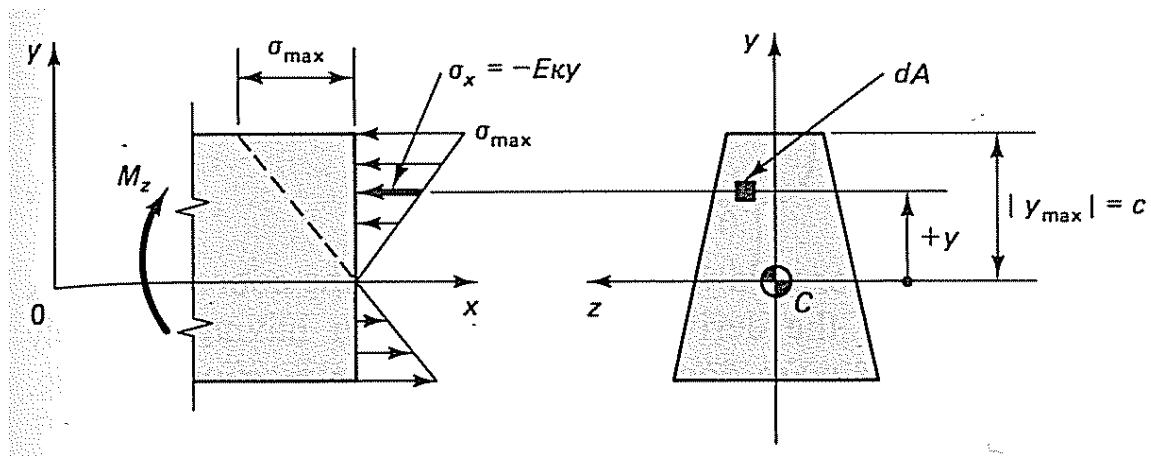


Figure 127 Stress distribution of prismatic beam in flexure with parameters defined.

$\sum M_0 = 0$:

$$M_z - \int_A \underbrace{Eky}_{\text{stress}} \underbrace{dA}_{\text{area}} \underbrace{y}_{\text{arm}} = 0$$

This gives

$$M_z = Ek \int y^2 dA = EkI_z$$

$$\therefore \kappa = \frac{M_z}{EI_z}$$

This means that

$$\sigma_x = -\frac{M_z}{I_z}y$$

This is a well-known expression is used throughout the academic circles in order to determine the normal stress acting on a section given an applied moment. Conversely it can also be used to determine the moment applied if the normal stresses are known. It is this principle that will be used to determine the moment capacity of SFRSCC beams in flexure. Throughout this research paper it has been mentioned many times that the SFRSCC mix has been designed for strain softening. Figure 128 will give a clear presentation of the stress-strain behaviour of a SFRSCC beam in flexure that has been designed to exhibit strain-softening behaviour.

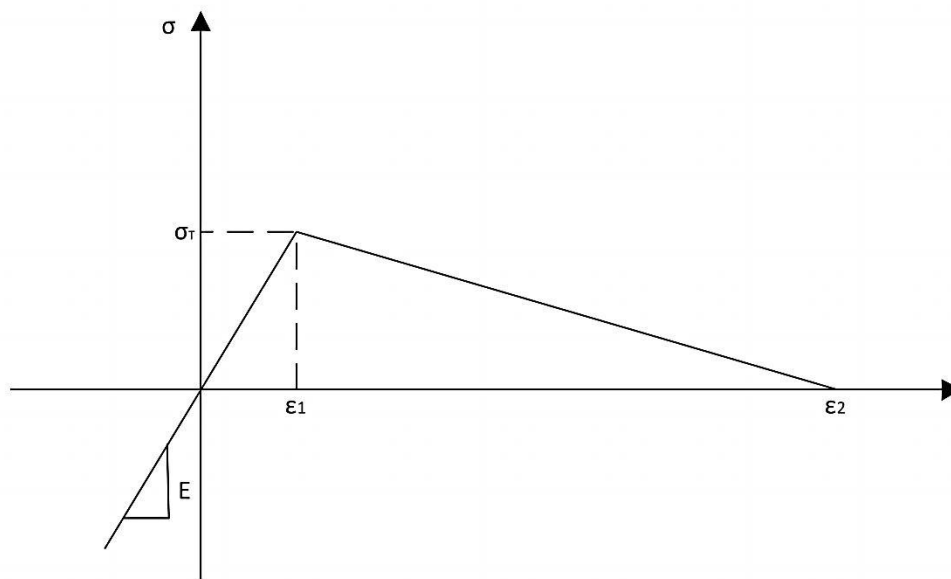


Figure 128 Graphical presentation of strain softening depicted linearly.

Figure 128 shows a typical case of tensile strain-softening behaviour that occurs in a SRFC beam in flexure. It is assumed that the material will fail in tension long before it will fail in compression, so in this case it can be assumed that the concrete is infinitely strong in compression. Upon inspection of the tensile stresses it can be seen that a maximum stress σ_T has been reached and that the steel fibres have provided some resistance, represented by the downward slope, until zero is reached.

From the beam theory it was seen that

$$\varepsilon_x = -\kappa y$$

And that

$$\sigma_x = -E\kappa y$$

By looking at the strain equation above it can be assumed that strain is a function of curvature, which means that the strains will increase as the curvature increases. By taking this into account and combining it with the strain softening behaviour presented above it is possible to distinguish three different zones as the beam experiences different stages of flexure:

1. $0 < \varepsilon_x \leq \varepsilon_1$
2. $\varepsilon_1 < \varepsilon_x \leq \varepsilon_2$
3. $\varepsilon_2 < \varepsilon_x$

In the expressions above ε_x represents the tensile strain that is dependent on the curvature κ_x , which increases. The first zone is in the elastic zone before failure takes place and the curvature hasn't caused the material to fail yet. As the curvature increases failure takes place at strain ε_1 and the resisting tensile stress is at its highest, meaning it becomes the ultimate tensile strength σ_T . The second zone is when initial failure already occurred and the resisting stresses decrease until it reaches zero at strain ε_2 . The third zone is when the curvature has increased to such an extent that the beam starts to fail.

The next step is to determine the moment resistances provided by the resisting stresses in the beam through different stages of flexure.

C.1 Zone 1:

$$0 < \varepsilon_x \leq \varepsilon_1$$

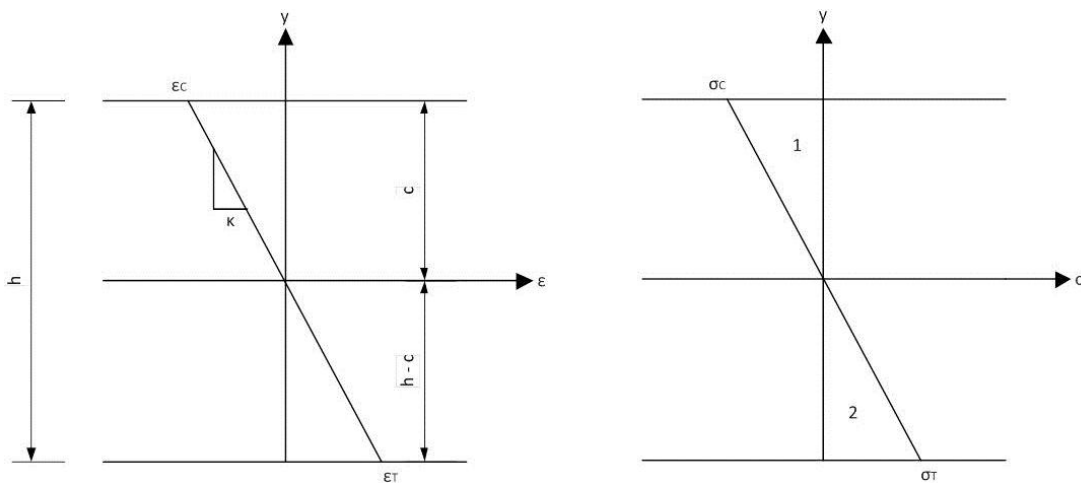


Figure 129 Strain - stress distribution in a section of a beam in flexure exhibiting purely elastic behaviour.

Note that the geometry depicting the stresses were numbered as 1 and 2.

$$\varepsilon = -\kappa y \quad \therefore \quad \kappa = -\frac{\varepsilon}{y} = -\frac{(-\varepsilon_1)}{c}$$

With $c = \frac{h}{2}$

$$\kappa = \frac{2\varepsilon_1}{h}$$

Using Hooke's Law:

$$\sigma = -E\kappa y$$

$$\sigma_c = -E(c) \left(\frac{\varepsilon_1}{c} \right) = -E\varepsilon_1$$

$$\sigma_T = -\sigma_c = E\varepsilon_1$$

By using equilibrium it is possible to determine the moment resistance of the section in the same method as Section 2 – Beam Section Theory. Determining the forces and acting moments:

$$F1 = \frac{1}{2}(c)(\sigma_c)(b) = \frac{1}{2} \left(\frac{h}{2} \right) (-E\varepsilon_1)(b) = -\frac{E\varepsilon_1bh}{4}$$

$$Arm1 = \frac{2}{3}c = \frac{2}{3} \cdot \frac{h}{2} = \frac{h}{3}$$

$$M1 = F1 \times Arm1 = -\frac{E\varepsilon_1bh^2}{12} = \frac{E\varepsilon_1bh^2}{12} \quad \mathcal{U}$$

$$F2 = \frac{1}{2}(h-c)(\sigma_T)(b) = \frac{1}{2} \left(h - \frac{h}{2} \right) (E\varepsilon_1)(b) = \frac{E\varepsilon_1bh}{4}$$

$$Arm2 = -\frac{2}{3}(h-c) = -\frac{2}{3} \cdot \frac{h}{2} = -\frac{h}{3}$$

$$M2 = F2 \times Arm2 = -\frac{E\varepsilon_1bh^2}{12} = \frac{E\varepsilon_1bh^2}{12} \quad \mathcal{U}$$

Through equilibrium:

$$\rightarrow \Sigma F_x = 0:$$

$$F1 + F2 = -\frac{E\varepsilon_1bh}{4} + \frac{E\varepsilon_1bh}{4} = 0$$

$$\cup \Sigma M = 0:$$

$M_R - M1 - M2 = 0$, where M_R is the resisting moment.

$$\therefore M_R = M1 + M2 = \frac{E\varepsilon_1bh^2}{6}$$

C.2 Zone 2:

$$\varepsilon_1 < \varepsilon_x \leq \varepsilon_2$$

Following the same process as Zone 1.

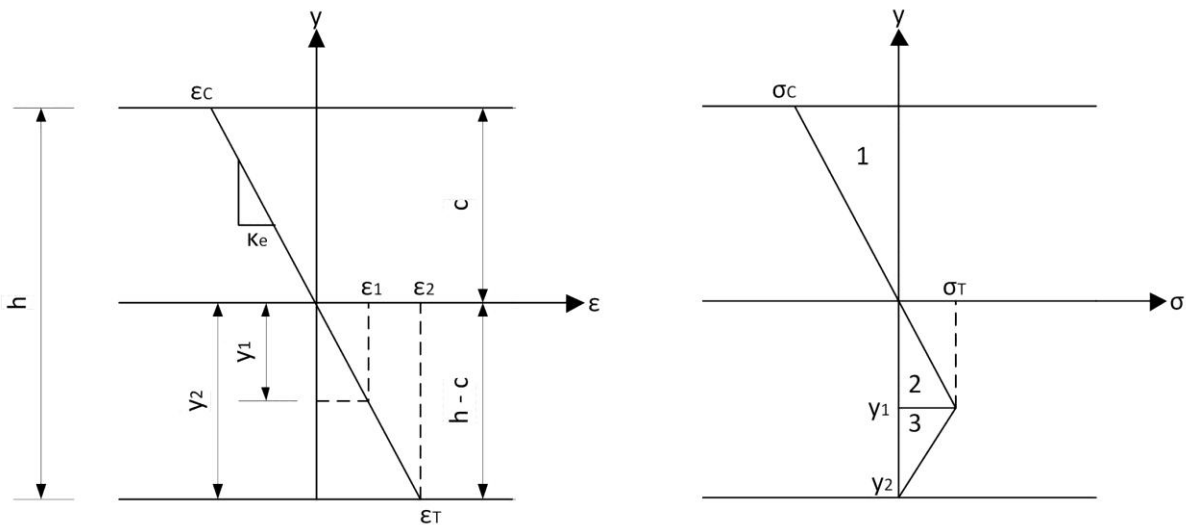


Figure 130 Strain - stress distribution in a section of a beam in flexure before initial failure.

It can be seen that:

$$\kappa_i = \frac{2\varepsilon_1}{h}, \text{ where } \kappa_i \text{ is the initial kappa}$$

$$h - c = y_2$$

$$\varepsilon_2 = \varepsilon_T$$

The initial kappa κ_i is the part in flexure where the elastic behaviour changes because of the initial failure of the beam. The position of the Neutral Axis will now change in order to retain equilibrium in the beam.

It is known that

$$\kappa = -\frac{\varepsilon}{y}$$

It can therefore be derived

$$\kappa_e = -\frac{\varepsilon_1}{(-y_1)} = -\frac{\varepsilon_T}{(-y_2)}, \text{ but } \varepsilon_T = \varepsilon_2$$

$$\therefore \kappa_e = \frac{\varepsilon_1}{y_1} = \frac{\varepsilon_2}{y_2} = \frac{\varepsilon_2}{h-c}$$

$$\therefore \kappa_e \leq \frac{\varepsilon_2}{h-c}, \text{ where } \kappa_e \text{ is the end kappa.}$$

The end kappa κ_e is the part in flexure just before the steel fibres offer no resistance. That means that it is the end of the zone where the strains range between ε_1 and ε_2 .

$$\varepsilon_c = -\kappa_e c \therefore \sigma_c = -E\kappa_e c = -Ec \left(\frac{\varepsilon_2}{h-c} \right) = -\frac{Ec\varepsilon_2}{h-c}$$

By using equilibrium it is possible to determine the moment resistance of the section in the same method as Section 2 – Beam Section Theory. Determining the forces and acting moments:

$$F1 = \frac{1}{2}(\sigma_c)(c)(b) = \frac{1}{2} \left(-\frac{Ec\varepsilon_2}{h-c} \right) (c)(b) = -\frac{Ec^2\varepsilon_2 b}{2(h-c)}$$

$$Arm1 = \frac{2c}{3}$$

$$M1 = \frac{2c}{3} \left(-\frac{Ec^2\varepsilon_2 b}{2(h-c)} \right) = -\frac{Ec^3\varepsilon_2 b}{3(h-c)} = \frac{Ec^3\varepsilon_2 b}{3(h-c)} \text{ } \mathcal{U}$$

$$F2 = \frac{1}{2}(\sigma_T)(y_1)(b) = \frac{\sigma_T}{2} \left(\frac{\varepsilon_1}{\kappa_e} \right) b = \frac{\sigma_T \varepsilon_1 b}{2} \left(\frac{h-c}{\varepsilon_2} \right) = \frac{\sigma_T \varepsilon_1 b (h-c)}{2\varepsilon_2}$$

$$Arm2 = \frac{2y_1}{3} = \frac{2\varepsilon_1}{3\kappa_e} = \frac{2\varepsilon_1(h-c)}{3\varepsilon_2}$$

$$M2 = \left(\frac{\sigma_T \varepsilon_1 b (h-c)}{2\varepsilon_2} \right) \left(\frac{2\varepsilon_1(h-c)}{3\varepsilon_2} \right) = \frac{\sigma_T \varepsilon_1^2 b (h-c)^2}{3\varepsilon_2^2} \text{ } \mathcal{U}$$

$$F3 = \frac{1}{2}(\sigma_T)(y_2 - y_1)(b) = \frac{1}{2}((h-c) - y_1)(\sigma_T)(b) = \frac{\sigma_T b}{2} \left((h-c) - \frac{\varepsilon_1(h-c)}{\varepsilon_2} \right)$$

$$\begin{aligned} Arm3 &= y_1 + \frac{(y_2 - y_1)}{3} = \frac{\varepsilon_1}{\kappa_e} + \frac{1}{3} \left((h-c) - \frac{\varepsilon_1(h-c)}{\varepsilon_2} \right) = \frac{\varepsilon_1(h-c)}{\varepsilon_2} + \frac{h-c}{3} - \frac{\varepsilon_1(h-c)}{3\varepsilon_2} \\ &= \frac{2\varepsilon_1(h-c)}{3\varepsilon_2} + \frac{h-c}{3} = \frac{2\varepsilon_1(h-c) + \varepsilon_2(h-c)}{3\varepsilon_2} = \frac{(h-c)(2\varepsilon_1 + \varepsilon_2)}{3\varepsilon_2} \end{aligned}$$

$$M3 = \frac{\sigma_T b(h-c)}{2} \left(1 - \frac{\varepsilon_1}{\varepsilon_2}\right) \left(\frac{(h-c)(2\varepsilon_1 + \varepsilon_2)}{3\varepsilon_2}\right) = \frac{\sigma_T b(h-c)^2 \left(1 - \frac{\varepsilon_1}{\varepsilon_2}\right) (2\varepsilon_1 + \varepsilon_2)}{6\varepsilon_2}$$

Through equilibrium:

$$\rightarrow \Sigma F_x = 0:$$

$$F1 + F2 + F3 = 0$$

$$-\frac{Ec^2\varepsilon_2 b}{2(h-c)} + \frac{\sigma_T \varepsilon_1 b(h-c)}{2\varepsilon_2} + \frac{\sigma_T b}{2} \left((h-c) - \frac{\varepsilon_1(h-c)}{\varepsilon_2} \right) = 0$$

After simplification:

$$0 = (\sigma_T - E\varepsilon_2)c^2 - 2\sigma_T h + \sigma_T h^2$$

Solving for c:

$$c = \frac{-2\sigma_T h \pm \sqrt{(-2\sigma_T h)^2 - 4(\sigma_T - E\varepsilon_2)(\sigma_T h^2)}}{2(\sigma_T - E\varepsilon_2)}$$

After simplification

$$c = \frac{2\sigma_T h + \sqrt{4\sigma_T h^2 E\varepsilon_2}}{2(\sigma_T - E\varepsilon_2)}$$

Or

$$c = \frac{2\sigma_T h - \sqrt{4\sigma_T h^2 E\varepsilon_2}}{2(\sigma_T - E\varepsilon_2)}$$

$$\cup \Sigma M = 0:$$

$M_R - M1 - M2 - M3 = 0$, where M_R is the resisting moment.

$$M_R = \frac{Ec^3\varepsilon_2 b}{3(h-c)} + \frac{\sigma_T \varepsilon_1^2 b(h-c)^2}{3\varepsilon_2^2} + \frac{\sigma_T b(h-c)^2 \left(1 - \frac{\varepsilon_1}{\varepsilon_2}\right) (2\varepsilon_1 + \varepsilon_2)}{6\varepsilon_2}, \text{ with } c \text{ calculated above}$$

Looking at the points of flexure between κ_i and κ_e :

$$\kappa_i < \kappa_x \leq \kappa_e:$$

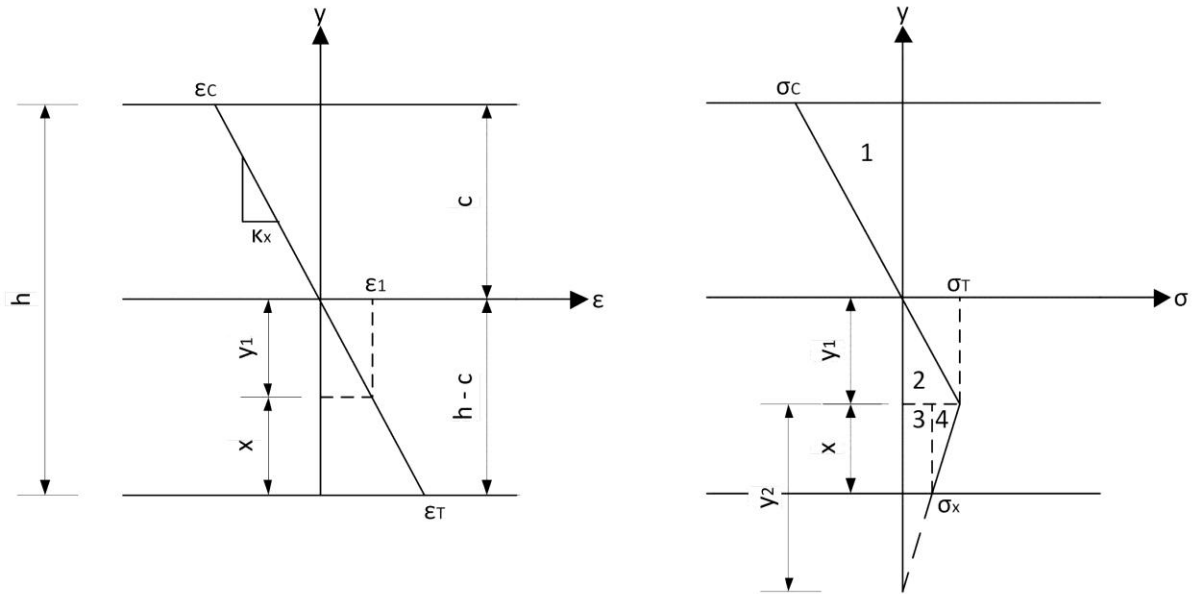


Figure 131 Strain - stress distribution in a section of a beam in flexure after initial failure.

$$\tan \theta = \frac{\sigma_T}{y_2} = \frac{\sigma_x}{y_2 - x} \therefore \sigma_x = \frac{\sigma_T(y_2 - x)}{y_2}$$

$$\varepsilon = -\kappa y \therefore \sigma = -E\kappa y$$

By using equilibrium it is possible to determine the moment resistance of the section in the same method as Section 2 – Beam Section Theory. Determining the forces and acting moments:

$$F1 = \frac{1}{2}(\sigma_c)(c)(b) = \frac{1}{2}(-E\kappa_x c)(c)(b) = -\frac{E\kappa_x c^2 b}{2}$$

$$Arm1 = \frac{2c}{3}$$

$$M1 = -\frac{E\kappa_x c^3 b}{3} = \frac{E\kappa_x c^3 b}{3} \text{ } \mathcal{U}$$

$$F2 = \frac{1}{2}(\sigma_T)(y_1)(b) = \frac{1}{2}(\sigma_T) \left(\frac{\varepsilon_1}{\kappa_x} \right) (b) = \frac{\sigma_T \varepsilon_1 b}{2\kappa_x}$$

$$Arm2 = \frac{2}{3}y_1 = \frac{2\varepsilon_1}{3\kappa_x}$$

$$M2 = \left(\frac{\sigma_T \varepsilon_1 b}{2\kappa_x} \right) \left(\frac{2\varepsilon_1}{3\kappa_x} \right) = \frac{\sigma_T \varepsilon_1^2 b}{3\kappa_x^2} \text{ } \mathcal{U}$$

$$F3 = (\sigma_x)(x)(b) = \sigma_x b x$$

$$Arm3 = y_1 + \frac{x}{2}$$

$$M3 = \sigma_x bx \left(y_1 + \frac{x}{2} \right) \cup$$

$$F4 = \frac{1}{2}(\sigma_T - \sigma_x)(x)(b) = \frac{(\sigma_T - \sigma_x)bx}{2}$$

$$Arm4 = y_1 + \frac{x}{3}$$

$$M4 = \frac{(\sigma_T - \sigma_x)bx}{2} \left(\frac{\varepsilon_1}{\kappa_x} + \frac{x}{3} \right) \cup$$

Through equilibrium:

$$\rightarrow \Sigma F_x = 0:$$

$$F1 + F2 + F3 + F4 = 0$$

And

$$\cup \Sigma M = 0:$$

$$M_R - M1 - M2 - M3 - M4 = 0, \text{ where } M_R \text{ is the resisting moment.}$$

The expressions above can all be rewritten so that they become dependent on κ_x . The solution of κ_x can be found through the data solving function of Microsoft Excel. From this solution the moment resistance can be determined for the κ_x obtained.

C.3 Zone 3:

$$\varepsilon_2 < \varepsilon_x$$

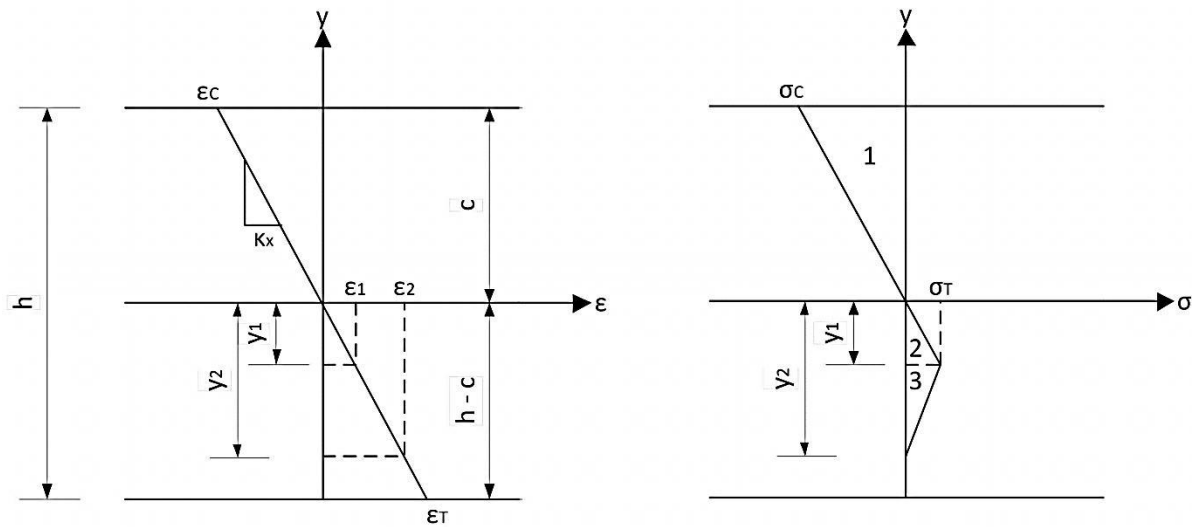


Figure 132 Strain - stress distribution in a section of a beam in flexure after total failure occurred.

In this case the flexure κ_x has extended beyond κ_e , which means that $\kappa_e < \kappa_x$.

$$\varepsilon = -\kappa y \therefore \sigma = -E\kappa y$$

$$\therefore \kappa_x = \frac{\varepsilon_1}{y_1} = \frac{\varepsilon_2}{y_2}$$

From Figure 132:

$$\frac{\sigma_c}{c} = \frac{\sigma_t}{y_1} \therefore y_1 = \frac{\sigma_t c}{\sigma_c}, \text{ where } \sigma_c = -E\kappa_x c$$

$$\therefore y_1 = \frac{\sigma_t c}{-E\kappa_x c} = -\frac{\sigma_t}{E\kappa_x} = \frac{\sigma_t}{E\kappa_x} \text{ downwards}$$

By using equilibrium it is possible to determine the moment resistance of the section in the same method as Section 2 – Beam Section Theory. Determining the forces and acting moments:

$$F1 = \frac{1}{2}(\sigma_c)(c)(b) = \frac{1}{2}(-E\kappa_x c)(c)(b) = -\frac{E\kappa_x c^2 b}{2}$$

$$Arm1 = \frac{2c}{3}$$

$$M1 = -\frac{E\kappa_x c^3 b}{3} = \frac{E\kappa_x c^3 b}{3} \curvearrowright$$

$$F2 = \frac{1}{2}(\sigma_T)(y_1)(b) = \frac{\sigma_T^2}{2E\kappa_x}$$

$$Arm2 = \frac{2y_1}{3} = \frac{2\sigma_T}{3E\kappa_x}$$

$$M2 = \left(\frac{\sigma_T^2}{2E\kappa_x}\right)\left(\frac{2\sigma_T}{3E\kappa_x}\right) \cup$$

$$F3 = \frac{1}{2}(\sigma_T)(y_2 - y_1)(b) = \frac{\sigma_T b(y_2 - y_1)}{2} = \frac{\sigma_T b\left(\frac{\varepsilon_2}{\kappa_x} - \frac{\sigma_T}{E\kappa_x}\right)}{2} = \frac{\sigma_T b\left(\frac{\varepsilon_2}{\kappa_x} - \frac{\sigma_T}{E}\right)}{2\kappa_x}$$

$$Arm3 = y_1 + \frac{y_2}{3} = \frac{\sigma_T}{E\kappa_x} + \frac{\varepsilon_2}{3\kappa_x} = \frac{1}{\kappa_x}\left(\frac{\sigma_T}{E} + \frac{\varepsilon_2}{3}\right)$$

$$M3 = \left(\frac{\sigma_T b\left(\frac{\varepsilon_2}{\kappa_x} - \frac{\sigma_T}{E}\right)}{2\kappa_x}\right)\left(\frac{1}{\kappa_x}\left(\frac{\sigma_T}{E} + \frac{\varepsilon_2}{3}\right)\right) \cup$$

Through equilibrium:

$$\rightarrow \Sigma F_x = 0:$$

$$F1 + F2 + F3 = 0$$

And

$$\cup \Sigma M = 0:$$

$$M_R - M1 - M2 - M3 = 0, \text{ where } M_R \text{ is the resisting moment.}$$

The expressions above can all be rewritten so that they become dependent on κ_x . The solution of κ_x can be found through the data solving function of Microsoft Excel. From this solution the moment resistance can be determined for the κ_x obtained.

From the calculations made in this sections it can be seen that the moment resistance depends on the flexure of the beam. Even though the whole process was quite laborious, it was shown that it is possible to determine the moment resistance of a SFRC beam designed for strain – softening. This makes it possible to design for pure SFRC members in flexure if desired. The only step that is left is to determine the parameters σ_T , σ_C , ε_1 and ε_2 , which can be acquired from experimental testing.